Universitat Politècnica de València

Escuela Técnica Superior de Ingenieros Industriales
Valencia Nanophotonics Technology Center

Ph.D. Thesis

Theoretical and experimental study of light-nanoparticle interactions in high efficiency solar cells

Author:
Frederic Cortés Juan

Directed by:
Dr. Pablo Sanchis Kilders
Dr. James Patrick Connolly

in collaboration with:
Dr. Carlos Sánchez Díaz

16th December 2015

.

In loving memory of José Cortés García
I wish you could have seen this finished...

.

"Success seems to be largely a matter
of hanging on after others have let go"
William Feather

(So now, mom, aren't you glad that I was such a stubborn child?)

"There is a driving force more powerful than steam,
electricity and atomic energy: The will".
Albert Einstein

(If only I had known this before becoming a photovoltaics specialist...)

In what year was one plus one?
The answer is: The amazing Ralph!
Ralph Wiggum

(My best advise ever: No matter what happens... **never stop smiling!**)

.

Too many people to be thankful to...
and too much gratitude to be summarised...

To my family

To V.M.
just because you truly love me

to Mari Carmen and Lisbeth
because you believed in me
when I needed it the most

To Óscar, Guillermo, Esther, James, Salva, Pablo and Carlos
for all the headaches we have had to see this thesis finished...

To all my colleagues at the NTC
for all the times you have encouraged me

To Stéphane Collin and his group at CNRS-LPN
as well as to his colleagues Jean-Paul Hugonin and Jean-Jacques Greffet
for their time and interest in my work and for all their valuable help

To all the difficulties, fake friends and disappointments
because you made me stronger and more self-confident than ever

.

Summary

This thesis studies the optical properties of random arrays of metal nano-particles in multi-layered substrates such as a solar cell, as well as the electro-optic consequences for those substrates.

This study differs from traditional models which assume independent spherical particles in an homogeneous medium. Moreover, the effects beyond the near-field range are studied because substrates thicker than 150μm are used.

The study in this thesis uses two main approaches:

- A theoretical approach based on simulations and analytical models. Starting with the traditional methods (Mie), alternatives are considered for considering the substrate effect, the shape of the nanoparticles as well as the effect of the surrounding nanoparticles. For this, the use of Green functions and the Sommerfeld identity are presented as interesting strategies against traditional numerical model that are not suitable due to the complexity of the system that leads to huge power, time and memory consumptions. Nevertheless, the analytical approach has its limits and difficulties, that are analysed in this thesis.

  The results obtained in the thesis are compared with experimental data and a critical analysis is performed to check the real suitability and the scope of this strategy for simulating these kinds of systems.

- An experimental approach, in which special attention has been paid to the self-aggregation method as a quick way of integrating the nanoparticles on the final device. Some issues have been detected and studied related with the degradation of the nanoparticles, and some strategies to minimise this effect are presented.

  Integrated samples have been prepared using different integration approaches. From the measurements and their analysis the influence of the substrate and other factors on the nanoparticle behaviour is confirmed, and the enhancement potential of the solar cell is studied.

This thesis has been carried out at Valencia Nanophotonics Technology Center (NTC, in Spain) partly in the context of the LIMA european project (FP7-ICT-2009.3.8) and has included a short term scientific mission at the Laboratory of Photonics and Nanostructures (CNRS-LPN) at Marcoussis (France).

.

Resumen

En esta tesis se realiza un estudio de las propiedades ópticas de agrupaciones aleatorias de nanopartículas metálicas cuando éstas se depositan en un sustrato multicapa como una célula solar, así como las consecuencias electroópticas sobre dicho sustrato.

Este estudio supone una diferencia importante con respecto a las hipótesis de modelos tradicionales en los que se suponen partículas individuales, perfectamente esféricas y en medios homogéneos. Además, estudia los efectos más allá del campo cercano al utilizar sustratos de más de 150μm de grosor.

El trabajo de esta tesis gira en torno a dos enfoques principales:

- Un enfoque más teórico basado en simulaciones y modelos analíticos. Partiendo de los métodos tradicionales (Mie), se estudian métodos para incluir el efecto del sustrato, de la forma de las partículas y el efecto de las partículas cercanas. Para este fin, el uso de funciones de Green y de la identidad matemática de Sommerfeld se presentan como alternativas de gran interés frente al uso de modelos numéricos, inviables dada la complejidad del sistema y los recursos de memoria y tiempo necesarios. Aún así, los modelos analíticos presentan sus propias limitaciones y dificultades que son analizadas en esta tesis.

  Las soluciones obtenidas con estos modelos se han comparado con datos experimentales y un análisis crítico se ha llevado a cabo para determinar el alcance y la fiabilidad de estas estrategias de simulación.

- Un enfoque más experimental, en el que se ha hecho especial hincapié en la autoagregación de capas finas como vía rápida para integrar las partículas en el dispositivo final. También se han estudiado los problemas asociados a la estabilidad de las nanopartículas con el tiempo y a cómo minimizar la degradación.

  Por otro lado, se han preparado varios dispositivos integrados siguiendo distintas estrategias y de cuyas medidas y análisis se ha confirmado el efecto del sustrato y otros factores sobre el comportamiento de las nanopartículas, así como estudiado la potencial mejora de la eficiencia en células solares.

Esta tesis se ha realizado en su mayoría en el Centro de Tecnología Nanofotónica de Valéncia (NTC, en España) enmarcada parcialmente en el proyecto europeo LIMA (FP7-ICT-2009.3.8) y ha incluido una estancia investigadora en el Laboratorio de Fotónica y Nanoestructuras (CNRS-LPN) en Marcoussis (Francia).

.

Resum

En aquesta tesi es realitza un estudi de les propietats òptiques d'agrupacions aleatòries de nanopartícules metàliques quan aquestes es depositen sobre un substrat multicapa com una cèl·lula solar, així com les consequències electroòptiques resultants en el substrat.

Aquest estudi presenta una diferència important amb les hipòtesi de models tradicionals en els quals es suposa una partícula tota sola, perfectament esfèrica i en un medi homogeni. A més a més, s'estudiaran els efectes més enllà del camp proper a l'utilitzar substrats de més de 150μm d'espessor.

El treball d'aquesta tesi es farà mitjançant dues estratègies principalment:

- Un enfocament més teòric emprant simulacions i models analítics. Començant amb models tradicionals (Mie), s'estudiaran estratègies per a incloure l'efecte d'un substrat, de la forma de les partícules així com el de la presència de partícules al voltant. Amb aquesta finalitat, les funcions de Green i la identitat matemàtica de Sommerfeld es presenten com unes eines de gran interés comparat amb l'ús de mètodes numèrics tradicionals, els quals tenen uns requeriments excessius de memòria i temps de càlcul. Amb tot, aquests models analítics també tenen les seues limitacions i dificultats que són estudiades en la tesi.

  Les solucions obteses amb aquests models s'han comparat amb dades experimentals i s'ha fet un anàlisi crític per determinar l'abast de la validesa i la fiabilitat d'aquestes estratègies de simulació.

- Un enfocament més experimental, en el qual s'ha posat l'accent en l'auto-agregació de pel·lícules fines com a estratègia per a l'integració de les partícules en el dispositiu final. També s'han estudiat els problemes associats a l'estabilitat de les partícules amb el temps així com vies per a minimitzar aquesta degradació.

  D'altra banda, s'han preparat diversos dispositius integrats mitjançant diferents estratègies i a partir de les mesures de les quals s'ha confirmat l'efecte del substrat i d'altres factors en el comportament de les nanopartícules i s'ha estudiat la potencial millora de l'eficiència de la cèl·lula solar.

Aquesta tesi s'ha dut a terme majoritàriament en el Centre de Tecnologia Nanofotònica de València (NTC) parcialment enmarcada en el projecte europeu LIMA (FP7-ICT-2009.3.8), i inclou la realització d'una estància al Laboratori de Fotònica i Nanoestructures (CNRS-LPN) en Marcoussis (França).

.

Table of contents

Chapter 1

Objectives and motivation

1.1 Sustainability and c-Si photovoltaics

In the last years of the 20th century, energy consumption has increased. As shown in fig.1.1, the energy consumption has doubled in the last 30 years. The ratio of biofuels and natural gas has not changed whereas the electricity production and the use of clean energies has increased. This has allowed to reduce oil and coal consumption. However, those still are the source of more than half of the energy consumed in 2012.

This increase of energy consumption, together with the limited amount of coal and oil that still predominate as energy source and together with the environmental issues related with the greenhouse effect, have made many goverments to develop roadmaps focused to reduce the negative effects of this energetic model.

This started with the Brundtland report *Our common future* in 1987 [2] defining the concept of sustainable development. From there, the principles to achieve that sustainable development were summarised in 1992 with the Rio Declaration on Environment and Development[3]. During the World Summit on Sustainable Development in Johannesburg in 2002, the Johannesburg declaration [4] was adopted by many countries.

Several organisations were created in order to coordinate efforts towards the objectives and principles of these declarations: The international Energy Agency[1] (from whose studies is taken fig.1.1), the american department of energy[2], the european World Energy Technology and climate Policy Outlook[3] with the Horizon 2020[4] are some examples for this. They all publish periodically reports with statistics and roadmap proposals.

In particular, Horizon 2020 is focused on research programmes that lead to *secure, clean and efficient energy* (whose last version can be found in [5]). From there, many research project have found their funding, including many topics in the renewable energy field.

One of these topics is the photovoltaic research. In fact, this technology has been highly developped in the last years with new technologies, but c-Si is

---

[1]www.iea.org
[2]www.energy.gov
[3]http://ec.europa.eu/research/energy
[4]http://horizon2020projects.com/
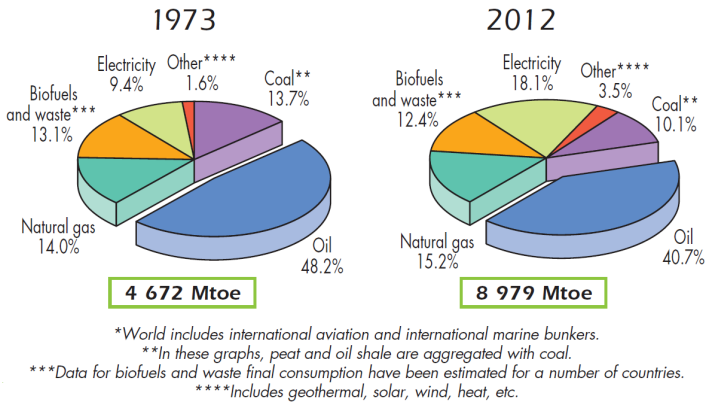
Figure 1.1: Increase of energy consumption in the last 30 years and final share of sources, according to the international Energy Agency[1].

still the main technology[6] and many efforts are done to make it more efficient. There are two approaches for this:

- Increasing solar cell efficiency. From this point of view, some international research projects have been carried out. One of these was the european project LIMA (Improve Photovoltaic efficiency by applying novel effects at the limits of light to matter interaction, FP7-ICT-2009.3.8). This thesis has partially been done in the scope of this project.

- Reducing costs in order to make it more profitable and competitive. Nowadays, about 51% of the cost of the solar cell is due to the wafer itself. The varying price of silicon is difficult to predict and the final saving costs are not well defined, but reducing the amount of material will reduce that cost for sure. That is why in the roadmaps this strategy is planned, as shown in fig.1.2

Reducing the thickness can reduce price, but also the solar cell efficiency. In fact, c-Si has a poor absorption of light when compared to other materials. This makes it necessary to include light trapping strategies in the solar cell device. Texturing does not seem a promising strategy for thinner cells because it is expected to increase the breakage during its fabrication [6]. Moreover, it has been demonstrated that texturing is not the best light trapping strategy and that the use of plasmonic technologies is an interesting approach that can improve the light trapping[7] beyond texturing.

For this reason, the research on nanotechnology seems a promising strategy because it can act on both of the proposed ways of improving the c-Si tech-
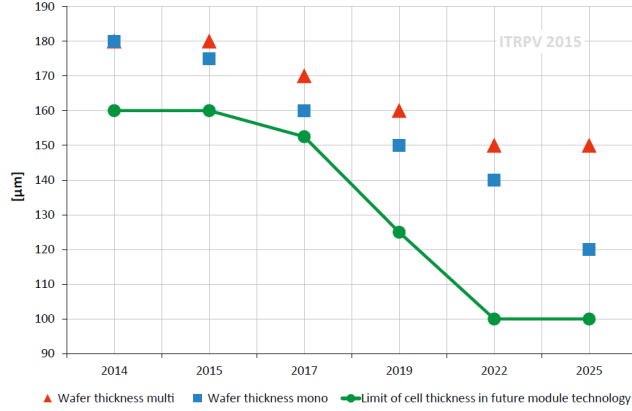
Figure 1.2: Expected thickness evolution in the as-cut c-Si wafers in the photovoltaic market[6].

nology: By enhancing the efficiency and by assuring a good light trapping for thinner (cheaper) solar cells.

1.2 The LIMA project

The aim of the LIMA project was to integrate different nanotechnologies enhancing light-matter interation on a high efficiency c-Si based solar cell. For that, an interdigitated back contact solar cell (IBC) was designed as a reference cell and two different strategies were integrated in order to improve the efficiency:

- A silicon oxide layer with Si quantum dots embedded formed by annealing a silicon rich oxide (SRO) ayer. The aim of this layer is to improve the overall efficiency of the solar cell by absorbing the low efficient ultraviolet (UV) photons and re-emit lower energy photons which are more efficiently converted to photocurrent by the solar cell in a technique called *down-shifting*[8]. Therefore, the SRO layer has photoluminiscence (PL) properties and acts as a down-shifting layer.

- A metal nanoparticle layer that increases the light trapping due its scattering properties. This thesis has contributed to the study of this layer. Initially, the LIMA project was supposed to focus only on the front side of the solar cell because of the particular structure of those kind of cell:

3

It has the front surface completely free and independent of the rest of the geometry, so it is suitable for easy integration of a nanoparticle layer[5].
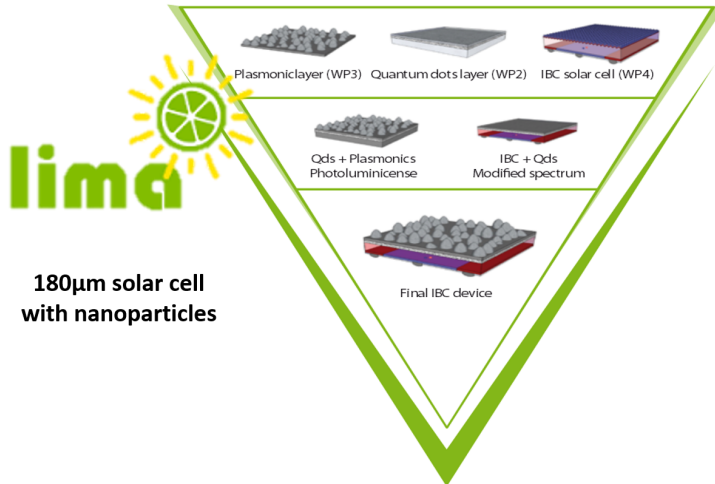
Figure 1.3: LIMA solar cell structure

Fig.1.3 summarises the integration strategy initially planned in LIMA. One of the particularities of LIMA structure is that the nanoparticles are usually applied in thin film technologies. In this case, however, the solar cell has between 150 and 180 μm. This implies that the mechanisms that are involved in the plasmonic effect have to be studied not only from the near field point of view, but also from the far field. Fig.1.4 summarises those phenomena.

In fig.1.4, three main terms are introduced: The scattering, the absorption and the plasmonic resonance condition. All these will be explained in detail in this thesis. For the moment, let us say that the scattering is the desired effect of the nanoparticle and that it is expected to be the main enhancement mechanism at long distances. The absorption losses, however, are undesirable but also unavoidable. They are related with the intrinsic resistivity of the material so usually noble metals are used. In this thesis, Silver (Ag) will be the choice because it is not as expensive as gold and it has a low resistivity. The resonance condition is specially important in the short range but it is closely related with the absorption losses as well as to other less known phenomena such as the Fano resonances that may appear.

One of the particularities of this thesis is that it combines different areas of knowledge: Energy, optics and communications. It is from the last area where

---

[5]As second reason, that was not finally developped in LIMA, was to study the nanoparticle-quantum dot interaction.
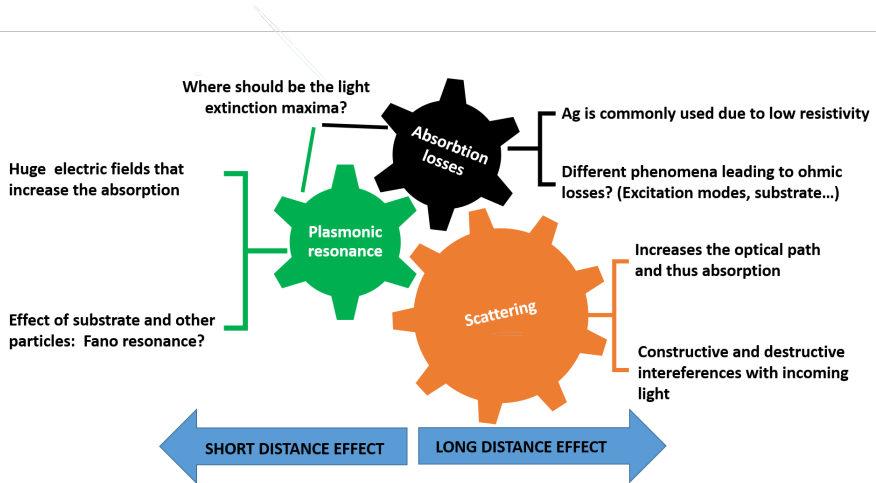
Figure 1.4: Main phenomena during plasmon generation in a nanoparticle

several of the analytical approaches are found. In fact, there is a huge interest on plasmonics and nanophotonics as this kind of phenomena open the door to new, smaller and more efficient devices such as antennas and sensors. But the applicability of the models is broader than those. In fact, many of the antena analysis strategies are valuable for our aim.

The main differences with traditional approaches is that in this thesis the structure to simulate is a randomly distributed array of non-spherical nanoparticles in an heterogeneous surrounding medium with different materials defining a multilayered structure that represent the solar cell. This implies several things, summarised in fig.1.5.

- The random aspect suggests the need of a statistical approach that has to be representative of the whole system.

- Different sizes of nanoparticles may lead to different independent behaviours.

- The random distribution also makes difficult the use of traditional numerical approaches such as the periodicity condition. Therefore, the amount of memory needed to solve many particles at the same time is impratically large.

- The interaction of the nanoparticles should not be completely neglected.

For our purpose, the analytical models that use trending mathematical approaches such as the Green Functions are particularly interesting because

5
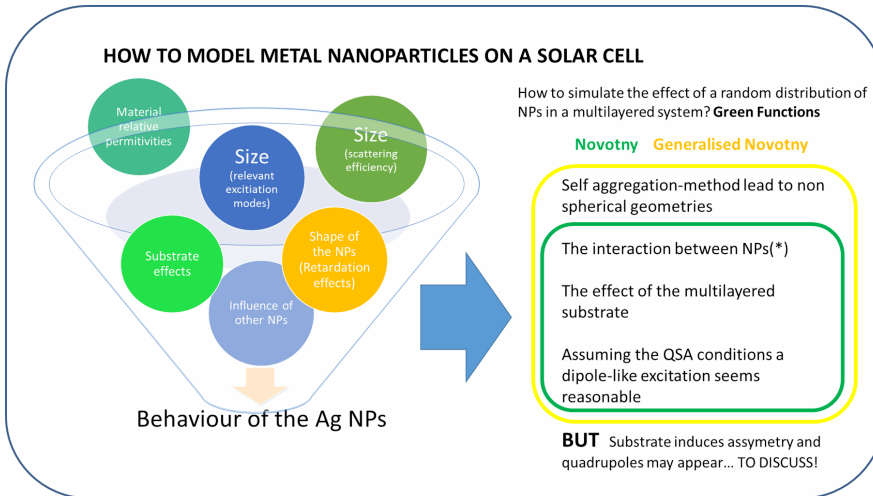
Figure 1.5: Different phenomena involved in the simulation of a nanoparticle.

they allow solving complex equations with matrix methods. This thesis includes a study of this method.

1.3 Thesis structure

In order to study how the nanoparticles can be applied and the consequences that they will have on a solar cell, the following structure has been followed in this thesis.

In chapter 2 the scientific fundamentals of photovoltaics are presented. From the discrete energy levels that lead to the energy bands, the electric properties of the materials are explained. This allows us to understand the particularities of the P-N junctions that make them suitable for photovoltaic devices. Moreover, some models and characteristic parameters are presented to define and compare the efficiency of solar cells, as well as strategies to understand the frequency dependent behaviour in the absorption of light and in the final collection probability.

In chapter 3, the concept of plasmon, surface plasmon polariton and localised surface plasmon are defined. Some simple equations and the dispersion diagram allow a qualitative comprehension of the radiation properties of each one. Then, more strategies are explained to study specifically the localised surface plasmon in metal nanoparticles: The definition of equivalent cross sections for quantifying its energy balance, the Mie approach for solving the light ex-

tinction in a sphere (both from the mathematical and from the physical point of view) as well as simplifications and deviations from Mie's solution such as the substrate effects or the Fano resonance.

In chapter 4, the frequency dependent scattering properties of metal nanoparticles is studied from well-known analytical models for the electrical properties such as the Drude model. Different regimes are found, including a resonant one, and the relative phase shift between the exciting source of light and the scattered field are shown in a simplified model.

Another study is presented showing how the Green functions are a powerful tool to solve the scattered field by a nanoparticle taking into account the effect of surrounding nanoparticles as well as a multilayered substrate. In particular, the substrate effect is analysed using the Sommerfeld identity and the numerical issues to solve the resulting expressions are explained.

A third study analyses the shape effect of the nanoparticles through a model developped for truncated spheres on a substrate that opens the door to a matrix polarisability that can be easily combined with the Green functions presented before. The main numerical difficulties and the range of validity of the solution is analysed.

Finally, the general trend on the extinction properties of spherical nanoparticles when modifying the size and the surrounding media is studied, as well as the relative importance of the different extinction modes. This defines a limit where the electric dipole is the main contribution.

Chapter 5 is focused on the fabrication techniques of nanoparticles. It is focused on the two techniques that are used in this thesis: The e-beam lithography and the self-aggregation, dealing with its particularities and limitations. Special attention has been paid to understand the self-aggregation method and how the models that have already been developped shed light on how to modify and control the resulting array of nanoparticles. Also, the image analysis leading to the statistics of random distributions and the strategies to summarise the main results and trends is also presented, as well as some limits on the fabrication techniques used in this thesis. Finally, a strategy to avoid the nanoparticles atmospheric degradation is presented without any need of a PECVD reactor. This approach, based on a flowable oxide resist, will be used for other purposes than a capping protective layer.

Chapter 6 summarises the integration of random arrays of nanoparticles on solar cells during the LIMA project, from the preliminary samples on glass, the first trials to estimate the effect on the final solar cell to the final integration. Different strategies are used in the final integrated samples: On the front side of the solar cell, embedded within an anti-reflection coating and finally on the back side. An analysis of the results is done, from the theory and the mechanisms that lead to those results as well as for the advantages and disadvantages for each integration strategy. An experimental validation of the Green's function

is presented, together with the underlying assumptions, and the results are discussed.

Finally, in chapter 7 an overall conclusion is presented and the new proposed research lines are explained.

Bibliography

[1] Key world energy statistics 2014. Free Download, 2014. URL http://www.iea.org/publications/freepublications/publication/keyworld2014.pdf.

[2] Gru Brundtland, Mansour Khalid, Susanna Agnelli, Sali Al-Athel, Bernard Chidzero, Lamina Fadika, Volker Hauff, Istvan Lang, Ma Shijun, Margarita Morino de Botero, et al. Our common future ('the brundtland report'). 1987.

[3] United Nations. Rio declaration on environment and development, June 1992. URL http://www.un-documents.net/rio-dec.htm.

[4] United Nations. Johannesburg declaration on sustainable development, September 2002. URL http://www.un-documents.net/jburgdec.htm.

[5] Horizon 2020. work programme 10: Secure, clean and efficient energy (revised). Technical report, European Commission, April 2015.

[6] International technology roadmap for photovoltaic (itrpv.net) results 2014. Technical report Rev.1., ITRPV, July 2015.

[7] Dennis M Callahan, Jeremy N Munday, and Harry A Atwater. Solar cell light trapping beyond the ray optic limit. *Nano letters*, 12(1):214–218, 2012.

[8] Zhizhong Yuan, Georg Pucker, Alessandro Marconi, Fabrizio Sgrignuoli, Aleksei Anopchenko, Yoann Jestin, Lorenza Ferrario, Pierluigi Bellutti, and Lorenzo Pavesi. Silicon nanocrystals as a photoluminescence down shifter for solar cells. *Solar Energy Materials and solar cells*, 95(4):1224–1227, 2011.

Chapter 2

Scientific background of photovoltaics

2.1   Atomic energy levels and band theory

The electrons in an atom spin around its nucleus without a fixed trajectory. However, electrons bound to atoms tend to occupy the space described by wavefunctions which are solutions to the Schrödinger equation. Those areas are known as atomic orbitals [1]. In Fig 2.1 it there are some examples of s orbitals (allowing up to 2 electrons), p orbitals (allowing up to 6 electrons). There exist other more complex orbitals, called d and f type, that can hold up to 10 and 14 electrons respectively.
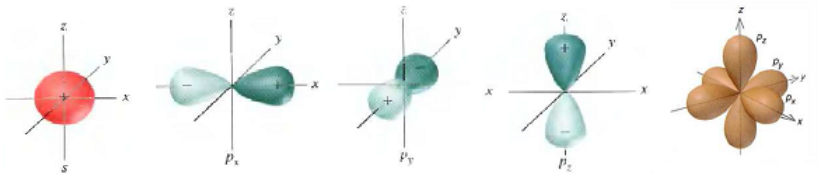
(a) 1s orbital   (b) Three degenerate (same energy) 2p orbitals and its combination

Figure 2.1: Example of different atomic orbitals

An essential parameter to define an electronic state (and thus its orbital) is its energy. Quantum mechanics stipulates that the energy of an electron is limited to certain discrete states. As a consequence, when an electron changes from an orbital of energy E_1 to another orbital with energy $E_2 > E_1$, it must absorb an exact amount of energy (energy quantum) of $\Delta E = E_2 - E_1$ (or release it if $E_1 > E_2$).

This energy conservation can be fulfilled e.g. by the absorption or emission of a photon [2].

Electromagnetic theory states that the energy of a photon (E, in Joules J) is related with its wavelength (λ, in nm) through the Planck constant ($h= 6.62 \cdot 10^{-34} J \cdot s$) and the light speed ($c = 3 \cdot 10^{17}$nm/s), as shown in Eq.2.1:

$$E = \frac{h \cdot c}{\lambda} \tag{2.1}$$

As a conclusion, in order to change the energy of an electron from E_1 to $E_2 > E_1$, this one absorbs a photon which wavelength corresponds to a energy $\Delta E = E_2 - E_1$. Any other photon with another wavelength will not produce any interaction.

When an electron occupies the state with lowest energy it is said to be in the ground state. When it absorbs a photon and reaches a more energetic state it is in an excited state. This process is reversible. Fig.2.2 shows schematically this phenomena [3]
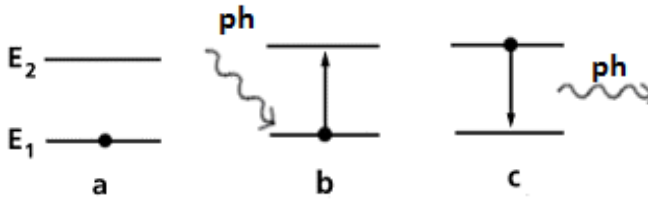
Figure 2.2: Light-matter interaction schema. In (a) the electron is in its ground state. In (b) an incoming photon is absorbed and the electron is excited. In (c) an excited electron returns to its fundamental state by releasing a quantum of energy as a photon.

This concept is specially important for the outer electrons in the atom, also called *valence* electrons and they interact and establish chemical bonds with another atoms. As they are in the higher occupied energy levels in the atom, they are the more exposed to the external perturbations.

The definition of the valence electron energy levels becomes much more complicated when chemical bonds of any kind are established (covalent, ionic or metallic). In fact, when a chemical bond is established between two atoms, their valence electron's orbitals (from now molecular orbitals) are modified, both in energy and shape. As a consequence, the energy of the valence electrons in molecular orbitals are different from the energy they would have in atomic orbitals[3]. This is shown in Fig.2.3

From what has been presented, it can be deduced that the higher the number of atoms that interact with chemical bonds is, the higher the number of molecular orbitals involved will be. Thus, the number of possible and different energy levels is increased even if the atoms correspond to the same element.
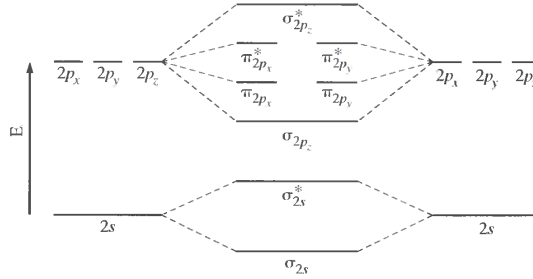
Figure 2.3: Molecular orbital splitting schema. When two identical atomic orbitals interact, new different energy levels are obtained by splitting the original orbitals.

Considering a bulk material, where uncountable atoms are bounded, uncountable energy levels will be found under this approach. Moreover, the splitting phenomena makes different consecutive energy levels closer as the number of atoms increase (see Fig.2.4). In fact, it can be considered that all the molecular orbitals form a continuous energy band. As they correspond to the energies of the valence electrons, it is called valence energy band.
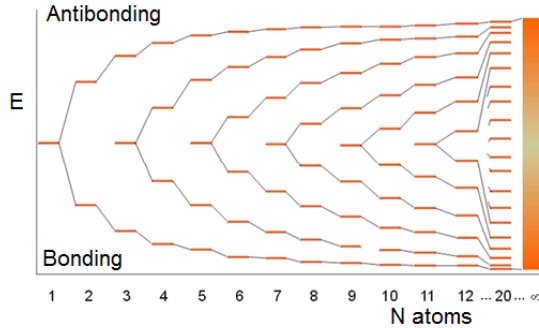
Figure 2.4: Energy band construction as a sum of uncountable splitted molecular orbitals. As the number of atoms is increased, the discrete energy levels look closer to a continuous system.

As shown in Fig.2.5, Li is an atom with only one electron in its valence energy level, type s. Each s orbital can allow up to two electrons with different spin number [2]. Thus, when two atoms of Li form a chemical bond, there are more molecular orbitals than electrons to occupy them. Electrons tend to fill

the lower energy states (ground states)[1]. As conclusion, in a valence energy band of a crystal lattice the energy levels will be differently occupied depending on the type of atoms involved. The more occupied the atomic orbitals are, the more occupied the valence band will be. In fig.2.5, as only half atomic orbitals are occupied by electrons, only half molecular orbitals will be occupied in a crystal lattice of Li.
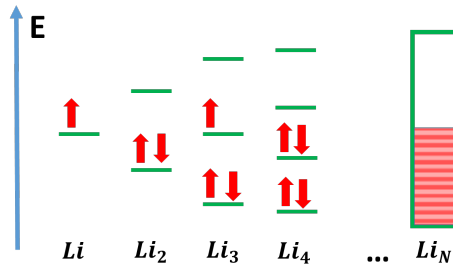
Figure 2.5: Electron distribution in a complex molecular orbital. The electrons tend to occupy the lower energy levels they can.

As explained previously, there exist different energy states corresponding to higher energy atomic orbitals. A similar reasoning could be followed in order to define an energy band formed by the addition of those higher energy orbitals, usually called conduction band. Also, most of these energy states will be empty as the excited atomic orbitals are usually unoccupied.

Once the discrete concept of the energy levels is approximated by continuous bands of energy, a third energy band can be defined as the forbidden band of energy: It corresponds to the band of energy levels between the valence band and the conduction band. Therefore no electron can be found in this region. Of course, this definition assumes that only one forbidden gap is possible, whereas this reasoning can be generalised in real materials.

To sum up: the valence band is the energy band formed by the superposition of a high number of atomic orbitals that are split when interacting with other atoms. It is possible to distinguish between the valence band (formed by the valence orbitals) and the conduction band (formed by other orbitals corresponding to excited states). The forbidden band, if any, is the energy band between the valence and the conduction band. This is a first and simple approach, because the splitting of the energy levels can lead to more complex structures. In any case, this approach can explain the electrical properties of materials.

---

[1] This is exact at 0K whereas at higher temperatures a statistical distribution can be defined, as explained in section2.3

2.2 Electrical properties of materials

In order to contribute to an electrical current, electrons have to change its movement when a bias is applied. This can only occur when there are available empty states that are also unbounded (the nucleus attraction is weak enough). Different situations can lead to this and they can be understood from the energy band approach. Fig.2.6 show these possibilities:

(a) Conductor   (b) Semiconductor   (c) Insulator
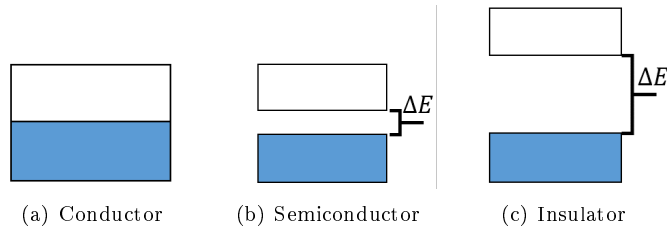
Figure 2.6: Different conduction behaviours of a materials explained from the energy band theory. In (a) the energy band gap is missing so the electrons will move easy when an electric field is applied to it, leading to a conductor. In (c) there is an insulator because the electrons need a huge external drift to overcome the forbidden band gap. In (b) there is an intermediate case, where there actually is an energy band gap, but easy enough to overcome with thermal drift or light photons.

In case of conducting materials, the energy gap that the electrons have to overcome is very low, if any. This is typical in metals where the atomic valence orbitals have few electrons (like the Li example in Fig.2.5). As a consequence, the energy band is not completely filled and an electron can reach a higher energy levels very easily as there is no real forbidden band to overcome.

In the case of insulators, the valence band is full and the gap in the forbidden energy band is wide, so electrons need a high energy to reach the conduction band.

In case of semiconductors, even if the valence band is full the gap in the forbidden energy band is narrow enough so that some electrons can reach the conduction band by thermal excitation or by doping processes.

The bands energy model allows not to focus on every single electron, but to consider them as a group. At this point, to understand how electrons fill the energy levels it is useful to define the Fermi level.

2.3 Fermi level and intrinsic carrier concentration

The generic definition for the Fermi Energy or Fermi Level (E_f) is the highest energy level that is occupied by an electron at absolute zero temperature (0K or $-273.16°C$) [4]. In other words, it is the highest energy level that is reached when all the electrons fulfill, from lower to higher energies, every possible energy state in the valence band.

As the band energy approximation allows to consider not every electron individually, a Fermi distribution can be defined as the probability for an energy level to be occupied (eq.2.2) and depends on the temperature (T), the Fermi level E_f and the Boltzmann constant k_B:

$$F_f(E) = \frac{1}{1 + e^{\frac{E - E_f}{k_B \cdot T}}} \qquad (2.2)$$

From Eq.2.2, at absolute zero the Fermi energy probability distribution corresponds to a step function where its value is 1 up to the Fermi Energy and then is 0. As temperature increases, there will be more electrons that will be thermally excited. Thus the probability to find electrons at higher energies than Fermi level increases whereas the probability of finding an electron at lower energy levels than Fermi's is not necessarily 1. This is shown in Fig.2.7

(a) T=0K   (b) $T > 0K$
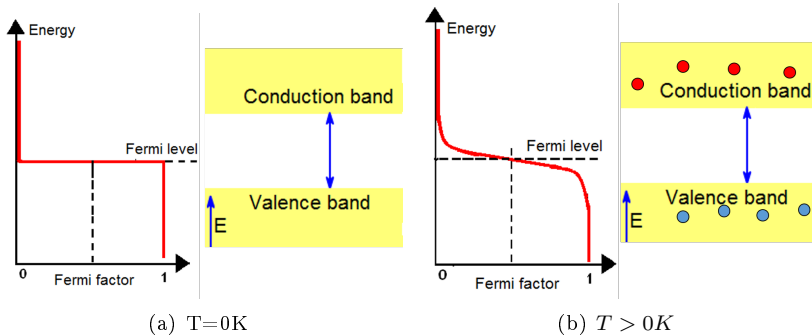
Figure 2.7: Differences in the Fermi factor depending on the temperature.

This fact implies that, for temperatures higher than the absolute zero, a semiconductor presents a concentration (cm^{-3}) of excited electrons in its conduction band (n_e) and the same number of holes in its valence band (n_h). The concentration of this charge carriers is usually called intrinsic carrier concen-

tration (n_i, in cm^{-3}). The behaviour is ruled by the law of mass action [5], so it can be expressed as eq.2.3:

$$n_h \cdot n_e = n_i^2 \qquad (2.3)$$

Where n_i is the intrinsic carrier concentration (cm^{-3}) [6]. In this case, as $n_h = n_e$, it is deduced that: $n_h = n_e = n_i$.

From here, another more general definition of the Fermi level is the energy level for which its Fermi factor is 0.5, that is, the energy level that has a probability of 0.5 to be occupied by an electron.

As shown previously, a conductive material has its valence band half-empty and then it can allow excited electrons: The Fermi level will be within the valence band.
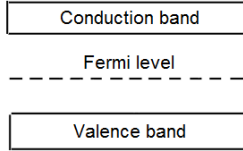
Figure 2.8: Theoretical Fermi Level in a Semiconductor

Also, a semiconductor has its valence band fullfilled (Fermi Factor=1) and its conduction band empty (Fermi Factor=0). Thus, from the theoretical point of view, Fermi level has necesarily to be within the forbiden band[2].

2.4 Different approaches to a P-N junction

Before defining a P-N junction it is necessary to define what is a P semiconductor and a N semiconductor. In fact, eq.2.3 is not valid in case the material is doped with another one.

Let us start with an intrinsic semiconductor such silicon (Si atoms have 4 valence electrons) to which some impurities (dopant) have been added. There are several possibilities:

1. In case those impurities come from an element with more valence electrons than the silicon such as phosphorous (P) with 5 valence electrons. This kind of dopant is called a donor and increases the Fermi level: Each dopant atom shares more electrons than expected if all the material was made of Si. The excess of electrons given by the donor is usually called N_d, and this kind of doped semiconductors is called N-type semiconductor.

---

[2]Notice that E_f is a thermodynamically deefined potential and not the energy of the electron, so it can be defined there even if no electron can be in it

17

2. In case those impurities come from an element with less valence electrons than the silicon, such as Boron (B) with 3 valence electrons. This kind of dopant is called an acceptor and decreases the Fermi level: Each dopant atom share less electrons than expected if all the material was made of Si. The lack of electrons is usually expressed as an excess of holes N_a and this kind of semiconductor is called P-type semiconductor.

Fig.2.9 represents how changes the Fermi Level (E_f) depending on the kind of dopant used.

Ec ——————— Ec ——————— Ec ———————
                          Ef ------------------- Ef -------------------

Ef ------------------
Ev ——————— Ev ——————— Ev ———————
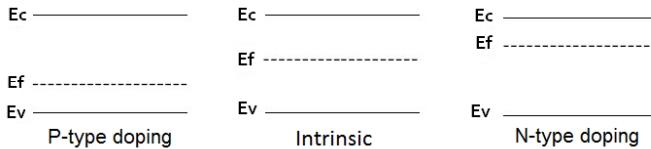   P-type doping   Intrinsic   N-type doping

Figure 2.9: Evolution of the Fermi Level when doping a semiconductor.

As defined before, in a N semiconductor there are N_d more electrons than expected in the equilibrium (and so N_a extra holes in the P semiconductor). From eq.2.3 now it is possible to generalise for doped materials:

When the doping is made essentially with a donor, the instrinsic carrier concentration n_i remains unchanged as it depends only on the type of semiconductor and on the temperature [6]. However, the electron concentration n_e is increased by N_d. So the resulting concentration of holes n_h in the bulk can be obtained from Eq.2.4 as:

$$(n_i + N_d) \cdot n_h = n_i^2 \xrightarrow{N_d >> n_i} n_h = \frac{n_i^2}{N_d} \tag{2.4}$$

And if the doping is mainly done with an acceptor, the electron concentration will be:

$$(n_i + N_a) \cdot n_e = n_i^2 \xrightarrow{N_a >> n_i} n_e = \frac{n_i^2}{N_a} \tag{2.5}$$

Eq.2.4 and 2.5 are of particular interest because they allow to calculate the *minority carrier* concentration in doped semiconductors. This concept is very important to understand a photovoltaic device, as explained in section 2.7.

Up to this point, P-type and N-type doped semiconductor have been explained in terms of the intrinsic semiconductors, the doping and the Fermi levels. From here, a P-N junction can be obtained by combining a P-doped material with a N-doped material or, from the thermodynamics point of view, it is a structure that combines two materials with different Fermi Levels. This

second approach is too general[3] but very useful to understand the properties of this kind of structure.

As a P-type semiconductor and a N-type semiconductor are combined in the same structure, the electrons go from the N side to the P side due to the difference in E_f until equilibrium is reached. This leads to a diffusion current of electrons from the N zone to the P zone (or a hole current in the opposite sense).

As the electrons diffuse from the N to the P zone, they leave behind atomic nuclei with positive charge. Analogously, thinking on a hole diffusion, a net negative charge will appear in the P zone. This induces another electric field that will increase as more electrons diffuse to the P zone (or holes to the N zone).

In equilibrium, there is no net current between the P and the N part of the P-N junction, meaning that the diffusion and the drift current cancel. However, a new region can be defined in a P-N junction as the depletion region, that is, a region covering both the region where there is a net positive charge in the N semiconductor and the region with negative charges in the P semiconductor (Fig.2.10).
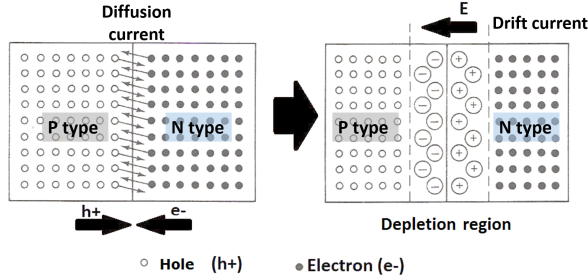
Figure 2.10: Schema of the depletion region in a P-N junction

In order to relate the energy band model with the P-N junction, it is important to understand why all the band diagrams have a band bending: As seen before, doping modifies the Fermi Level (Fig.2.9) but this parameter is indeed a thermodynamic property so, in thermodynamical equilibrium it has to be the same for all the P-N junction [4]. Thus, the band diagram has to be "forced" to keep the same Fermi Level without changing the energy gaps of each side of the junction. The resulting diagram is shown here:

---

[3]In fact, the P-N junction is an example of combining to materials with different Fermi Levels, but not the only: Batteries and cathodic protection in corrossion systems are other examples. Therefore, in the scope of this thesis, only doped semiconductors will be considered.
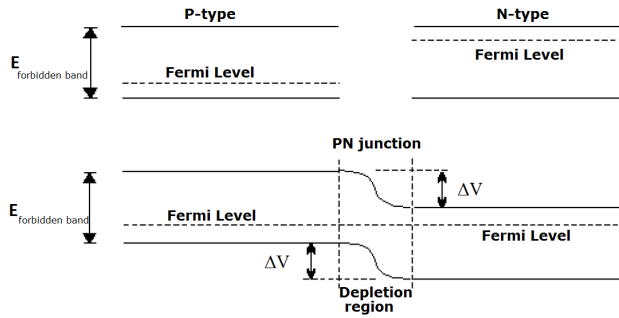
Figure 2.11: Construction of a PN junction energy band diagram

In Fig.2.11 it is showed that, as the energy bands are bended, there is a energy difference between both sides of the depletion region. This energy can be expressed as a potential difference ΔV. This ΔV makes an electron on the valence band in the P zone to be pushed towards the valence band in the N region. An analogous situation can be thought with the holes in the conduction band. This situation is equivalent to the drift current explained above.

Another electronic current is produced from the N to the P side due to a charge (or electron concentration) at both sides of the depletion region. This current corresponds to the diffusion current presented above.

As before, in equilibrium both currents get cancelled so that there is no net current though the P-N junction (Fig.2.12)

Figure 2.12: Spontaneous currents across the depletion region in a PN junction represented on its band diagram. In red the saturation current related with the difference in charge concentration. In blue, the diffusion current related with the built-in potential at both sides of the depletion region.

Until now, several phenomena have been exposed and explained related with the P-N junctions: Why an internal electric field is produced and why in equilibrium there is no net current. But there is still a missing piece of the p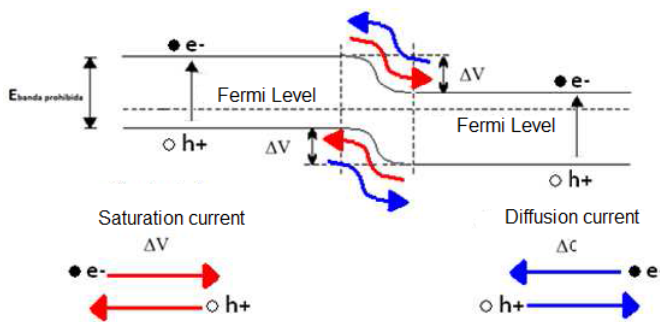uzzle: What does anything of this has to do with a photovoltaic device?. To answer to this, it is necessary to introduce what happens in a non-equilibrium P-N junction like when it is biased (an external voltage is applied on it).

2.5 Bias of a PN junction

A P-N junction is biased when an external driving force is applied between the P zone and the N zone. Depending on how is this external force applied, two different bias can be found:

1. Direct bias (Fig.2.13). In this case the external driving force (a bias) is opposite to the electric field at the depletion region. This has two consequences: First, that minority carriers are injected within the depletion region and an increase in the diffusion current is produced. This makes the Fermi level to be artificially modified (to the Quasi-Fermi Levels) and the resulting ΔV between both sides of the depletion region is reduced. Second, as the drift current remains almost constant as it mainly depends on the thermal generation [4] there is a net current flowing through the P-N junction. In general terms, this current will be higher as the direct bias increases.
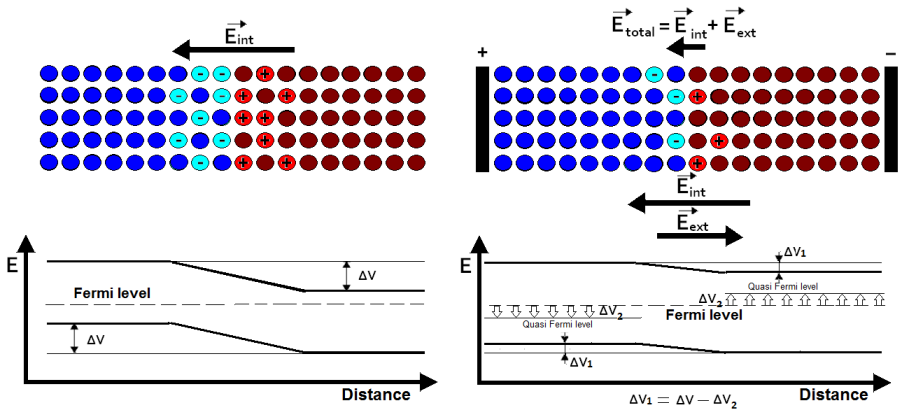
Figure 2.13: Effect of direct bias on the energy band diagram and the P-N junction representation

21

2. Reverse bias (Fig.2.14). In this case the driving force is in the same sense that the depletion region electric field, so the Fermi level is again artificially modified leading to a bigger voltage difference ΔV at both sides of the depletion region. Again, the drift current remains almost constant at constant temperature. However, the diffusion current is now reduced very slightly. So in this case the resulting net current flowing through the P-N junction is almost independent on the external driving force and quite small[4].
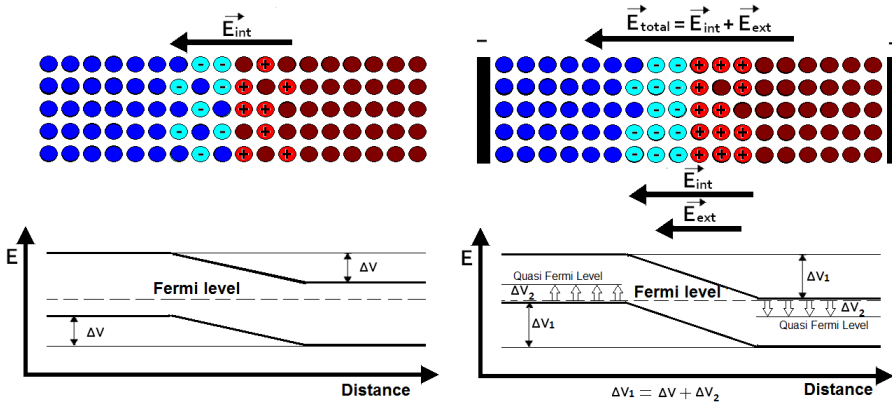
Figure 2.14: Effect of reverse bias on the energy band diagram and the P-N junction representation

In both Fig.2.13 and 2.14 a new term is presented: The Quasi Fermi Levels. This new approach is done to describe the population of electrons separately in the conduction band and valence band, when they are displaced from equilibrium [7]. So this is useful when the P-N junction is biased.

If the Energy Fermi Levels are also expressed in terms of electric potential energy, the change in ΔV between both sides of the depletion region when the P-N junction is biased can be expressed as eq.2.6:

$$\Delta\left(\Delta V\right) = \Delta V_{BIAS \neq 0} - \Delta V_{BIAS=0} = V_{Fermi} - V_{QuasiFermi} \qquad (2.6)$$

If a graph is made by drawing all the pairs of values Bias (V)- Current (A), from negative bias values (reverse bias) to positive bias values (direct bias), a very characteristic curve can be obtained, as presented in fig.2.15.

---

[4]This current values and its bias dependence are not neglected in photovoltaic devices as they are used to fit analytical models of the devices as well to determine some fabrication problems related with shunting and ohmic resistance (see section 6.1)

Figure 2.15: Qualitative representation of the Bias-Dependent Current flowing through a P-N junction

Let us define the dark current I as the sum of the drift (or saturation) current I_0 due to the electric field in the depletion region and the diffusion current $I_{Diffusion}$ due to the charge concentration gradient between both s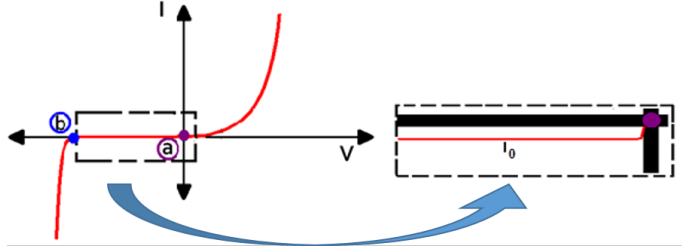ides of the P-N junction when there are no photogenerated carriers. And let us define the dark saturation current I_s as the resulting current when there is reverse bias (almost constant).

In Fig.2.15 there several remarked points that are of particular interest. The point marked as "a" corresponds to null bias: No direct nor reverse bias is applied. At that point, as there must be an equilibrium, the dark current is zero as the drift and the diffusion current are cancelled: $I = 0$. When there is direct bias, the dark current increases exponentially because the diffusion current increases while the drift current remains constant. Similarly, for reverse bias I remains constant as there is almost no diffusion current and the drift current does not depend on the bias.

Another particular point in Fig.2.15 is the point marked as "b". This point is called the breakdown point because the P-N junction losses its properties: When the reverse bias is high enough, electrons can tunnel through a thin depletion region from the valence band in the P side to the conduction band in the N side[8] and there is a net current flow[5].

As the dark saturation current I_S is almost constant and mainly equivalent to the drift current, let us consider hereunder that $I_s = I_0$.

Up to here, it has been shown that the behaviour of a P-N junction is dependent on external driving forces. This external driving force can be an electric bias directly applied on the P-N junction but a special case would be that where the bias is created internally by photogenerated carriers. In fact, when a P-N junction is defined with photoactive materials and this system is illuminated, there is a photogeneration of carriers both in the N part and

---

[5]These new phenomena have not been explained here as they are not essential to understand a photovoltaic device. Only when thinking of commercial photovoltaic devices and systems, for security reasons, this phenomena should be studied.

in the P part of the junction. The photogeneration disturbs the equilibrium minority carrier concentration. This leads to an excess density of minority carriers managing to diffusing towards the depletion region where they are swept across the junction, leading to a net current. In fact, even if the total carrier concentration increases, the driving force arising from the carrier concentration difference at both sides of the depletion region can be considered constant, as represented in fig.2.16.

(a) No light   (b) Illuminated
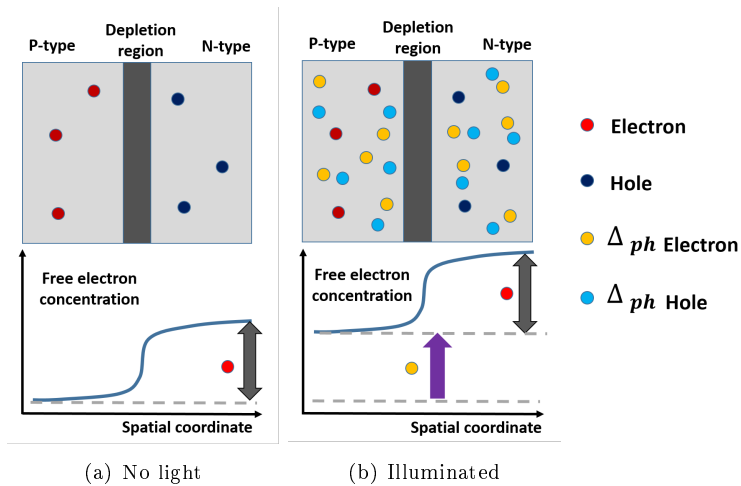
Figure 2.16: Qualitative representation of the invariant driving force for the diffusion current when the PN junction is illuminated. In a) The only net charges are generated thermally, whereas in b) some charges are photogenerated.

However, even if the diffusion current is almost kept constant, there is an important consequence of illuminating: The minority carrier population is increased[6] and this creates an additional current corresponding to those carriers being swept across the depletion region. This current is mostly dependent on the illumination and hardly on the applied bias, so the resulting characteristic electric curve when a PN junction is iluminated is changed [9] from fig.2.15 to fig.2.17

Finally, the reader should note that, as defined, the sense of the illumination current (fig.2.17), make it a negative current by definition. However, when measuring the characteristic I-V curve of a solar cell, it is very common to

---

[6] As introduced in eq.2.4 and 2.5, the minority carriers are the electrons in the P doped area and the holes in the electron hole area. They are likely to recombine before they contribute to the photocurrent and therefore they contribute to the overall efficiency of a solar cell.
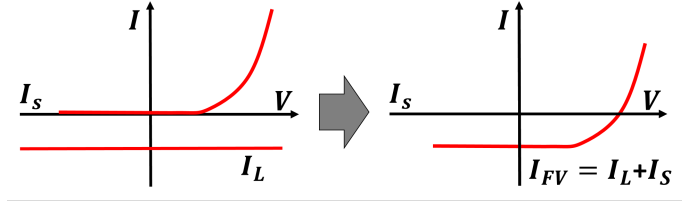
Figure 2.17: Effect of illumination on the characteristic I-V curve for a solar cell

change the sign convention and define the photocurrent as possitive, leading to representations like fig.2.18.
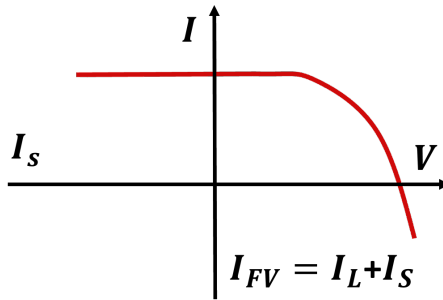
Figure 2.18: Photovolaic convention sign for illuminated I-V curves in solar cells.

A PN junction acts as a diode, so they can be described by analytic diode models. As shown in Fig.2.15, a P-N junction can act as a rectifier because current can only flow easily in one sense, that is, under forward bias. For this reason, in the dark, the current of an ideal solar cell can be modelled as a diode [10, section 6.1.4]:

$$I(V) = I_0 \cdot \left(e^{\frac{q}{n \cdot k_B \cdot T} \cdot V} - 1 \right) \tag{2.7}$$

In Eq.2.7, q is the electron charge ($1.6 \cdot 10^{-19}$ C) and n is an ideality factor that accounts for departures from the ideal diode model. It fits experimentally the behaviour of a P-N junction. In this sense, the ideality factor has no physical meaning in a strict sense. Moreover, it can be rearranged as follows:

$$I(V) = I_0 \cdot e^{\frac{q}{n \cdot k_B \cdot T} \cdot V} - I_0 = I_{Diffusion} - I_0 \tag{2.8}$$

From Eq.2.8 and Fig.2.18 the main properties presented as characteristic of a P-N junction are fulfilled:

- The dark current I results from the addition of the diffusion current $I_{Diffusion}$ and the drift current I_0. Both currents opposed to each other and the diffusion current is assumed to be possitive.

- When there is no bias ($V = 0$) the current is also zero, because the diffusion current and the drift current cancelled to each other. Only the photocurrent, if any, is present.

- If there is a reverse bias ($V < 0$) the dark current, even if it is small, is considered negative. Moreover, as its main contribution is the drift current, it can be approximated by I_0.

There are mainly two differences between real diodes behaviour that are not included in Eq.2.8. The first one is the breakdown voltage. The second is that the ideality factor n is bias dependent. However, this is still a good model to ideal diodes and a first approximation to real solar cells.

2.6 Light absorption on a solar cell

In previous sections, the electric behaviour of materials has been presented as a consequence of the energy band distribution, and that distribution as the combination of uncountable energy levels arising from the solution of the Schrödinger equation (eq.2.9).

$$\left[-\frac{(\frac{h}{2\pi})^2}{2m} \nabla^2 + V(\vec{r}) \right] \phi_k(\vec{r}) = E_k \phi_k(\vec{r}) \tag{2.9}$$

However, the description that has been done is not complete. In fact, in fig.2.3, 2.4, 2.5 and 2.7 only the energy axis was taken into account, whereas the real Energy bands have two components. Therefore, a more accurate description of the Energy Bands should be presented in order to understand new concepts. The strategy for this would be the following:

1. Any periodic lattice can be described using a single unit cell[7] with specific lattice parameters. As an example, fig.2.19a for a cubic face-centered stucture is shown.

---

[7]Some materials show different structures depending on the temperature or even in metastable conditions reached during the fabrication process. For simplicity let us obliviate this.

2. A Fourier transform is applied to the spatial distribution defined by the individual unit cell. Thus, instead of working in spatial coordinates and a unit cell, the solution is going to be obtained in term of a reciprocal lattice expressed in terms of reciprocal units. Those reciprocal space and units are usually called, respectively, Brillouin zone and wavevector $\vec{k}$ [11, ch. 5]. It can be prooved that all the states outside the first Brillouin zone are equivalent to the inner ones. As an example, the corresponding Brillouin zone for the cubic face-centered stucture is shown in fig.2.19b

3. The Bloch theorem [12] states that the solution for the Schrödinger equation for a periodic structure (like a cristal lattice of a semiconductor) can be expressed in terms of the general form shown in eq.2.10.

$$\phi_k(\vec{r}) = e^{j\vec{k}\cdot\vec{r}} U_n(\vec{k}, \vec{r}) \tag{2.10}$$

where $\vec{k}$ is the wavevector corresponding to the spatial coordinate $\vec{r}$ in terms of the reciprocal space, the U_n term is the Bloch function for the nth band and it has the same spatial periodicity that the direct lattice. Thus, any electric state can be studied for $\vec{k}$ values within the Brillouin zone and for $\vec{r}$ values within the unit cell.
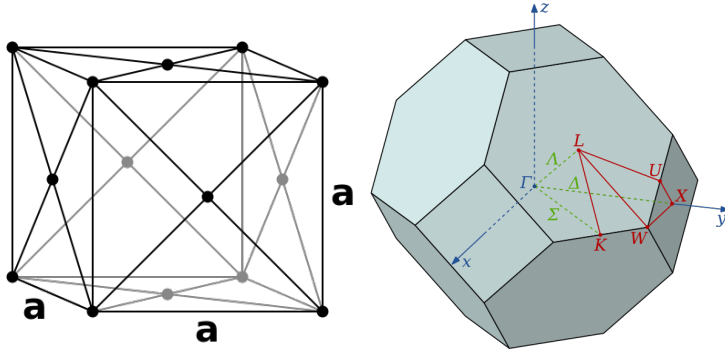
(a) Cubic face centered (FCC)unit cell (b) Brillouin zone for a FCC unit cell

Figure 2.19: Schemic (a) FCC lattice and (b)corresponding 1st Brillouin zone.

Notice that for any value of the wavevector $\vec{k}$, different solution to the Schrödinger equations are found by changing the n order in the expression for $U(\vec{k}, \vec{r})$. Thus, For each value of k, there are multiple solutions to the Schrödinger equation labelled by the index n, which simply differentiate the

possible energy bands. The definition that has been followed until now neglected the influence of $\vec{k}$, as each of the n energy levels depends on it. Thus, the real energy bands for the electron are more complex than previously defined. Fig.2.20 show schematically the relation between the simplificated and real dispersion diagram
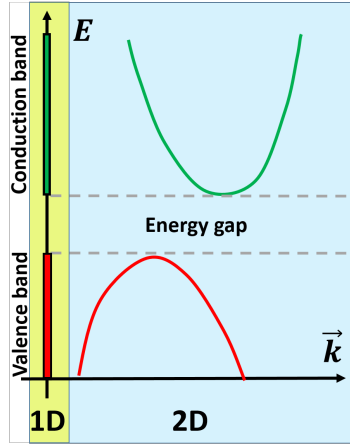
Figure 2.20: Schema of a real Energy-momentum band diagram and the simplified band diagram concept as a projection of it on the Energy axis.

This new dimension in the diagram band implies that the transition between different energy levels must fullfil not only and energy condition, but also a momentum conservation. This means that even if a photon has enough energy to overcome the band gap the transition may not occur if the momentum of $\vec{k}$ is not compensated (usually with a phonon[8]). From this point of view, two different semiconductors can be defined:

- Direct semiconductors. In this case, the maximum of the valence band has the same $\vec{k}$ value than the minimun of the conduction band. This makes the transition much more efficient between energy bands.

- Indirect semiconductors. In this case, the maximum and the minimun correspond to different $\vec{k}$ values. The transition is less likely.

There is a strong conclusion from this new definition of the energy gaps: Photons with different energies will have different probabilities to photogenerate a carrier in a semiconductor, even if all of them are more energetic than

---

[8]A phonon is another quasi-particle that is related with the vibrational energy of a crystal lattice.

the bandgap. It is really difficult to estimate which are those probabilities from
an analytical point of view. Therefore, absorption is described by an empirical
parameter which can be measured: The absorption coefficient α. In brief, the
probability function P^{abs} for a photon to being absorbed in a substrate i at a
depth z can be expressed as shown in eq.2.11:

$$P_i^{abs}(z, \lambda) = 1 - e^{-\alpha_i(\lambda)z} \tag{2.11}$$

The α parameter is closely related with a well-known optical parameter:
the imaginary part of the refractive index κ:

$$\alpha_i(\lambda) = \frac{4\pi}{\lambda}\kappa_i(\lambda) \tag{2.12}$$

In fig.2.21 the absorption coefficients for different materials is shown. It is
possible to see that the absorption coefficient decreases quite steeply for a given
wavelength. That wavelenghts are close to the gap energy, so the probability
of absorption tends to zero. Thus, fig.2.21 gives an idea of which is the range
where each material is photoactive and the wavelength range in which they
whould be better in relative terms: Si is worse than many other materials such
as the GaAs, CdTe and InP, because it is an indirect semiconductor, but it has
a larger absorption range as it energy gap is smaller. Notice that the silicon,
when amorphous, has better absorption properties: Even if it is the same
material, the band structure[9] is much more similar to a direct semiconductor
when compared with the cristalline structure.

2.7 Collection probability and lifetime of photo-generated carriers

When thinking on the power production of a solar cell, not only the absorption
or generation within the material has to be taken into account, but also how
many the photogenerated carriers are collected to contribute to the extracted
current.

Up to here, the illumination current has been defined to the current due
to the charges going *across* the PN junction. And there is always a part of
the photogenerated carriers that do not reach the junction because electrons
and holes have always a chance to recombine. The recombination mechanisms
are well-known and has already been explained in detail elsewhere [14]. Re-
combination cannot be completely avoided because, from the physical point of
view, it will always be present due to the Plank law of radiation[15] and to the

---

[9]Of course, an amorphous structure has not a real periodic lattice, but when finding the
energy band diagram it is found that behaviour.
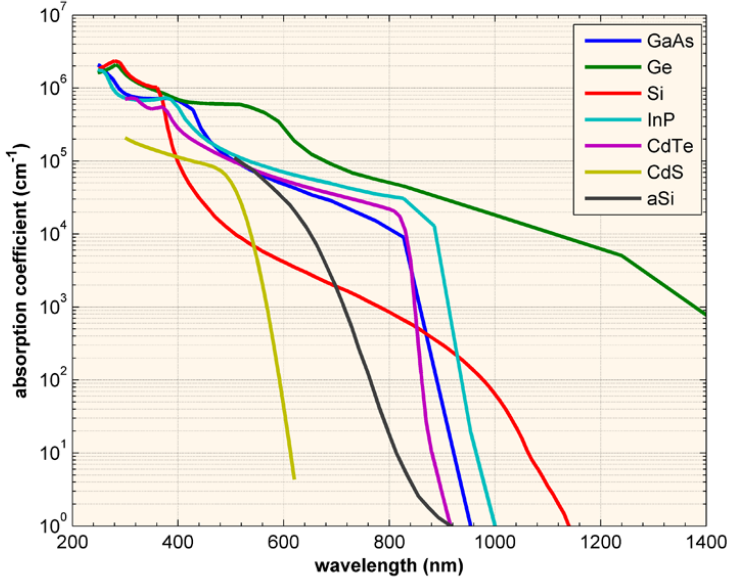
Figure 2.21: Absorption coefficient for different materials[13]

radiative recombination [16, 17] However, from the practical point of view, the defect-related recombination processes are given by:

- Surface recombination. Any surface implies a discontinuity in the substrate lattice and any discontinuity implies defects on it. Thus, even if the surface of the material has been treated to reduce the deffects (passivation process), the recombination will always be higher at the surface than at the bulk of the material. Thus, any photogenerated carrier close to a surface will be more likely to recombine.

- Bulk recombination. The bulk material will always have defects in the lattice that will induce the recombination of the photogenerated carriers. For high quality bulk materials, such as the c-Si float zone this recombination will be very low, but for others like the pc-Si will be as important as in a surface.

Analogously to the absorption probability, the collection probability is difficult to estimate anallytically from the different recombination equations and the geometry. There are softwares that allow to estimate this collection probability functions such as Silvaco[18], PC1D[19, 20] including both the material

and the geometrical dependency when they are too difficult to be solved analytically. However, for real and finite systems, the effect of the surface, the presence of other elements such like the metallic contacts, local deffects, etc. make the real collection probabilities much more difficult to calculate in an accurate way with no experimental data.

There is an easy experimental approach related with the concept of the effective minority carrier lifetime [21], that is, the average time that a photogenerated carrier can exist before it recombines. In order to estimate the lifetime, a very commonly used approach are those based on the photoconductance, as explained in section 6.2.2.

The bigger the lifetime is, the further a photogenerated carrier can reach before recombining. Therefore, the bigger the collection probability will be.

For simple geometries and some simplifications, it is possible to understand the main mechanisms that rule the process: For an homogeneous semi-infinite photoactive substrate it is possible to estimate the collection probability in terms of the lifetime and mobility using diffusion-like equations[10]. For complex systems, the best-accurate models need from both numerical software and from experimental data.

The scope of this thesis is not focused on the optimisation of the recombination processes, but it will be useful to estimate the collection probability in an easy and experimental way from a different experimental approach: the Quantum Efficiency (QE) measurements. Those measurements, explained in detail in section 6.1, include both the absorption and collection effects, but are a very important tool to understand the wavelength dependency on the efficiency of a photovoltaic device.

---

[10]Lifetime is related to recombination and mobility to momentum relaxation. Diffusion length depends on both.

Bibliography

[1] Ira N. Levine. *Química cuántica*. Number ISBN:84-205-3096-4. Prentice Hall, 5th edition, 2001.

[2] Ralph H. Petrucci, William S. Harwood, and Herring F. Geoffrey. *Química General*. Prentice Hall, 2003.

[3] Martin S. Silberberg. *Principles of General Chemistry*. Mc Graw Hill, 2007.

[4] Jenny Nelson. *The physics of solar cells*. Number ISBN-13-978-1-86094-340-9. Imperial College Press, 2009.

[5] S. Salivahanan and Kumar N. Suresh. *Electronic Devices and Circuits*. Mc Graw Hill Education, 2011.

[6] Martin A. Green. Intrinsic concentration, effective densities of states, and effective mass in silicon. *Journal of Applied Physics*, 67(6):2944–2954, 1990. doi: http://dx.doi.org/10.1063/1.345414. URL http://scitation. aip.org/content/aip/journal/jap/67/6/10.1063/1.345414.

[7] Alan H. Marshak and Karel M. van Vliet. On the separation of quasi-fermi levels and the boundary conditions for junction devices. *Solid-State Electronics*, 23(12):1223 – 1228, 1980. ISSN 0038-1101. doi: http://dx. doi.org/10.1016/0038-1101(80)90116-1.

[8] Otwin Breitenstein, Jan Bauer, Karsten Bothe, Wolfram Kwapil, Dominik Lausch, Uwe Rau, Jan Schmidt, Matthias Schneemann, Martin C. Schubert, Jan-Martin Wagner, and Wilhelm Warta. Understanding junction breakdown in multicrystalline solar cells. *Journal of Applied Physics*, 109(7):071101, 2011. doi: http://dx.doi.org/10.1063/1.3562200.

[9] F.A. Lindholm, J.G. Fossum, and E.L. Burgess. Application of the superposition principle to solar-cell analysis. *IEEE Transactions on Electron Devices*, 26(3):165–171, 1979. ISSN 0018-9383.

[10] Robert F Pierret et al. *Semiconductor device fundamentals*. Addison-Wesley Reading, MA, 1996.

[11] Neil W. Ashcroft and David N. Mermin. *Solid State Physics*. Thomson Learning, 1976. ISBN 0030839939. URL http://www.amazon.com/exec/obidos/redirect?tag=citeulike07-20&path=ASIN/0030839939.

[12] Charles Kittel. *Introduction to Solid State Physics*. John Wiley & Sons, Inc., New York, 6th edition, 1986.

[13] Christiana Honsberg and Stuart Bowden. Pvcdrom, July 2015. URL www.pveducation.org.

[14] VL Bonch-Bruevich and EG Landsberg. Recombination mechanisms. *physica status solidi (b)*, 29(1):9–43, 1968. doi: 10.1002/pssb.19680290102.

[15] K Schick, E Daub, S Finkbeiner, and P Würfel. Verification of a generalized planck law for luminescence radiation from silicon solar cells. *Applied Physics A*, 54(2):109–114, 1992.

[16] W Michaelis and MH Pilkuhn. Radiative recombination in silicon p-n junctions. *physica status solidi (b)*, 36(1):311–319, 1969.

[17] T Trupke, Mr A Green, P Würfel, PP Altermatt, A Wang, J Zhao, and R Corkish. Temperature dependence of the radiative recombination coefficient of intrinsic crystalline silicon. *Journal of Applied Physics*, 94(8): 4930–4937, 2003.

[18] S Michael, AD Bates, and MS Green. Silvaco atlas as a solar cell modeling tool. In *Photovoltaic Specialists Conference, 2005. Conference Record of the Thirty-first IEEE*, pages 719–721. IEEE, 2005.

[19] Halvard Haug, Achim Kimmerle, Johannes Greulich, Andreas Wolf, and Erik Stensrud Marstein. Implementation of fermi–dirac statistics and advanced models in pc1d for precise simulations of silicon solar cells. *Solar Energy Materials and Solar Cells*, 131:30–36, 2014.

[20] Chetan S. Solanki, Brij M. Arora, Juzer Vasi, and Mahesh B. Patil. Solar cell simulation using pc1d simulator. In *Solar Photovoltaics*, pages 130–146. Foundation Books, 2012. ISBN 9789382993254. URL http://dx.doi.org/10.1017/9789382993254.017. University Publishing Online.

[21] Mark J. Kerr, Andres Cuevas, and Ronald A. Sinton. Generalized analysis of quasi-steady-state and transient decay open circuit voltage measurements. *Journal of Applied Physics*, 91(1):399–404, 2002. doi: http://dx.doi.org/10.1063/1.1416134. URL http://scitation.aip.org/content/aip/journal/jap/91/1/10.1063/1.1416134.

Chapter 3

Scientific background on plasmonics and optics

3.1 The plasmonic effect and the dispersion diagrams

The plasmonic effect is studied by the nanophotonics area, that is, the science that studies the confinement and control of light at the "nano" scale[1]. Thus, the study of the plasmonic effect has been developed as the nanoscience and nanotechnology have focused more attention in the last century.

The aim of the nanophotonics science is to study the interaction bewteen electromagnetic radiation and matter, such as the electrons in a metal surface. The term *plasmon* is used to refer at the oscillation of the plasma[2] just like if it was described by an oscillating particle. Thus, a plasmon is a quasi-particle just as electrons are.

The plasmonic effect, however, goes beyond the simple presence of a plasmon. A plasmon, as any moving charge, will induce another electromagnetic field. This new field can excite too the metal surface. In order to model the interaction between an electromagnetic field and oscilating charges, another pseudo-particle is defined: The *polariton* or *plasmon polariton*.
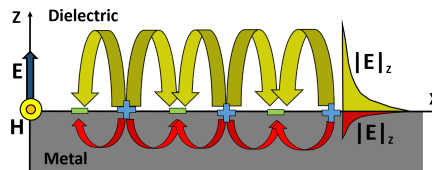
Figure 3.1: Surface plasmon polariton at a flat dielectric-metal interface.

---

[1]Usually, the term "nano" is applied when dealing with orders of magnitude below the micron ($10^{-6}m$ (the U.S.A National Nanotechnology Initiative includes in "Nanotechnology" from 1 to 100nm [1], but this is not a fundamental law)

[2]The concept of plasma is quite ambiguous. In the scope of this thesis, the plasma will be considered like an electron cloud, similar to a gas. As it is formed by electrons, there is no charge balance and therefore it can be easily excited by an external electromagentic field.

UNIVERSITAT
POLITÈCNICA
DE VALÈNCIA

Valencia Nanophotonics Technology Center

ESCUELA TÉCNICA
SUPERIOR INGENIEROS
INDUSTRIALES VALENCIA

As a consequence of this coupling plasmon-polariton, a self-maintained ex-itation can be found,in which the photon induces a plasmon and the elec-tromagnetic field induced by the plasmon keeps the plasma oscillation of the plasmon. This is known as *Surface Plasmon Polariton* (SPP) and can be easily understood in a dielectric-metal planar interface, where the electric field of an incident photon $\vec{E}_{ph}$ is represented as:

$$\vec{E}_{ph} = \vec{E}_0 e^{i(\vec{k}\cdot\vec{r}-\omega t)} \tag{3.1}$$

The study of the SPP is done using a decomposition of the wavevector $k\hat{k}$ in normal $k_z\hat{z}$ and tangential $k_\rho\hat{\rho}$ components related to the interface between the dielectric(subindex 1) and the metal(subindex 2) shown in fig.3.1. Of course, those components have to fulfill:

$$k^2 = k_\rho^2 + k_z^2 = k_x^2 + k_y^2 + k_z^2 \tag{3.2}$$

From the boundary conditions needed to solve the Maxwell equations in a system such as that shown in fig.3.1 a system of three coupled equations is found that relates the different components of the wavevectors, the permitivity functions and the frequency [2, section 2.2]:

- From the wavevector decomposition in the air (medium 1), and applying the definition of wavevector, it is found for the choice of axis shown in fig.3.1:

$$k_{x1}^2 + k_{z1}^2 = \epsilon_1 \left(\frac{\omega}{c}\right)^2 \tag{3.3}$$

- Analogously, for the metal (medium 2), it is found:

$$k_{x2}^2 + k_{z2}^2 = \epsilon_2 \left(\frac{\omega}{c}\right)^2 \tag{3.4}$$

- Moreover, due to the continuity of the tangential component at the in-terface $k_{x1} = k_{x2}$, a new condition is added:

$$\frac{k_{z1}}{\epsilon_2} = \frac{k_{z2}}{\epsilon_1} \tag{3.5}$$

From eqs.3.3 to 3.5 the solution defining the SPP is:

$$k_x = \frac{\omega}{c}\sqrt{\frac{\epsilon_1\epsilon_2}{\epsilon_1 + \epsilon_2}} \tag{3.6}$$

Eq.3.6 is a key equation to understand the phenomena and the implications of the SPP as it gives the dispersion relation of a surface plasmon[3]. It can be demonstrated [2, p.27] that no SPP is supported for TE polarisation (see section 3.5 for more details). Thus, the whole plasmon can be properly defined with a tangential wavevector. For simplicity, the axis will be taken as in fig.3.1 in order to simplify the tangential component as $k_\rho = k_x$.

In this thesis, however, the study is not going to be focused on continuous flat metal-dielectric interfaces, but in discrete metal nanoparticles surrounded mainly by dielectric materials. Thus, eq.3.6 is no valid anymore. In fact, now the concept of Surface Plasmon Polariton is not longer valid as the plasmon is not propagating along a surface but remains localised in a small space much smaller than the wavelength. This lead to the concept of Localised Surface Plasmon (LSP).

In a general way, the electrons in the conduction band of a metal can interact with a photon and they will move accordingly to this external driving electromagnetic field. This light-matter interaction leads to charges changing its velocity and then, to scattered electric fields[3].
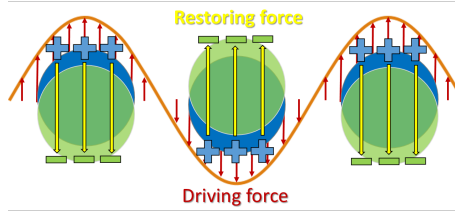

Figure 3.2: Plasmon representation as a plasma movement around the geometrical center of a nanoparticle.

It is possible to assume that the metallic structure behave, at least locally, like an electron cloud (usually called plasma) that oscillate collectively when an external driving force is applied on them, such like an electromagnetic field or a photon. Of course, there are also other forces, like the restoring forces arising from the finiteness of the particles and the existence of the positive atomic nucleus that create an elecrostatic force. The LSP is therefore the plasmon related with this oscillating charges around a localised point, as shown in fig.3.2.

---

[3]The dispersion relation relates the wavelength of a wave and its velocity. This may seem trivial, but in real media there is a frequency dependent dispersion that make each frequency behave differently. In fact, when dispersion is taken into account, the wave velocity is defined using two different velocities: The propagation velocity of the phase or phase velocity and the group velocity, that is, the velocity at which its envelope (in short, its shape) propagates in space.

Light propagating in vaccum has a constant dispersion relation, so both phase and group velocity are the same. However, complex systems like the SPP are not so easy.

It is difficult to find in the literature the dispersion diagram of a LSP[4]. However, it can be represented by even simpler expressions than eq.3.6: As it is considered "localised", a zero dimensional approach would be valid. From this point of view, no angular dependence should be found and therefore the tangential component would not have a significant influence on the dispersion relation [4]. In fig.3.3 the comparison between the dispersion relation of a SPP and a LSP is shown.
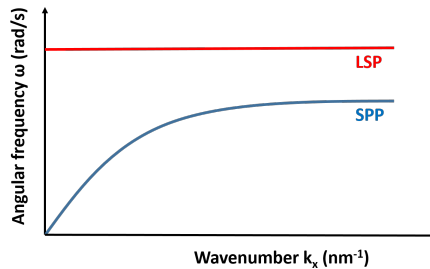

Figure 3.3: Dispersion diagram for a Surface Plasmon Polariton (SPP) and a Localised Surface Plasmon (LSP).

In Fig.3.3 the LSP can be excited with any wavevector k_x (thus for any angle for given materials). Notice that the excitation of the LSP is done at a given arbitrary frequency[5]. This implies another key difference between LSP and SPP: LSP are not only excited independently on the incidence angle, but also at different frequencies keeping this angular behaviour. SPP only occur at some frequencies and incident angles.

Under certain conditions there is a particular behaviour, usually referred as *resonance*, where the interaction between the external driving force and the charges shown in fig.3.3 is maximised, leading to huge electromagnetic fields near the interfaces. The study of these conditions is not always easy and usually numerical models have to be used, but in some cases with a simple geometry and under certain conditions some analytical models have been developed, most of them referred in this thesis in section 3.3. In brief, the resonance frequency depends on the size and the shape of the nanostructure where the plasmon takes place, as well as its dielectric function and the dielectric function of

---

[4]This is probably because it is not the best strategy to deal with LSP: As it is localised, the k_x is not a good quantum number or it is not very useful to use a Fourier transformation to it. However, this approach sheds light on the physical and practical aspects, as well as on the differences, between SPP and LSP

[5]In fact, as shown in section 3.3.4, the excitation is done at mainly any frequency even if the response may differ

the surrounding media. Moreover, the resonance frequency is not unique, as different resonances can take place in the same nanostructure.

Dispersion diagrams do not offer any information about how strong is the light-matter interaction, so they are only valuable from the qualitative point of view, whereas other strategies are needed for a quantitative approach.

The first exact solution for a Localised Surface Plasmon resonance was given by Mie already in 1908 [5] and lead to a quantification of the resonances in metallic spheres in homogeneous media. However, several years before Lord Rayleigh gave an approximation to it [6] assuming a zero dimensional sphere. Thus, the zero dimensional and angular-free dependency case is not exact in many cases. For instance, in the case of a LSP in an inhomogeneous media (as angular dependency would be present), but it is a good starting point to understand them.

3.2 Radiation and non-radiation condition

In general, when a LSP is excited, the moving charges lead to two main phenomena with the same origin but with different consequences: Scattering and absorption. Absorption is related with the intrinsic resistivity of the metal that lead to ohmic losses during the plasmon movement. In fact, the challenge in plasmonics is how to overcome the Joule losses [7].

From the scattering point of view, and acccording to the Larmor formula in classical electromagnetism[3, 8], a single charge that is affected by driving force that induces in it an acceleration will produce electromagnetic radiation. This, however, is usually is misunderstood as if the electrons in the LSP must "radiate" light. The scattered electromagnetic field by a LSP can, lead to light emission but this it is not assured. In fact, it is possible to find examples where no radiation is emitted [9]. To understand the condition on radiation or non-radiation it is useful to check the work made by Hermann A. Haus which is based on the Fourier components of the current produced by a moving point charge [10].

In brief, Hauss studies a single particle whose charge density σ can be defined as:

$$\sigma(\vec{r}, t) = q_0 \delta(\vec{r} - \vec{r}_0(t)) \tag{3.7}$$

where $\vec{r}_0$ is the time-dependent position vector for the charge q_0, $\vec{r}$ is the position vector of the studied spatial point and $\delta(x)$ is the delta function. From this the current density $\vec{J}$ comes as:

$$\vec{J}(\vec{r}, t) = q_0 \frac{d\vec{r}_0(t)}{dt} \delta(\vec{r} - \vec{r}_0(t)) \tag{3.8}$$

The spatial Fourier transform $\vec{J}$ of this current density (thus in terms of the wavevector $\vec{k}$) is obtained as:

$$\vec{J}(\vec{k},t) = \iiint \vec{J}(\vec{r},t)e^{-i\vec{k}\cdot\vec{r}}dxdydz = q_0\frac{d\vec{r}_0(t)}{dt}e^{-i\vec{k}\cdot\vec{r}_0} \tag{3.9}$$

Thus, the complete time and spacial Fourier transform of the current density is:

$$\vec{J}(\vec{k},\omega) = \int \vec{J}(\vec{k},t)e^{i\omega t}dt = \int q_0\frac{d\vec{r}_0(t)}{dt}e^{-i\vec{k}\cdot\vec{r}_0}dt \tag{3.10}$$

What Hauss demonstrates in his paper is that the electric field $\vec{E}_{FF}$ radiated at long distances from the source is:

$$\vec{E}_{FF} = 2\pi q_0\vec{v}\delta(\omega - \vec{k}\cdot\vec{v}) \tag{3.11}$$

where $\vec{v}$ is the linear velocity of the charge q_0 defined as $\vec{v} = \frac{d\vec{r}_0}{dt}$. Thus, the electric field will be zero unless:

$$\omega = \vec{k}\cdot\vec{v} \rightarrow |\vec{k}| = \frac{\omega}{|\vec{v}|cos\theta_{kv}} \tag{3.12}$$

with $\theta_{kv} = \widehat{\vec{k}\vec{v}}$

This is the why Hauss states that *a distribution of accelerated charges will radiate if and only if it has Fourier components synchronous with waves traveling at the speed of light.*

It is obvious that the linear velocity of a moving particle particle, even an electron, is lower that the speed of light c, so the condition shown at eq.3.12 at which the electric field far away of the source $\vec{E}_{FF} \neq 0$ can be expressed as:

$$|\vec{k}| > \frac{\omega}{c} \tag{3.13}$$

From eq.3.13 it is quite easy to understand the dispersion diagram in terms of which are the radiated and the non radiated modes. In fig.3.3 only the general shape of a SPP and a LSP was presented. Now, once the radiation conditions has been presented, it is useful to complete the dispersion diagram with the limit shown in eq.3.13, leading to fig.3.4

Fig.3.4 shows that in the case of SPP no radiating ligth is obtained and thus all the radiation emmited by the plasmon is confined in the plane of the wavevector k_x. The case of the LSP is different, as it can easily be coupled in radiated light as it fulfills the Hauss condition shown in eq.3.13. Thus, LSPs do not only scatter energy into electromagnetic energy (a general term), but also into light.
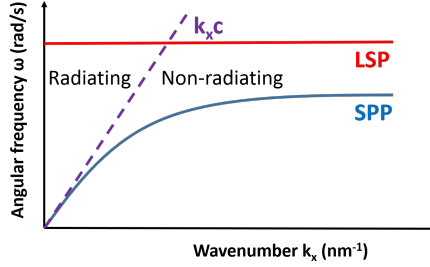
Figure 3.4: Dispersion diagram for a Surface Plasmon Polariton (SPP) and a Localised Surface Plasmon (LSP), including the limit for light coupling.

3.3   Scattering of light by single nanoparticles

It is possible to calculate the amount of scattered light (I_{sca}) or absorbed light (I_{abs}) by defining an absorption cross-section σ_{abs} and a scattering cross-section σ_{sca} as [11, section 3.4]:

$$I_{sca} = \frac{I_0(\omega)}{A} \cdot \sigma_{sca} \tag{3.14}$$

$$I_{abs} = \frac{I_0(\omega)}{A} \cdot \sigma_{abs} \tag{3.15}$$

where $\frac{I_0(\omega)}{A}$ is the light intensity per area unit that excites the nanoparticle. It is common to make a power balance by defining the transmitted light $I_{trans} = I_0 - (I_{sca} + I_{abs})$. Fig.3.5 summarises this balance.
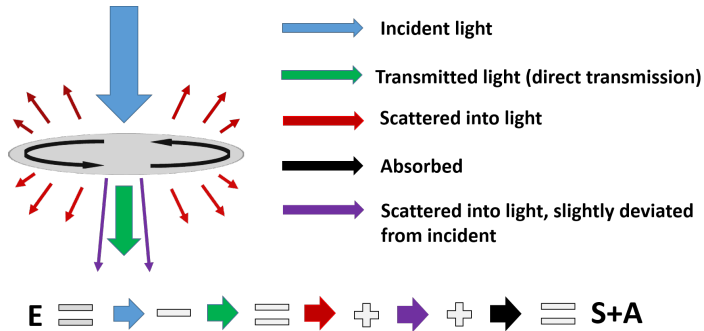

Figure 3.5: Visual definition of the scattering and the absorption as components of the extinction

In fig.3.5, the extinction is the total amount of light that interacts in any way with the nanoparticle. The term extinction is used because, from the experimental point of view, optical measurements of direct transmission always allow to determine the amount of light which is not transmitted, i.e., extinct, due to the interaction with a nanostructure, similarly with the extinction studies defining the Beer-Lambert law[12]. Thus, the extinction includes both the scattering and the absorption losses. Fig.3.5 summarises this concept. The absorption is the amount of light that is lost during its interaction with the nanoparticle. This means that it is not trasmitted nor reflected, even in different directions.

Of course, the difference between the extinction and the absorption gives the scattering: The amount of light that interacts with the nanoparticle and is scattered as light towards any other direction other than the incident source direction. In the following section some more comments are done to understand the cross section approach to quantify absorption, scattering and thus extinction.

3.3.1   Effective cross sections

The advantage of dealing with cross sections is that usually it is necessary not only to quantify scattering and absorption but also to compare their relative magnitudes. The cross section approach allows this quite easily.

A cross section σ is a magnitude, in terms of a surface, that expresses the probability of interaction with a defined domain.When normalising those cross-sections σ with the geometrical particle cross-section (for spheres,πr^2) they result in the scattering, absorption and extinction efficiencies (Q_{sca},Q_{abs} and Q_{ext}, respectively). It is remarkable that, from this approach, it is possible to find values bigger than unity. This means than the scattering or the absorption can take place not only in the nanostructure where the LSP is, but beyond it, at its vicinity. This allows light to interact with matter even if the photon is not directly incident on the nanostructure. Fig.3.6 summarises this effect for a sphere.

In fig.3.6 the light matter interaction between photons and a nanosphere is represented schematically. For effective cross sections higher than the physical cross section of the nanoparticle, there are photons that interact, and thus are deviated from its original trajectory, beyond the physical cross section of the nanoparticle.

Looking at fig.3.5, there is an important remark with the cross sections: The overall cross section value only makes a balance between the incident and transmitted photons with and without interaction. This means that no
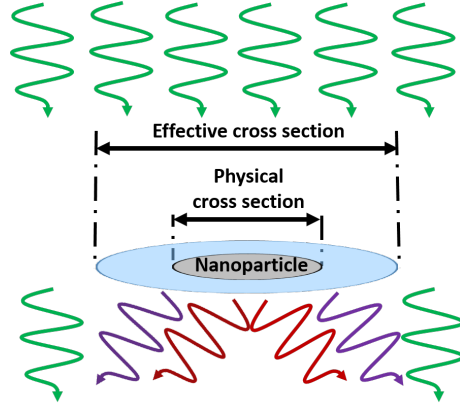
Figure 3.6: Schema of the difference between the physical cross section of the nanostructure and the effective cross section in terms of scattering.

information on how deviated is the scattered light when compared with the incident is given by a this parameter[6].

The main question that follows is: How can extinction and cross sections be calculated? In fact, their calculation implies to solve the electromagnetic Maxwell equations (see section 3.3.2). And this is not always easy to do without numerical models and specific software. However, there are some special cases that can be studied analytically and have been extensively used. Moreover, when studying scattering and absorption cross sections, it is mandatory to refer to Mie's work. In order to better understand it, a brief review of Maxwell equations is needed.

3.3.2 Maxwell equations and Helmoltz approach

Light scattering is an electromagnetic phenomenon and thus it can be treated using Maxwell's equations. Those equations can be expressed in differential form as the Gauss's Law (eq.3.16 that relates charges with electric field), the magnetic Gauss's Law (eq.3.17 that states that there can not be any magnetic monopole), the Maxwell-Faraday equation (eq.3.18 that shows the induction of an electric field from a magnetic field) and finally the Ampere circuital law

---

[6]However, is is possible to calculate the angular dependency on the scattered light in order to define the angular dependent cross-section. These are complex expressions that will not be considered until necessary.

(eq.3.19 that shed light on the induction of magnetic fields from a combination of currents and electric fields).

$$\nabla \cdot \vec{E} = \frac{\rho}{\epsilon} \tag{3.16}$$

$$\mu_0 \nabla \cdot \vec{H} = 0 \tag{3.17}$$

$$\nabla \times \vec{E} = -\mu \frac{\partial \vec{H}}{\partial t} \tag{3.18}$$

$$\nabla \times \vec{H} = \vec{J} + \epsilon \frac{\partial \vec{E}}{\partial t} \tag{3.19}$$

where: $\vec{E}$ is the electric field, $\vec{H}$ is the magnetic field, $\vec{J}$ is the current density, ρ is the total charge density, ϵ is the material electric permittivity and μ is the magnetic material permeability.

From basic vector calculus, when there is a vector field $\vec{v}$ where $\nabla \times \vec{v} = 0$, then $\vec{v}$ is said to be irrotational. As the curl of the gradient of any scalar field is always the zero vector, for $\vec{v}$ there exists an equivalent scalar field Φ so that $\vec{v} = -\nabla \Phi$ and thus $\nabla \times \nabla \Phi = 0$.

In a similar way, for a scalar field F that satisfies $\nabla \cdot F = 0$, there exists an equivalent vector field $\vec{A}$ so that $\nabla \cdot (\nabla \times \vec{A}) = 0$.

This implies that the Maxwell equations can be rearranged using the equivalent scalar field Φ and the equivalent vector field $\vec{A}$. In order to do that, an assumption is done to consider monochromatic and harmonic waves (eq.3.20). This assumption leads to much simpler time derivatives in the Fourier domain that will be used in the following development.

$$\vec{E}(\vec{r}, t) = E_0 e^{(\omega t - \vec{k} \cdot \vec{r} + \phi_0)} \tag{3.20}$$

where $E_0 = |\vec{E}(\omega, t)|$, ϕ_0 is the initial phase and $\vec{k}$ is the wavevector, defined for a medium i as:

$$\vec{k} = |\vec{k}|\hat{k} = k\hat{k} = \frac{\omega}{c}\hat{k} = \frac{2\pi}{\lambda}\sqrt{\epsilon_i}\hat{k} \tag{3.21}$$

- From the magnetic Gauss law (eq.3.17), using the equivalent potential approach, a vector potential $\vec{A}$ can be defined:

$$\nabla \cdot \vec{H} = 0 \longrightarrow \vec{H} = \nabla \times \vec{A} \tag{3.22}$$

- From the Maxwell-Faraday equation (eq.3.18) and from the expression just found for $\vec{A}$ (eq.3.22), it is deduced:

$$\nabla \times \vec{E} = -i\mu\omega\vec{H} = -i\mu\omega(\nabla \times \vec{A}) \qquad (3.23)$$

Thus, it is possible to obtain the scalar potential ϕ by rewriting eq.3.23 as:

$$\nabla \times \left(\vec{E} + i\mu\omega\vec{A}\right) = 0 \rightarrow -\nabla\phi = \vec{E} + i\omega\mu\vec{A} \qquad (3.24)$$

- From the Ampere circuital law (eq.3.19) and eq.3.23 the relation between the current $\vec{J}$, the electric field $\vec{E}$ and the vector potential $\vec{A}$ is found as[7]:

$$\nabla \times (\nabla \times \vec{A}) = \nabla(\nabla \cdot \vec{A}) - \nabla^2\vec{A} = \vec{J} + i\epsilon\omega\vec{E} \qquad (3.25)$$

From where, expressing the electric field $\vec{E}$ in terms of the scalar potential (eq.3.24), the following expression is found, relating both the scalar and the vector potentials:

$$\nabla(\nabla \cdot \vec{A}) - \nabla^2\vec{A} = \vec{J} - i\epsilon\omega\nabla\Phi + \epsilon\mu\omega^2\vec{A} \qquad (3.26)$$

Eq.3.27 can be rearranged by using eq.3.21 and recalling that $\frac{1}{c^2} = \mu\epsilon$, leading to:

$$\nabla(\nabla \cdot \vec{A}) - \nabla^2\vec{A} - k^2\vec{A} = \vec{J} - i\epsilon\omega\nabla\Phi \qquad (3.27)$$

Many different vector $\vec{A}$ and scalar Φ potentials can be defined that fulfill those equations. In order to fully define the system, the following relation between $\vec{A}$ and Φ is chosen[8]:

$$\nabla \cdot \vec{A} = -i\epsilon\omega\Phi \rightarrow \nabla(\nabla \cdot \vec{A}) = -i\epsilon\omega\nabla\Phi \qquad (3.28)$$

Finally, under all these assumptions, it is found:

$$\nabla^2\vec{A} + k^2\vec{A} = -\vec{J} \qquad (3.29)$$

Notice that eq.3.29 is a Helmoltz-like non-homogeneous linear second order differential equation and this may be difficult so solve. The inhomogeneous term correspond to the currents involved in the phenomena. These currents are always present during the scattering of light by nanoparticles. Therefore, the approach of the equivalent potentials is useful when studying scattering systems.

---

[7]It is useful to recall that $\nabla \times (\nabla \times \vec{F}) = \nabla(\nabla \cdot \vec{F}) - \nabla^2\vec{F}$.

[8]This is usually known as the Lorenz Gauge.

3.3.3 Mie scattering model

The Mie model is considered as an exact solution for metal spheres obtained by solving Maxwell equations. However, more than a model or a solution by itself, it is a strategy to find the solution. The full details and mathematical development of the following strategy can be found in [11, ch.4] and it is too complicated to be repeated here. Let us, however, make a quick overview to understand the strategy.

In section 3.3.2, from Maxwell equations the wave equation (Helmoltz) is found. For that, virtual scalar and vector potentials had been defined. In a similar way, it is possible to define two vector functions ($\vec{M}$ and $\vec{N}$) and a scalar function(ψ) that accomplish the following conditions:

Let us define a scalar function ψ and an arbitrary constant vector $\vec{c}$, from which the first vector function $\vec{M}$ is defined:

$$\vec{M} = \nabla \times (\vec{c}\psi) \tag{3.30}$$

The vector field $\vec{M}$, as defined in eq.3.30 is perpendicular to the vector $\vec{c}$. Also, as the divergence of any curl is zero:

$$\nabla \cdot \vec{M} = 0 \tag{3.31}$$

The second vector function $\vec{N}$ is defined from the first one as:

$$\vec{N} = \frac{\nabla \times \vec{M}}{k} \tag{3.32}$$

which, analogously to $\vec{M}$, fulfills:

$$\nabla \cdot \vec{N} = 0 \tag{3.33}$$

From this definition of $\vec{M}$, the following identity can be obtained:

$$\nabla^2 \vec{M} + k^2 \vec{M} = \nabla \times \left[\vec{c}\left(\nabla^2\psi + k^2\psi\right)\right] \tag{3.34}$$

Eq.3.34 implies that the as defined vector function $\vec{M}$ fulfills the wave equation if the scalar function ψ from which it has been defined also fulfills it.

$$\nabla^2\psi + k^2\psi = 0 \tag{3.35}$$

Under this assumption, the vector field $\vec{N}$ also fulfills the following conditions:

$$\nabla^2 \vec{N} + k^2 \vec{N} = 0 \tag{3.36}$$

$$\nabla \times \vec{N} = k\vec{M} \tag{3.37}$$

Therefore, the vector fields M and N share the same properties that the electric and magnetic fields, respectively:

- Both fulfill the wave equation (eq.3.34 with condition in eq.3.35 and eq.3.36)

- Both are divergence free (eq.3.31 and eq.3.33)

- The curl of each field is proportional to the other (eq.3.32 and eq.3.37)

Thus, as $\vec{N}$ is defined from $\vec{M}$ and $\vec{M}$ is defined from ψ, the problem of finding solutions to the field equations is equivalent to solving the scalar wave equation shown in eq.3.35. This is simpler than solving the vector equation. Moreover, expanding eq.3.35 in spherical coordinates, analytical solutions are available. Most of the mathematical difficulty for using Mie's strategy is related with how to find that analytical solution. In brief, after an ansatz[9] it is found that the solution is not unique.

In the case of a spherical geometry, and using spherical coordinates $(r, \phi, \theta$, two groups of solutions are found that are linearly independent (expressed with superscripts (i) and (ii) in eq.3.38 and eq.3.39). Moreover, so that the ansatz fulfills the boundary conditions, there are two splitting indexes (called m and n) for the solutions. The generating functions that lead to any possible solution are:

$$\psi_{mn}^{(i)}(r, \phi, \theta) = \cos(m\phi)P_n^m(\cos\theta)z_n(kr) \tag{3.38}$$

$$\psi_{mn}^{(ii)}(r, \phi, \theta) = \sin(m\phi)P_n^m(\cos\theta)z_n(kr) \tag{3.39}$$

In eq.3.38 and eq.3.39, P_n^m are associated Legendre Polynomials, k is the wavevector and the $z_n(kr)$ term corresponds to a spherical Bessel function that can be chosen regardless on the validity of the solution between:

- Spherical bessel function of first kind $j_n(x)$, from the Bessel function of first kind $J_n(x)$:

$$j_n(x) = \sqrt{\frac{\pi}{2x}}J_{n+\frac{1}{2}}(x) \tag{3.40}$$

---

[9]An *ansatz* is a commonly used strategy of solving differential equations with partial derivatives consisting on assuming a generic form of the solution where different terms are being multiplied, each one depending on one of the variables (this is why it is usually called a variable separation). From this generic form and using the boundary conditions an expression for the solution is found. As this is an ad-hoc method, the solution must be verified at the end of the process to check whether the initial hypothesis is consistent.

- Spherical bessel function of second kind $y_n(x)$, from the Bessel function of second kind $Y_n(x)$:

$$y_n(x) = \sqrt{\frac{\pi}{2x}} Y_{n+\frac{1}{2}}(x) \tag{3.41}$$

- Spherical bessel function of third kind or Hankel functions. In this case, two possible functions can be defined as a combination of the two first functions:

$$h_n^1(x) = j_n(x) + i y_n(x) \tag{3.42}$$

$$h_n^2(x) = j_n(x) - i y_n(x) \tag{3.43}$$

From the solutions shown in eq.3.38 and eq.3.39 it is possible to obtain the vectorial solutions of the field using eq.3.31 and eq.3.32. As two groups of scalar solutions are found, two groups of vector solutions appear: $\vec{M}_{nm}^{(i)}$ and $\vec{N}_{nm}^{(i)}$ versus $\vec{M}_{nm}^{(ii)}$ and $\vec{N}_{nm}^{(ii)}$. With those, it is possible to obtain the internal and external electric and magnetic fields in a sphere as a sum of terms[10].

For the fields induced internally in the sphere by an external excitation $\vec{E}_0$, the resulting expressions are:

$$\vec{E}_i = |\vec{E}_0| \sum_{n=1}^{\infty} i^n \frac{2n+1}{n(n+1)} \left(c_n \vec{M}_n^{(ii)} - i d_n \vec{N}_n^{(i)} \right) \tag{3.44}$$

$$\vec{H}_i = \frac{-k_{sph}}{\omega \mu_{sph}} |\vec{E}_0| \sum_{n=1}^{\infty} i^n \frac{2n+1}{n(n+1)} \left(d_n \vec{M}_n^{(i)} + i c_n \vec{N}_n^{(ii)} \right) \tag{3.45}$$

where n is the summation index (whose meaning will be explained in section 3.3.4), i is the imaginary unit, ω is the frequency, k_{sph} and μ_{sph} are the wavenumber and the magnetic permeability of the sphere and a_n,b_n,c_n and d_n are weighting coefficients applied to each vector solution.

Additional mathematical treatment that is not included in this text demonstrates that only terms with m=1 are different to zero. Thus, the dependency of the solutions on the subindex m will not be included anymore. Moreover, eq.3.44 and eq.3.45 define the vector solution $\vec{N}_{1n}^{(i)}$ and $\vec{M}_{1n}^{(ii)}$ using the scalar function solutions (eq.3.38 and eq.3.39) with the z_n choice of the spherical bessel function of first kind (eq.3.40).

---

[10]The solution is obtained as a linear combination of the vectors that define the generating basis. As the dimension of this basis is infinite, the sum should include infinite terms.

Analogously, the solution for the scattered electric and magnetic fields lead to similar expressions for the fields induced externally in the sphere:

$$\vec{E}_s = |\vec{E}_0| \sum_{n=1}^{\infty} i^n \frac{2n+1}{n(n+1)} \left(ia_n \vec{N}_n^{(i)} - b_n \vec{M}_n^{(ii)} \right) \tag{3.46}$$

$$\vec{H}_s = \frac{k}{\omega\mu} |\vec{E}_0| \sum_{n=1}^{\infty} i^n \frac{2n+1}{n(n+1)} \left(ib_n \vec{N}_n^{(ii)} + a_n \vec{M}_n^{(i)} \right) \tag{3.47}$$

However, in this case the vector solution $\vec{N}_{1n}^{(i)}$ and $\vec{M}_{1n}^{(ii)}$ are defined using the spherical hankel function of first kind (eq.3.42).

It should be noticed that eq.3.44 to eq.3.47) are very similar. The vector functions $\vec{M}$ and $\vec{N}$ are mathematical expressions that depend on the spatial coordinates and the properties of the materials involved. Therefore, there are only 4 parameters that are still not known: The coefficients a_n, b_n, c_n and d_n.

These coefficients can be solved with additional boundary conditions assuming a plane wave excitation. In order to simplify their expressions, the following terms have to be defined:

- The relative permitivity of the medium, m, between the sphere (ϵ) and the surrounding medium (ϵ_m):

$$m = \frac{\epsilon}{\epsilon_m} = \epsilon' + i\epsilon'' \tag{3.48}$$

- The size parameter. This adimensional parameter relates the radius of the sphere r with the wavelength λ through:

$$\breve{x} = \frac{2\pi\tilde{\epsilon}_m r}{\lambda} \tag{3.49}$$

- The Riccati-Bessel function of first kind Ψ, obtained from the spherical-bessel function (eq.3.40) as:

$$\Psi(x) = xj_n(x) \tag{3.50}$$

- The Riccati-Bessel function of second kind ξ, obtained from the hankel function of first kind (eq.3.42) as:

$$\xi(x) = xh_n^{(1)}(x) \tag{3.51}$$

With these terms, the expressions for the well-known Mie coefficients[11] are:

$$a_n = \frac{m\Psi_n(m\breve{x})\Psi'_n(\breve{x}) - \Psi_n(\breve{x})\Psi'_n(m\breve{x})}{m\Psi_n(m\breve{x})\xi'_n(\breve{x}) - \xi_n(\breve{x})\Psi'_n(m\breve{x})} \tag{3.52}$$

$$b_n = \frac{\Psi_n(m\breve{x})\Psi'_n(\breve{x}) - m\Psi_n(\breve{x})\Psi'_n(m\breve{x})}{\Psi_n(m\breve{x})\xi'_n(\breve{x}) - m\xi_n(\breve{x})\Psi'_n(m\breve{x})} \tag{3.53}$$

Finally, once the Mie coefficients are determined, the scattering and extinction cross sections are found as:

$$\sigma_{scat} = \frac{2\pi}{k^2} \sum_{n=1}^{\infty} (2n+1)(|a_n|^2 + |b_n|^2) \tag{3.54}$$

$$\sigma_{ext} = \frac{2\pi}{k^2} \sum_{n=1}^{\infty} (2n+1)(Re(a_n + b_n)) \tag{3.55}$$

As previously defined, the absorption cross section correspond to the difference between the exctinction and scattering.

Probably, it is a good idea to make a short summary of the Mie strategy to keep the key ideas:

1. It has been shown that there exist two vector functions $\vec{M}$ and $\vec{N}$ that fulfill the wave and the Maxwell equations. Those vector functions are defined from the same scalar function ψ, so it is possible to solve both fields by solving the scalar function ψ.

2. It has been shown that the solution of the scalar function ψ can be done analytically in some special geometries such as spheres using an ansatz in spherical coordinates. This variable separation leads to a general solution in the form of a sum two groups of linearly independent generating functions that are based on $\vec{M}$ and $\vec{N}$ and that depend on two parameters m and n (eq.3.38 and eq.3.39). The generic solution, whose development is not presented in this thesis, is valid for any of the spherical bessel functions (eq.3.40 to eq.3.43).

3. From the general solution of a sphere, explicit expressions for the scattered and internal electric and magnetic fields (eq.3.44 to eq.3.47) are presented. The solution is obtained as a sum of particular solutions that are combined linearly. At this step, several coefficients a_n, b_n, c_n and d_n are introduced. Those are usually called Mie coefficients.

---

[11]Only the a_n and b_n coefficients are presented as the extinction and the absorption cross sections depend on it. In the reference [11, p.100] it is possible to find the two others.

4. In order to completely define the solution, the Mie coefficients have to be solved. The boundary conditions used to solve them include a plane wave excitation condition. Also, some adimensional parameters are defined, as well as the Ricatti-Bessel functions, in order to have simpler expressions for a_n and b_n, as presented on eq.3.52 and 3.53.

5. Finally, expressions for the extinction and absorption cross sections that mainly depend on the Mie coefficients a_n and b_n are presented. As the Mie coefficients have been fould for single spheres on an homogeneous medium when excited with a plane wave, eq.3.52 and 3.53 are only valid in this case.

A final comment should be done to remark that even if the expressions shown in eq.3.52,eq.3.53,eq.3.52 and eq.3.52 are valid only for single spheres in an homogeneous medium, the strategy can be used for other geometries such as cilynders using different ansatz.

3.3.4 LSP resonances in a sphere

In section 3.3.3, the overall strategy to solve the scattering and extinction from a sphere is summarised. In this section, some comments are done to better understand the equations form the physical point of view. From eq.3.52 and eq.3.53, two main conclusions can be obtained:

First, that the overall extinction is obtained as series using the different Mie coefficients. This sum was explained as the combination of linearly independent solutions but no more details were given.

In fact, each of the orders that are added up in the series include the contribution of different (and independent) solutions $\vec{M}$ and the $\vec{N}$. Independent solutions correspond to different scattering modes that take place at the same time and whose global influence is weighted by the Mie coefficients. Fig.3.7 shows the first 4 modes for both the $\vec{M}$ and the $\vec{N}$ contributions in eq.3.46

In fig.3.7, the field lines of the electric field scattered by a sphere are shown. There are in fact two different scattering modes for each excitation order n. Each order has two contributions or solutions, related to the $\vec{M}$ and the $\vec{N}$ fields defined in section 3.3.3. There, the equivalence of those fields with the electric $\vec{E}$ and the magnetic fields $\vec{H}$ was shown. The relationship can be easily seen, as the $\vec{M}$ contribution to the scattering solutions correspond to different TM excitation modes (with no radial $\vec{H}$ component) and the $\vec{N}$ components correspond to TE excitation modes (with no radial $\vec{E}$ component). In short, for n=1 there is an electric (TE contribution) and magnetic (TM contribution) dipole radiating mode, for n=2 there are electric and magnetic quadrupoles and so on. Again, the relative importance of each TE and TM contribution is weigthed by the Mie coefficients.
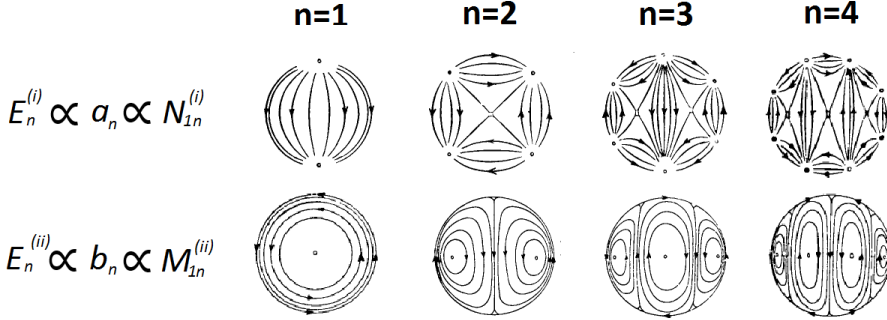
UNIVERSITAT
POLITÈCNICA
DE VALÈNCIA

Valencia Nanophotonics Technology Center

ESCUELA TÉCNICA
SUPERIOR INGENIEROS
INDUSTRIALES VALENCIA

Figure 3.7: Electric field lines for the independent sphere solutions for the scattering of a sphere. Different excitations terms $(n = 1..4)$[11, p.98].

In short, the different individual scattering modes are well known and any scattering solution in a sphere can be expressed from a weighted sum of those TE and TM modes.

Some readers may ask that after the summary and all the comments on Mie strategy, no resonance is still named. But once the strategy of resolution is understood, once the different contribution to the overall solutions are explained, and once the Mie Coefficients are quantified in eq.3.52 and eq.3.53, the resonance is very easy to understand.

The extinction is proportional to the Mie coefficients, so the resonances will appear when, at least one of the coefficients tends to infinity. This can happen because the dielectric function of the materials are wavelength dependent. This will lead to different resonances corresponding to the poles of each individual mode. Thus, TE dipole resonance can be found, as well as TM dipole resonance, TE quadrupole resonance, TM quadrupole resonance, etc.

From the definitions of the Mie coefficients in eq.3.52 and eq.3.53 it can be seen that there are two special cases:

- When the numerator goes to zero. From the numerical point of view, this happens when the m parameter approaches unity and would lead to a zero scattering. From the physical point of view, this happens when the surrounding media of the sphere has the same permittivity function than the sphere. In this case, no plasmon is produced as no real interface would be found. Therefore, no scattering should be produced.

- When the denominator goes to zero. In this case, the scattering would tend to infinite. This would correspond to a resonance in the plasmon. However, the infinite value is not achieved as the poles of the coefficients

correspond to complex frequencies. However, maxima values can be found in the coeffcients, and those wavelengths are considered as resonances.

The bessel functions are not periodic, but they present an oscillatory behaviour, as shown in fig.3.8. Thus, more than a single maximum could be found for each excitation order. However, only the first one (at lower energies) will be considered as resonance.
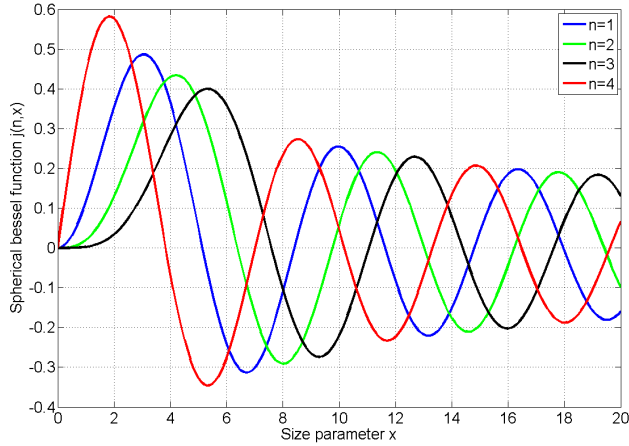

Figure 3.8: Spherical bessel function of first kind at different orders

A last comment about eq.3.54 and 3.55 is that even if the summation goes from 1 to infinity, only the lower orders are usually excited and, in practice, for small particles the dipole excitation is predominant. Also, for metallic nanoparticles in the visible range usually the TM contribution is negligible for small particles.

3.3.5 Quasi-static approximation

The quasi-static (or electrostatic) approximation (QSA) is a simplification to avoid solving Maxwell equations under the assumption that the nanostructure being excited is small enough to see a constant field everywhere in its domain. Thus, the Laplace equation for electrostatics can correctly model the system.

This has several advantages from the numerical point of view as under these assumptions the scattering and absorption cross section come as:

$$\sigma_{sca} = \frac{k^4}{6\pi\epsilon_0^2}|\alpha|^2 \tag{3.56}$$

Valencia Nanophotonics Technology Center

ESCUELA TÉCNICA
SUPERIOR INGENIEROS
INDUSTRIALES VALENCIA

UNIVERSITAT
POLITÈCNICA
DE VALÈNCIA

and

$$\sigma_{abs} = \frac{k}{\epsilon_0} Im(\alpha) \tag{3.57}$$

where α is the electrostatic polarisability, that depends on the volume of the nanoparticle V and the relative permittivity of eq.3.48 through the Clausius-Mossotti relation [13] (ec.3.58):

$$\alpha = 3\epsilon_0 V \frac{\tilde{\epsilon}_{rel} - 1}{\tilde{\epsilon}_{rel} + 2} \tag{3.58}$$

This is the usual approach from the electrostatic point of view, and it is usually valid for small nanoparticles. This approach usually considers that only a dipole can be excited within the nanoparticle. However, another approach to the quasi static approximation would be starting with Maxwell equations, solving the scattering problem using the Mie approach and taking limits when the size parameter $\breve{x}$ in eq.3.49 tends to zero.

However, not only the dipole mode can be found under this assumption. The spherical bessel functions can be expressed as series expansions [14]:

$$j_n(z) = z^n \sum_{k=0}^{\infty} \frac{\left(-\frac{1}{2}z^2\right)^k}{k! \, (2n + 2k + 1)!!} \tag{3.59}$$

$$
\begin{aligned}
y_n(z) = - \frac{1}{z^{n+1}} \sum_{k=0}^{\infty} \frac{(2n - 2k - 1)!! \left(-\frac{1}{2}z^2\right)^k}{k!} + \\
+ \left(\frac{-1}{z}\right)^{n+1} \sum_{k=n+1}^{\infty} \frac{\left(-\frac{1}{2}z^2\right)^k}{k! \, (2k - 2n - 1)!!}
\end{aligned} \tag{3.60}
$$

Notice that eq3.59 and 3.60 have a double factorial dependency. Thus, even for small excitation orders n, where most of the scattering contribution is supposed to be, the increasing summation terms k tend quickly to zero. Moreover, if the product of the relative permittivity (eq.3.48) and the size parameter (eq.3.49) is $|m|x \ll 1$, the magnetic contribution (b_n coefficients) is much smaller than the electric contribution. Under this approximation, the following Mie coefficients are found:

$$a_1^{QSA} \simeq \frac{4x^6}{9} \left(\frac{m^2 - 1}{m^2 + 2}\right) - \left(\frac{2x^3}{3} \frac{m^2 - 1}{m^2 + 2} - \frac{2x^5}{5} \frac{(m^2 - 2)(m^2 - 1)}{(m^2 + 2)^2}\right) i \tag{3.61}$$

$$b_1^{QSA} \simeq -\frac{x^5}{45}(m^2 - 1) \tag{3.62}$$

Notice that, as $x \ll 1$ the x^5 term in the magnetic dipole contribution is much smaller than the x^3 term in the electric dipole contribution. Thus, the magnetic dipole is usually neglected.

For higher excitation orders n, there is a very small contribution both for magnetic and electric excitation modes. It is possible however, conclude that the resonance would be determined by:

$$m^2 = \frac{n+1}{n} \tag{3.63}$$

Eq.3.63 correspond to the pole condition in denominators of eq.3.52 in the limit of very small particles, that is, with $\tilde{x}$ tending to zero. This means that the resonances of the sphere, under the QSA and neglecting any magnetic contribution, would be found at the frequencies that fulfill the conditions in table3.1

Excitation order	Resonance condition
n=1	$m^2 = \frac{2}{1} = 2$
n=2	$m^2 = \frac{3}{2}$
n=3	$m^2 = \frac{4}{3}$
n=4	$m^2 = \frac{5}{4}$

Table 3.1: Resonance condition for different excitation orders under the quasi-static approximation.

3.3.6 Retardation effects

One of the main consequences of the QSA is that the resonances depend only on the materials and not on the size of the nanoparticles. This means that the retardation effects are neglected [15, 16].

The retardation effects are related with the finitness of the light speed: When the particle becomes big enough, the electrons movement is not homogenous as the photon's electric field is not constant across the nanoparticle. Thus, different accelerations are experienced by different the electrons in the nanoparticle. This has several consequences:

- Higher order excitation modes are created as the perfect dipole electronic movement disapears. This does not mean that the dipole is no longer present, but not necessarily the only remarkable mode.

- As there are electrons that cannot follow perfectly the external driving field movement, the scattered light has a lower frequency. This is commonly referred as a redshift effect as the scattered light is shifted to the red or the infrared.

It is notable that in 2008 Myroshnychenko et al [17] proposed a corrected QSA model using both eq.3.56 and 3.57 but changing the expression of the polarisability from ec.3.58 to the following:

$$\alpha_{Mie} = 3\epsilon_0 V \frac{\frac{1}{\tilde{\epsilon}_m} - 0.025(\tilde{\epsilon}_{rel} + 1)\breve{x}^2}{\frac{1}{\tilde{\epsilon}_m}\frac{\tilde{\epsilon}_{rel}+2}{\tilde{\epsilon}_{rel}-1} - 0.25(0.1\tilde{\epsilon}_{rel} + 1)\breve{x}^2 - i\sqrt{\tilde{\epsilon}_m}\frac{2}{3}\breve{x}^3} \tag{3.64}$$

3.4 Deviations from Mie solution

Some time has been invested to understand Mie approach for solving the extinction of individual spheres in homogeneous media. This is an exact solution to Maxwell equations in this case and many studies can be found in the literature based on this approach. In fact, it is a good starting point to understand the general trends and the scattering behaviour of a nanoparticle.

However, in real structures with other conditions, the validity of Mie approach is not always reliable. In fact, just by the fact that the nanoparticles are placed over a substrate, makes the medium non homogeneous. One of the motivations of this thesis is to study how this can change Mie conclusions.

Moreover, the NPs are usually found in arrays. This introduces interactions among nanoparticles. Which kind of interactions and how strong they are is another point to take into account in order to study the conditions for which Mie can still approximate a result.

Finally, real nanoparticles are not perfect spheres. Thus, Mie would not be the exact solution that it is claimed to be from the theoretical point of view. Using the Mie approach, however, it is possible to find analogous expressions for spheroids in the QSA, as well as expressions for coated spheres.

3.4.1 Non-spherical particles

A special focus on the overall strategy rather than in the mathematical details of the solution has been done to understand the Mie approach and the QSA. There are different expressions found for other geometries as spheroids and coated spheres that share the same approach. No more details will be given for them as this is beyond the scope of this thesis, but they should be perfectly understandable for any at this point.

There are expressions found using the Mie strategy but with different assumptions that lead to Mie coefficients for spheroids [18], cilynders [19], coated particles [20].

For arbitrary shapes, usualy purely numerical approaches are used to solve the Maxwell equations and obtain the extinction and scattering of a nanoparticle. Most comercial softwares such as COMSOL Multiphysics[21], Silvaco[22] and CST[23] can solve the problem. There are other free codes developped ad hoc for scattering problems, such as the Discrete Dipole Scattering (DDSCAT) [24, 25] and the T-Matrix method[26].

3.4.2 Nanoparticle interaction

The solution obtained by using Mie approach and shown in this thesis correspond to a single sphere. This is not the real case, where an array of particles is studied. Thus, in order to understand which deviations could be expected (as well to avoid misunderstandings), some comments will be done.

First, any reader should keep in mind that the plasmon definition has been done in terms of a quasi-particle, that is, a particle that behaves like a wave (or a wave that has properties of a particle). From this point of view, some of the conclusions found for electrons are analogous for plasmons[12].

In fact, as explained in section 2.1, the electrons can be modelled with a wavefunction that defines atomic orbitals. Those orbitals may interact and lead to molecular orbitals, producing a split in the energy levels. In order for this to happen, the atomic electrons have to be close enough to interact.

In a similar way, the plasmon energy levels can be split [27]. This will occur when two spheres are close enough so that the excitation is not only done by an external plane wave, but also from the scattered field by the other sphere. This can produce very different solutions from those predicted from Mie[13]. In fact, these cases correspond to what are usually called "dark modes": Excitation modes that cannot be obtained by an external plane wave, but only with a near field excitation[28]. An example of the energy splitting can be found in [29], where the dipolar resonance frequency is split into higher energy (shorter wavelength) resonance where the electromagnetic power tends to concentrate in between the nanoparticles and lower energy modes with different charges distributions (some of them that lead to a net scattering cancellation). Moreover, the isotropy is also lost as different TE and TM light polarisation lead to different results [30]. Of course, not only the dipole but the quadrupolar and higher

---

[12]No many details of this is presented here, as the mathematical demonstration goes beyond the scope of this thesis. Nevertheless, in the references that are cited (as well as the references therein) more details can be found.

[13]Remember that the a_n and the b_n coefficients where solved assuming a plane wave excitation.

order resonances can also be split in energy, and even interact with the dipolar modes [31].

In any case, as previously explained, the resonance is only a particular condition for the solution where at least one of Mie Coefficients's pole is reached. Therefore, there is a solution for the scattering of a sphere at any frequency and any of them can be directly coupled into light. Thus, even if a LSP is always coupled to radiated light, it is at the resonance that the intensity of the electromagnetic fields is maximised, and therefore the hybridization is more likely to occur at a fixed distance.

There are some examples in the litterature, such as Ekinci et al [32], where periodic structures are used in order to study the interference between elements. This comes in handy to introduce an easy-to-misunderstand phenomena when dealing with LSP and the interaction between them. Another conclusion in traditional electron wavefunction study, is related with the Bloch Modes [33] that appear due to the periodicity of the wavefunction itself, leading to:

$$\Psi_{e^-}(x) = \Psi_{e^-}(x \pm X) \tag{3.65}$$

where X is a period. In fact, it is possible to applying an analogous approach to the wavefunction of the SPP and include the effect of periodicity through periodic patterns [2], leading to new solutions. Assuming that the individual dispersion relation of the planar interface is similar to those for the pattern surface, the solution would become something like what is schematised in 3.9
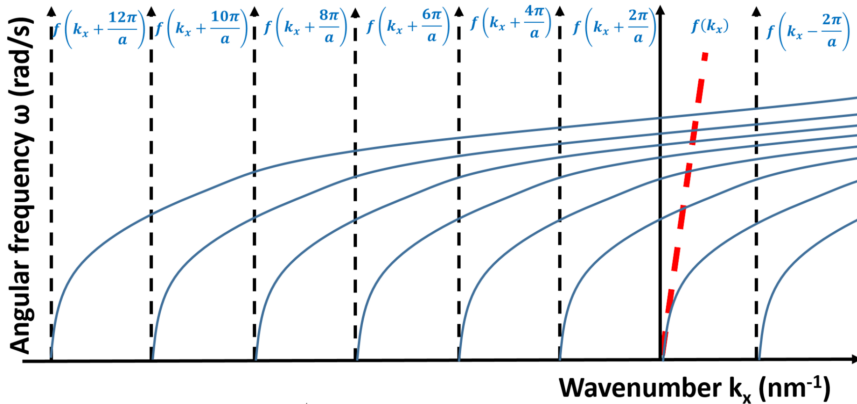
Figure 3.9: Periodicity effect on the solution of a SPP.

The periodicity is defined by a periodic pattern in the metal. Moreover, the whole structure can be summarised in a single interval, as shown in fig.3.10
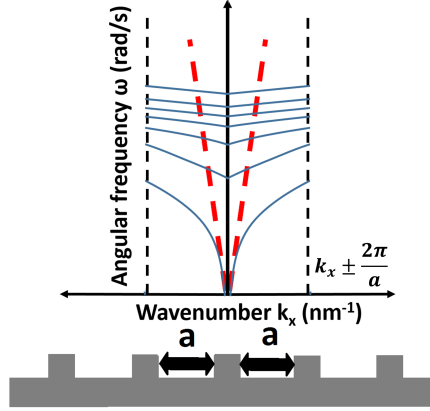
Figure 3.10: Simplified dispersion diagram for a SPP in a periodic structure.

This way, the SPP can be coupled to light as several parts of the solution fulfill eq.3.13 and are over the limit $k = \omega c \sqrt{\epsilon}$. The grating can even be done with a dielectric [34] and by controlling its shape it is even possible to control the propagation direction of the SPP [35]. This effect can even be achieved with a metallic surface with a periodic roughness [36]. But in any case, this is only valid when a continuous metallic surface is present, that is, when dealing with SPP and not with LSP. Thus, to avoid any misunderstanding, studies like [32], even in an array of NPs, cannot be related with this effect.

This difference has been remarked to be sure that it is properly understood that, in this thesis, it is not suitable to use the gratings approach to study the arrays of metallic nanoparticles not because there is not a clear periodicity but because the plasmons are LSP and not SPP.

3.4.3 Substrate effects

As recently stated, the presence of a substrate (or a multilayered system) makes the assumption of homogeneous media for the Mie solution invalid. Thus, the substrate effect has to be somehow taken into account . There exist different approaches for this. Some of them are more complex than the others.

Defining and average refractive index around the nanoparticle is the simplest way to include the substrate effect[37]. This method assumes that the mainly contribution of the substrate is going to be the displacement of the resonance peak due to a different refractive index. Thus, by taking an intermediate refractive index an easy and quick correction can be done.

The effect of the substrate, however, goes beyond a different refractive index. In fact, the presence of a substrate implies that there will be reflections and transmissions that make the exciting electromagnetic field different from a single plane wave. Moreover, the scattered field by the nanoparticle will also be partially reflected by the interface, leading to a much more complex excitation system. In order to take into account all this, there is a strategy, usually known as the *image dipole approximation*[38].

In brief, this approach assumes that there is another radiating source underneath the real nanoparticle and whose magnitude depends on the first one. When the distance between both tends to zero, the substrate effect can be approximated. This is a much more complex system than the effective index approach but it is also more exact.

There is an approach that combines these first two strategies. Some authors propose to define an effective refractive index not only using the porperties of the involved materials, but also the effect of the induced dipole[39]. This approach is complex and does not yield much improvement to the modelling.

The substrate effect can lead to more complex consequences, as the particle can be excited by its own scattered electric field (such as in the image dipole approximation). This can lead to new scattering modes such as *dark modes*, in this case excited not from other particle, but form its own reflected field [40].

3.4.4 Fano interference

The Fano interference is a physical phenomena that was first observed by Ugo Fano when he studied the inelastic scattering of electrons and found a characteristic asymmetric lineshape[41]. However, this interference is found in many other phenomena that can be modelled using waves [42, 43]. As plasmons have a wave-like behaviour, this phenomena can also appear.

Briefly, the Fano interference is produced between two resonant systems with similar resonant frequencies. This interaction changes the theoretical Lorentzian lineshape (eq.3.66) into an assymetrical form that can be modelled.

$$L(x) = \frac{1}{1 + x^2} \tag{3.66}$$

In the literature, it is usual to find the first resonating system as a "bright" mode and the second one "dark" mode. As both systems have close resonant frequencies they interfere between themselves. In fig.3.11, a plane wave excites a nanoparticle and lead to a LSP. The scattered field is able to induce different currents in the second nanoparticle that cannot be excited by the external plane wave (a dark mode). The dark mode, also, can interact with the first particle with the near field that it produces. The Fano interference is related with those two particles that become coupled as their excitations are dependent. The dark excitation mode has a phase shift when compared with the bright
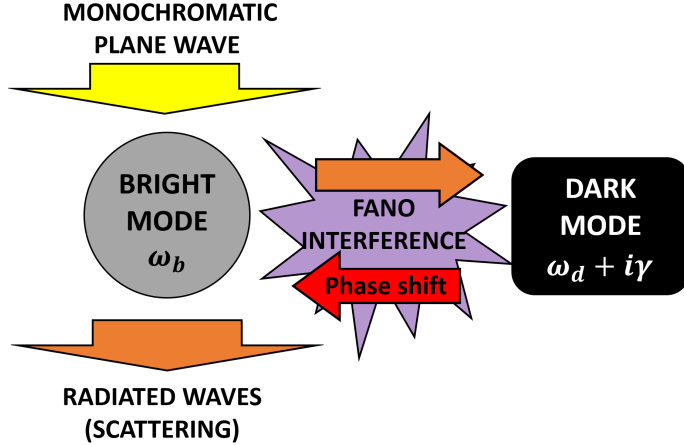
Figure 3.11: Schema of the Fano interference in the plasmon domain

mode, and has a similar resonant frequency. It is notable that for finding a Fano resonance there is no need of two particles: A single particle can interact with its own scattered field when a substrate is present due to the mirror effect that the latter has [44], analogously with what is assumed in the image dipole approximation.

From the analytical point of view, the Fano interference can be modelled as the product of a Lorentzian lineshape (eq.3.66) and a second asymmetric term. In order to define the second one, several parameters have to be defined previously:

- The bright (ω_{bright}) and dark (ω_{dark}) resonances, that is, the frequencies at which the intensity of each independent mode is maximised. It is usually expressed in terms of energy (eV). In order to find a Fano resonance, usually a broad bright mode intercts with a narrow dark mode whose resonances are close.

- The *reduced energy* κ. This adimensional parameter depends on the frequency and is related to how close is the bright mode resonance.

$$\kappa(\omega) \propto \omega^2 - \omega_{bright}^2 \qquad (3.67)$$

- The asymmetric parameter q. This addimensional parameter depends on how close are the bright and dark resonances.

$$q \propto \omega_{dark}^2 - \omega_{bright}^2 \qquad (3.68)$$

The Fano correction is given by:

$$F(\omega) = \frac{(\kappa + q)^2}{\kappa^2 + 1} \tag{3.69}$$

The resulting system when a Fano interference occurs is the product of the Fano lineshape (eq.3.69) and a Lorentzian-like system (eq.3.66):

$$f(\omega) = L(\omega) \frac{(\kappa(\omega) + q)^2}{\kappa(\omega)^2 + 1} \tag{3.70}$$

Let us, at this point, make a remark about the idea of a complex frequency shown in fig.3.11. Usually, the expression for an attenuating field includes a complex refractive index in order to express a distance r dependent loss that appears as a negative exponential term e^{-ar}. However, when dealing with a complex frequency, the final effect would be a localised attenuation (that is, not dependent on the distance), such an ohmic loss within a LSP. In this case, there appears a negative exponential time attenuation $e^{-\gamma t}$.

Among the applications where the Fano interference can be found there is one specially interesting for this thesis. In [43] it is possible to find an example of a plasmonic Fano interference where there is a term related with the non-conservative behaviour of the energy in a nanoparticle. In fact, there are two mechanisms that lead to a energy loss within the nanoparticle: The first one is related with the radiative losses (mainly the scattering) and the second one are the intrinsic ohmic losses in the nanoparticles. This term is not usually included in the traditional Fano model but is very interesting when applied to the study of nanoparticles. Thus, eq.3.69 is modified as:

$$F(\omega) = \frac{(\kappa + q)^2 + b}{\kappa^2 + 1} \tag{3.71}$$

where b is the non-conservative parameter that depends on the imaginary part γ of the dark resonant frequency ω_d in fig.3.11. An important consequence of this is that the higher the b parameter is, the smoother will the Fano interference be, as shown in fig.3.12

In some cases it is possible to fit the Fano parameters from eq.3.70 in order to shed light on how strong are the Fano interferences[41].
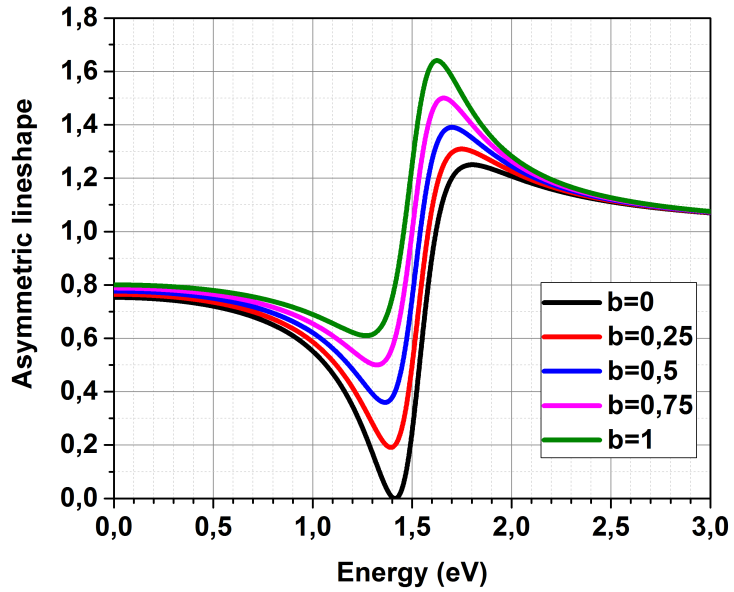
Figure 3.12: Fano interference simulated for different values of the b parameter. Simulation done for $\omega_{bright} = 1.50$eV, $\omega_{dark} = 1.58$eV and $q = 0.5$.

3.5   Light polarisation

Any electromagnetic wave (EMW) is formed by an electric field $\vec{E}$ and a magnetic field $\vec{H}$ that propagate in a direction defined by its wavevector $\vec{k}$. Both fields $\vec{E}$ and $\vec{H}$ are perpendicular one to the other and in most cases[14] also perpendicular to the propagation direccion defined by its wavevector $\vec{k}$. So, most of EMW are usually called "transverse" waves, as shown in fig.3.13, where it has been suposed[15] that $\hat{k} = \hat{z}$.
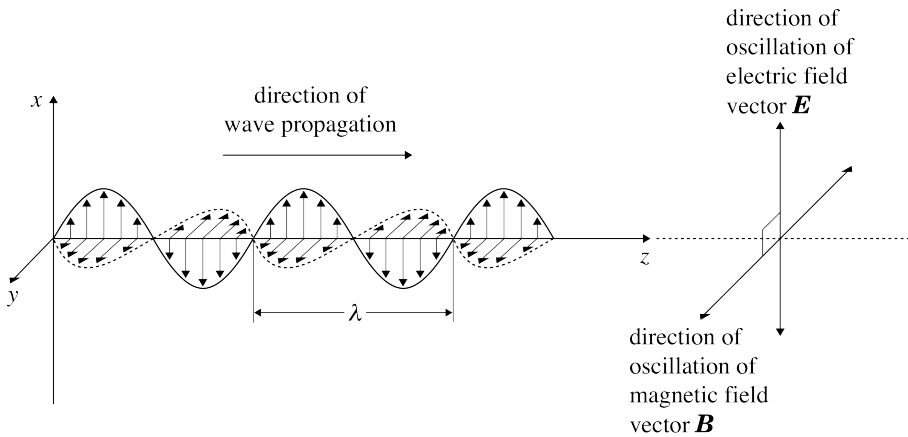
Figure 3.13: Schema of a transverse EM wave

Moreover, $\vec{E}$ components (and thus those of $\vec{H}$) can oscillate in different directions. This makes the system even more complex to study and for this reason the concept of polarisation becomes important. A light is polarised when the spatial evolution of the electric (or magnetic) field is known. In most cases, the polarisation refers to the electric component. For transverse waves, as the propagation is normal to $\vec{E}$ only two components have to be determined. And the relationship between the phase of those lead to 4 main different polarisations depending on the projection of the electric field on the plane normal to the wavevector $\vec{k}$:

---

[14]There are some special cases, however, where the propagation is not perpendicular to $\vec{E}$ and $\vec{H}$. These are called inhomogeneous waves and usually involved a lossy media with a high imaginary part of the refractive index (such like metals).

[15]All along this thesis, the circumflex symbol ˆ means a unit vector.

- Linear polarisation (fig.3.14a and b). In this case,the components of $\vec{E}$ have no phase shift between them. Assuming that the propagation is on the z direction ($\vec{k} = \hat{z}$, the expression would be:

$$\vec{E}(x, y, z, t)_{linear} = \begin{pmatrix} E_x^0 \cos{(kz - \omega t + \phi)} \\ E_y^0 \cos{(kz - \omega t + \phi)} \\ 0 \end{pmatrix} \qquad (3.72)$$

A special case will be when $\vec{Ex} = 0$ or $\vec{Ey} = 0$. (fig.3.14b)

- Elliptical polarisation (fig.3.14c). In this case, there is a phase difference between the two components of the electric field. Under the same assumptions than for the linear polsarisation, the expression would be:

$$\vec{E}(x, y, z, t)_{Elliptic} = \begin{pmatrix} E_x^0 \cos{(kz - \omega t + \phi_x)} \\ E_y^0 \cos{(kz - \omega t + \phi_y)} \\ 0 \end{pmatrix} \qquad (3.73)$$

- Circular polarisation (fig.3.14d). This is a special case of the elliptical polarisation, in which the difference of phases between the two components of the electric field corresponds to $\pi/2$. Thus, it could be expressed as:

$$\vec{E}(x, y, z, t)_{Circular} = \begin{pmatrix} E_x^0 \cos{(kz - \omega t)} \\ E_y^0 \sin{(kz - \omega t)} \\ 0 \end{pmatrix} \qquad (3.74)$$

- Random polarisation: This is not really a polarisation because there is no periodic behaviour on the spacial evolution of the electric (or magnetic) fields, but it is common to refer as random "polarisation" the lack of polarisation of a wave.

Light propagating in free space or in an isotropic medium (such as air, glass, SiO_x, SiN_x and many others) can me modelled as a plane transverse wave. In most materials, the polarisation of light is not changed and most simulations can be done assuming that it is kept constant. Moreover, even if most sources of light are formed as a sum of different polarisations, wavelengths, phases... any study can be done with a weighted combination of individual solutions for harmonic (sinusoidal dependent), single wavelength and determined polarisation waves.

In order to do this, two main approaches are commonly used: The Jones Vector [45, 46] for polarised sources and the The Mueller and Stokes Matrices [47] for partially polarised sources. The details of these approaches are not
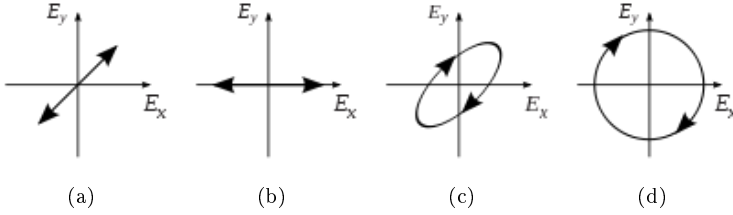
Figure 3.14: Different polarisation schema. (a) and (b) Linear polarisation (c) Elliptical polarisation (d) Circular polarisation, as a particular case of (c).

useful for this thesis but can be found in the references. In brief, the key point in the strategies is to choose several polarisation states from whose combinations it is possible to construct any polarisation state[16]. This is why in most studies there are mainly two polarisation states that are studied: The Transversal Electric polarisation (TE) and the Transversal Magnetic polarisation (TM). From them it would be possible to study more complex polarisations states. In fig.3.15 there is a schema of those polarisations, as well as in eq.3.75 and 3.76

The TE polarisation is defined as the polarisation where the electric field is normal to the plane defined by the direction of propagation and a imaginary plane interface, at any particular non-zero incidence angle. It is also known as s-polarisation. The TM polarisation is defined as the case where the electric field is parallel to that plane and, obviously, the magnetic field is normal to it. It is also known as p-polarisation.
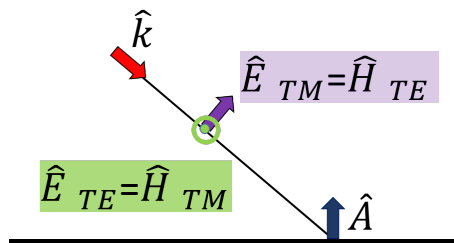
Figure 3.15: Schema of a TE and TM polarisation states

$$\hat{E}_{TE} = \hat{H}_{TM} = \hat{k} \times \hat{A} \tag{3.75}$$

---

[16]From the mathematical point of view, this means to find a basis for the vector space of all possible polarisations. The choice of this basis has to fulfill the independence (normality) of the vectors, but it is not unique. However, the choice of the TE and the TM mode has its advantages. Moreover, notice that already in the Mie solution for the scattering in a sphere, the TE and the TM modes were presented as independent *contributions* to the solution.

$$\hat{E}_{TM} = \hat{H}_{TE} = (\hat{k} \times \hat{A}) \times \hat{k} \tag{3.76}$$

Notice that, as the The TE and TM modes have been defined, they are ortogonal polarisation states. This means that its inner product is zero and therefore they are independent. Thus, they can indeed be used to construct any polarised transversal wave.

However, as stated at the beginning, even if most waves can be considered as transversal, there are some cases in which they cannot. And this usually happens when dealing with anisotropic media(birefringent crystals, for instance) or, even if isotropic, with highly attenuating media[48, pp.51-52].

The main consequence of this is that $\vec{E}$ and $\vec{H}$ are no longer purely transverse to the wavevector $\vec{k}$ and a tangential component appears. This means that the Poynting vector is no longer collinear with the direction of propagation. Thus, the analytical treatment of this becomes much more difficult and the plane wave approximation is not feasable. In fact, the use of bivectors[49, ch.1] is necessary to properly represent and define this situation. This has arleady been properly studied[50, 51] and the main implications and differences from the transverse waves are known. In this thesis, all materials are chosen to avoid these effects.

3.6 Fresnel coefficients

Most people are used to think on reflection and transmission in terms of the well-known Snell law [52, eq.1.1-3]:

$$n_1 sin(\theta_1) = n_2 sin(\theta_2) \tag{3.77}$$

Equation 3.77 relates the incident angle (θ_1) and refracted angle (θ_2) of an incident wave from a medium with refractive index n_1 to a medium with refractive index n_2. This allows us to obtain information about the reflexion and propagation direction, but nothing about the energy balance and the phase shifts. In order to obtain that information, the Fresnel coefficients should be used and depend on the polarisation state chosen. For the TE and the TM, the expressions are summarised in table 3.2:

Coefficient	TE	TM
Reflexion	$r_{TE} = \frac{n_1 \cos\theta_1 - n_2 \cos\theta_2}{n_1 \cos\theta_1 + n_2 \cos\theta_2}$	$r_{TM} = \frac{n_2 \cos\theta_1 - n_1 \cos\theta_2}{n_1 \cos\theta_2 + n_2 \cos\theta_1}$
Transmission	$t_{TE} = \frac{2n_1 \cos\theta_1}{n_1 \cos\theta_1 + n_2 \cos\theta_2}$	$t_{TM} = \frac{2n_1 \cos\theta_1}{n_1 \cos\theta_2 + n_2 \cos\theta_1}$

Table 3.2: Fresnel coefficients in terms of angular dependency

The expressions shown in table 3.2 allow to calculate the Fresnel coefficients in terms of the angles of incidence and transmission as well as the materials refractive indexes. Those expressions can also be combined with eq.3.77 in order to remove the transmission angle dependency. Those are the best known expressions for the Fresnel coefficients even if they are not always the best ones: In the angular domain, it is difficult to properly understand some effects such as the total internal reflection and the plasmon generation. Therefore, the frequency domain is prefered for this thesis. Alternative expressions for Fresnel coefficients can be obtained using the wavevector decomposition from eq.4.59 and keeping the continuity condition for the tangential component k_ρ across the interface [52, eq.2.4-2]. The resulting expressions are shown in table 3.3, where it has been supposed that the relative magnetic permeability μ in all media is 1.

Coefficient	TE	TM
Reflexion	$r_{TE} = \frac{k_{z1}-k_{z2}}{k_{z1}+k_{z2}}$	$r_{TM} = \frac{\epsilon_2 k_{z1}-\epsilon_1 k_{z2}}{\epsilon_2 k_{z1}+\epsilon_1 k_{z2}}$
Transmission	$t_{TE} = \frac{2k_{z1}}{k_{z1}-k_{z2}}$	$t_{TM} = \frac{2\epsilon_2 k_{z1}}{\epsilon_2 k_{z1}-\epsilon_1 k_{z2}}\sqrt{\frac{\epsilon_1}{\epsilon_2}}$

Table 3.3: Fresnel coefficients in terms of wavevector decomposition

Bibliography

[1] U.S.A. National Nanotechnology Initiative. Nanotechnology definition. url: www.nano.gov/nanotech-101/what/definition, May 2014.

[2] SA Maier. *Plasmonics: Fundamentals and Applications*. Springer, 2007. URL `http://www.springer.com/west/home/librarians/springer+ news?SGWID=4-40157-22-173660338-0`.

[3] Joseph Larmor. A dynamical theory of the electric and luminiferous medium. *Proceedings of the Royal Society of London*, 54(326-330):438–461, 1893.

[4] Mathieu L Juan, Maurizio Righini, and Romain Quidant. Plasmon nano-optical tweezers. *Nature Photonics*, 5(6):349–356, 2011.

[5] Gustav Mie. Beiträge zur optik trüber medien, speziell kolloidaler metallösungen. *Annalen der Physik*, 330(3):377Ű445, 1908.

[6] John Strutt. On the transmission of light through an atmosphere containing small particles in suspension, and on the origin of the blue of the sky. *Philosophical Magazine, series 5*, 47:375–394, 1899.

[7] Alexandra Boltasseva and Harry A. Atwater. Low-loss plasmonic metamaterials. *Science*, 331(6015):290–291, 2011. doi: 10.1126/science.1198258.

[8] Fritz Rohrlich. Dynamics of a charged particle. *Phys. Rev. E*, 77:046609, Apr 2008. doi: 10.1103/PhysRevE.77.046609. URL `http://link.aps. org/doi/10.1103/PhysRevE.77.046609`.

[9] Philip Pearle. Classical electron models. In *Electromagnetism*, pages 211–295. Springer, 1982.

[10] H. A. Haus. On the radiation from point charges. *American Journal of Physics*, 54(12):1126–1129, 1986. doi: http://dx.doi.org/10.1119/1.14729. URL `http://scitation.aip.org/content/aapt/journal/ajp/54/12/ 10.1119/1.14729`.

[11] Craig F. Bohren and Donald R. Huffman. *Absorption and Scattering of Light by Small Particles*, chapter Absorption and Scattering by a Sphere, pages 82–129. Wiley Interscience, 2007.

[12] DF Swinehart. The beer-lambert law. *Journal of chemical education*, 39 (7):333, 1962.

[13] S Sivasubramanian, A Widom, and YN Srivastava. The clausius–mossotti phase transition in polar liquids. *Physica A: Statistical Mechanics and its Applications*, 345(3):356–366, 2005.

[14] F. W. J. Olver, D. W. Lozier, R. F. Boisvert, and C. W. Clark, editors. *NIST Handbook of Mathematical Functions.* Cambridge University Press, New York, NY, 2010. National Institute of Standards and Technology.

[15] Timothy J. Davis, Kristy C. Vernon, and Daniel E. Gómez. Effect of retardation on localized surface plasmon resonances in a metallic nanorod. *Opt. Express*, 17(26):23655–23663, Dec 2009. doi: 10.1364/OE. 17.023655. URL http://www.opticsexpress.org/abstract.cfm?URI= oe-17-26-23655.

[16] Jerome Nappa, Isabelle Russier-Antoine, Emmanuel Benichou, Christian Jonin, and Pierre-François Brevet. Wavelength dependence of the retardation effects in silver nanoparticles followed by polarization resolved hyper rayleigh scattering. *Chemical Physics Letters*, 415(4âĂŞ6):246 – 250, 2005. ISSN 0009-2614. doi: http://dx.doi.org/10.1016/j.cplett.2005. 08.143. URL http://www.sciencedirect.com/science/article/pii/ S0009261405012480.

[17] Viktor Myroshnychenko, Jessica Rodríguez-Fernández, Isabel Pastoriza-Santos, Alison M Funston, Carolina Novo, Paul Mulvaney, Luis M Liz-Marzán, and F Javier García de Abajo. Modelling the optical response of gold nanoparticles. *Chemical Society Reviews*, 37(9):1792–1805, 2008.

[18] Shoji Asano and Giichi Yamamoto. Light scattering by a spheroidal particle. *Appl. Opt.*, 14(1):29–49, Jan 1975. doi: 10.1364/AO.14.000029. URL http://ao.osa.org/abstract.cfm?URI=ao-14-1-29.

[19] I. Gurwich, N. Shiloah, and M. Kleiman. The recursive algorithm for electromagnetic scattering by tilted infinite circular multilayered cylinder. *Journal of Quantitative Spectroscopy and Radiative Transfer*, 63 (2-6):217–229, 1999. doi: 10.1016/S0022-4073(99)00017-5. URL http: //www.scopus.com/inward/record.url?eid=2-s2.0-0032694504& partnerID=40&md5=1e8f94f04debeb9331b025a6451cb9d1. cited By 16.

[20] I. Gurvich, N. Shiloah, and M. Kleiman. Calculations of the mie scattering coefficients for multilayered particles with large size parameters. *Journal of Quantitative Spectroscopy and Radiative Transfer*, 70(4âĂŞ6):433 – 440, 2001. ISSN 0022-4073. doi: http://dx.doi.org/10.1016/S0022-4073(01) 00021-8. URL http://www.sciencedirect.com/science/article/pii/ S0022407301000218. Light Scattering by Non-Spherical Particles.

[21] Yuriy A Akimov and Wee Shing Koh. Design of plasmonic nanoparticles for efficient subwavelength light trapping in thin-film solar cells. *Plasmonics*, 6(1):155–161, 2011.

[22] Kim Un-Chol and Jiang Xiao-Qing. Numerical analysis of efficiency enhancement in plasmonic thin-film solar cells by using the silvaco tcad simulator. *Chinese Physics Letters*, 29(6):067301, 2012.

[23] Luigi La Spada, Renato Iovine, and Lucio Vegni. Nanoparticle electromagnetic properties for sensing applications. *Advances in Nanoparticles*, 1(2):9–14, August 2012. doi: 10.4236/anp.2012.12002.

[24] Piotr J. Flatau. Improvements in the discrete-dipole approximation method of computing scattering and absorption. *Opt. Lett.*, 22(16):1205–1207, Aug 1997. doi: 10.1364/OL.22.001205. URL http://ol.osa.org/abstract.cfm?URI=ol-22-16-1205.

[25] Bruce T Draine and Piotr J Flatau. User guide for the discrete dipole approximation code ddscat 7.3. *arXiv preprint arXiv:1305.6497*, 2013.

[26] DW Mackowski and MI Mishchenko. A multiple sphere t-matrix fortran code for use on parallel computer clusters. *Journal of Quantitative Spectroscopy and Radiative Transfer*, 112(13):2182–2192, 2011.

[27] E. Prodan, C. Radloff, N. J. Halas, and P. Nordlander. A hybridization model for the plasmon response of complex nanostructures. *Science*, 302 (5644):419–422, 2003. doi: 10.1126/science.1089171. URL http://www.sciencemag.org/content/302/5644/419.abstract.

[28] Shu-Chun Yang, Hiromu Kobori, Chieh-Lun He, Meng-Hsien Lin, Hung-Ying Chen, Cuncheng Li, Masayuki Kanehara, Toshiharu Teranishi, and Shangjr Gwo. Plasmon hybridization in individual gold nanocrystal dimers: Direct observation of bright and dark modes. *Nano Letters*, 10(2): 632–637, 2010. doi: 10.1021/nl903693v. URL http://dx.doi.org/10.1021/nl903693v. PMID: 20058898.

[29] Prashant K. Jain and Mostafa A. El-Sayed. Plasmonic coupling in noble metal nanostructures. *Chemical Physics Letters*, 487(4âĂŞ6):153 – 164, 2010. ISSN 0009-2614. doi: http://dx.doi.org/10.1016/j.cplett.2010.01.062. URL http://www.sciencedirect.com/science/article/pii/S0009261410001193.

[30] Fuyi Chen, Negash Alemu, and Roy L. Johnston. Collective plasmon modes in a compositionally asymmetric nanoparticle dimer. *AIP Advances*, 1(3):032134, 2011. doi: http://dx.doi.org/10.1063/1.3628346. URL http://scitation.aip.org/content/aip/journal/adva/1/3/10.1063/1.3628346.

[31] P. Nordlander, C. Oubre, E. Prodan, K. Li, and M. I. Stockman. Plasmon hybridization in nanoparticle dimers. *Nano Letters*, 4(5):899–903, 2004. doi: 10.1021/nl049681c. URL `http://dx.doi.org/10.1021/nl049681c`.

[32] Y. Ekinci, A. Christ, M. Agio, O. J. F. Martin, H. H. Solak, and J. F. Löffler. Electric and magnetic resonances in arrays of coupled gold nanoparticle in-tandem pairs. *Opt. Express*, 16(17):13287–13295, Aug 2008. doi: 10.1364/OE.16.013287. URL `http://www.opticsexpress.org/abstract.cfm?URI=oe-16-17-13287`.

[33] Giuseppe Parisi, Pierfrancesco Zilio, and Filippo Romanato. Complex bloch-modes calculation of plasmonic crystal slabs by means of finite elements method. *Opt. Express*, 20(15):16690–16703, Jul 2012. doi: 10.1364/OE.20.016690. URL `http://www.opticsexpress.org/abstract.cfm?URI=oe-20-15-16690`.

[34] DS Kim, SC Hohng, V Malyarchuk, YC Yoon, YH Ahn, KJ Yee, JW Park, J Kim, QH Park, and Ch Lienau. Microscopic origin of surface-plasmon radiation in plasmonic band-gap nanostructures. *Physical review letters*, 91(14):143901–143901, 2003.

[35] HL Offerhaus, B van den Bergen, M Escalante, FB Segerink, JP Korterik, and NF van Hulst. Creating focused plasmons by noncollinear phasematching on functional gratings. *Nano letters*, 5(11):2144–2148, 2005.

[36] H. Ditlbacher, J. R. Krenn, G. Schider, A. Leitner, and F. R. Aussenegg. Two-dimensional optics with surface plasmon polaritons. *Applied Physics Letters*, 81(10):1762–1764, 2002. doi: http://dx.doi.org/10.1063/1.1506018. URL `http://scitation.aip.org/content/aip/journal/apl/81/10/10.1063/1.1506018`.

[37] Grzegorz Grzela, Djamila Hourlier, and Jaime Gómez Rivas. Polarization-dependent light extinction in ensembles of polydisperse vertical semiconductor nanowires: A mie scattering effective medium. *Physical Review B*, 86(4):045305, 2012.

[38] Marc A. Taubenblatt and Tuyen K. Tran. Calculation of light scattering from particles and structures on a surface by the coupled-dipole method. *J. Opt. Soc. Am. A*, 10(5):912–919, May 1993. doi: 10.1364/JOSAA.10.000912. URL `http://josaa.osa.org/abstract.cfm?URI=josaa-10-5-912`.

[39] Kristy C Vernon, Alison M Funston, Carolina Novo, Daniel E Gómez, Paul Mulvaney, and Timothy J Davis. Influence of particle- substrate interaction on localized plasmon resonances. *Nano letters*, 10(6):2080–2086, 2010.

[40] Shunping Zhang, Kui Bao, Naomi J.Halas, Hongxing Xu, and Peter Nordlander. Substrate-induced fano resonances of a plasmonic nanocube: A route to increased-sensitivity localized surface plasmon resonance sensors revealed. *Nano Letters*, 11(4):1657–1663, 2011. doi: 10.1021/nl200135r.

[41] Gallinet Benjamin and Olivier J.F.Martin. Influence of electromagnetic interactions on the line shape of plasmonic fano resonances. *ACS Nano*, 5 (11):8999–9008, 2011. doi: 10.1021/nn203173r.

[42] Joe S. Yong, Satanin Arkady M., and Kim Chang Sub. Classical analogy of fano resonances. *Physica S*, 74:259–266, 2006. doi: 10.1088/0031-8949/ 74/2/020.

[43] Benjamin Gallinet, A. Lovera, T. Siegfried, H. Sigg, and O.J.F.Martin. Fano resonant plasmonic systems: Functioning principles and applications. volume 18, 2012. doi: http://dx.doi.org/10.1063/1.4750081.

[44] Mikael Svedendahl and Mikael Käll. Fano interference between localized plasmons and interface reflections. *Acs Nano*, 6(8):7533–7539, 2012.

[45] D.S. JONES. {CHAPTER} 1 - {THE} {REPRESENTATION} {OF} {THE} {ELECTROMAGNETIC} {FIELD}. In D.S. JONES, editor, *The Theory of Electromagnetism*, pages 1 − 99. Pergamon, 1964. ISBN 978-0-08-013686-8. doi: http://dx.doi.org/10.1016/B978-0-08-013686-8. 50006-X. URL `http://www.sciencedirect.com/science/article/ pii/B978008013686850006X`.

[46] I.V. Lindell. Time-domain te/tm decomposition of electromagnetic sources. *Antennas and Propagation, IEEE Transactions on*, 38(3):353– 358, Mar 1990. ISSN 0018-926X. doi: 10.1109/8.52242.

[47] SergeyN. Savenkov. Jones and mueller matrices: structure, symmetry relations and information content. In AlexanderA. Kokhanovsky, editor, *Light Scattering Reviews 4*, Springer Praxis Books, pages 71–119. Springer Berlin Heidelberg, 2009. ISBN 978-3-540-74275-3. doi: 10.1007/978-3-540-74276-0_3. URL `http://dx.doi.org/10.1007/ 978-3-540-74276-0_3`.

[48] D.J. Griffiths. *Introduction To Electrodynamics 3Rd Ed*. Prentice-Hall Of India Pvt. Limited, 2007. ISBN 9788120316010. URL `https://books. google.es/books?id=3LbMygAACAAJ`.

[49] P. Boulanger and M.A. Hayes. *Bivectors and Waves in Mechanics and Optics*. Applied Mathematics. Taylor & Francis, 1993. ISBN 9780412464607. URL `https://books.google.es/books?id=QNOKs3fTPpAC`.

[50] MA Dupertuis, B Acklin, and M Proctor. Generalization of complex snell–descartes and fresnel laws. *JOSA A*, 11(3):1159–1166, 1994.

[51] MA Dupertuis, B Acklin, and M Proctor. Generalized energy balance and reciprocity relations for thin-film optics. *JOSA A*, 11(3):1167–1174, 1994.

[52] Malvin Carl Teich Bahaa E.A. Saleh. *Fundamentals of Photonics*. Wiley-Interscience, 2nd edition edition, 2007. ISBN: 978-0-471-35832-9.

Chapter 4

Simulated properties of Ag Nanoparticles

4.1 Frequency dependent scattering properties of induced dipoles in metallic nanoparticles

In this section, one of the best-known analytical models for the dielectric function of a metal is presented, as well as its relation with some of the scattering properties for induced scattering dipoles in nanoparticles.

Drude´s model [1] is a well-known model developed in 1900 to explain the electrical properties of a material. It is specially appropiate for metals. It has been corrected in 1905 as the Drude-Lorentz model [2, 3] and later in 1933 as the Drude Sommerfeld model [4].

Depending on the frequency of the exciting photons the behaviour will be different:

1. At low frequencies (corresponding to infrared) the metal acts as a perfect electric conductor (PEC). This condition implies that the electrons will be able to move according to the external driving electromagnetic field so the scattered field will cancel the internal induced electric field in the metal. Under these conditions, no electric field penetrates in the volume of the particle.

2. At intermediate/ high frequencies (visible light) the electrons show a phase lag when compared with the external driving photon. This leads to a field inside the metal up to a finite distance called the *skin depth*[5, table 3.1]. This non-perfect behaviour is important to understand some effects and properties of the excitation of the particles, such as the retardation effects introduced in section 3.3.6.

Drude proposed that a metal could be considered as an array of positive charges surrounded by electrons[1].

One of the limitations of Drude´s model is that it neglects any interaction between electrons but direct collisions between them, that is, it neglects the

---

[1]A neutral atom can be decomposed in a positive ion corresponding to an atom without some electrons and those electrons that can move among the lattice as they are delocalised

long-range interactions. Let τ_{Drude} be the average time between successive collisions between electrons (also known as the relaxation constant) and σ the electric conductance of the material, with σ_0 being the direct current (DC) value, that is, at frequency $\omega = 0$ rad/s. Then the Drude model frequency dependent conductivity is:

$$\sigma(\omega) = \frac{\sigma_0}{1 + i\omega\tau_{Drude}} \tag{4.1}$$

Eq.4.1 assumes that the electrons behave like an ideal gas. A more precise model that includes the effect of interactions is the Fermi-Dirac distribution. However, in 1957 Lev Landau [6] showed that a gas of interacting particles (such as the electrons in a metal) can be described by an equivalent system of quasiparticles with a negligible interaction. This makes the Drude model a simple way to accurately model the behaviour of the movement of electrons in a metal when an external field is applied to it as well as the frequency dependent behaviour of the response.

Lorentz proposed that when an atom is exposed to an harmonic oscillating electric field there is a spring-like behaviour describing the delocalized electrons movement. As the electron mass $m = 9.1 \cdot 10^{-31} kg$ is much lower than the nucleus mass, it is possible to assume that the nucleus will not move at all during the electron movement.

This approach lead to equations corresponding to harmonic oscillators in which the time evolution of the displacement of the electrons attached to the nucleus corresponds to a second-order linear differential equation.

In a first simple case, without any driving force and any damping factor (related with the ohmic losses of the electrons movement), applying the Hook Law and Newton second law, the expression for a linear movement of the electrons around its nucleus becomes:

$$F(\vec{x}) = -k\vec{x} \implies m\frac{d^2\vec{x}}{dt^2} = -k\vec{x} \tag{4.2}$$

Eq.4.2 is usually presented as follows, once defined the resonant frequency, natural frequency or fundamental frequency as $\omega_0 = \sqrt{\frac{k}{m}}$

$$\frac{d^2\vec{x}}{dt^2} = -\omega_0^2\vec{x} \tag{4.3}$$

In a general case, considering both a driving force and a damping factor, there is a more general equation:

$$m\frac{d^2\vec{x}}{dt^2} = \vec{F}_{Hook} + \vec{F}_{Damping} + \vec{F}_{Driving} \tag{4.4}$$

The damping force is directly proportional to both the mass and to a damping factor γ. The force corresponding to the equivalent Hook´s Law pseudo-spring is $k\vec{x}$, where the Hook´s proportionality factor k can be expressed in terms of the natural oscillating frequency ω_0. The resulting equation is:

$$\vec{F}_{Driving} = m\frac{d^2\vec{x}}{dt^2} + m\gamma\frac{d\vec{x}}{dt} + m\omega_0^2\vec{x} \tag{4.5}$$

Here, the damping is assumed to be produced by internal collisions in the solid (ohmic losses) but also by the resulting radiation from accelerating and decelerating electrons (radiating losses).

In Eq.4.5 the driving force term is still undefined. In the field of interest in this thesis, the driving force is produced by an external electromagnetic wave such as a photon. This means that the driving force will have an harmonic-like and frequency dependent shape:

$$\vec{F}_{Driving} = -q\vec{E}_{ph} \tag{4.6}$$

In Eq.4.6, $q = 1.6 \cdot 10^{-19}$ C is the electron charge. The photon field $\vec{E}_{ph}(\omega, t)$ is an harmonic wave and thus the driving electric field is:

$$\vec{E}_{ph}(\omega, t) = E_0 e^{i\omega t} \tag{4.7}$$

where E_0 is the maximum of the amplitude of the wave, or equivalently:

$$E_0 = |\vec{E}(\omega, t)| \tag{4.8}$$

Before going on, the concept of polarisation has to be defined. And there are two possible ways to do it: Using the concept of susceptibility χ or using the concept of dipole moment $\vec{p}$.

- In the first case, the polarisation $\vec{P}$ is defined as the density of the dipole moments $\vec{p}_i$ that can be defined as the product of the charge and the displacement vector $d\vec{x}$. The displacement $d\vec{x}$ is measured from the nucleus (whose position is taken as $\vec{x} = 0$) as an average distance. This means that the expression for the polarisability obtained by a dipole moment density consisting on N dipoles can be expressed as:

$$\vec{P} = N\vec{p}_i = Nq\delta\vec{x} = Nq(0 - \vec{x}) = -Nq\vec{x} \tag{4.9}$$

- In the second case, the polarisation is presented in terms of the electric susceptibility χ. This parameter depends on the material and relates the amount of polarization (in terms of the number of dipoles and/or the charge displacement) with the external electric field:

$$\vec{P} = \epsilon_0 \chi \vec{E}_{ph} \tag{4.10}$$

From both definitions of polarisation, an expression for the position of the electron $\vec{x}$ (from Eq.4.5) can be deduced:

$$\vec{x}(t) = \frac{-\vec{P}}{Nq} = \frac{\epsilon_0 \chi}{Nq} \vec{E}_{ph} \qquad (4.11)$$

and then, the Eq.4.5 can be expressed as:

$$\frac{d^2\vec{P}}{dt^2} + \gamma \frac{d\vec{P}}{dt} + \omega_0^2 \vec{P} = \frac{Nq^2}{m} \vec{E}_{ph} \qquad (4.12)$$

It is possible to define the *plasma frequency*[2] ω_p as:

$$\omega_p = \sqrt{\frac{Nq^2}{m\epsilon_0}} \qquad (4.13)$$

Now, Eq.4.12 can be expressed in terms of three main parameters of the metal: the damping factor γ, the square the resonant frequency ω_0 and the plasma frequency ω_p :

$$\frac{d^2\vec{P}}{dt^2} + \gamma \frac{d\vec{P}}{dt} + \omega_0^2 \vec{P} = \epsilon_0 \omega_p^2 \vec{E}_{ph} \qquad (4.14)$$

Eq.4.14 is easily solved in frequency domain by assuming that the polarisation $\vec{P}$ has the same harmonic variation that the driving external electric field E_{ph} (eq.4.7). This leads to:

$$\vec{P}(\omega) = \frac{\epsilon_0 \omega_p^2}{(\omega_0^2 - \omega^2) + i\gamma\omega} E_{ph}(\omega) \qquad (4.15)$$

Eq.4.15 is important as it relates the polarisability (and thus the position, as shown in Eq.4.11) with the external driving force. By comparing eq.4.15 with eq.4.10, the susceptibility χ is found as:

$$\chi = \frac{\omega_p^2}{(\omega_0^2 - \omega^2) + i\gamma\omega} \qquad (4.16)$$

The complex relative permittivity ϵ_r can be then expressed as $\epsilon_r = 1 + \chi$ and thus:

$$\epsilon_r = 1 + \frac{\omega_p^2}{(\omega_0^2 - \omega^2) + i\gamma\omega} \qquad (4.17)$$

---

[2]This concept assumes that the charges moving around the nucleus can be well represented by the center of mass of the electrons. When there is an oscillating spring-like movement of the electrons, this mass center will also move accordingly. The plasma frequency is then defined as the frequency at which this movement shows resonance effects.

Eq.4.17 shows how the permittivity depends on the frequency of the external electric field, as well as on the studied material through the plasma frequency and the damping factor. This behaviour is mainly important for plasmonics and typical of dispersive phenomena where the scattering is frequency dependent.

Real materials are easily modelled by eq.4.17. In fact, Johnson and Christy [7] is a well-known reference to obtain ϵ_r for noble metals. In their publications they fit the corrected Drude-Lorentz model [2]. Therefore, they assume that the natural frequency of resonance ω_0 is much lower than the frequency ω and that there is a limit $\epsilon_\infty \neq 1$ when $\omega \to \infty$. This leads to the following expression for the permittivity:

$$\varepsilon(\omega) = \varepsilon_\infty - \frac{\omega_p^2}{\omega^2 - i\gamma\omega} \tag{4.18}$$
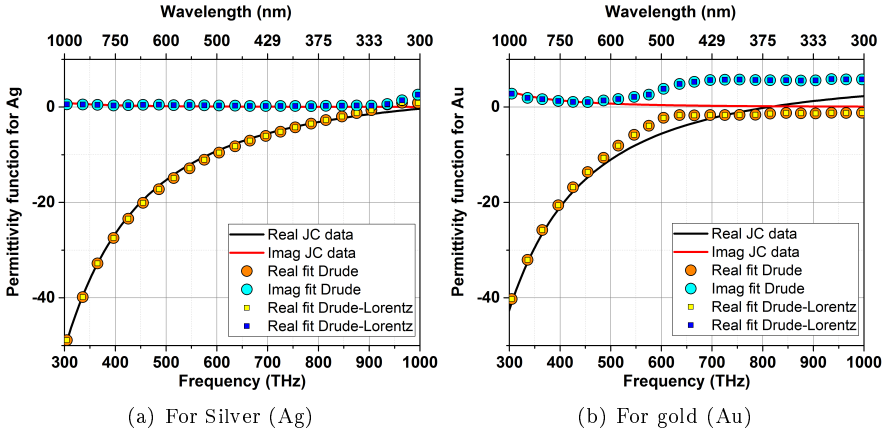
Figure 4.1: Comparison of Ag and Au experimental permittivity data with a fit using Drude and Drude-Lorentz model.

Fig.4.1a and 4.1b show a comparison between experimental data and a fitting done using the Drude-Lorentz model (eq.4.18). The general trend shows a good agreement in both cases, so this models would be interesting due to its simplicity. However, when the energy increases (or the wavelength decreases), the model starts to deviate from the experimental data. This is mainly due to the fact that the free electron movement that rules the Drude model starts not to be so suitable when other phenomena, such as the interband transition of the electrons appear. This deviation is much more important for some metals like Au than for others like Ag. Notice that those two metals have analogous electron configuration (they are in the same column in Mendeleiev's periodic

table). However, Au has a higher electronic number and thus it has more energetic levels that can lead to more electronic transitions.

The best approach when focusing on a material (such as Ag, that will be mostly the only used in this work) is to use experimental data, for instance, from Johnson and Christy. In fact, unless specified, this data will be used in this thesis. However, Drude model is useful due to its simplicity and because it can model correctly the trend of most metals with only a few parameters. For this reason, this will be the choice to estimate analytically the scattering properties of metal nanoparticles. For this, it is assumed that the main scattering is due to a dipole-like mode. This allows to use the suceptibility expressions in eq.4.16 and rewrite it using the Euler formula using a module and a phase ϕ_χ as:

$$\vec{P} = \epsilon_0 \chi(\omega)\vec{E}(\omega) \longrightarrow \vec{P}(\omega) = \epsilon_0 |\chi(\omega)| e^{i\phi_\chi(\omega)} \vec{E}(\omega) \tag{4.19}$$

To calculate the module and the phase, the relative susceptibility of the material is decomposed into its real (eq.4.20) and its imaginary parts (4.21)

$$Re(\chi) = Re\left(\frac{\omega_p^2}{(\omega_0^2 - \omega^2) + i\gamma\omega}\right) = \frac{\omega_p^2(\omega_0^2 - \omega^2)}{(\omega_0^2 - \omega^2)^2 + \omega^2\gamma^2} \tag{4.20}$$

$$Im(\chi) = Im\left(\frac{\omega_p^2}{(\omega_0^2 - \omega^2) + i\gamma\omega}\right) = \frac{-\omega\gamma}{(\omega_0^2 - \omega^2)^2 + \omega^2\gamma^2} \tag{4.21}$$

Leading to:

$$|\chi(\omega)| = \sqrt{\chi\chi^*} = \frac{\omega_p^2}{(\omega_0^2 - \omega^2)^2 + \gamma^2\omega^2} \sqrt{(\omega_0^2 - \omega^2)^2 + \gamma^2\omega^2} \tag{4.22}$$

and

$$\phi_\chi(\omega) = \arg(Re(\chi) + iIm(\chi)) \tag{4.23}$$

where the arg function depends on the relative signs of $Re(\chi)$ and $Im(\chi)$ as[8, pp.29]:

$$\arg(a + ib) = \arctan\frac{b}{a} + sign(b)\frac{\pi}{2}(1 - sign(x)) \tag{4.24}$$

where the sign function is defined as:

$$sign(x) = \begin{cases} 1 & if \quad x > 0 \\ -1 & if \quad x < 0 \\ 0 & if \quad x = 0 \end{cases} \tag{4.25}$$

Notice that the different expressions for the arg function are done in order to find the principal value[3] in the interval $[-\pi, \pi]$. However, as eq.4.21 is always negative, the arg function definition will always be within $[-\pi, 0]$. Notice too that eq.4.24 is not defined when both $Re(\chi)$ and $Im(\chi)$ are 0. This will never happen for real materials.

Once all the particularities of the expressions are shown, it is possible to study the amplitude and the phase of the dielectric function. For this, three different frequency regimes can be considered:

- Low frequency regime (for $\omega \to 0$). In this case the imaginary part is $Im(\chi) \to 0$ and the real part is $Re(\chi) \approx \frac{\omega_p^2}{\omega_0^2} > 0$. Therefore $|\chi(\omega)| \approx \frac{\omega_p^2}{\omega_0^2}$ and the argument is $\phi_\chi = \arctan(Im(\chi)/Re(\chi)) \to 0$. This implies that the amplitude of the displacement of charges is not near its maximum but is in phase with the varying electric field (the phase shift is negligible).

- High frequency regime (for $\omega \to \infty$). In this case both $Im(\chi)$ and $Re(\chi)$ tend to zero and are always negative: The first one because of eq.4.21 and the second because $(\omega_0^2 - \omega^2) < 0$. It comes easily that $|\chi(\omega)| \to 0$ whereas the argument of χ comes as $\arg(\chi) = \arctan(Im(\chi)/Re(\chi)) - \pi$.

  The direct substitution of $Re(\chi)$ and $Im(\chi)$ would lead to a 0/0 type indetermination. In order to avoid this, the following expression has to be used:

$$\phi_\chi(\omega) = \arctan\left(\frac{|Im(\chi)|}{|Re(\chi)|}\right) - \pi = \arctan(\frac{\omega\gamma}{\omega^2 - \omega_0^2}) - \pi \qquad (4.26)$$

  leading to $\phi_\chi = 0 - \pi = -\pi$. Thus, in high frequency regime there is a shift between the displacement and the external electric field of $-\pi$.

- Near resonance regime (for $\omega \to \omega_0$). The imaginary term $Im(\chi) \to \frac{-\omega_p^2}{\omega_0^2\gamma}$ (always negative). The sign of the real term $Re(\chi) \to 0$ is defined by the sign of $\omega_0^2 - \omega^2$. Therefore, different expressions for ϕ_χ are found:

  - If $\omega < \omega_0$: This implies that the real part is $Re(\chi) > 0$, leading to an expression for the argument like $\phi_\chi = \arctan(\frac{-\omega_p^2}{\omega_0^2\gamma}/0) \to -\frac{\pi}{2}$.

---

[3]In complex calculus, different solutions may arise from the fact that, in polar form, there is a periodicity in the phase of a complex number:

$$z = a + ib = Ae^{iB} = Ae^{i(B+2n\pi)}$$

Therefore, the principal value is defined as the solution whose n makes the result fit within a defined range.

Valencia Nanophotonics Technology Center

UNIVERSITAT
POLITÈCNICA
DE VALÈNCIA

ESCUELA TÉCNICA
SUPERIOR INGENIEROS
INDUSTRIALES VALENCIA

– If $\omega > \omega_0$: Now the real part is $Re(\chi) < 0$ and the expression for the argument becomes $\phi_\chi = \arctan(\frac{-\omega_p^2}{\omega_0^2 \gamma}/0) - \pi = +\frac{\pi}{2} - \pi = \frac{\pi}{2}$.

For the module, in any case $|\chi(\omega)| \to \frac{\omega_p^2}{\gamma \omega_0}$. Notice that the intensity near the resonance ω_0 is the biggest of all studied regimes (As $\gamma << \omega_0$, the module at low frequency will be smaller than near ω_0). In any case, this second module will be attenuated by the damping factor γ and that it will only tend to infinity when $\gamma \to 0$.

In fig.4.1, the conclusions that have been obtained by the analytical study of eq.4.16 are confirmed with an example for an arbitrary metal with $\gamma = 9.23$THz, $\omega_p = 668.4$THz and $\omega_0 = 500$THz.

From fig.4.1, a resonance is found at a certain frequency, as expected from Mie approach with the exact solution for a sphere (shown in section 3.3.4). The position of this resonance would depend mainly on the material involved, but not on the size or the surrounding media. Therefore, even if the study of the permittivity function is a good approach to have a general behaviour, other more precise models should be used for more complex comparatives.

The equivalent dipole induced in a nanoparticle is usually expressed in terms of the external radiating source. In order to do that, the polarisability α is defined, in brief, as the proportionallity factor between the induced dipole and the incident wave $\vec{E}_{inc}$ (eq.4.27)

$$\vec{P} = \alpha \vec{E}_{inc} \tag{4.27}$$

Of course, the polarisability concept α is nothing but a rearrangement of eq.4.15. Therefore, the study of the wavelength dependency of the induced dipoles will correspond with the trend shown for the susceptibility χ. Therefore, α is a complex value and and both the real and imaginary parts are meaningful. For an harmonic time dependent dipole, after Fourier transform, it is found:

$$\vec{P}_0 = (a + bi) = Ae^{\phi_0} \to \begin{cases} A = |\vec{P}_0| = (a + bi)(a - bi) = a^2 + b^2 \\ \\ \phi_0 = \arg(a + ib) \end{cases} \tag{4.28}$$

Thus, there is a phase shift between the dipole radiated field and the external incoming dipole-inducing electric field analogous to what it is shown in fig.4.1. The latter will be always considered as the reference phase ($\phi_0 = 0$).

$$\vec{E}_{ext} + \vec{E}(\vec{P}_0) = \vec{E}_0 e^{i\omega t} + \vec{E}(\vec{P}_0)e^{i\omega t + \phi_0} \tag{4.29}$$

The implications of this phase shift would lead to constructive or destructive interferences between the incoming and the scattered light. This is only a simple

(a) Real part

(b) Module

(c) Imaginary part

(d) Phase
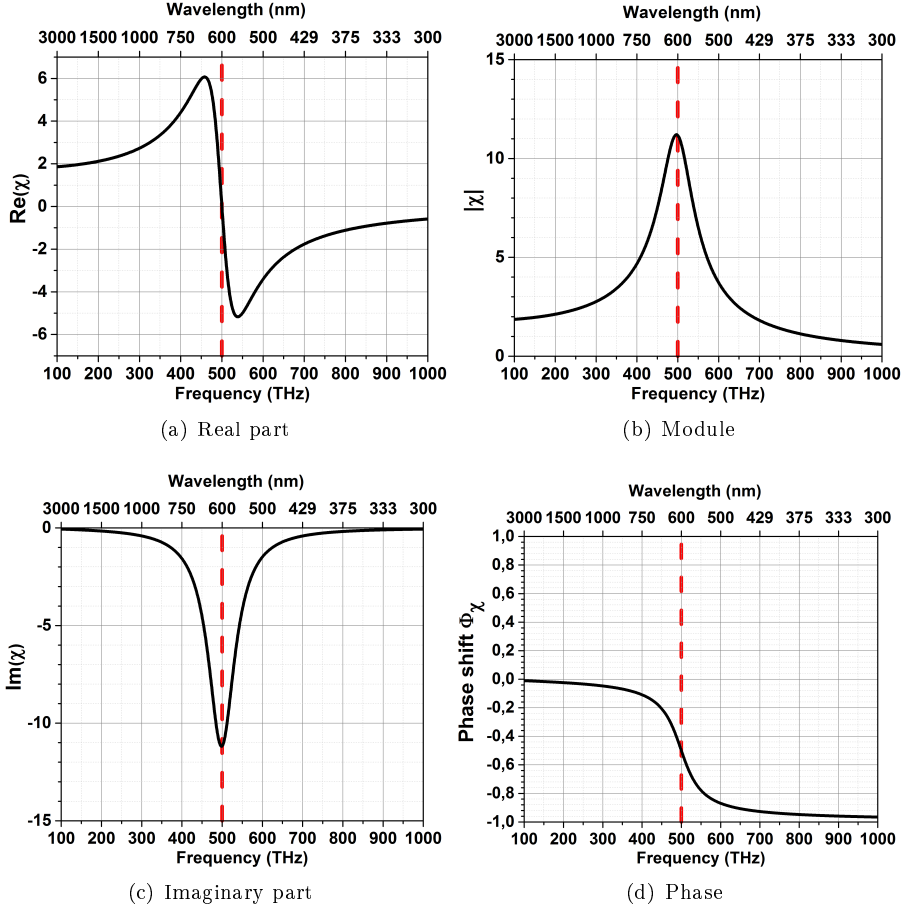
Figure 4.2: Example of frequency dependent behaviour on the susceptibility function of a metallic nanoparticle obtained assuming, $\gamma = 9.23 THz$, $\omega_p = 668.4 THz$ and $\omega_0 = 500 THz$ (red line in graphs).

approach and it gives no information about the directivity or the real size of the particle. However, it is a first proof that different materials not only have different dielectric functions (and thus, different resonant frequencies), but also different phase-shift related interactions with the incoming light.

4.2 Green Functions

A Green function $G(a, b)$ can be defined as the kernel $K(a, t)$ (sometimes called nucleus[9, p.376] of a general integral operator L defined like:

$$L\{f(t)\} = \int f(a)K(a, t)da \tag{4.30}$$

This definition is incomplete but allows one to see the relationship with other well-known integral transformations as the Fourier Transformation (eq.4.31) and the Laplace Transformation (eq.4.32)

$$F_F(a) = L_F\{f(t)\} = \frac{1}{\sqrt{2\pi}} \int_{-\infty}^{\infty} e^{-iat}f(t)dt \tag{4.31}$$

$$F_L(a) = L_L\{f(t)\} = \int_{0}^{\infty} e^{-at}f(t)dt \tag{4.32}$$

In the case of the Fourier Transform L_F, the Kernel is $K_F(a, t) = \frac{1}{\sqrt{2\pi}}e^{-iat}$ and in the case of the Lapace Transform L_L, the Kernel is $K_L(a, t) = e^{-at}$.

The Green's Function definition, thus, has to be completed. In order for this to be done let us define a linear differential operator D acting on a space of functions Σ defined over a subset x of a domain Ω. A non homogeneous linear differential equation can be defined as:

$$D\{g(x)\} = f(x) \tag{4.33}$$

with $g(x) \in \Sigma$ and $x \in \Omega$. The Green function $G(a, b)$ is defined so that it fulfils:

$$D\{G(a, b)\} = \delta(a - b) \tag{4.34}$$

This way, the solution $g(x)$ to the ec.4.33 is given by:

$$g(x) = L_G\{f(x)\} = \int f(s)G(x, s)ds \tag{4.35}$$

because, independently of $f(s)$ and as it has been defined:

$$D\{g(x)\} = \int f(s)D\{G(x, s))\}ds = \int f(s)\delta(x - s)ds = f(x) \tag{4.36}$$

This strategy is independent of the non homogeneous term $f(x)$. In fact, as it has defined $D \circ L_G = L_G \circ D \longrightarrow D^{-1} = L_G$.

Some important facts not to forget about the Green Function. First, that not any differential linear operator D has a corresponding Green Function.

Moreover, the Green function may not be unique and, in practise, boundary conditions are needed to completely define them [10, Ch.1].

To sum up, the Green function is a good strategy to solve non-homogeneous linear differential equations. It may not be easy to find a Green functions for new problems, but there are several common equations and systems in which their Green function has already been found[11]. Some of them can be found in table 4.1, where $r = \sqrt{x^2 + y^2 + z^2}$, $\rho = \sqrt{x^2 + y^2}$ and $\theta(t)$ is the Heaviside step function.

Differential operator D	Green's function G	Application
$\frac{\partial}{\partial t} + \gamma$	$\theta(t)e^{-\gamma t}$	
$(\frac{\partial}{\partial t} + \gamma)^2$	$\theta(t)te^{-\gamma t}$	
$(\frac{\partial^2}{\partial t^2} + 2\gamma\frac{\partial}{\partial t}) + \omega_0^2$	$\theta(t)e^{-\gamma t}\frac{\sin(\sqrt{\omega_0^2 - \gamma^2}t)}{\sqrt{\omega_0^2 - \gamma^2}}$	Harmonic oscillator
$\frac{\partial^2}{\partial x^2} + \frac{\partial^2}{\partial y^2}$	$\frac{\ln \rho}{2\pi}$	2D Laplacian
$\frac{\partial^2}{\partial x^2} + \frac{\partial^2}{\partial y^2} + \frac{\partial^2}{\partial z^2}$	$\frac{-1}{4\pi r}$	3D Laplacian
$\nabla\nabla + k^2$	$\frac{e^{ikr}}{4\pi r}$	Helmoltz equation
$\frac{1}{c^2}\frac{\partial^2}{\partial t^2} - \nabla\nabla$	$\frac{\delta(t - \frac{r}{c})}{4\pi r}$	Wave equation
$\frac{\partial}{\partial t} - k\nabla\nabla$	$\theta(t)\sqrt[3]{(\frac{1}{4\pi kt})^2}e^{\frac{-r^2}{4kt}}$	Mass diffusion

Table 4.1: Examples of Green's Functions for different common differential operators.

In order to solve the inhomogeneous Helmoltz equation presented in section 3.3.2 it is possible to use the Green function strategy. This way, from eq.3.29 and from eq.4.35, the equivalent vector distribution $\vec{A}$ (from now called the Hertz Vector) is:

$$\vec{A}(\vec{r}) = \iiint \vec{J}(\vec{r'})G(\vec{r}, \vec{r'})dr' \tag{4.37}$$

where $\vec{r}$ are the field points where $\vec{A}$ (and thus $\vec{E}$) is being evaluated and $\vec{r'}$ are the source points of the electromagnetic field. As shown in table 4.1, the

Green function for the Helmoltz equation is (including the frequency dependency through k):

$$G(k, \vec{r} - \vec{r'}) = \frac{e^{ik|\vec{r}-\vec{r'}|}}{4\pi|\vec{r} - \vec{r'}|} \tag{4.38}$$

Notice that the electromagnetic field has been solved in eq.4.37 in terms of the vector potential $\vec{A}$. If the relation between $\vec{A}$ and $\vec{E}$ is used (eq.3.23), the solution would correspond to the well-known *Electric Field Integral Equation* (EFIE):

$$\vec{E} = i\omega\mu \iiint W(k, \vec{r} - \vec{r'}) \cdot \vec{J}(\vec{r'}) dr' \tag{4.39}$$

where now $W(\vec{r}, \vec{r'})$ is the dyadic homogeneous Green's Function[10], given by:

$$W(k, \vec{r} - \vec{r'}) = \frac{1}{4\pi} \left[\mathbf{I} + \frac{\nabla^2}{k^2} \right] G(k, \vec{r} - \vec{r'}) \tag{4.40}$$

where $\mathbf{I}$ is the identity matrix.

The EFIE describes how to obtain a radiated field from current sources. This approach is commonly used in antenna design as the current is usually (not always) a known design parameter. And it can also be used for modelling the scattering of metallic nanoparticles. There are two main key points that should be kept in mind about ec.4.40:

- It allows to solve the scattered electric field $\vec{E}(\omega, \vec{r})$ only once the currents involved in that scattering are known. In the case of metallic nanoparticles, the currents are going to be induced by an external (known) incident electric field $\vec{E}_i(\omega, \vec{r})$. And as the starting data does not include the currents it is necessary to define the boundary conditions on the incident and scattered field, so that it is possible to write ec.4.40 in terms of only $E_i(\omega, \vec{r})$.

- By using this formulation boundary conditions can be easily defined at the infinity. This is consistent with the Sommerfeld radiation condition[4]

The EFIE is the basis of many commercial softwares that solve scattering problems numerically. However, it takes quite a long time to model structures

---

[4]The 3 dimensional non-homogeneous Helmoltz equation applied to $g(x)$ is usually solved assuming the Sommerfield radiation condition:

$$\lim_{|x|\to\infty} |x|(\frac{\partial}{\partial|x|} - ik)g(x) = 0 \tag{4.41}$$

This assumption forces the energy to be radiated from the sources towards the infinity.

with many particles and usually it is supposed that all them are equal (it is an homogeneous array). If many different and randomly distributed particles are modelled, it is hard to find a solution.

4.2.1 Electric Field scattered by a dipole

In section 3.3.3 and 3.3.4 it has been shown that any scattered field can be expressed as a sum of the fields scattered by different excitation modes (dipoles, quadrupoles, etc.). However, let us assume that the electric dipole is the main contribution whereas the rest of orders can be neglected. This will be verified in section 4.4 and experimentally in section 6.4. Therefore, the study of the electric dipole is of particular interest.

When the dipole magnitude is known, the radiated electric field can be calculated[12, pp.69] as shown in eq.4.42

$$\vec{E}_{dipole} = \frac{e^{ikr}}{4\pi\epsilon_0\epsilon_m} \left[\frac{k^2}{r}(\hat{n} \times \vec{p}_i) \times \hat{n} + [3\hat{n}(\hat{n} \cdot \vec{p}_i) - \vec{p}_i]\left(\frac{1}{r^3} - \frac{ik}{r^2}\right) \right] \quad (4.42)$$

This is the exact expression for the electric field radiated by any dipole, valid at any wavelength and distance from the source. However, working with it is difficult because the dipole term cannot be isolated. From this point of view, the use of a Green function it has its advantages. In fact, eq.4.37 can be solved easily when the current $\vec{J}(r')$ is that from an infinitesimal dipole with a time dependent behaviour such shown in eq.4.7:

$$\vec{J}(r') = \frac{\partial \vec{P}}{\partial t} \longrightarrow \vec{J}(r') = i\omega\vec{P} \quad (4.43)$$

Inserting this current $\vec{J}$ into ec.4.37, it yields:

$$\vec{A}(k,\vec{r}) = \iiint i\omega\vec{P}(\omega)\delta(\vec{r} - \vec{r}')G(k,\vec{r} - \vec{r}')dr' \longrightarrow \vec{A}(\vec{r}) = i\omega\vec{P}(\omega)G(k,\vec{r} - \vec{r}')$$
$$(4.44)$$

Or directly on eq.4.39, leading to:

$$\vec{E}(k,\vec{r}) = \omega\mu\vec{P}(\omega)W(k,\vec{r} - \vec{r}') \quad (4.45)$$

Eq.4.45 is usually used in spherical coordinates as it is easier to apply the gradients. However, if several dipoles are modelled it is useful to have the solution in cartesian coordinates as the individual solutions are much easier to be added up into a global solution involving many dipoles. To do this, the expression of $W(\vec{r}, \vec{r}')$ in eq.4.40 has to be developed.

W is a 3×3 matrix

$$W(k,r) = \begin{pmatrix} W_{xx} & W_{xy} & W_{xz} \\ W_{yx} & W_{yy} & W_{yz} \\ W_{zx} & W_{zy} & W_{zz} \end{pmatrix} \tag{4.46}$$

whose elements can be expressed as follows [13]

$$W_{uv} = \frac{e^{ikR}}{4\pi} \cdot \frac{R_u R_v}{R^2} \cdot \left(\frac{3}{R^3} - \frac{3ik}{R^2} - \frac{k^2}{R} \right) + \delta(u,v) \cdot \frac{e^{ikR}}{R^3} \cdot \left(\frac{ik}{R} - 1 \right) \tag{4.47}$$

where u, v are all possible combinations of $\{x, y, z\}$, and $\vec{R}$ and its components are defined as follows:

$$\vec{R} = \vec{r} - \vec{r}' = \begin{pmatrix} r_x \\ r_y \\ r_z \end{pmatrix} - \begin{pmatrix} r'_x \\ r'_y \\ r'_z \end{pmatrix} = \begin{pmatrix} R_x \\ R_y \\ R_z \end{pmatrix} \longrightarrow R = \sqrt{R_x^2 + R_y^2 + R_z^2} \tag{4.48}$$

and $\delta(u,v)$ is a delta function:

$$\delta(u,v) = \begin{cases} 1 & if \quad u = v \\ 0 & if \quad u \neq v \end{cases} \tag{4.49}$$

4.2.2   Arrays of nanoparticles

Using eq.4.45 it is possible to obtain the electric field scattered by a infinitesimal dipole from its polarisation $\vec{P}$. But this strategy allows one to study more than one dipole (that is, more than a single particle) at the same time. Moreover, it allows one to study the influence of every particle on the rest of the array, because the calculated polarisation $\vec{P}$ will include that interaction. This is quite interesting as in many scattering studies only the effect of a single particle is shown and the interaction between them is often neglected.

Given an array of N nanoparticles and an external electric field acting on them $\vec{E}_i^{ext}$, it is possible to obtain the polarisation $\vec{p}$ of the mth nanoparticle from its polarisability α_m and from the electric field induced from the dipoles at the rest of the $N-1$ nanoparticles. The latter term also depends on the rest of polarisabilities α_i and through the Green function W (eq.4.46). In summary:

$$\vec{p}_m = \alpha E_m^{ext} + \sum_{n \neq m} W(k, R_m - R_n) \cdot p_n] \tag{4.50}$$

This allows us to solve the problem without any interaction as the Green function enables us to express it like a system of linear equations:

$$
\begin{pmatrix} \vec{p}_1^{ext} \\ \vec{p}_2^{ext} \\ \vdots \\ \vec{p}_N^{ext} \end{pmatrix} = \left[Id - \breve{W} \right]^{-1} \cdot M_\alpha \cdot \begin{pmatrix} \vec{E}_1 \\ \vec{E}_2 \\ \vdots \\ \vec{E}_N \end{pmatrix} \tag{4.51}
$$

where: M_α is $3N \times 3N$ diagonal matrix with the different polarisabilities of the nanoparticles and $\breve{W}$ is a $3N \times 3N$ matrix formed by the N matrices corresponding to the Green Functions from eq.4.46:

$$
\breve{W} = \begin{pmatrix} W(k, \vec{r_1} - \vec{r_1}) & W(k, \vec{r_1} - \vec{r_2}) & \cdots & W(k, \vec{r_1} - \vec{r_N}) \\ W(k, \vec{r_2} - \vec{r_1}) & W(k, \vec{r_2} - \vec{r_2}) & \cdots & W(k, \vec{r_2} - \vec{r_N}) \\ \vdots & \vdots & \ddots & \vdots \\ W(k, \vec{r_N} - \vec{r_1}) & W(\vec{r_N} - \vec{r_2}) & \cdots & W(\vec{r_N} - \vec{r_N}) \end{pmatrix} \tag{4.52}
$$

One of the limits of this model is that to give the best results the different dipoles have to see to each other like infinitesimal dipoles. In that sense, most authors have proposed a distance between centers of 3 times the radius of the nanoparticle.

Eq.4.53 can be expressed in a simple form, making an analogy with eq.4.27 as:

$$
\begin{pmatrix} \vec{p}_1^{ext} \\ \vec{p}_2^{ext} \\ \vdots \\ \vec{p}_N^{ext} \end{pmatrix} = \alpha_{eff} \cdot \begin{pmatrix} \vec{E}_1 \\ \vec{E}_2 \\ \vdots \\ \vec{E}_N \end{pmatrix} \tag{4.53}
$$

This way, for each particle, an effective polarisability $\alpha_{eff}(m)$ can be defined.

Some papers study the eigenvalues of the matrix α_{eff} (ec.4.53) for simple geometries analytically. It has been demonstrated there the relationship between those values and the scattering and absorption cross sections σ_{sca} and σ_{abs} [13].

Once the magnitude and phase of the induced dipoles on a nanoparticle is known, it is possible to calculate the electric field due to it using again the Green Function (eq.4.46)

There is another approach much easier and faster from the computational point of view: The use of array factors (AF). This approach is used with antenna arrays [14, ch.6] and can be generalised for random distributions. However, it is only useful when the interaction between the dipoles is only at the far field and when the dipoles are already known (something easy if the first

condition is accepted by calculating the polarisability.) . In brief, in spherical coordinates, the Array Factor is defined:

$$AF = \sum_{i=1}^{N} \vec{P}_i e^{i\vec{k}\cdot\vec{r}_Q} = \begin{pmatrix} \sum_{i=1}^{N} p_i^r e^{i\frac{2\pi}{\lambda}\hat{k}\cdot\hat{r}_i} \\ \sum_{i=1}^{N} p_i^\theta e^{i\frac{2\pi}{\lambda}\hat{k}\cdot\hat{r}_i} \\ \sum_{i=1}^{N} p_i^\phi e^{i\frac{2\pi}{\lambda}\hat{k}\cdot\hat{r}_i} \end{pmatrix} = \begin{pmatrix} AF_r \\ AF_\theta \\ AF_\phi \end{pmatrix} \tag{4.54}$$

where Q is the point where the $\vec{E}_Q$ is desired. Using the coordinate transformation matrices it is possible to re-write this to:

$$\begin{pmatrix} AF_x \\ AF_y \\ AF_z \end{pmatrix} = \begin{pmatrix} \sum_{i=1}^{N} p_i^x e^{i2\pi(\frac{x_i}{\lambda}\sin\theta\cos\phi + \frac{y_i}{\lambda}\sin\theta\sin\phi + \frac{z_i}{\lambda}\cos\phi)} \\ \sum_{i=1}^{N} p_i^y e^{i2\pi(\frac{x_i}{\lambda}\sin\theta\cos\phi + \frac{y_i}{\lambda}\sin\theta\sin\phi + \frac{z_i}{\lambda}\cos\phi)} \\ \sum_{i=1}^{N} p_i^z e^{i2\pi(\frac{x_i}{\lambda}\sin\theta\cos\phi + \frac{y_i}{\lambda}\sin\theta\sin\phi + \frac{z_i}{\lambda}\cos\phi)} \end{pmatrix} \tag{4.55}$$

The array factor allows one, for far field, to express:

$$E_{rad}^Q = \begin{pmatrix} E_{rad\{1,0,0\}}^Q \cdot AF_x \\ E_{rad\{0,1,0\}}^Q \cdot AF_y \\ E_{rad\{0,0,1\}}^Q \cdot AF_z \end{pmatrix} \tag{4.56}$$

The AF, even if simpler, is much more restrictive, so it will be avoided unless the dipoles are very distant one from the others. Moreover, the expressions showed do not include any substrate effect.

One of the key ideas that can be deduced from these strategies to modelling arrays, is that not only the number of particles are important, but also the relative position between them. Both strategies would be valid for periodic arrays of NPs, but the difficult part is how to deal with random distributions. From this point of view, two approaches are proposed:

a) **Quasi-random arrays**. In this case, a pseudo-random distribution can be obtained by combining two vectors with values from a normalised random distribution. A threshold $T \in [0,1]$ is defined to choose whether in a vector position its value corresponds to a particle. In the case $T = 0.5$, there is a chance over two. The two vectors are combined so that its product defines a $[x, y]$ distribution. In order to make random radii, a similar approach can be done. Eq.4.57 shows a code done in Excel and fig.4.3 the resulting distribution

$$RAND(0,1) * RANDBETWEEN(Rmin, Rmax) \tag{4.57}$$

Another similar strategy is to define a periodic distribution and use the random values to translate the centers in a random direction defined by

(a) Quasi-random particle distribution using the Excel template

(b) Resulting quasi-random particle distribution from Excel as read and used in Matlab
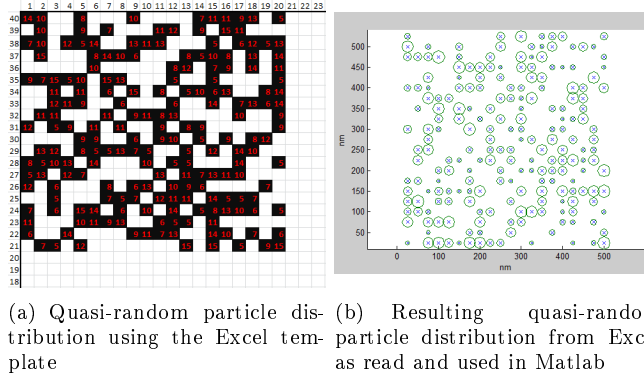
Figure 4.3: Resulting array from random number distributions

a random value between 0 and 2π. This is more complex but leads to even more realistic distributions.In both cases, a scale factor has to be provided in order to transform the numerical position into a real distance. Moreover, a final check on the resulting array must be done to verify that all the nanoparticles are independent and there is no virtual intersection among them.

b) **Random arrays**. From this point of view, the best fully randon distribution is the real nanoparticle distribution. Thus, real SEM images are analysed using the software ImageJ[15] in order to obtain more realistic center positions and equivalent radius of the particles. More details on the results of this image analysis will be shown in section 5.2.

In this case, the array may be considered as truly randomly distributed as both the sizes and the distances are random. However, it still has the disadvantage of considering all the particles as spheres, while they are not.

4.2.3 Infuence of a substrate

Most of the analytical studies are done assuming that the nanoparticle is in an homogeneous medium. And only a few deal with nanoparticles over a substrate. The equations in this case become more complex as the reflection and transmission effects have to be included. The strategy to solve this problem is to use the Sommerfield identity (eq.4.58) to rewrite the exponential term in the homogeneous media Helmoltz operator Green Function (eq.4.38). Notice that the Sommerfeld identity leads to a variable separation in cylindrical co-

UNIVERSITAT
POLITÈCNICA
DE VALÈNCIA

Valencia Nanophotonics Technology Center

ESCUELA TÉCNICA
SUPERIOR INGENIEROS
INDUSTRIALES VALENCIA

ordinates and that the exponential term is decomposed as a sum (an integral) of multiple solutions.

$$\frac{e^{ikR_0}}{R_0} = i \int_0^\infty dk_\rho \frac{k_\rho}{k_z} J_0(k_\rho\rho)e^{ik_z|z-h|} \tag{4.58}$$

In eq.4.58, $R_0 = \sqrt{\rho^2 + (z-h)^2}$. This implies that the source is placed over the substrate at a distance of h: $\vec{r}_0 = (0, 0, h)$. The wavevector $\vec{k}$ is decomposed in to components (eq.4.59): One parallel to the substrate k_ρ and another normal to the surface k_z.

$$|\vec{k}| = \sqrt{k_x^2 + k_y^2 + k_z^2} = \sqrt{k_\rho^2 + k_z^2} \longrightarrow \vec{k} = k_\rho\hat{\rho} + k_z\hat{z} \tag{4.59}$$

The Sommerfeld identity is very useful to handle with the modifications that the presence of a substrate makes on the original Green Function. In fact, as the solution will depend on the boundary conditions that define the *Hertz Vector*[5] $\vec{\Pi}$, it will depend on whether it is a vertical dipole or an horizontal dipole (taking as reference the substrate plane). For an arbitrarily oriented dipole the solution will be a linear combination of those. The details of the resolution for a double interface can be found in Novotny [16, 17].

It is easy to visualise how the Sommerfeld identity helps to include the effect of a substrate. In fig.4.4 it can be seen how the multiple transmission and reflections are included by correcting the integrand with two terms:

- An expotential term $e^{ik_i d}$ that corrects the phase due to the propagation of the wave in the ith medium trough a distance d.

- A coefficient $A_i(k_\rho)$ that can be expressed in terms of the Fresnel coefficients and that takes into account the different interfaces that are present.

Notice that multiple internal reflections are present in a real system and this can be taken into account in the $A_i(k_\rho)$ coefficients. When different upcoming or downcoming waves are present (such as in the case of the medium 2 in fig.4.4), the two solutions are added by the addition of two Sommerfeld integrals (or integrands).

The $A_i(k_\rho)$ coefficients deal with the reflected or transmitted waves, so are the correction for the Sommerfeld integrals applies only for the reflected and transmitted terms in each on the layers (what is commonly named as "secondary fields"). This implies that, in order to include the field that is directly radiated by the nanoparticle/dipole (the "primary field"), it is not worth using the Sommerfeld identity with $A(k_\rho) = 1$ but rather using the

---

[5]In section 3.3.2 it has already been proved that the Maxwell equations can be solved using a mathematical approach based on a vector potential, that later in the text has been named as the *Hertz Vector*.

Figure 4.4: Schematic of how the Sommerfeld identity is useful for including the substrate effect of radiating sources in multilayered systems.

exponential term itself corresponding to the Green function in the homogeneous medium.

Of course, the primary field has to be added only in the medium where the source is located. Constructive or destructive interferences are found when adding in that medium, the primary and the secondary fields.

An even more complex system is when the dipole is not over a substrate and in a semi-infinite media (like air), but embedded into the intermediate layer (such as embedded in the Anti Reflection Coating (ARC)). The strategy is analogous to the previous point but the boundary conditions for the Hertz Vector $\vec{A}$ will be different[18]. The general case can be found in[19].

In this thesis, the main structure of interest is related with a double interface: The first one between the air and the Anti Reflection Coating (ARC) material (usually silicon oxide or silicon nitride) and the second interface between the ARC and the silicon itself. In some cases, a third interface can be defined when a finite thickness of the silicon is considered.

The full details of how the boundary conditions are applied to find the Green functions in every case are not in the scope of this thesis. However, it is important to understand the mathematical and physical aspects of using the Sommerfeld identity.

In fact, using the wavevector domain, it is easy to understand that the integral in eq.4.58 can be split in two different integrals: The first one, from 0 to $k_\rho = k$ that includes the radiative part of the solution and the second one from k_ρ to infinite that includes the evanescent part of it. In fact, fig.4.6

shows how this decomposition is related with the dispersion diagram presented in sections 3.1 and 3.2, now generalising the radiation condition as a *light cone*. In fact, for each frequency considered, a different cut of the light cone will be used to define which k_ρ corresponds to a radiated wave (that is, whether $k_\rho < k$). For the same reasons, the light cone can be cut by any plane including its axis and a dispersion diagram would be found for k_ρ.
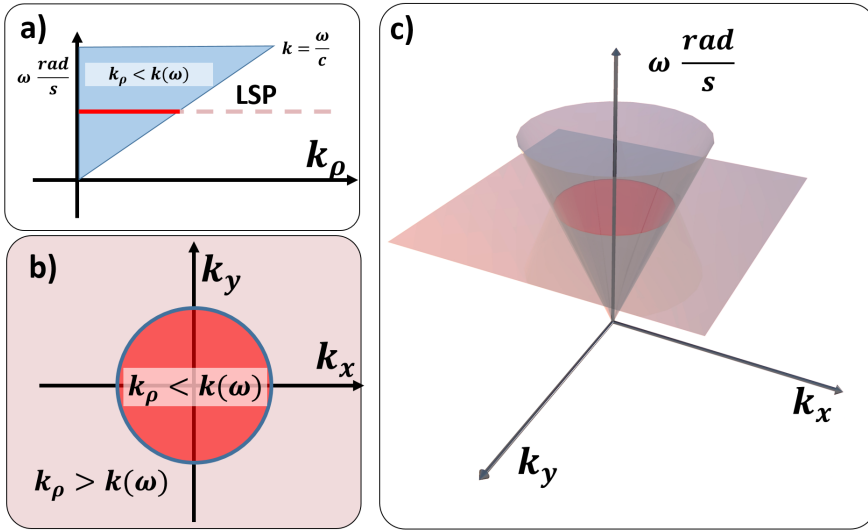
Figure 4.5: Relation between the dispersion diagram (a), the wavevector decomposition to study the evanescent waves (b) and the light cone (c).

There is a fundamental aspect to be careful with: In order to assure the right solution to eq.4.58, all the values of k_z have to satisfy that $Im\{k_z\} > 0$. Thus, eq.4.60 has to be also fulfilled:

$$k_z\left(k_\rho\right) = \begin{cases} \sqrt{k^2 - k_\rho^2} & if \quad Im\left\{\sqrt{k^2 - k_\rho^2}\right\} \geq 0 \\ i\sqrt{k_\rho^2 - k^2} & if \quad Im\left\{\sqrt{k^2 - k_\rho^2}\right\} < 0 \end{cases} \qquad (4.60)$$

The explanation for eq.4.60 comes from the fact that, when expanding $f(z)$ in the complex plane (that is, allowing $z \in \mathbb{C}$), the square root has a double sheet Riemann surface. An example, for $k_\rho = 1$, is shown in fig.4.6. Both solutions have the same module, but different phase.

Therefore, it is mandatory to choose correctly the right solution at any k_ρ. Indeed, different solutions lead to different physical interpretations. In the
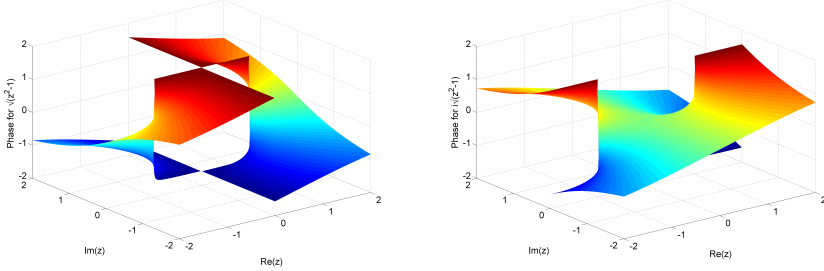
(a) Phase representation for the first Riemann sheet

(b) Phase representation for the second Riemann sheet
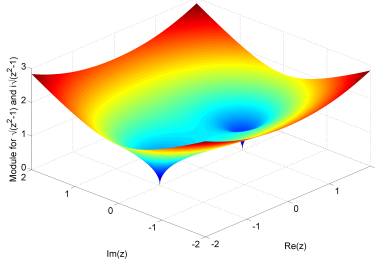
(c) Module representation for both Riemann sheets

Figure 4.6: Representation of the complex double sheet Riemann surface for $f(z) = \sqrt{z^2 - 1}$

case of a source of power, a careful choice of phase in k_z must be done in order to avoid expressions corresponding to increasing power waves with increasing distance from the source, that are physically meaningless in this context.

$$Ae^{ik_z z} = Ae^{i(a \pm bi)z} = Ae^{iaz \mp bz} = Ae^{iaz}e^{\mp bz} \quad (4.61)$$

Notice that $i = e^{i\frac{\pi}{2}}$, so for any complex value $z = a + bi = Ae^{iB}$ when multiplying by i a phase shift of $\frac{\pi}{2}$ is applied (see eq.4.62). Thus, eq.4.60 is an analytical expression to choose correctly the right solution of k_z.

$$Ae^{iB}i = Ae^{iB}e^{i\frac{\pi}{2}} = Ae^{i(B+\frac{\pi}{2})} \quad (4.62)$$

This consideration are important because the improper integral in eq.4.58 (and its variants that include the substrate effect) are usually solved using a contour integral in the complex plane. To do so, usually eq.4.58 is expressed

not in terms of the bessel function J_n but the Hankel function H_n^i of the first ($i = 1$) and second ($i = 2$) kind. Due to the symmetry of those, this leads to:

$$\frac{e^{ikR_0}}{R_0} = \frac{i}{4} \int_{-\infty}^{+\infty} dk_\rho \frac{k_\rho}{k_z} (H_0^1(k_\rho\rho) + H_0^2(k_\rho\rho)) e^{ik_z|z-h|} \qquad (4.63)$$

With this improper integral, now it is possible to define a complex contour integral by extending the function to the complex plane ($k_\rho \in \mathbb{C}$) as:

$$\oint_C f(k_\rho)dk_\rho = \lim_{R\to\infty} \int_{-R}^{+R} f(k_\rho)dk_\rho + \lim_{R\to\infty} \oint_{Re^{ip}} f(k_\rho)dk_\rho \qquad (4.64)$$

By choosing a big enough R parameter (ideally $R \to \infty$) and due to the atenuation condition defined by the right choice of the phase in k_z with eq.4.60, it can be concluded that $f(z) \to 0$ as $R \to \infty$. This means that, by applying Jordan's Lemma [21, Ch.9.3] the contribution of the semicircle to the contour integral in eq.4.64 is negligible, leading to eq.4.65:

$$\lim_{R\to\infty} \oint_{Re^{ip}} f(k_\rho)dk_\rho = 0 \to \lim_{R\to\infty} \int_{-R}^{+R} f(k_\rho)dk_\rho = \oint_C f(k_\rho)dk_\rho \qquad (4.65)$$

It could be asked what is the advantage of defining a real improper integral (eq.4.63) in terms of a complex plane contour integral (eq.4.64). The main advantage is that it allows one to apply the Residue theorem (eq.4.66). In fact, a strategy to solve complicated improper integrals in the real axis is to expand the integrand in the complex plane and then applying this theorem[21, see 8.3]. When combined with eq.4.65 it leads to one of the most important equations in this thesis, eq.4.67:

$$\oint_C f(z)dz = 2\pi i \sum_{j=1}^{m} res(f, c_j)) \qquad (4.66)$$

$$\int_{-\infty}^{+\infty} dz f(z) = \oint_C f(z)dz = 2\pi i \sum_{j=1}^{m} res(f, c_j)) \qquad (4.67)$$

In order to be able to apply this strategy there must be at least a pole c_j. This has been verified for the complete expressions found in [16], related with the poles of the reflexion and transmission coefficients in the complex plane.

In eq.4.63 it can be seen that there is at least one pole related with $k_z = 0$. Thus, for non-absorbing materials (with purely real refractive index), the integrand poles lay on the same integration path (the real axis). In this case, it is possible to proove [22, ch.9.13] that, without loss of generality from what

has already been exposed[6], those poles can be treated by small contours in the complex plane, as shown in fig.4.7. This leads to the *extended residue theorem* (eq.4.68).
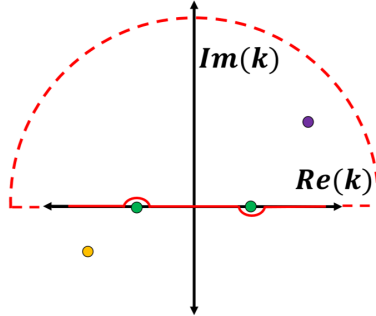
Figure 4.7: Generalised contour path for calculating an improper real integral using the residue theorem when some of the poles are on the real axis.

$$\oint_C f(z)dz = 2\pi i \sum_{j=1}^{m} res^{\mathbb{C}}(f,c_j) + \pi i \sum_{k=1}^{n} res^{\mathbb{R}}(f,c_k)) \qquad (4.68)$$

In eq.4.68 different kind of poles are presented. The first group of c_j poles correspond to the poles that are taken into account in the traditional Residue Theorem, that is, those lying inside the contour path except for those c_k poles lying on the real axis that correspond to the second group. In fig.4.7 the first group is shown in purple whereas the second is showed in green.

There is a final remark that has to be done as sometimes branch cuts are found in the complex plane. In this case, the contour path has to be deformed in order to avoid it, as shown in fig.4.8

The effect of the branch cut changes the conclusions and the strategy that has been showed. In this case, eq.4.65 is no longer valid as the extra contour path needed to avoid the branch cut (let us call it Γ) is not necessarily negligible. It might seem easy to cancel the effect of Γ as it defines and forward-back path and this seems to be cancelled analytically when calculated. However, this would only be true in holomorphic (thus, continuous) domains whereas the branch cut is a discontinuity by definition. Thus, the Γ contribution to the integral has to be calculated in order to correct eq.4.65.

---

[6]Notice that one of the conditions for all this to be true is that the contour has to fulfill the same continuity conditions that the complex area that it encloses. Thus, the choice of the upper or the lower semicircle in the poles located at the real axis must be done carefully attending to this continuity.
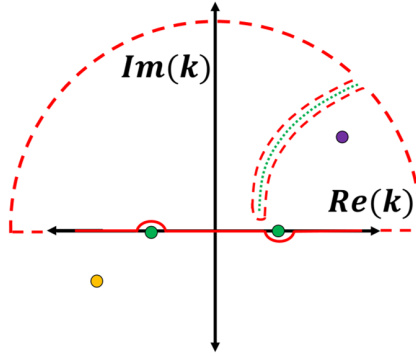
Figure 4.8: Generalised contour path for calculating an improper real integral using the residue theorem when a branch cut in the Riemann sheet is present.

In eq.4.64, the p range would be generally $p \in [0, \pi]$ or $p \in [\pi, 2\pi]$. In any case the contour should be followed counterclockwise to fullfil the Cauchy integral theorem correctly and, in extension, the Residue theorem (eq.4.66)[21, Ch.6,8]. Fig.4.8 shows a representation of eq.4.64:

There is a good strategy to find numerically the poles involved in a multilayered structure [23, 24]. At one hand, when an integration contour does not include any pole, eq.4.66 must be zero, so any small contour plot around an arbitrary complex z_0 value must also tend to zero unless z_0 is a pole. On the other hand, from the numerical point of view, it is quite common to use the approach of an *effective refractive index*, that makes the wavevector decomposition numerically easier than eq.4.59 as it normalises the huge wavenumbers values around unity. For a single interface, the expression for n_{eff} corresponds to eq.4.69.

$$k_z = n_{eff} k \rightarrow k_z = \sqrt{1 - \frac{k_\rho^2}{k^2}} k \rightarrow n_{eff} = \frac{k_z}{k} = \sqrt{1 - \frac{k_\rho^2}{k^2}} \qquad (4.69)$$

As a proof of concept, fig.4.9 shows a contourplot with the local Cauchy integrals $\oint_C n_{eff}(z)dz$ (eq.4.66). The simulated structure corresponds to a 100nm SiO_2 antireflection coating on a c-Si infinite substrate. Notice that the colorscale is not included in that figure as the values have not a physical meaning and only a relative comparison between areas is intented: Red colours are related with discontinuities whereas blue colors are holomorphic (continuous) regions for the integrand.
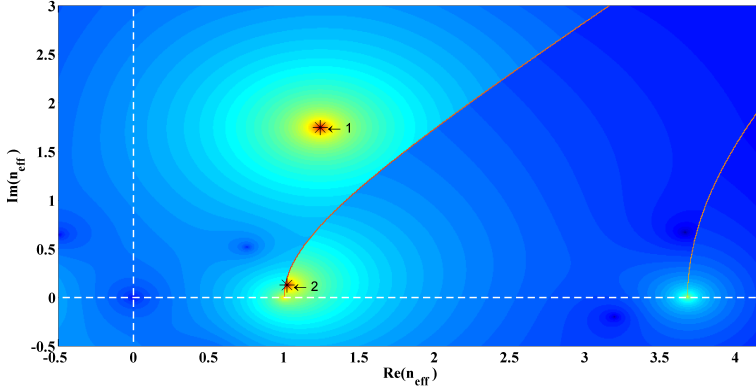
Figure 4.9: Determination of the poles in terms of n_{eff} for a Sommerfeld integral corresponding to a 100nm SiO_2 ARC between two semi-infinite domains of air (upper) and Si (lower), for $\lambda = 800nm$ and TM polarisation.

In fig.4.10 the same structure is simulated, this time considering a finite Si substrate of $1\mu m$ surrounded by air. In this case there are more poles because there is a new internal reflectivity due to the Silicon-Air interface.
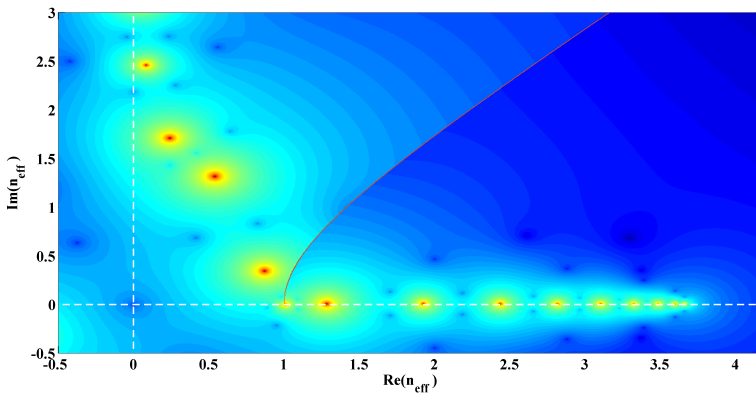
Figure 4.10: Determination of the poles in terms of n_{eff} for a Sommerfeld integral corresponding to a 100nm SiO_2 ARC between and a $1\mu m$ of Si between two semi-infinite domains of air, for $\lambda = 800nm$ and TM polarisation.

When the Si layer thickness increases even more (see fig.4.11), the number of poles become uncountable and the Sommerfeld-like integrals become extremely difficult to evaluate analytically. In this case, a long distance approximation can be done, such as presented in [25, Appendix D].
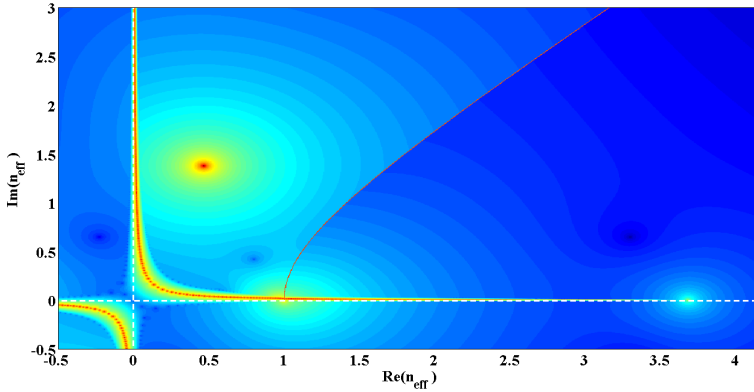
Figure 4.11: Determination of the poles in terms of n_{eff} for a Sommerfeld integral corresponding to a 100nm SiO_2 ARC between and a $180\mu m$ of Si between two semi-infinite domains of air, for $\lambda = 800nm$ and TM polarisation.

In order to avoid unnecessary numerical issues when considering a finite Si layer, a Si substrate will be considered when the imaginary part of the refractive index is high enough so that no energy will reach the second Si-Air interface. In both cases, transmission through the silicon will be zero.

All these strategies for expanding into the complex plane the Sommerfeld integral from eq.4.58 are done because the traditional real axis integration is very difficult to solve. The main issues are related with the highly oscillating behaviour of the integrands involved that make numerical integration specially difficult. This implies that adaptative quadrature methods such as the Gauss-Konrod [26] are the most suitable in this case, but usually the improper integrals have to be divided into smaller subintervals anyway. This leads to a slow convergent calculation that makes the Green's approach less interesting, even if it is a very powerful tool for this thesis. Moreover, the solution algorithm has to be coded and it becomes very difficult to do it efficiently.

An example for the developed code in this thesis using Novotny's equations is shown in fig.4.12. It corresponds to an horizontal dipole at 1nm of the substrate, consisting of 100nm of SiO_x and c-Si. The dipole corresponds to a Ag nanoparticle of $r = 10nm$ excited at 400nm with an electric field $E_x = 1V/m$. Only the secondary field (the reflected and transmitted components) are shown

for better clarity and the primary radiated field by the dipole is not included. The c-Si is considered as semiinfinite.
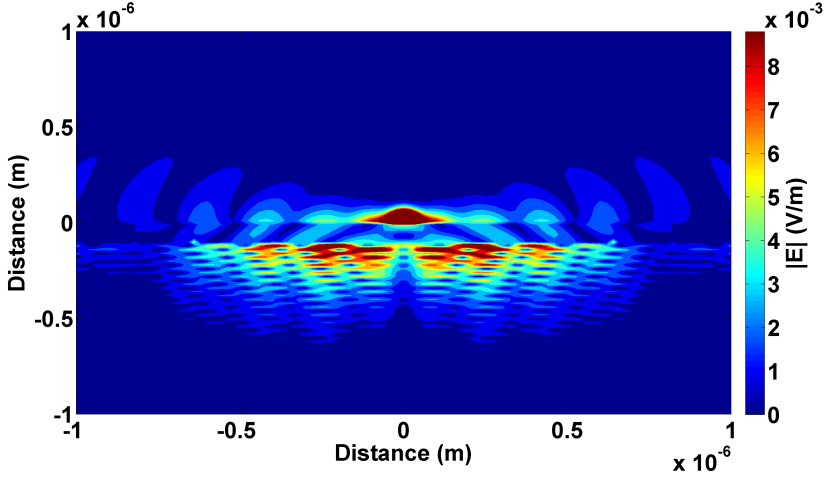
Figure 4.12: Example of simulated secondary field from Novotny's Green function dealing with a horizontal dipole induced in a $r = 10$nm Ag nanoparticle on a 100nm SiO_2 ARC on a semiinfinite c-Si substrate.

Some efforts have been done to find faster algorithms for the calculation of Sommerfeld integrals. A complete review for those is shown in [27] and references therein. In this thesis, in order to overcome the computational difficulties of this method, the code developped previously by Dr. Jean-Paul Hugonin[7] from the Insitute d'Optique CNRS-Université de Paris Sud has been used and modified. The details of the Green Functions that are finally implemented can be found in [28].

In short, Dr. Hugonin's code has already been tested and overcomes all the computational (thus, numerical) issues that have been presented in this thesis. Moreover, his code allows to define a periodised Green Function to simulate infinite arrays of nanoparticles as a periodised random subarray of N particles.

---

[7]jean-paul.hugonin@u-psud.fr

4.3 Polarisability of truncated nanoparticles

Most studies involving nanoparticles consider that the nanoparticles are spherical because the models to determine its polarisability are simple and easy to handle. This is a reasonable assumption for chemically synthetised spheroidal nanoparticles but it seems to be not so realistic in the case of interfacial self-aggregated nanoparticles, where the wettability of the material on the substrate usually leads to truncated spheroids. In this case a more appropriate ideal model would be to assume the nanoparticles are truncated spheres.

Recently, J.Jung and T.G. Pedersen [29] developped a model that perfectly fits on this approach and, moreover, includes the effect of the substrate. Even if their model involves very complex mathematical tools and they do not present an explicit expression, they show the methodology to follow as well as some tips on the most suitable numerical methods to solve the model. Thus, their paper summarises a general method to obtain a vertical and an horizontal polarisability for a truncated sphere supported on a substrate.

4.3.1 Analysis on the model

The structure studied in [29] is summarised in fig.4.13: It assumes a sphere that is partially embedded between two semi-infinite media whose dielectric functions are ϵ_1 (upper medium) and ϵ_4 (lower medium). An angle θ is defined in order to include the extent of the sphere that is embedded in the lower media.
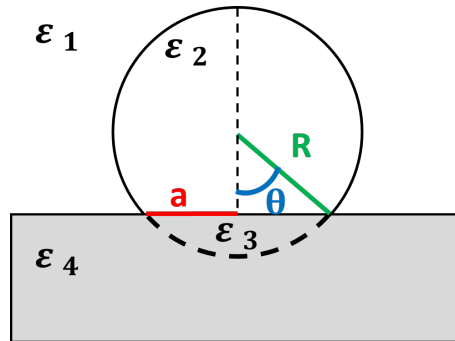
Figure 4.13: Schema of the nanoparticle geometry studied by Jesper Jung.

A circle is defined as the intersection between the sphere and the interface between the semi-infinite media. As a geometrical restriction of the model, its radius is kept constant and equal to 1 (so, the sphere radius R changes with θ). The model also allows to decompose the sphere into two materials: The one corresponding to the truncated sphere in the upper medium (with dielec-

tric function ϵ_1) and the other corresponding to the complementary truncated sphere within the lower medium (with dielectric function ϵ_3).

In this thesis the complex approach described in [29] will not be repeated. However, it has been analysed in order to include some additional comments on the numerical stability of this model.

The key steps in Jung and Pedersen solution are related with a 4 dimensional vector Fredholm's integral equation (FIE), as shown in eq.4.70.

$$\mathbf{f}(x,\theta) = \mathbf{A}(x,\theta,\epsilon_i)\mathbf{b}(x,\theta,\epsilon_i) + \int_0^\infty \mathbf{G}(\kappa(x,y,\theta),\epsilon_i)\mathbf{b}(y,\theta,\epsilon_i)dy \qquad (4.70)$$

The matrix kernel $\mathbf{G}(\kappa(x,y,\theta),\epsilon_i)$ in eq.4.70 is constructed element by element using two integral Kernels $\kappa(x,y,\theta)$(eq.4.71 and eq.4.72). The choice of each internal kernel will define which polarisability (vertical or horizontal) will be calculated.

$$\kappa_V(x,y,\theta) = \int_0^\infty \frac{P_{-1/2+ix}(\cosh z)P_{-1/2+iy}(\cosh z)}{\cosh z - \cos\theta}\sinh z dz \qquad (4.71)$$

$$\kappa_H(x,y,\theta) = -\int_0^\infty \frac{P_{-1/2+ix}^{-1}(\cosh z)P_{-1/2+iy}^1(\cosh z)}{\cosh z - \cos\theta}\sinh z dz \qquad (4.72)$$

Each one of the integral Kernel is expressed in terms of the Legendre functions and those are expressed in terms of the hypergeometric function[30, ch.15-16] and the gamma function[30, ch.5]. In all cases, the integrands in the Kernels are attenuated oscillating functions. Therefore, the improper integrals in eq.4.71 and eq.4.72 can be aproximated by a truncated quadrature up to 20 (fig.4.14).

Notice that the Integral Kernels $\kappa(x,y,\theta)$ do not depend on the materials involved in fig.4.13 and only on the geometry. It is when defining the matrix kernel $\mathbf{G}(\kappa(x,y,\theta),\epsilon_i)$ and the matrix $\mathbf{A}(x,\theta,\epsilon_i)$ that the permittivities are included. Thus, two important remarks should be done here: First that once the integral kernels have been calculated, they are still valid for any combination of materials. This is a favourable point for this method and it is closely related with the quasi-static approximation that is intrinsically done in this approach. Second, that the frequency dependency is implicitly included in the permittivities ϵ_i $(i = 1\ldots 4)$ of the materials involved.

Another important remark concerns the numerical particularities of the matrices $\mathbf{A}(x,\theta,\epsilon_i)$. As the solution proposed by Jung and Pedersen uses toroidal coordinates, a variable transformation involving hyperbolic trigonometrical functions is done. This implies that the components of both matrices

(a) $P_{\frac{1}{2}+ix} \cosh(U)$

(b) $P^1_{\frac{1}{2}+ix} \cosh(U)$

(c) $P^{-1}_{\frac{1}{2}+ix} \cosh(U)$
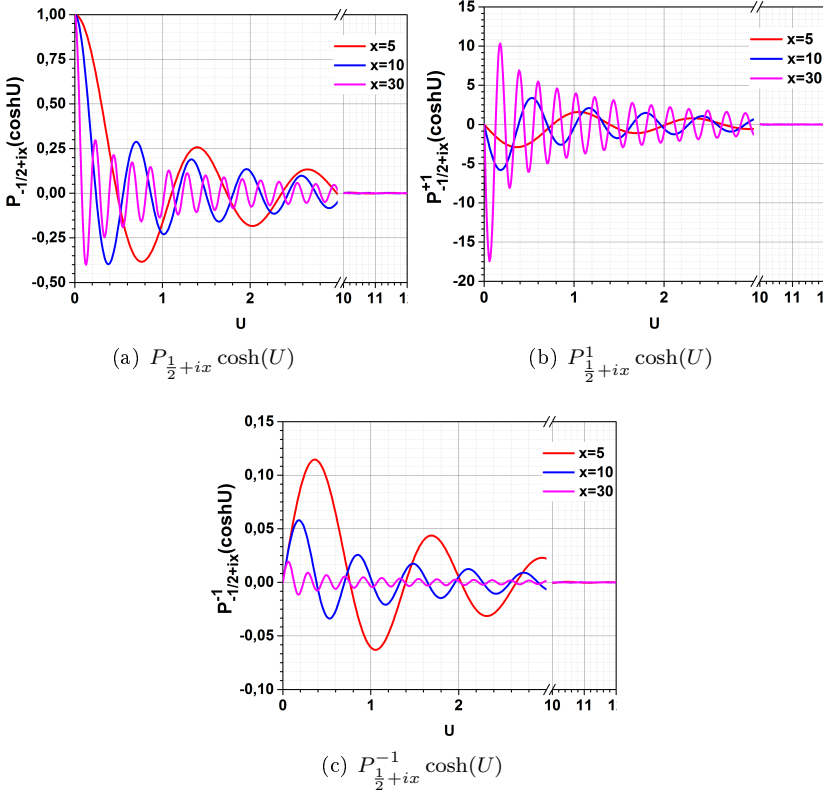
Figure 4.14: Attenuated oscillating behaviour for the integrands of the integral Kernels.

$\mathbf{A}(x, \theta, \epsilon_i)$ and $\mathbf{G}(\kappa(x, y, \theta), \epsilon_i)$ include very big and very small values, and therefore they are ill-conditioned. This scaling issue is fundamental, as small differences in the elements of the matrix will lead to very different results. From the numerical point of view this has to be controlled and taken into account.

The main consequence of this numerical issue is that the matrix $\mathbf{A}(x, \theta, \epsilon_i)$ becomes numerically singular when the x parameter is higher than about 9 or 10 (fig.4.15). This is an important issue as, in order to solve the $\mathbf{b}(x, \theta, \epsilon_i)$ vector from eq.4.70, that matrix has to be inverted.

In fact, in order to be able to solve eq.4.70, a Gauss-Laguerre quadrature is proposed, as follows.

$$[\mathbf{f}_i] = [\mathbf{G}_{ij}\omega_j + \mathbf{A}(z_i)\delta(i, j)] [\mathbf{b}_i] \qquad (4.73)$$

104
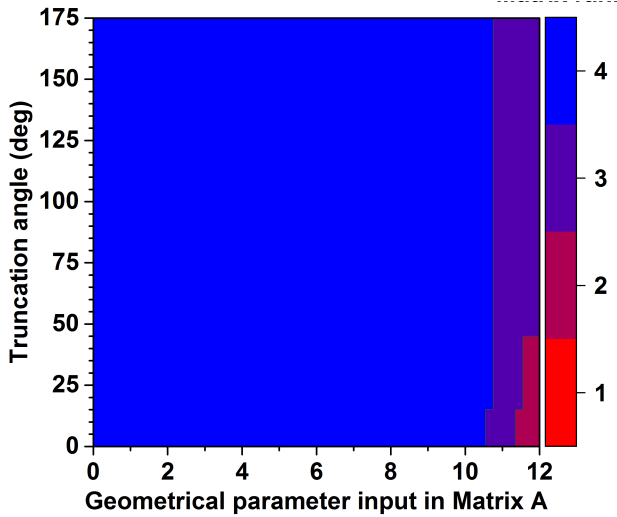
Figure 4.15: Rank of the A matrix depending on the matrix /kernel parameter. The example corresponds to truncated Ag nanoparticles on a SiO_2 substrate in air. The wavelength is 600nm.

or, equivalently:

$$\left[\mathbf{A}^{-1}(z_i)\mathbf{f}_i\right] = \left[\mathbf{A}^{-1}(z_i)\mathbf{G}_{ij}\omega_j + \delta(i,j)\right]\left[\mathbf{b}_i\right] \tag{4.74}$$

One of the basis of the Gauss-Laguerre quadrature is that the abscissas chosen to evaluate the integrand are determined by the quadrature's order N[8]. In table 4.2 the Gauss-Laguerre quadrature abscissas for different number of summands is shown:

---

[8]Reader is reminded that the Gauss-Laguerre quadrature is:

$$\int_0^\infty e^{-x}f(x) \simeq \sum_{i=1}^N f(\gamma_i)\omega(\gamma_i) \tag{4.75}$$

Where γ_i correspond to the zeros of the N degree Laguerre polynomial $\mathcal{L}$ and $\omega(\gamma_i)$ are the weighing factors for the quadrature and are obtained as:

$$\omega(\gamma_i)\frac{\gamma_i}{(N+1)^2\left(\mathcal{L}_{N+1}(\gamma_i)\right)^2}; \tag{4.76}$$

It is easy to find tables with the weigthing factors of several quadratures, including the Gauss-Laguerre, for different values of N. Attention must be paid to the fact that the integrand does not include explicitly a negative exponential term, so this quadrature is usually generalised as follows:

$$\int_0^\infty f(x) = \int_0^\infty e^{-x}f(x)e^x = \int_0^\infty e^{-x}g(x) \tag{4.77}$$

N=1	N=2	N=3	N=4	N=5	N=6
1	0.5858	0.4158	0.3225	0.2636	0.2228
-	3.4142	2.2943	1.7458	1.4134	1.1889
-	-	6.2899	4.5366	3.5964	2.9927
-	-	-	9.3951	7.0858	5.7751
-	-	-	-	12.6408	9.8375
-	-	-	-	-	15.9829

Table 4.2: Gauss-Laguerre quadrature abscissas for different degrees of the Laguerre Polynomial

From the values in table 4.2 it is possible to see that in order to focus in the [0-10] interval to avoid numerical issues, only N=4 should be considered.

The eigenpolarisabilities can be found by comparing the solution to the Laplace problem with the FIE solution vector $\mathbf{b}(x, \theta, \epsilon_i)$. During this comparison, and a third quadrature has to be done, as shown in eq.4.78 and 4.79. A new Gauss-Laguerre quadrature could be done using the same interpolation abcissas that for the second quadrature. This procedure is more efficient in comparison with Jung and Pedersen but the final result will have a higher error.

$$\alpha_V = 8\pi\sqrt{2} \int_0^\infty x b_4(x, \theta, \epsilon_i) dx \qquad (4.78)$$

$$\alpha_H = -\pi\sqrt{2} \int_0^\infty (1 + 4x^2) b_2(x, \theta, \epsilon_i) dx \qquad (4.79)$$

In eq.4.78 and eq.4.79, the subindex in the $b_i(x, \theta, \epsilon_i)$ terms correspond to the position in the $\mathbf{b}(x, \theta, \epsilon_i)$ vector solution of eq.4.73. Notice that the index changes between the vertical and the horizontal polarisabilities, as well as the whole $\mathbf{b}(x, \theta, \epsilon_i)$ as the integral kernel used also changes (eq.4.71 or 4.72).

In the paper, the normalised polarisability $\alpha'(\omega)$ for different truncation angles ω is shown. It is important to notice that this normalisation leads to unitless variables. Thus, the non-normalised polarisabilities $\alpha_{a=1}(\omega)$ are in m^3 units. The subscript $a = 1$ refers to the geometrical restriction shown in fig.4.13 that makes always the parameter $a = 1$. The explicit expression (not shown in

---

and then the quadrature is applied. It is also easy to find in tables the corrected weighting factors including the positive exonential term. However, numerical problems may arise in this generalisation of the Gauss-Laguerre quadrature.

the paper) for having the real polarisability instead of the eigen-polarisability is, therefore:

$$\alpha' = \frac{\alpha_{a=1}[m^3]}{V_{a=1}[m^3]} = \alpha_{a=1}\frac{sin\omega}{1+cos\omega} \tag{4.80}$$

In order to obtain the polarisability in $\left(\frac{Cm^2}{V}\right)$ the following transformation has to be done:

$$\alpha(\omega, a) = \alpha_{a=1}(\omega)a^3 4\pi\epsilon_0 \tag{4.81}$$

With this expression and following the mathematical model from[29], it is possible to define values for the "horizontal" polarisability α_H as well as the "vertical" polarisability α_V. It should be understood "horizontal" as parallel to the substrate interface shown in fig.4.13, and "vertical" as normal to this interface.

Bohren and Huffman [31, p.150] deal with the possibility of an arbitrarily oriented dipole induced in a nanoparticle through a tensor polarisability. The main condition to do this and keep valid all their well-known expressions is that the polarisability components have to be defined along the main axes of the sphere/spheroid. Thus, the polarisability relating the external exciting electric field $\vec{E}$ with the resulting induced dipole in the nanoparticle $\vec{P}$ can be generalised from a single scalar value α. Thus, the resulting dipole, taking into account both the direction of the electric field as well as the shape of the nanoparticle, is (eq.4.82):

$$\vec{P} = [\alpha]\,\vec{E} = \begin{bmatrix} \alpha_H & 0 & 0 \\ 0 & \alpha_H & 0 \\ 0 & 0 & \alpha_V \end{bmatrix} \begin{bmatrix} E_x \\ E_y \\ E_z \end{bmatrix} \tag{4.82}$$

Notice that this approach has a special interest because the method based in Green Functions presented in section 4.2 can also be generalised from a scalar (isotropic) polarisability, leading to a more realistic model.

4.3.2 Results

As explained in section 4.3.1, there are several reasons related with the numerical issues during the calculation of the directional polarisability of a truncated sphere that make think that the results may not be accurate. In fig.4.16 the results for a particle with $r = 10nm$ are shown.

There are evident similarities between the behaviour of the curves shown in fig.4.16 and those obtained from the electric properties of a metal (fig.4.1 in section 4.1). This is a first consistency proof on the general trend obtained by the model.

Fig.4.16 shows that as the truncation angle increases, an important redshift is found for the resonance of the parallel polarizability, whereas a slight blueshift occurs for the vertical one. This is consistent with the flattened particles behaviour, as when increasing the aspect ratio the longer axis supports lower energy resonances and the short axis supports higher ones[32]. The smaller difference in the blueshifted resonances is mainly due to the differences between the wavelength and the energy scales.

Moreover, both polarisabilities decrease with the truncation angle as the particles become smaller in volume and there are less charges to be polarised. However, the vertical polarizability decreases faster than the parallel as the Feret diameter in the vertical axis always decreases with increasing truncation angles and this is not true for the parallel direction. This dimensional comparison in terms of the Feret Diameter[33, pp.37] also explains why the redshift is even more important at truncation angles beyond 90degrees.

In brief, as shown in Fig.4.16, even if the Gauss-Laguerre quadrature is limited to four terms (N=4), the resulting eigenpolarisabilities for a Ag nanoparticle on a silicon oxide substrate show a resonance that fits with the expected behaviour at increasing truncation angles. Moreover, the Mie theory predicts a polarizability for spherical Ag nanoparticles in the range of $10^{-31} - 10^{-33}Cm/V$. However, the exact values may not be too accurate as there are several quadratures involved and because their accuracy is limited by the numerical issues that have been described.

In order to have an accurate solution that allows us to shed light on the real consequences of the QSA assumptions, numerical simulations using CST have been carried out. In order to make comparable results, a truncated sphere has been simulated in an homogeneous media[9] and a plane wave excitation is done assuming an incidence angle of 90deg[10]. TE and TM polarisations are defined under this angle of indicende. Fig.4.17 summarises this model. Under these

---

[9]Numerical softwares calculate the Radar Cross Section (RCS) and the Absroption Cross Section (ACS) analogously to the cross sections defined in3.3.1. The presence of a substrate makes the RCS no longer representative of the nanoparticle behaviour because it interferes with the final values. This is why in this case an homogenous media has been modelled.

[10]The angle is defined relative to the surface normal where the NP would be lying on

(a) $Re(\alpha_H)$

(b) $Re(\alpha_V)$

(c) $Im(\alpha_H)$

(d) $Im(\alpha_V)$

(e) $|\alpha_H|$

(f) $|\alpha_V|$
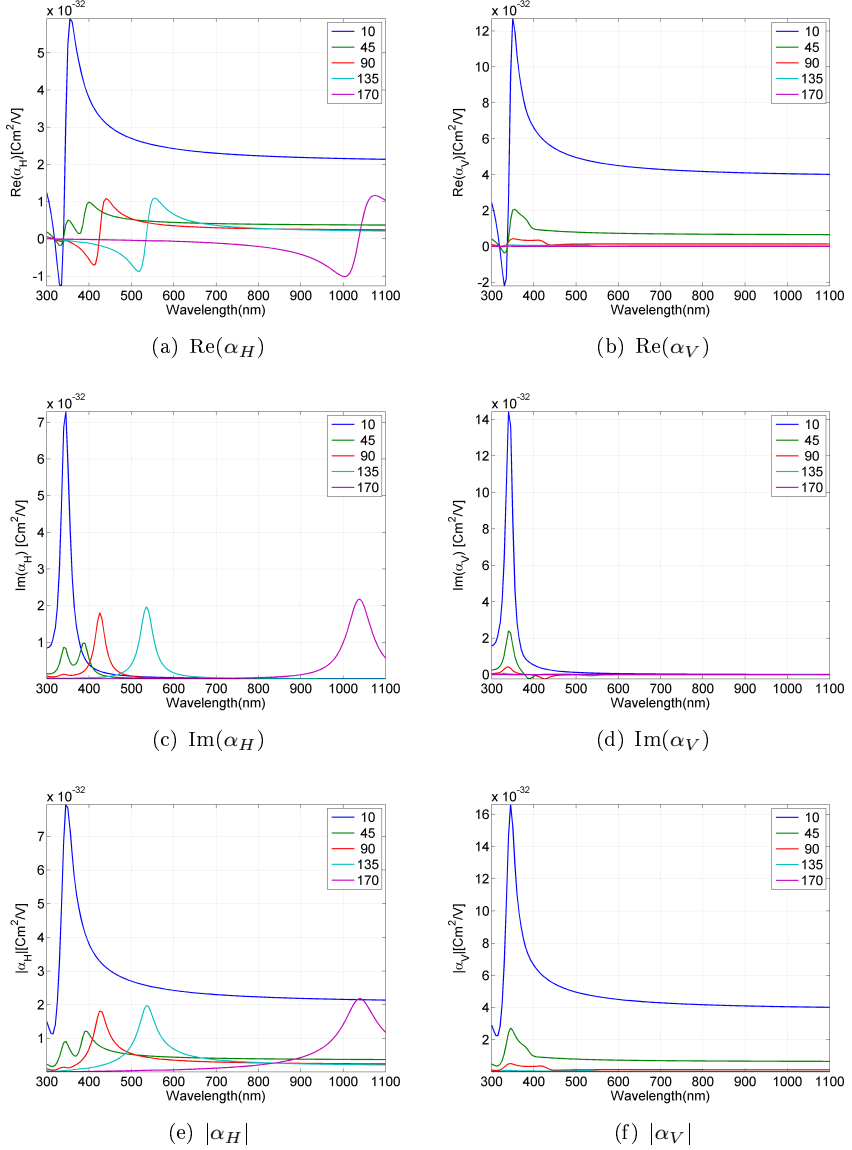
Figure 4.16: Analytical results for the horizontal α_H and vertical α_V polarisability of truncated Ag spheres at different truncation angles supported by a SiO_x substrate in air.

assumptions, it comes easily that the RCS will follow the vertical polarisability α_V for TM polarisation and the parallel polarisability α_H for TE polarisation. The numerical results are shown in fig.4.18.

(a) Vertical polarisability α_H model   (b) Parallel polarisability α_V model
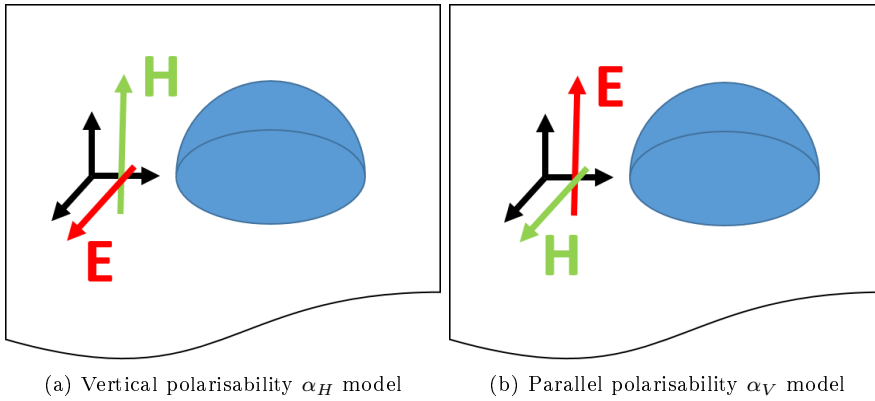
Figure 4.17: Simulated structure using numerical methods with CST to represent the effect of the parallel polarisability (α_H) and the vertical polarisability (α_V)

In Fig.4.18 it is shown that the trends seen in Fig.4.16 are correct. However, the numerical solution is redshifted when compared with the analytical one. This points towards retardation effects that are completely neglected by the electrostatic approximation. In addition, different excitation modes appear, as seen in Fig.4.18 where several maxima for each curve can be found. Those modes, probably quadrupoles, are not so clear in fig.4.16 and should be analysed in further studies for better results. Therefore, even if Mie model predicts that the main contribution for scattering for Ag NPs under 80nm at visible frequencies is due to a dipole (see section 4.4 for more details), and even if the QSA approximation is quite accurate for $r = 10nm$, the presence of a substrate makes less accurate this asumption.

(a) TE polarisation (α_H) in n=1

(b) TM polarisation (α_V) in n=1

(c) TE polarisation (α_H) in n=1.5

(d) TM polarisation (α_V) in n=1.5

(e) TE polarisation (α_H) in n=2

(f) TM polarisation (α_V) in n=2
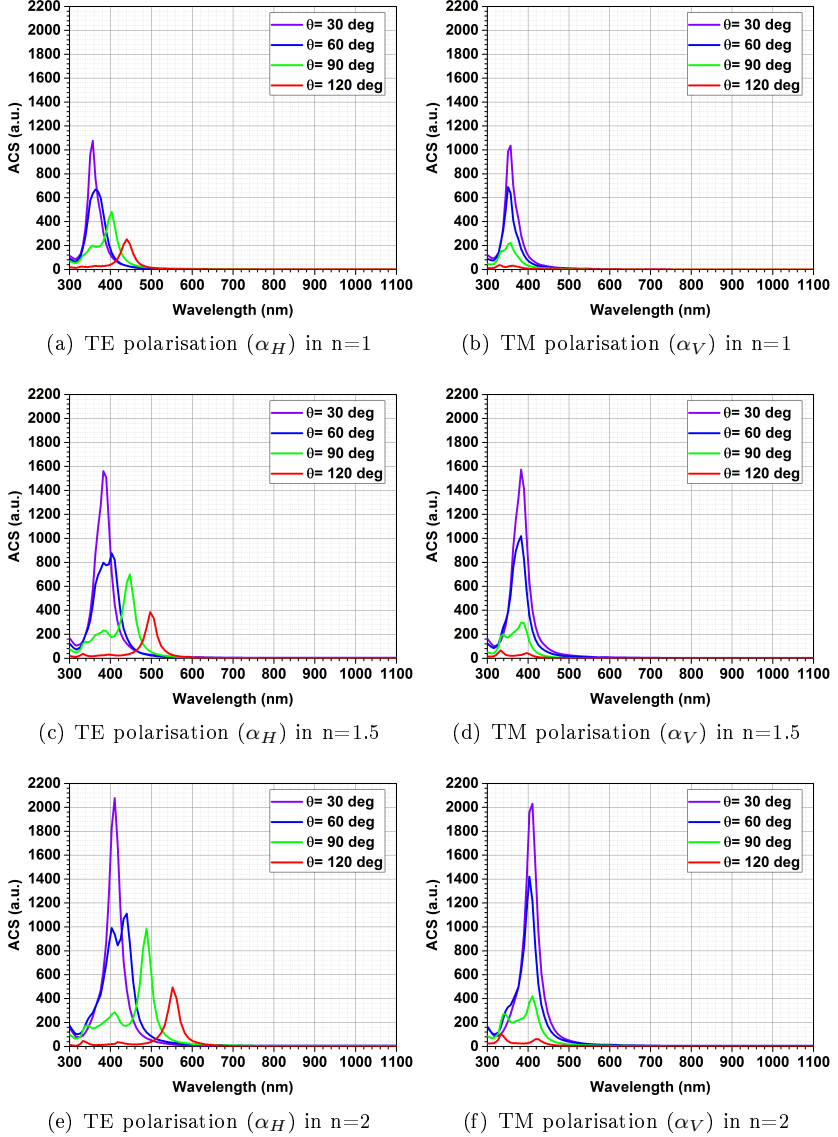
Figure 4.18: Numerical results for Absorption Cross section of Ag truncated spheres of $r = 10nm$ at different truncation angles and surrounded by different refractive index media.

4.4 Mie generic calculations

In section 3.3.3 the expressions for the Mie scattering σ_{scat} and extinction σ_{ext} cross sections was presented as a infinite sum of terms (eqs.3.54 and 3.55). Later, in section 3.3.4, the physical interpretation of each one of those terms was explained as the contribution of different excitation orders: Dipole, quadrupole,etc. In section 4.1, the scattering properties were estimated analytically under the assumption on a linear oscillator and from there an electric dipole was defined. Finally, in section 4.2 the Green function has been solved for an electric point dipole. However, no proof has been given on the hypothesis of the accuracy of an electric dipole when modelling a nanoparticle.

In this section, some comments on this assumption will be done. Moreover, the general trends expected for Ag nanoparticles are calculated from Mie approach. This implies that they will only be true for spherical, independent and in homogeneous media particles. However, even if the values will not be correct, the general trends will be considered as a guide to understand the real case presented in this thesis.

4.4.1 Size and surrounding media effects on the dipole limit

Let us start with the different excitation modes. As the Mie coefficients depend on the relative size of the particle to the wavelength through the size parameter $\breve{x}$ (eq.3.49) as well as on the relative permittivity of the involved materials m (eq.3.48), those will be the main parameters whose influence will be studied. The frequency dependency is implicitly included within the m parameter.

From the size point of view, fig.4.19 shows the different individual and global extinction cross sections of Ag spheres of different sizes surrounded by a SiO_x medium (whose refractive index is considered constant at $n = 1.5$)

As expected, the global extinction is the sum of the individual extinctions for each mode. Moreover, as predicted from the Quasi-Static Approximation (section 3.3.5) where usually only dipoles are considered, the first excitation order that appears at small sizes corresponds to a dipole. As the particle size increases, several conclusions are obtained:

- The different excitation modes become relevant with size in increasing order: The n=3 term in eq.3.55 only becomes relevant once the n=2 has appeared as well as the n=4 can be seen only at higher sizes than for the n=3 mode. This is perfectly understandable from the retardation effect point of view: For a given frequency, the secondary currents that arise from the retardation effects will be more complex (therefore leading to higher excitation modes) for bigger particles. Analogously, for a given size, shorter wavelenghts are needed to find higher excitation modes.

(a) $r = 10nm$

(b) $r = 50nm$

(c) $r = 100nm$

(d) $r = 200nm$
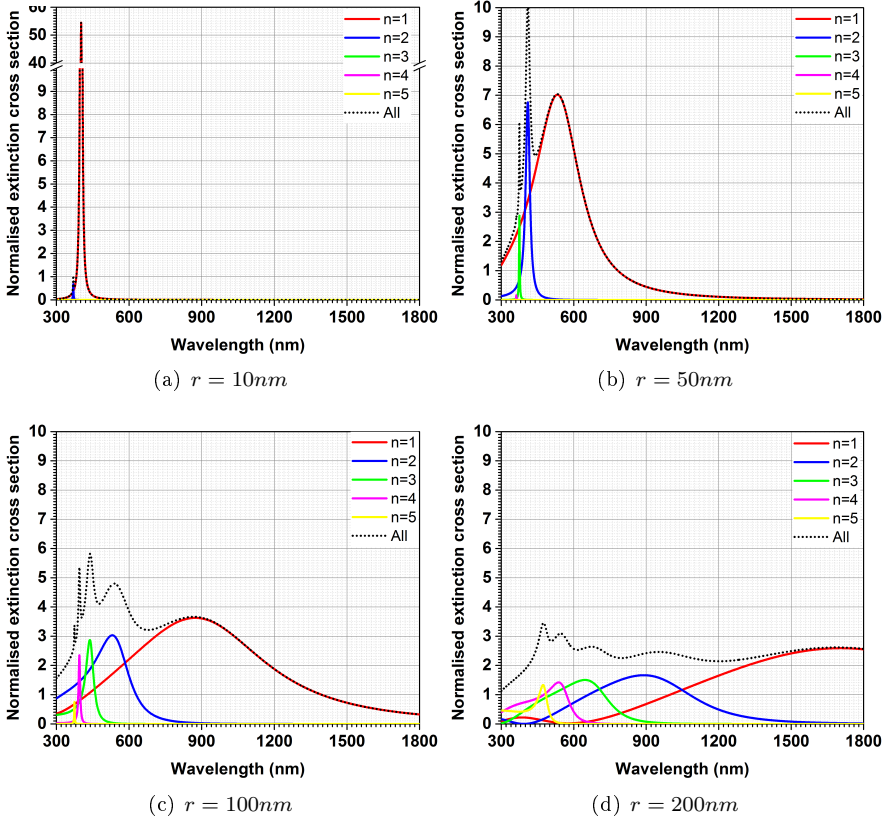
Figure 4.19: Different excitation orders in the global light extinction obtained by Mie for Ag spheres in SiOx for different sizes and wavelengths. Only electric contribution is taken into account.

- As introduced in section 3.3.6, there is a redshift in the resonance of each of the modes when the size increases. This was understood from the fact that the charge movement defined for each mode in fig.3.7 lead to higher travelled distances at increasing particle sizes. Therefore, the resonance is found at lower frequencies (longer wavelengths) as the coupling of the incident and the extincted light is done more easily.

- There is also a broadening in frequency (or in wavelength) for each mode with increasing sizes, together with a lower resonance intensity. This is related with the local differences in the dielectric function when retardation effects occur[34, 35].

- As conclusion of all these facts, as the particle becomes bigger, the relative weight of each mode on the total scattering becomes homogeneous. This implies that not a clear resonance but almost a constant cross section can be found to the many different orders involved and its broadened shape. Moreover, the maximum of the resulting global cross section is not so different from the average lineshape and it becomes closer to the unity (as expected for a continuous surface).

An easy way to study the behaviour of the different modes is the position of the resonance. It is expected to find macroscopical particularities at those points, such as maxima or minima in reflectivity or transmission values. A more complete study would include the weight at half height for each resonant mode, but in order to study the influence of the material of the surrounding media, only the maxima will be used.

Fig.4.20 shows the maxima position of each individual order for different sizes and refractive indexes. The studied range has been from 300 to 1900nm (that is, from 3 to 19 $nm/100$ in the colorscale). The white areas mean that the maxima are beyond this range. It is already known that the size effect produces not only a redshift, but also an intensity reduction of the resonance (the maxima). The second effect is not considered here and only the resonance position is looked at.

It can be seen that the refractive index has a similar effect than increasing the particle size: There is a redshift of the resonance. In fact, the size parameter $\check{x}$ is also increased with the refractive index. Moreover, there is an important combined effect of these two parameters: This can clearly be seen in fig.4.20a.

In fig.4.20 it can also be clearly seen that, independently of the origin of the redshift (size or refractive index), there is a smaller redshift for the $n + 1$ mode when compared with the n mode. In fact, for the surrounding materials that could be found in this thesis (antireflection coatings usually with $n < 2$), only at big sizes (radii above 70nm) small differences are found than in the resonant frequencies of orders $n > 1$. Analogously, for particles whose radii is $r < 50nm$, there are small differences on the resonant positions for $n > 1$ with an increasing refractive index.

This trend can be understood from fig.3.7. From the field lines, the travelled distance by the charges defining those currents is highly reduced from $n = 1$ to $n = 2$. However, this relative distance reduction is less important as the excitation order is increased from there. Therefore, the consequence on the resonance position due to the retardation effects are relevant mainly for n=1.

Looking at fig.4.19 it can be seen that for big particles there is not a clear general predominanting mode within the wavelength range of interest (400-1100nm). For small particles, however, the dipole mode can be assumed the predominating in that range. The limits where the dipole can be assumed the main contribution is a key point in this thesis.

(a) First order ($n = 1$)

(b) Second order ($n = 2$)

(c) Third order ($n = 3$)

(d) Fourth order ($n = 4$)
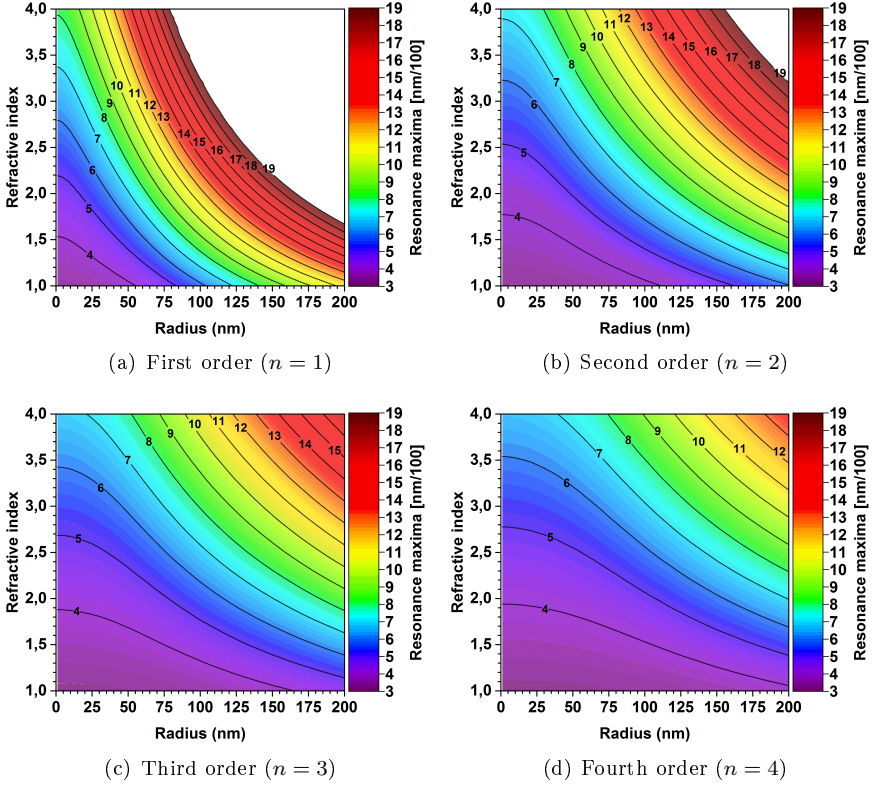
Figure 4.20: Extinction resonances (maxima values) for different excitation orders for Ag spheres of different sizes and refractive index of the surrounding media.

Fig.4.21, shows the ratio between the scattering of an electric dipole (that is, if only the a_1 term is considered in eq.3.54) and the whole scattering calculation (considering all the a_n and b_n terms $n = 1..\infty$). Thus, values close to the unity correspond to a dominant contribution of the electric dipole to the total scattering whereas values close to zero are related to higher order excitation contribution or magnetic contributions that make the electric dipole excitation neglible.

As expected, and as a summary of the previous comments in this section, as the radius of the nanoparticle is increased for a given wavelength, the contribution of higher order excitations becomes more important. Also, as the wavelength is increased, the size range where the scattering behaviour is dominated by an electric dipole is broadened.

(a) In air, $n = 1$

(b) In SiO_x, aprox $n = 1.5$

(c) In SiN, aprox $n = 2$
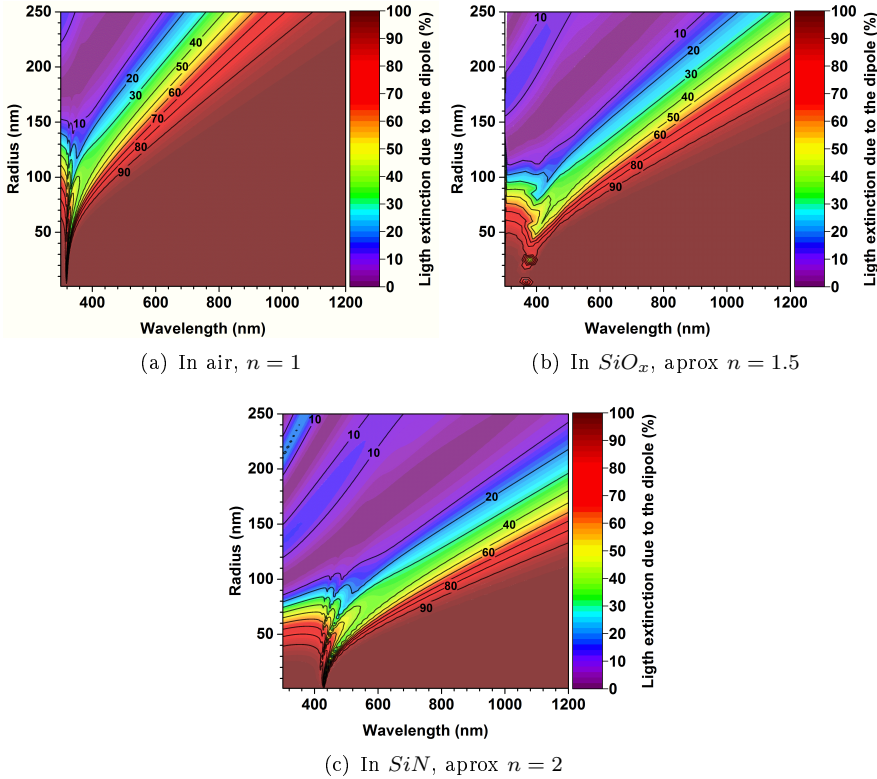
Figure 4.21: Relative effect of the dipole mode on the overall normalised extinction cross section of a Ag sphere at different sizes and surrounding media.

For Ag spherical nanoparticles in an homogeneous media of refractive index $n = 1$ the dipole largely predominates over the rest of the excitation modes from 400 to 1000nm for radius under 80nm. Larger particles still behave like dipoles for long wavelengths (700-1000nm) but not for short wavelengths (400-600nm) as higher excititation modes start to be relevant. The dipole becomes negligeable for short wavelengths at sizes bigger than $r = 200nm$.

As the refractive index of the surrounding media is increased, the maximum size at which the electric dipole is predominant is reduced. Therefore, if a refractive index of $n = 1.5$ (such as the silicon oxide SiO_x) is considered, for sizes above $r = 50nm$ are only clear dipoles from $\lambda > 450nm$. From 400 to 450, even if the dipole still predominates, the dipole-like approach will be less accurate.

For even higher refractive indexes such as $n = 2$ (more or less the SiN antireflection coatings), the dipole is not assured under 450nm at any size. However, due to the real system studied in this thesis, at the interface between the air and the antireflection coating an intermediate refractive media can be considered (just like explained in section 3.4.3.

To conclude with, for the 400-1000nm range, spherical silver nanoparticles will be correctly modelled as electric dipoles for low refractive indexes (up to approximately 1.5). Therefore, the analytical approaches developped in this chapter will be consistent in the case of perfect spheres. Deviations from the Mie hypothesis can change this conclusions when applied to the fabricated arrays of nanoparticles, but still they will be used as a reference starting point.

4.4.2 Scattering efficiency

As explained in chapter 1, one of the aims of integrating nanoparticles on a solar cell is to use their scattering properties to enhance the light trapping and therefore the global efficiency. Usually, the main effect in thin substrates is related with near field effects of the plasmon and coupled guided modes within a guide (the absorbing photoactive substrate). This kind of enhancement has already been reported [36] by using self-aggregated nanoparticles of different materials. However, this approach for estimating the enhancement due to the nanoparticles is not the best for thick (180 mum) solar cells as the substrate thickness makes difficult to define clear propagation modes (see fig.4.11 where each pole corresponds to a mode). In that case, the best approach is to max-imise the scattering efficiency of the nanoparticles. However, as introduced in fig.1.4 and detailed in section 3.3 the intrinsic losses are closely related with the plasmonic phenomena and cannot be removed. For this reason, the albedo is defined to quantify the relative importance between the scattering and the losses. The albedo is defined from eqs.3.54 and 3.55 as:

$$Albedo = \frac{\sigma_{scat}}{\sigma_{scat} + \sigma_{abs}} = \frac{\sum\limits_{n=1}^{\infty} \sigma_{scat}^{(n)}}{\sum\limits_{n=1}^{\infty} \sigma_{scat}^{(n)} + \sum\limits_{n=1}^{\infty} \sigma_{abs}^{(n)}} \neq \sum\limits_{n=1}^{\infty} \frac{\sigma_{scat}^{(n)}}{\sigma_{scat}^{(n)} + \sigma_{abs}^{(n)}} \qquad (4.83)$$

Thus, the albedo η_{scat} is a simple parameter (ranging from 0 to 1) that shows the scattering efficiency. Just to recall, sometimes the extinction term is misunderstood. As it has already been explained in section 3.3.1, it corresponds to the total amount of light that interacts with the nanoparticle so it includes both the absorption losses and the scattering of light.

An intersting result is found from the albedo point of view when individual excitation orders are considered: Even if the overall scattering seems to be

always enhanced for bigger particles, the individual order albedo is maximised for the dipole mode (fig.4.22)
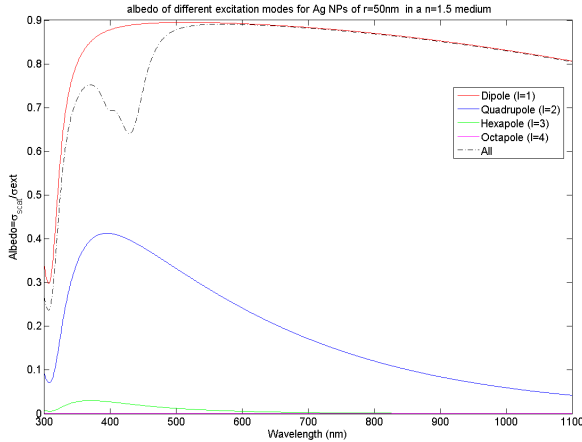
Figure 4.22: Albedo or scattering efficiency for different excitation modes (individually and globally) for a spherical Ag nanoparticle of r=50nm in a surrounding medium with refractive index n=1.5.

The most interesting at this point is that the individual albedos of the individual excitation modes show a behaviour different from the global resulting albedo: In contrast with what happens with the absorption and the scattering where the global value corresponds with the addition of the values of the different excitation modes independently, in the case of the albedo this is not true, as shown in eq.4.83

In this case, even if the individual albedos seem to show that higher order excitation will contribute to increase the global albedo, the actual result show that the dipole has the higher scattering efficiency whereas higher excitation modes are less efficient. Thus, as these more complex excitation modes become important, the final and global scattering efficiency is reduced.

This lower scattering efficiency for the quadrupoles and higher excitation modes excitation is explained due to the higher absorption losses for increasing modes: In fig.4.23, even if the scattering for high excitation modes is almost negligeable, the absorption losses are always bigger.

In global terms, the bigger the NP are the higher the albedo is. But at certain wavelengths, it is decreased when compared with the albedo of the dipole (most efficient excitation order). This conclusion leads to the following question: Is it always worth to look for bigger particles to increase the scattering?
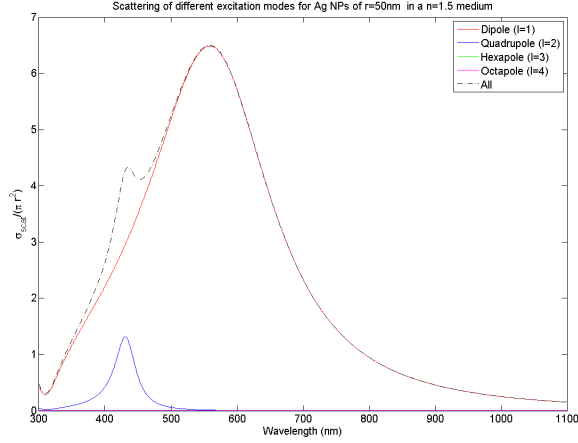
(a) σ_{scat} of different excitation modes calculated in n=1.5
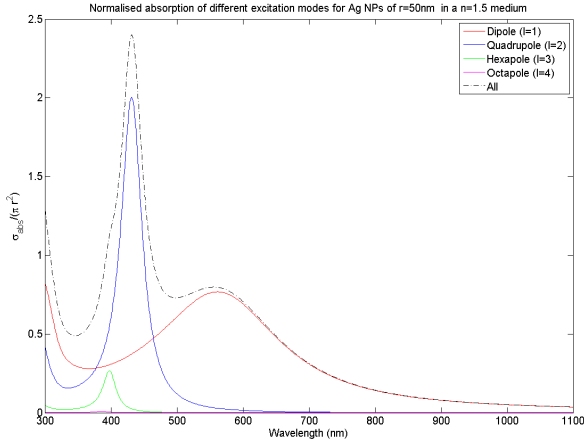
(b) σ_{abs} of different excitation modes calculated in n=1.5

Figure 4.23: Normalised absorption and scattering cross sections for a spherical Ag nanoparticle of r=50nm.

Or is it preferable to stay at the limit conditions to find a dipole (before other modes become significant)? In [37] an analysis is done to study, among others, the influence of the size and the excitation orders on the scattering efficiency

and they state that *The radiative efficiency decreases with increasing mode order* and that *The absorption initially increases as the radius increases, but then reaches a peak and decreases with increasing radius. The peak absorption is due entirely to the dipolar mode.* This fits well with the albedo definition made in eq.4.4.2.

In any case, another conclusion of [37] is that there are other parameters such as the surface coverage and the array distribution will also affect the scattering efficiency and these effects cannot be included in eq.4.4.2. Those are parameters difficult to control as explained in section 5.2.

Another key point that has also to be taken into account, is to know whether the albedo decrease is found in a range whose wavelengths are particularly important for the final application. In our case, this corresponds with the espectral response of the solar cell that has been introduced in section 2.7 and that will be detailed in section 6.1.

Bibliography

[1] Paul Drude. Zur elektronentheorie der metalle. *Annalen der Physik*, 306: 566, 1900. doi: DOI:10.1002/andp.19003060312.

[2] H.A. Lorentz. The motion of electricity in metals. In *Collected Papers*, pages 307–332. Springer Netherlands, 1935. ISBN 978-94-015-2216-8. doi: 10.1007/978-94-015-3449-9_13.

[3] K.H. Lee, I. Ahmed, R.S.M. Goh, E.H. Khoo, E.P. Li, and T.G.G Hung. Implementation of the fdtd method based on lorentz-drude dispersive model on gpu for pplasmonic applications. *Progress in Electromagnetics Research*, 116:pp. 441–456, 2011.

[4] A. Sommerfeld and H. Bethe. Elektronentheorie der metalle. In *Aufbau Der ZusammenhÃďngenden Materie*, volume 24/2 of *Handbuch der Physik*, pages 333–622. Springer Berlin Heidelberg, 1933. ISBN 978-3-642-89260-8. doi: 10.1007/978-3-642-91116-3_3.

[5] M. Quinten. *Optical Properties of Nanoparticle Systems: Mie and Beyond*. Wiley, 2010. ISBN 9783527633159. URL `https://books.google.es/books?id=X9hDAfDAP-kC`.

[6] J. V. Ortiz. Quasiparticle approximations and electron propagator theory. *International Journal of Quantum Chemistry*, 95(4-5):593–599, 2003. ISSN 1097-461X. doi: 10.1002/qua.10632.

[7] P.B. Johnson and R.W. Christy. Optical constants of the noble metals. *Physical Review B*, 6:4370–4379, 1972. doi: 10.1103/PhysRevB.6.4370.

[8] E.J. Borowski and J.M. Borwein. *Collins Dictionary of Mathematics*. Collins Dictionary of Series. HarperCollins, 2002. ISBN 9780007102952. URL `https://books.google.es/books?id=XyA6AQAAIAAJ`.

[9] E.T. Whittaker. *The Calculus of Observations - A Treatise on Numerical Mathematics*. Read Books, 2012. ISBN 9781447457657. URL `https://books.google.es/books?id=Htk3MAEACAAJ`.

[10] Ivar Stakgold and Michael J Holst. *Green's functions and boundary value problems*, volume 99. John Wiley & Sons, 2011.

[11] Dean G. Duffy. *GreenŠs Functions with Applications*, volume 99. John Wiley & Sons, second edition edition, 2015.

[12] SA Maier. *Plasmonics: Fundamentals and Applications*. Springer, 2007. URL `http://www.springer.com/west/home/librarians/springer+news?SGWID=4-40157-22-173660338-0`.

[13] Kin Hung Fung and C. T. Chan. Analytical study of the plasmonic modes of a metal nanoparticle circular array. *Phys. Rev. B*, 77:205423, May 2008. doi: 10.1103/PhysRevB.77.205423. URL `http://link.aps.org/doi/10.1103/PhysRevB.77.205423`.

[14] C.A. Balanis. *Antenna Theory: Analysis and Design.* Number v. 1 in Antenna Theory: Analysis and Design. John Wiley & Sons, 2005. ISBN 9780471667827. URL `https://books.google.es/books?id=jwjeAwAAQBAJ`.

[15] JP Connolly, C David, P Rodriguez, A Griol, P Welti, L Belliéres, J Ayucar, J Hurtado, R Lopez, G Sanchez, et al. Analysis of plasmonic nanoparticle fabrication techniques for efficient integration in photovoltaic devices. In *Proceedings of the 25th European Photovoltaic Solar Energy Conference and Exhibition/5th World Conference on Photovoltaic Energy Conversion, Valencia, Spain*, pages 6–10, 2010.

[16] Lukas Novotny. Allowed and forbidden light in near-field optics. i. a single dipolar light source. *JOSA A*, 14(1):91–104, 1997.

[17] Lukas Novotny. Allowed and forbidden light in near-field optics. ii. interacting dipolar particles. *JOSA A*, 14(1):105–113, 1997.

[18] S.R.J. Brueck. Radiation from a dipole embedded in a dielectric slab. *Selected Topics in Quantum Electronics, IEEE Journal of*, 6(6):899–910, Nov 2000. ISSN 1077-260X. doi: 10.1109/2944.902140.

[19] Jesper Jung, Thomas Søndergaard, Thomas Garm Pedersen, Kjeld Pedersen, Arne Nylandsted Larsen, and Brian Bech Nielsen. Dyadic greenŠs functions of thin films: Applications within plasmonic solar cells. *Physical Review B*, 83(8):085419, 2011.

[20] Jerome Mertz. Radiative absorption, fluorescence, and scattering of a classical dipole near a lossless interface: a unified description. *J. Opt. Soc. Am. B*, 17(11):1906–1913, Nov 2000. doi: 10.1364/JOSAB.17.001906. URL `http://josab.osa.org/abstract.cfm?URI=josab-17-11-1906`.

[21] John M. Howie. *Complex Analysis.* Number ISBN:978-1-4471-0027-0. Springer, 1st edition, 2003.

[22] Gregory J Gbur. *Mathematical Methods for Optical Physics and Engineering.* Cambridge University Press, 2011.

[23] Didier Felbacq. Finding resonance poles by means of cauchy integrals. In *2011 13TH INTERNATIONAL CONFERENCE ON TRANSPARENT OPTICAL NETWORKS (ICTON)*, pages 1–4, 2011.

[24] Didier Felbacq. Numerical computation of resonance poles in scattering theory. *Phys. Rev. E*, 64:047702, Sep 2001. doi: 10.1103/PhysRevE. 64.047702. URL `http://link.aps.org/doi/10.1103/PhysRevE.64.047702`.

[25] Lukas Novotny and Bert Hecht. *Principles of nano-optics*. Cambridge university press, 2012.

[26] Walter Gautschi. Gauss-kronrod quadratureŮa survey. *Numerical methods and approximation theory III*, 3:39–66, 1988.

[27] Ruzica Golubovic, Athanasios G Polimeridis, and Juan R Mosig. Efficient algorithms for computing sommerfeld integral tails. *Antennas and Propagation, IEEE Transactions on*, 60(5):2409–2417, 2012.

[28] Mathieu Langlais, Jean-Paul Hugonin, Mondher Besbes, and Philippe Ben-Abdallah. Cooperative electromagnetic interactions between nanoparticles for solar energy harvesting. *Optics express*, 22(103):A577–A588, 2014.

[29] Jesper Jung and Thomas G Pedersen. Polarizability of supported metal nanoparticles: Mehler-fock approach. *Journal of Applied Physics*, 112(6): 064312, 2012.

[30] F. W. J. Olver, D. W. Lozier, R. F. Boisvert, and C. W. Clark, editors. *NIST Handbook of Mathematical Functions*. Cambridge University Press, New York, NY, 2010. National Institute of Standards and Technology.

[31] Craig F. Bohren and Donald R. Huffman. *Absorption and Scattering of Light by Small Particles*, chapter Absorption and Scattering by a Sphere, pages 82–129. Wiley Interscience, 2007.

[32] E. Stefan Kooij, Waqqar Ahmed, Harold J. W. Zandvliet, and Bene Poelsema. Localized plasmons in noble metal nanospheroids. *The Journal of Physical Chemistry C*, 115(21):10321–10332, 2011. doi: 10.1021/jp112085s. URL `http://dx.doi.org/10.1021/jp112085s`.

[33] H.G. Merkus. *Particle Size Measurements: Fundamentals, Practice, Quality*. Particle Technology Series. Springer Netherlands, 2009. ISBN 9781402090165. URL `https://books.google.es/books?id=lLx4GzA-7AUC`.

[34] S V Fomichev and D F Zaretsky. Vlasov theory of mie resonance broadening in metal clusters. *Journal of Physics B: Atomic, Molecular and Optical Physics*, 32(21):5083, 1999. URL `http://stacks.iop.org/0953-4075/32/i=21/a=303`.

[35] J Sancho-Parramon. Surface plasmon resonance broadening of metallic particles in the quasi-static approximation: a numerical study of size confinement and interparticle interaction effects. *Nanotechnology*, 20(23): 235706, 2009. URL `http://stacks.iop.org/0957-4484/20/i=23/a=235706`.

[36] Howard R. Stuart and Dennis G. Hall. Absorption enhancement in silicon on insulator waveguides using metal island films. *Applied Physics Letters*, 69(16):2327–2329, 1996. doi: http://dx.doi.org/10.1063/1.117513. URL `http://scitation.aip.org/content/aip/journal/apl/69/16/10.1063/1.117513`.

[37] Tristan L. Temple and Darren M. Bagnall. Broadband scattering of the solar spectrum by spherical metal nanoparticles. *Progress in Photovoltaics: Research and Applications*, 21(4):600–611, 2013. ISSN 1099-159X. doi: 10.1002/pip.1237. URL `http://dx.doi.org/10.1002/pip.1237`.

Chapter 5

Metal nanoparticles fabrication

5.1 Fabrication techniques: A general overview

The development of nanotechnology is strongly related with the development of fabrication techniques in the "nano" scale. There are plenty of fabrication techniques involving chemical, physical, and even biological methods. Nevertheless, all them can be summarized in two main strategies:

- Reaching the nano-scale starting from the atomic scale. This is usually called the bottom-up strategy. Most chemical processes are bottom-up, as they combine atoms to form small nanostructures, just like making a building by using bricks.

- Reaching the nano-scale starting from a higher scale. This is usually called the top-down strategy. For instance, lithography methods that start with a continuous layer in order to define the nanostructure by removing the excess of material, just like making a sculpture from a stone brick.

5.1.1 Lift-off using e-beam

The electron-beam lithography (from now, e-beam lithography) is a high accuracy top-down fabrication technique consisting in a lithography where the photoresist is attacked (cured) by an electron beam.

Like in other lithographies, the photoresist can become locally easier or harder to develop when it is cured. Thus, some specific areas will be protected or unprotected by the resist once it has been chemically revealed and this allows a patterning of the substrate.

The main advantage for the e-beam lithography is that allows to pattern even nano-structures. This could not be reached with traditional lithographies using Ultra-Violet(UV) radiation because there is a physical limit: The Rayleigh diffraction limit. This limit leads to a limit spot size d_0 at which a light source of wavelength λ can be focused with a lens of diameter D and a focal length f:

$$d_0 = \frac{2f\lambda}{D} \tag{5.1}$$

In a general way, $\frac{2f}{D}$ is hardly 1 for optical lenses and very often beyond 500 for e-beam equipments. This means that if the resolution of the lithography has to be in the "nano" range, no visible light (nor UV light) is suitable. For a 250nm wavelength[1] and assuming $\frac{2f}{D} = 1$, the minimum spot size that could be achieved would be of $d_0 = 250$nm, so in practice the accuracy would be even worse. This accuracy is suitable for micro-fabrication, but not for nanostructures.

In order to reach a 10nm precision structure, with the same assumptions than before, the resist should be attacked by a much higher frequency. This is where the electrons are useful. According to the what was proposed by Broglie and latter confirmed by Davisson and Germer [1], the wavelength of an electron can be expressed as:

$$\lambda_{e^-} = \frac{h}{p} = \frac{h}{\sqrt{2m_0 eU}} \qquad (5.2)$$

where h is the Planck constant,m_0 is the electron mass and eU is the electron energy in eV.

As the electrons are usually accelerated at high voltages and reach velocities comparable with the light velocity c, eq.5.2 could be corrected with some relativistic effects, leading to:

$$\lambda_{e^-} = \frac{h}{\sqrt{2m_0 eU}} \frac{1}{\sqrt{1 + \frac{eU}{2m_0 c^2}}} \qquad (5.3)$$

In fig5.1, some Broglie wavelengths are calculated for typical operation values of eU (in eV) using eq.5.2 and 5.3. It is shown that the relativistic correction is not so important until really high voltages are used (more typical for electronic microscopy than for lithography).

In fig5.1 the resolution will be given by multiplying the broglie wavelength by the $2f/D$ factor, as shown in eq.5.1. Several conclusion can be obtained from that figure. First, that the energy of the electron has to be high enough to increase the resolution. However, this is not always true because the behaviour is not linear. Many e-beam lithography systems work at 20-30keV as this seems to be the optimum energy.

It should be noted that the resolution obtained theoretically cannot be achieved in practice.

- From the practical point of view, the lithography is done on a chemical resist whose molecules are bigger than the theoretical resolution. Therefore, in most cases the resolution will not be limited by the diffraction limit but for the resist molecule that is broken. In this sense, the choice

---

[1]This correspond to the Ultra-Violet C as classified by the ISO 21348: Definitios of Solar Irradiance Spectral Categories.
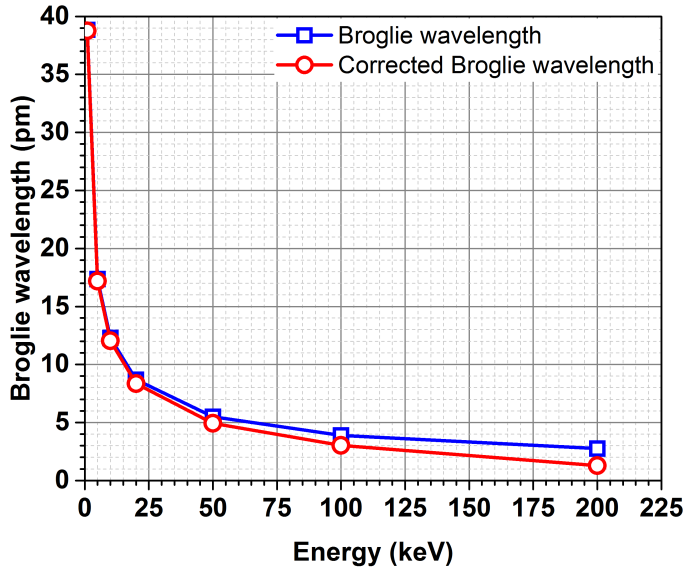
Figure 5.1: Theoretical Broglie wavelength for an electron at different energies for $2f/D = 1$.

of the resist has a huge impact. The use of PMMA is a good choice because it is a well-known polymer that can be polimerysed in only a few molecules, leading to higher resolutions.

- The incident beam is not produced by a single electron. In fact, there is a gaussian beam with some dispersion.

- The energy of the electron can affect the resist not only at the theoretical incident point, but in an area that will depend on the energy of the electrons, the sensitivity of the resist and to the applied radiation dose. Therefore, different resolutions can be obtained from the same resist and electron energy by changing the radiation dose, or with different resists keeping the same electron energy and dose.

- There is a scattering of the electrons that will also reduce the resolution of the theoretical electron beam. This scattering will be dependent on the materials involved, the energy and the thickness of the resist.

- There is a chemical effect in the structure of the resist when the e-beam incides on it. This effect may produce diffusion of compounds and therefore not only the incident area can be modified.

- Once the resist is attacked, and related with the previous point, the revealing process has its own limitations: The developper will remove some of the molecules but this has not a perfect selectivity. Again, the size of the resist molecules has its influence.

For this thesis, some preliminary samples for metal nanoparticles have been made by e-beam lithography. In order to do that a PMMA resist is put by spin coating on a glass substrate. Then, the e-beam lithography is made. The PMMA is a positive resist[2] Once the resist patterning is done, a metallic layer is evaporated (see section 5.3), both filling the voids and on the resist. The final step is a resist removal with a selective etching dilution that does not affect the metal. This strategy, called lift-off, leaves only the metallic patterning on the substrate . A summary of this can be found in fig.5.2
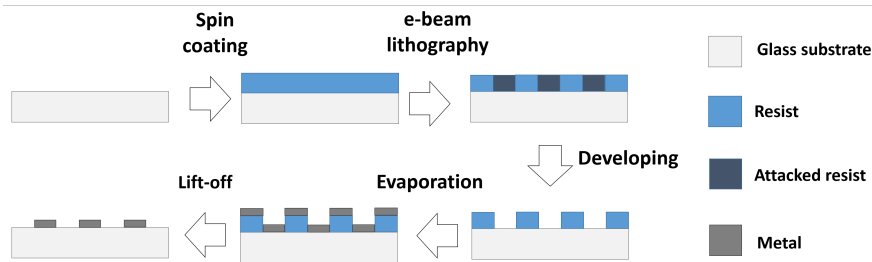
Figure 5.2: Lift-off process in order to fabricate regular arrays of metal nano-particles.

In a general way, optimised structures can reach reasonable resolutions of about 20-30nm. For large areas (such like in a solar cell) the e-beam is not economically feasable both in price and in time.

E-beam lithography is valuable when regular or semirandom arrays are wanted. But it takes a lot of time and the real resolution is not really good for small particles. Further studies could be done to improve this process. However, in the scope of this thesis, the main effort will be done on the self-aggregation process.

5.1.2   Self-aggregation method

The self-aggregation technique includes two different approaches:

---

[2]A positive resist is a resist whose structure is weakened selectively in the areas where the radiation exposure is done. Therefore it will be removed during the developing process only where attacked. They are complementary to negative resists, that are chemically crosslinked during radiation exposure and thus remain selectively after developing only where attacked.

(a) Template

(b) Experimental
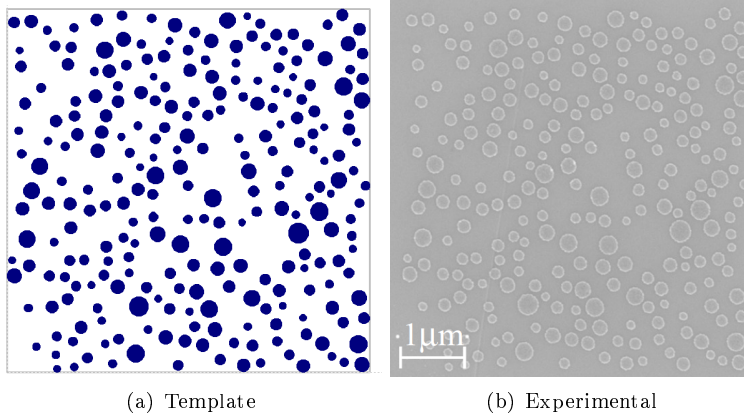
Figure 5.3: Comparison between the design template and the resulting random metal nanoparticle distribution using e-beam lithography.

- Growing nanoparticles in a liquid from micelle-stabilised precursors that grow by mass diffusion. This is a bottom-up method.

- Obtaining nanoparticles as islands on a substrate from the thermal induced self-aggregation of a continuous thin film. This could be assumed to be a top-down method. It can also be called *dewetting*.

Both methods are commonly used and lots of studies have been done to understand the thermodynamics and modelling the self-aggregation process. The most relevant and suitable references for this thesis are those studies related to epitaxial self-aggregation [2, 3, 4]. Let us make a brief summary of those studies.

An epitaxial thin film is always stressed because there is a mismatch between the substrate and the deposited film lattices. This stress can be related with a higher free Gibbs energy so, once the film has been deposited, some structural changes can occur towards a new thermodynamically lower energy state. In a general way:

1. The difference in the mechanical properties (stiffness) of the substrate and the deposited thin film induces a deformation of the theoretical flat thin film into a waved form with a critical wavelength[5] (Fig.5.4). In general, the critical wavelength will be longer for stiffer substrates and shorter for softer substrates.

2. The wetting interaction between the film and the substrate becomes more significant as the thickness of the deposited film is reduced. Thus, for nanometric thin films the wetting effect can be very important.

(a) $\lambda = \frac{D}{0} \to \infty$ (b) $\lambda = \frac{D}{2}$ (c) $\lambda = \frac{D}{3}$
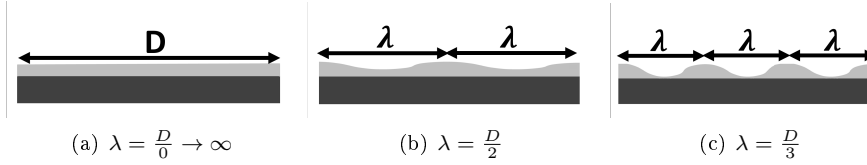
Figure 5.4: Wavelength approach to study the deformation of the film due to stress at the interface.

Under certain conditions, in order to reduce the free Gibbs energy, the structural changes lead not only to a deformation of the thin film towards a wavy surface (fig.5.4) but also to an island-type structure. In the context of this thesis, this leads to self-aggregated metal nanoparticles[6].

A common approach to model this phenomena is to assume that the self-aggregation is controlled only by the elastic strain energy U_E, the surface energy density γ and the wetting energy or potential U_W. Then, a chemical potential $\mu(x, y, t)$ for the film surface with respect to a reference plane, can be defined [7] as:

$$\mu(x, y, t) = \Omega \left(U_E - \gamma \cdot \kappa + U_W \right) \sqrt{1 + h_\alpha h_\alpha} \tag{5.4}$$

where Ω is the atomic volume, κ is the surface curvature, h_α is the gradient of the surface morphology $h_\alpha = \frac{\partial h(x,y,t)}{\partial \alpha}$ (with $\alpha = \{x, y\}$ and $h(x, y, t)$ the position dependent film thickness) and κ is the surface curvature[3].

This position dependent chemical potential $\mu(x, y, t)$ can be related with the mass diffusion J_D that reorganises the atoms while looking for thermodynamically more stable structures:

$$J_D = M \cdot \begin{pmatrix} J_x \\ J_y \end{pmatrix} = M \cdot \begin{pmatrix} \frac{\partial \mu(x,y,t)}{\partial x} \\ \frac{\partial \mu(x,y,t)}{\partial y} \end{pmatrix} \tag{5.5}$$

where M is the mobility of the surface atoms.

---

[3] For all the presented parameters there are some interesting expressions in [7].

From eq.5.5 and assuming mass conservation, (so the divergence of the global mass flux has to be zero), an expression is found for the time evolution of the local height $h(x, y)$ in the film:

$$\frac{\partial h(x, y)}{\partial t} = \Omega^2 M \sum_{i,j,k,l} \frac{\partial^2}{\partial i \partial j} \left[(U_E - \gamma \cdot \kappa + U_W) \sqrt{1 + h_k h_l} \right] \qquad (5.6)$$

where $\{i, j, k, l\} = \{x, y\}$ and the gradients of the surface morphology $h_{k,l}$ are defined as in eq.5.4. This local height evolution is what would define the wavy surface in fig.5.4.

Different treatments can be done from eq.5.6 depending on the expressions for the surface energy density γ and the wetting potential U_W. For instance, using a "transition-layer" model [8]:

$$\gamma(h) = \frac{1}{2} (\gamma_s + \gamma_t) + \frac{1}{\pi} (\gamma_s + \gamma_t) \arctan\left(\frac{h}{b}\right) \qquad (5.7)$$

the expression for the wetting potential becomes:

$$U_W = \frac{\gamma_t - \gamma_s}{\sqrt{1 + h_\alpha h_\alpha}} \frac{b}{\pi(b^2 + h^2)} \qquad (5.8)$$

in both eq.5.7 and eq.5.8 the subscripts "s" and "t" refer to the substrate and the thin-film materials respectively, b is a "shape" parameter[4] and, once more, h_α are the gradients of the surface morphology.

A critical thickness h_c can be defined with this model to distinguish in the thickness range where the film is stable or not.

$$h_c = \frac{\gamma_t}{\sigma_0^2} \frac{E_s}{1 - \nu_s^2} \sqrt[3]{\frac{b(\gamma_s - \gamma_t)\sigma_0^2(1 - \nu_s^2)}{\pi E_s \gamma_t^2}} \qquad (5.9)$$

This h_c concept is a common approach to classify different growing regimes in epitaxial growth. In fact, it is not always easy to separate both phenomena as the self-aggregation can occur at the same time that the epitaxy, leading to three possible epitaxial growing methods from vapour-phase:

- If the film material has lower surface energy than the substrate ($\gamma_t < \gamma_s$)and it wets it (ec.5.8 leads to $U_W < 0$). Then a positive critical thickness $h_c > 0$ can be defined[5]. Thus, two different growing methods arise from here:

---

[4]This parameter is related with the "transition" shape in height from from γ_s to γ_t and makes it sharper or smoother. Moreover, it is related with the value of the critical thickness h_c.

[5]This critical thickness h_c is proportional to the cubic root of the difference of surface energies: $h_c \propto \sqrt[3]{\gamma_s - \gamma_f}$

- – The Frank-Van der Merwe growth mode [9] while the thickness h is $h < h_c$. In this case, the growth is flat and stable.

- – The Stranski-Krastanov growth mode [10] from $h > h_c$. In this case, the growth becomes unstable so the new atoms added to the layer quickly move to form clusters and the growth changes from a 2D model to a 3D model.

- If the film material has lower surface energy than the substrate ($\gamma_s < \gamma_t$) then the critical thickness definition h_c lead to a negative value. This implies that from the beginning of the growing process the atoms do not form any continuous layer but grow directly on clusters until they become so big that they coalesce onto a continuous layer. This growth process is known as the Volmer-Weber mode[11].
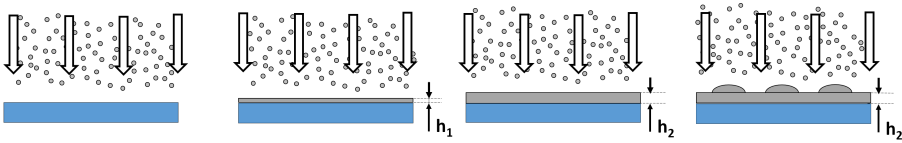
Figure 5.5: Frank-Van der Merwe growth mode. As the thickness increases, the Stranski-Krastanov growth mode is reached.
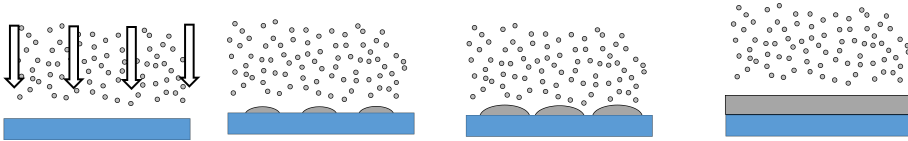
Figure 5.6: Volmer-Weber growth mode.

A key point in this thesis is that, unless the opposite is specified, the self-aggregation is going to be understood only as a thermally induced process that allows/accelerates the changes in the initial "as-deposited" structure of metallic thin-films. Thus, the growing details of that thin-films are neglected. This induced/accelerated process comes from the combination of two effects:

- As the expansion thermal coefficient α of the substrate and the film are different, an additional stress will be produced, regardless if the substrate has a similar crystalline lattice than the film or even if the substrate amorphous. This thermal stress will be proportional to $\epsilon_T = (\alpha_t - \alpha_s)\Delta T$.

- The mobility M of the diffusion equation (eq.5.5) is increased with temperature, leading to a faster diffusion process.

When the metallic thin film is deposited on an amorphous material, there is not a substrate lattice, so even if some minor stresses could be found locally (on a textured substrate, for instance), the main stress contribution in eq.5.4 will be the thermal stress.

As shown here, the self-aggretation is a complex process where several parameters are involved. However, the most significant can be resumed as:

- The thin-film deposited material.

- The substrate material.

- The temperature during the self-aggregation.

- The time left for the diffusion that leads to the self-aggregation.

- The thickness of the initial thin film.

From this point of view, some metals like Ag are commonly used for self-aggregation whereas other metals like Al are not suitable for this purpose (as its wetting properties make difficult to obtain proper and well-defined nanoparticles).

5.2 Self-aggregated nanoparticles

As a first approach, 20 nm of Ag are deposited on a ITO-covered glass. The ITO is useful in order to the later SEM characterisation in order to avoid the surface charge phenomena during the measurement that lead to visual artifacts. With a chosen thickness and substrate, different temperatures are studied. The resulting particles are shown in fig.5.8.

Before starting with the analysis of the arrays, it is useful to make an ad-hoc definition when referring at some of the nanoparticles. Thus, it is possible to find:

- *Coalesced* **particles**. The *coalesced* particles (as seen in fig.5.7a) are those which segregate incompletely compared to the average segregated nanoparticle size. That is, they are particles that result from incomplete segregation of a larger structure into separate smaller particles, or which have aggregated into structures larger than the average.

- *Isolated* **particles**. The *isolated* particles (fig.5.7b) are those particles arising from small areas whose material do not collapse with the bigger

surrounding particles. This might be produced by surface inhomogeneities as those *isolated* particles are always much smaller than the general trend. Moreover, sometimes it is not easy to distinguish between real *isolated* particles and image artifacts during measurements

(a) *Coalesced* nanoparticle   (b) *Isolated* nanoparticle
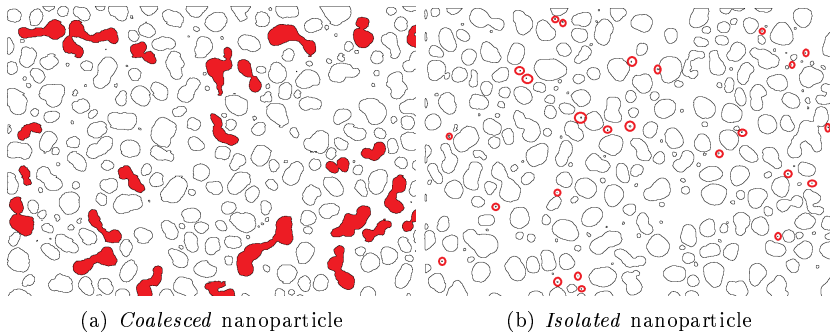
Figure 5.7: Example of the as-defined *coalesced* and *isolated* nanoparticles as the two main limits in the independent nanoparticle formation.

In [12] a very interesting work has been done to study experimentally the different behaviour of the resulting nanoparticle array from the thickness and the temperature. A structural-phase diagram is shown where the four behaviours that have been found in this thesis are included, dealing with coalesced particles, isolated particles, etc.

From the size and shape analysis of the images shown in fig. 5.8, it is possible to obtain an average diameter and a circularity for each individual particle found. The results of this are in fig.5.9 and fig.5.10. One of the first conclusions that can be obtained from these data is that the size distribution does not fit a gaussian distribution as there are many data outside the box-and-whisker limits[6]. This is due mainly to the presence of isolated and coalesced nanoparticles. As the nanoparticles do not fit properly a gaussian distribution, the average size or circularity is not a real representative value for the array. In these cases, the median is usually used as a better parameter to represent the whole structure.

---

[6]In this thesis, the maximum length of the whiskers will always be defined as 1.5 times the range between the first and third quartile, that is, 1.5 times the difference between the data corresponding to the 75% and the 25% position in the ordered values

(a) Original 300C   (b) Binary 300C   (c) Particle finding 300C

(d) Original 400C   (e) Binary 400C   (f) Particle finding 400C

(g) Original 500C   (h) Binary 500C   (i) Particle finding 500C

(j) Original 600C   (k) Binary 600C   (l) Particle finding 600C
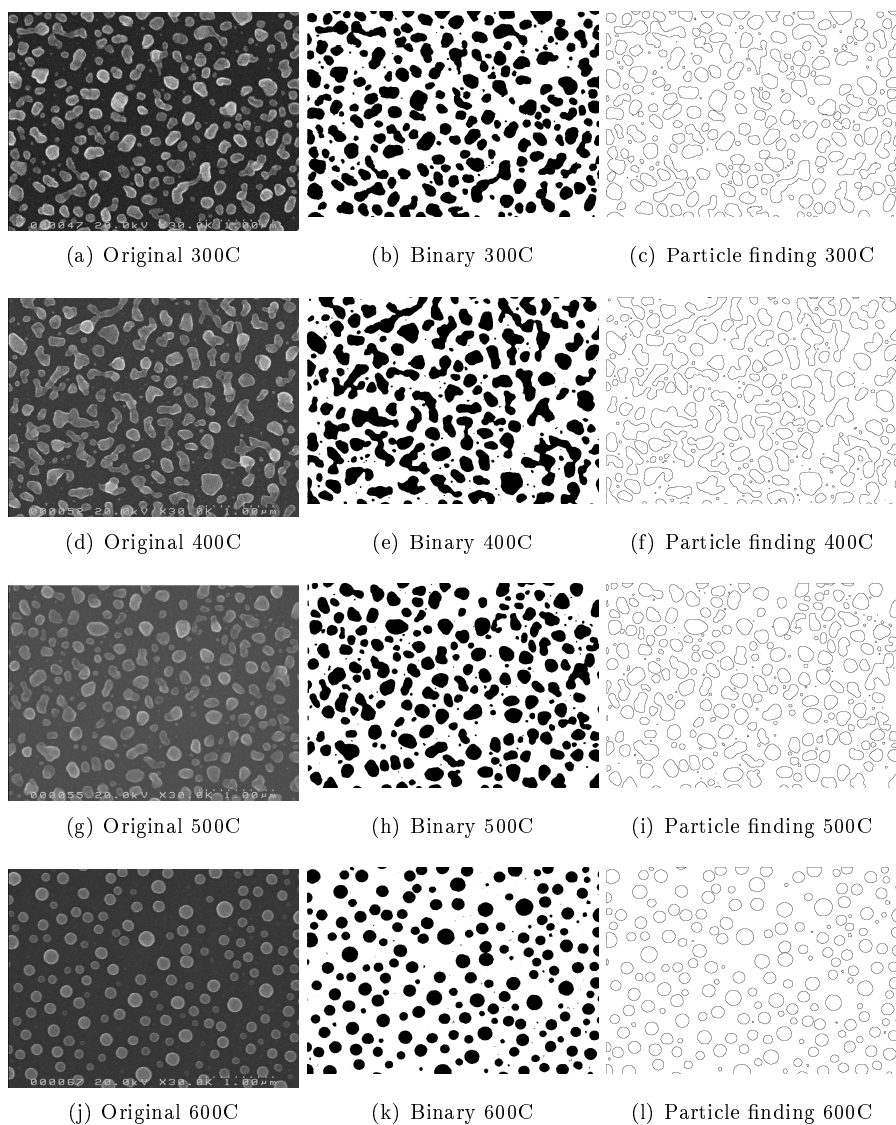
Figure 5.8: Resulting nanoparticles from the self-aggregation of 20nm of Ag on a ITO covered glass at different temperatures during 60min in inert gas. The corresponding image treatment is also shown. All SEM images are 4000nm x 3000nm

Equivalent diameter Deq

Time	60'	60'	60'	60'
Thickness	20nm	20nm	20nm	20nm
Temperature	300C	400C	500C	600C
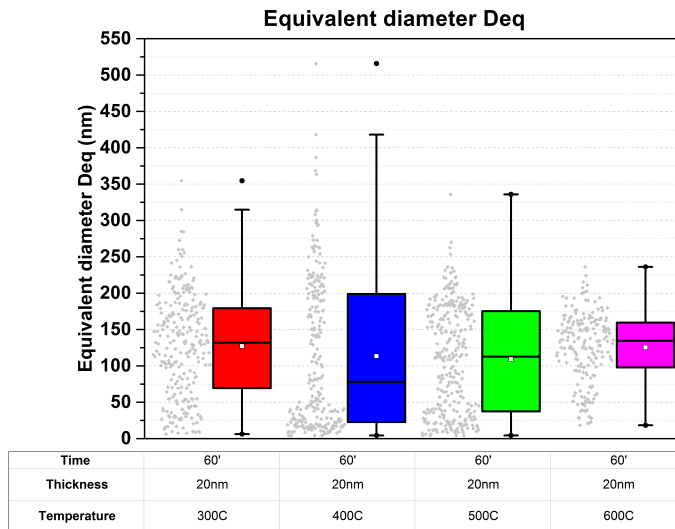
Figure 5.9: Size analysis the nanoparticle array resulting from 20nm of Ag on a ITO covered glass at different temperatures during 60min in inert gas: Equivalent diameter

Circularity

Time	60'	60'	60'	60'
Thickness	20nm	20nm	20nm	20nm
Temperature	300C	400C	500C	600C
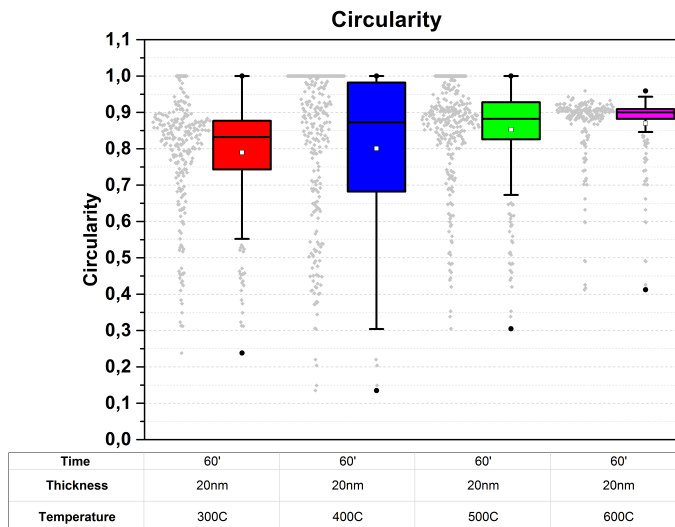
Figure 5.10: Size analysis the nanoparticle array resulting from 20nm of Ag on a ITO covered glass at different temperatures during 60min in inert gas: Circularity
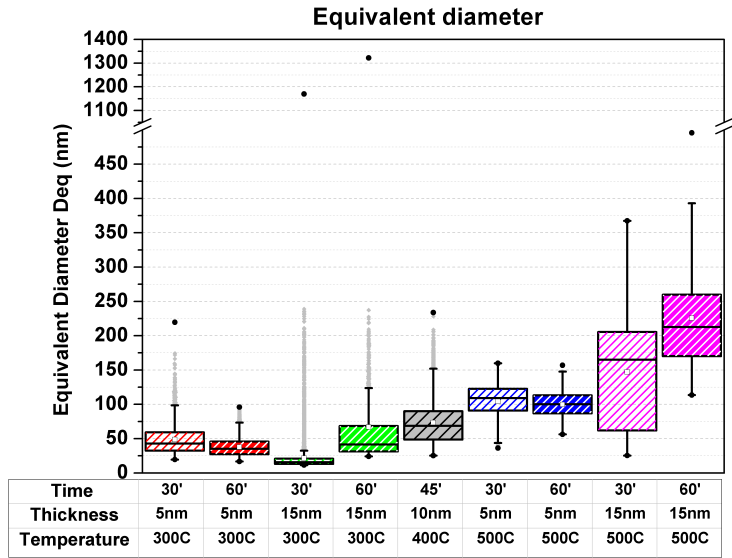
Figure 5.11: Equivalent diameter for the resulting nanoparticles obtained under different conditions of annealing time, Ag precursor thickness and annealing temperature using a glass covered with ITO as substrate.
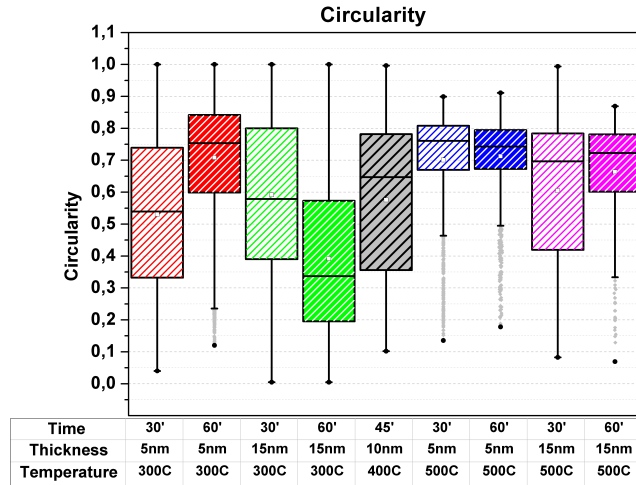
Figure 5.12: Circularity for the resulting nanoparticles obtained under different conditions of annealing time, Ag precursor thickness and annealing temperature using a glass covered with ITO as substrate.

The main trend that can be obtained with these data is that in order to have circular nanoparticles, the temperature has to be reached. The trend is quite clear: As the temperature has been increased from 300C to 600C the median value of the circularity is increased. However, the dispersion in shape does not follow so clearly the same trend. In fact, as the temperature increases, the kinetics processes (mainly the diffusion) are enhanced but the thermodinamical features (such as the surface energy) are much more difficult to predict.

In Tan et al [13] is that they achieve an interesting array of Ag nanoparticles that show good scattering properties (high scattering and low parasitic absorption losses) with big (100nm of radius) and disperse (coverage around 16%) particles. This has been done at temperatures beyond 400C and evaporation ratios under 1Å/s. The trend observed in this thesis also points towards the benefits of using high temperatures combined with increasing thickness precursor layers in order to have big round particles with a lower coverage. However, the vacuum level has not been reached due to the limitations in the evaporator system (see section 5.3) and the temperature had to be limited to 300C in the final integrated devices in order to avoid a degradation of the substrate (the solar cell). In this thesis, an approach for estimating the average distance between
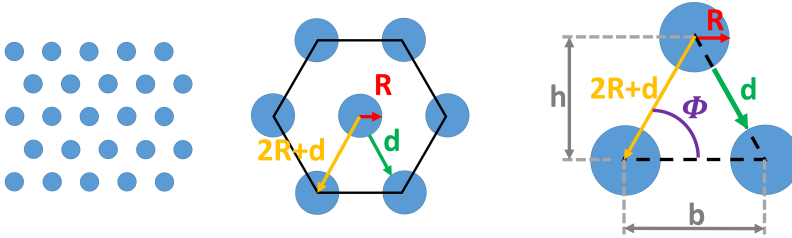
Figure 5.13: Regular distributed NPs and unit cell for the calculation of the average distance d separation between nanoparticles as well as the center to center distance $2R + d$.

particles is done by an assumption of equally spaced particles (fig.5.13). From this theoretical distribution, the separation between nanoparticles d can be calculated (eq.5.10), as well as the center to center distance $2R + d$, leading to the following expressions:

$$F = \frac{A_{NPs}}{A_{global}} = \frac{3 \cdot \frac{1}{6} A_{NP}}{\frac{1}{2} bh} = \frac{\pi R^2}{(2R+d)^2 \sin \phi} \longrightarrow d = R \left(\sqrt{\frac{\pi}{F \sin \phi}} - 2 \right)$$

(5.10)

The results obtained with eq.5.10 are incongruent showing that this approach is too far from reality. However, in [12] the dependence of the mean surface coverage size on the film thickness is found to follow a clear trend, independently on the temperature.

5.3 Limits of the evaporator

One of the main limitations in controlling properly the evaporation process is related with the evaporation itself. In fig.5.14 it is shown a schema of the it that will help to understand those limitations.

The evaporator that has been used is a high-vaccum e-beam metal evaporator. This means that it works in a vacumm around 10^{-8}bar, and that uses an electron cannon to heat the metal that has to be evaporated. This implies mainly two things:

- First, that the e-beam strategy makes the physical contact between the metal deposit and the cooling system very important when controlling the temperature of the metal. This temperature will be mainly defined by the incident e-beam source (very easy to control) and the heat dissipation by the cooling system (sometimes unstable when the metal source is replaced). Differences in the heat input and dissipation ratios source leads to different evaporation ratios for the same input power. From this point of view, a joule effect evaporation system would be preferred, as the thermal control is much better.

- Second, and related with the previous point, the evaporation ratio will also be controlled by the vaccum in the chamber. Therefore, the vaccuum achieved before starting with the e-beam heating has been fixed in $5 \cdot 10^{-8}$ bar. This value has been chosen in terms of thermodinamical aspects (for evaporating a metal a high vacuum value is needed) but also for a practical one: From 10^{-7} bar the vacuum ratio starts to be very low, and in order to reach 10^{-8} bar or less a lot of time is needed.

Moreover, there are some other aspects that should be remarked to understand the limitations on the reproducibility of the samples that are not directly related with the e-beam technology.

- Even if the whole surface of the evaporator is cooled, there is no control on which is the temperature in the substrate when the evaporation takes place. As explained previously in section 5.1.2, the temperature can be a key parameter to control. This is an uncontrolled parameter that should be studied in the future.

- The evaporation ratio is measured using a crystal quartz. The crystal is forced to vibrate and the resonance vibration frequency is shifted when it has more material evaporated on it. Therefore, the evaporation ratio measurement becomes each time less accurate, as the shift in the crystal resonance is less accurate. From this point of view, there is a parameter given by the evaporation called "crystal health". When crystal health comes to 90% the measurements are less accurate and when it comes to 80%, the crystal must be changed. Attention has been paid to this because the in some cases, the thickness evaporated are very thin and small errors lead to quite different results.

- Related with the previous point, the evaporating process is also controlled by a physical shutter that avoids the evaporated material to reach the substrate until the metal substrate is heating. This avoids to have a transient process because the shutter would not open until the temperature on the sample holder has been stabilised, as well as the evaporation ratio. However, for small thicknesses to be evaporated, transient conditions are difficult to reach because the typical evaporation ratios are between 5 and 7$\mathrm{\AA}/s$.

For further improvements, a study on the best evaporation conditions for high quality plasmonic films has been published very recently[14]. Among other considerations, a much higher vaccum is recommended, so several changes should be applied to the evaporator used in this thesis. A higher vacuum will reduce the temperature during evaporation and therefore some of the issues presented in this thesis will be minimised.

5.4 Degradation of Ag Nanoparticles

It has been verified during this thesis that the optical behaviour of Ag nanoparticles is not constant in time. This time-dependent behaviour is mainly due to the interaction between the nanoparticles and the surrounding air and, therefore, can be avoided with a protecting cap. This has already been reported by some authors [15, 16], as well as the effectiveness of these protective caps [17], obtained by Plasma Enhanced Chemical Vapor Deposition (PECVD) or Atomic Layer Deposition (ALD). In this thesis, none of this methods are suitable in order to avoid further metallic contamination issues in the chamber. Therefore, an alternative way to encapsulate and protect the NPs has to be found.

An alternative to the PECVD SiO_x deposition process is found in a flowable silicon oxide resist that can be deposited by a spin-coating process. This resist is called Hidrogen Silsesquioxane (HSQ) and it is dilluted in methyl isopropyl ketone (MIBK). The chemical structure of both is shown in fig.5.15

(a) Heating

(b) Evaporating once stabilised
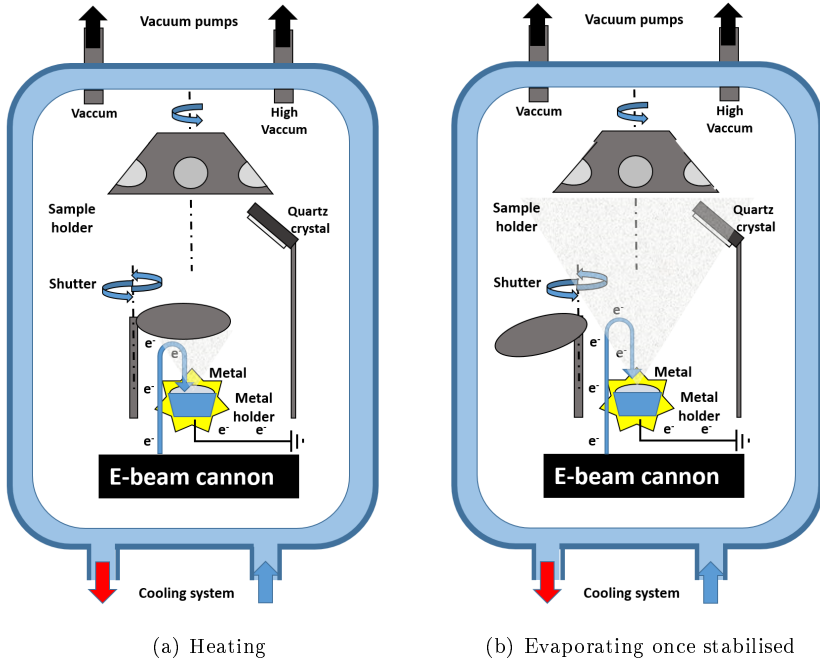
Figure 5.14: High vaccuum e-beam metal evaporator schema. In a) the e-beam is heating the metal while the shutter is closed to avoid undesirable evaporation on the sample. Once the system is ready, the shutter opens and the evaporated metal goes to both the sample and the thickness sensor.

In fig.5.15a it is shown that the Silicon silsesquioxane has a $RSiO_{1.5}$ composition. The monomer correspond to R=H and the resist corresponds to a bonding with other monomers.

The HSQ is a resist commonly used for e-beam lithography. Thus, it is quite expensive, so for industrial purposes would not be suitable (a PECVD reactor dedicated for metal containing samples would be more suitable instead). In any case, for this thesis is an interesting choice to avoid the metallic contamination in the chambers of the PECVD reactor.

The HSQ is very sensitive to the temperature and to gelation. Therefore, any glass operating tools such as pipers must be avoided when manipulating the resist. Moreover, small quantities of the resist have to be taken when it is still cool in order not to spoil the rest of the solution and then wait until room temperature before the spin-coating process to control the viscosity.

(a) HSQ generic structure   (b) MIBK generic structure
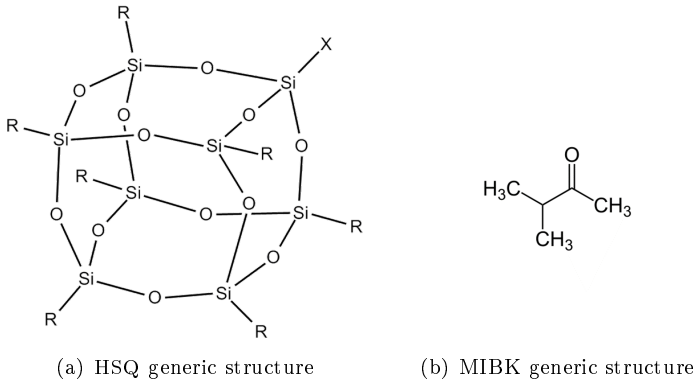
Figure 5.15: Chemical strucure of the resist and the solvent used for making SiO_x layers without a PECVD reactor.

As any resist, the spin coating conditions have to be studied in order to control the thickness and the homogeneity of the coatings. The main parameters in the process are the viscosity and the spin velocity (in rpm). The second one is easily controlled using the spin coater but for the first one is more difficult to control. The main variable that controls the viscosity is the dillution degree (D) with MIBK, defined:

$$D = a : b = a \; ml \quad HSQ \quad : \quad b \; ml \quad MIBK \tag{5.11}$$

All the deposits are done in a cleanroom with a controlled atmosphere at T=21.5C and relative humidity at 45%. With these conditions, the obtained thickness is summarised in fig.5.16.

In general, the homogeneity is much better for high spin velocities, so this will be taken into account when choosing different options for obtaining the same thickness.

As any other spin-coated resist, there is always a heating process to remove any solvent. For MIBK this can be done at about 150C.

In order to make the HSQ coverings even more similar to a real SiO_x layer, the structure can be oxydised and collapsed. This increases the density of the structure and, therefore, the refractive index. Two possibilities are available: Using an oxygen plasma or using an oven step at around 1000C. The first is difficult to control and it is risky if there is an array of NPs beyond the structure. The second one it is simply not feasable as such a high temperature step will completely change the array of nanoparticles.

Thus, an intermediate solution has been used and a thermal step has been done in the same conditions that during the nanoparticles formation. This
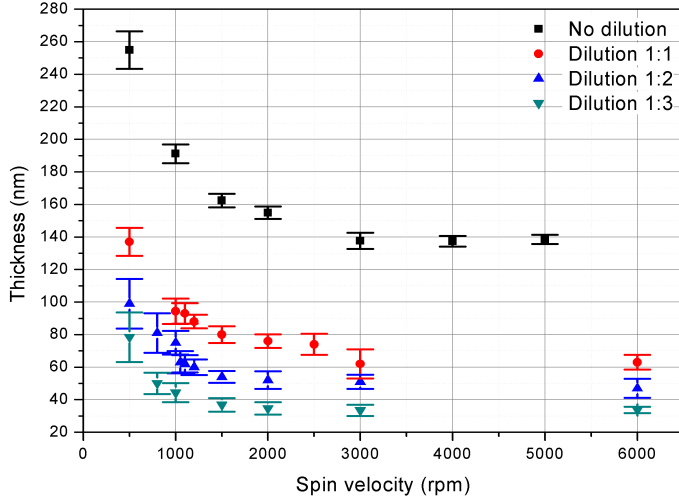
Figure 5.16: Thickness of the HSQ layers obtained at different dilutions and spin velocities.

will completely remove any remaining solvent and would help to collapse the structure, without changing in practice the nanoparticle distribution.

In fig.5.17 some measurements are showed.

(a) Thickness evolution

(b) Refractive index evolution
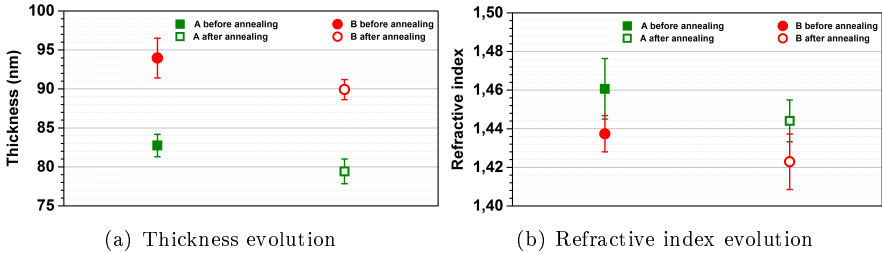
Figure 5.17: Thickness and refractive index evolution before and after the baking step to remove any remaining solvent from the HSQ spin-coated resist.

It can be seen that as expected the average thickness decreases. This may suggest a collapse of the structure, but also the refractive index is slightly reduced. Therefore, the density seems to be constant or slightly reduced. In this sense, only the solvent loss is produced. In any case, even if the structure does not completely collapse, the resulting refractive index of the layers is close to the 1.47 of the SiO_x obtained by PECVD.

In fig.5.18 it is possible to see that the temperature during self-aggregation does not affect the degradation process whereas when using an HSQ covering, the undesirable time evolution on the optical response of the Ag NPs is highly delayed (even if not completely removed). This evolution is seen as the intensity and positon of the reflection and transmission maxima and minima.

(a) As deposited Ag

(b) Annealed 1h at 200C

(c) Annealed 2h at 200C

(d) Annealed 1h at 200C and 1h at 200C after HSQ covering
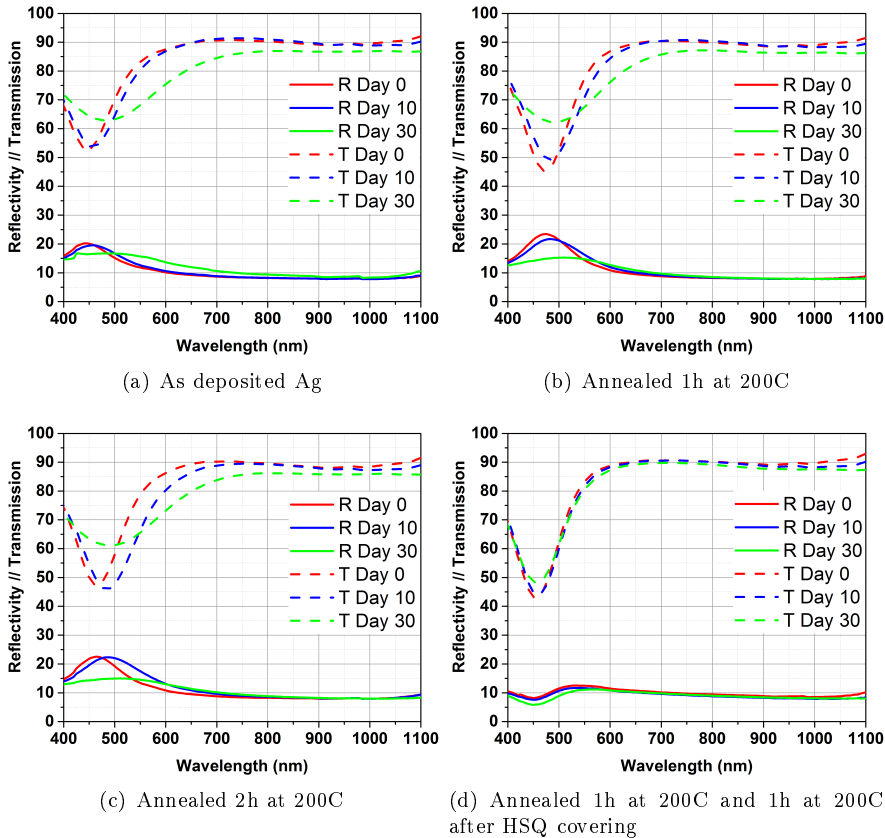
Figure 5.18: Aging effect on the optical measurements for a 3nm precursor layer sample in different fabrication steps, with and without a protective covering.

A more precise quantification of the time evolution in the peak/valley spectra with time with and without an HSQ protective layer can be found in fig.5.19 where the peak properties (position and weight at half height) is quantified. It can be seen that the use of HSQ keeps those values unchanged in time.

(a) Reflectivity peak position

(b) Transmission peak position

(c) Reflectivity peak width at half-height

(d) Transmission valley width at half-height
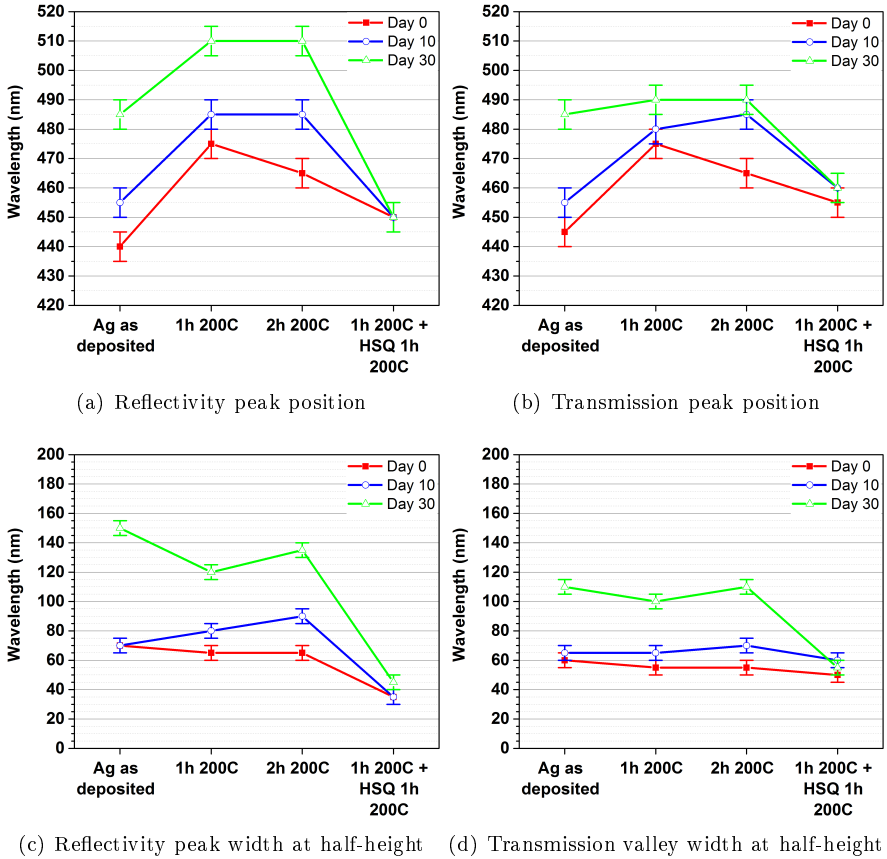
Figure 5.19: Aging effect on the reflection and transmission peak/valley and its half-height width for a 3nm precursor layer sample in different fabrication steps, with and without a protective covering.

Bibliography

[1] C.J. Davisson. The diffraction of electrons by a crystal of nickel. *Bell System Technical Journal, The*, 7(1):90–105, Jan 1928. ISSN 0005-8580. doi: 10.1002/j.1538-7305.1928.tb00342.x.

[2] B. J. Spencer, S. H. Davis, and P. W. Voorhees. Morphological instability in epitaxially strained dislocation-free solid films: Nonlinear evolution. *Phys. Rev. B*, 47:9760–9777, Apr 1993. doi: 10.1103/PhysRevB.47.9760.

[3] A. A. Golovin, S. H. Davis, and P. W. Voorhees. Self-organization of quantum dots in epitaxially strained solid films. *Phys. Rev. E*, 68:056203, Nov 2003. doi: 10.1103/PhysRevE.68.056203.

[4] W. T. Tekalign and B. J. Spencer. Evolution equation for a thin epitaxial film on a deformable substrate. *Journal of Applied Physics*, 96(10):5505–5512, 2004. doi: http://dx.doi.org/10.1063/1.1766084.

[5] Y. W. Zhang. Surface stability and evolution of biaxially strained epitaxial thin films. *Applied Physics Letters*, 87(12):121916, 2005. doi: http://dx.doi.org/10.1063/1.2053367.

[6] JP Connolly, C David, P Rodriguez, A Griol, P Welti, L Belliéres, J Ayucar, J Hurtado, R Lopez, G Sanchez, et al. Analysis of plasmonic nanoparticle fabrication techniques for efficient integration in photovoltaic devices. In *Proceedings of the 25th European Photovoltaic Solar Energy Conference and Exhibition/5th World Conference on Photovoltaic Energy Conversion, Valencia, Spain*, pages 6–10, 2010.

[7] Yaoyu Pang and Rui Huang. Nonlinear effects of stress and wetting on surface evolution of epitaxial thin films. *Physical Review B*, 74:075413–1, 075413–11, 2006. doi: 10.1103/PhysRevB.74.075413.

[8] B. J. Spencer. Asymptotic derivation of the glued-wetting-layer model and contact-angle condition for stranski-krastanow islands. *Phys. Rev. B*, 59:2011–2017, Jan 1999. doi: 10.1103/PhysRevB.59.2011.

[9] Jan H. van der Merwe. Misfit dislocation generation in epitaxial layers. *Critical Reviews in Solid State and Materials Sciences*, 17(3):187–209, 1991. doi: 10.1080/10408439108243751.

[10] D. J. Eaglesham and M. Cerullo. Dislocation-free stranski-krastanow growth of ge on si(100). *Phys. Rev. Lett.*, 64:1943–1946, Apr 1990. doi: 10.1103/PhysRevLett.64.1943.

[11] J. A. Floro, S. J. Hearne, J. A. Hunter, P. Kotula, E. Chason, S. C. Seel, and C. V. Thompson. The dynamic competition between stress generation and relaxation mechanisms during coalescence of volmer-weber thin films. *Journal of Applied Physics*, 89(9):4886–4897, 2001. doi: http://dx.doi.org/10.1063/1.1352563.

[12] Seweryn Morawiec, Manuel J Mendes, Salvatore Mirabella, Francesca Simone, Francesco Priolo, and Isodiana Crupi. Self-assembled silver nanoparticles for plasmon-enhanced solar cell back reflectors: correlation between structural and optical properties. *Nanotechnology*, 24(26):265601, 2013. URL http://stacks.iop.org/0957-4484/24/i=26/a=265601.

[13] Hairen Tan, Rudi Santbergen, Arno H. M. Smets, and Miro Zeman. Plasmonic light trapping in thin-film silicon solar cells with improved self-assembled silver nanoparticles. *Nano Letters*, 12(8):4070–4076, 2012. doi: 10.1021/nl301521z. URL http://dx.doi.org/10.1021/nl301521z. PMID: 22738234.

[14] Kevin M. McPeak, Sriharsha V. Jayanti, Stephan J. P. Kress, Stefan Meyer, Stelio Iotti, Aurelio Rossinelli, and David J. Norris. Plasmonic films can easily be better: Rules and recipes. *ACS Photonics*, 2(3):326–333, 2015. doi: 10.1021/ph5004237. URL http://dx.doi.org/10.1021/ph5004237. PMID: 25950012.

[15] T W H Oates, M Losurdo, S Noda, and K Hinrichs. The effect of atmospheric tarnishing on the optical and structural properties of silver nanoparticles. *Journal of Physics D: Applied Physics*, 46(14):145308, 2013. URL http://stacks.iop.org/0022-3727/46/i=14/a=145308.

[16] Wei Cao and Hani E. Elsayed-Ali. Stability of ag nanoparticles fabricated by electron beam lithography. *Materials Letters*, 63(26):2263 – 2266, 2009. ISSN 0167-577X. doi: http://dx.doi.org/10.1016/j.matlet.2009.07.052. URL http://www.sciencedirect.com/science/article/pii/S0167577X09005692.

[17] G. Baraldi, M. Carrada, J. Toudert, F. J. Ferrer, A. Arbouet, V. Paillard, and J. Gonzalo. Preventing the degradation of ag nanoparticles using an ultrathin a-al2o3 layer as protective barrier. *The Journal of Physical Chemistry C*, 117(18):9431–9439, 2013. doi: 10.1021/jp401421m. URL http://dx.doi.org/10.1021/jp401421m.

Chapter 6

NP integration on solar cells

6.1 Solar Cell Characterisation

The setup shown in fig.6.1 is intented to obtain the electrical characteristic of a solar cell, as introduced in section 2.5 and in fig.2.18. The setup uses a solar simulator (a Xe lamp combined with a NIR source as a tungsten bulb) with an emission spectra very similar to the standard $AM_{1.5G}$ spectrum. That source illuminates the sample at the standard of 1 sun of irradiance ($1000W/m^2$) and a bias source forces the solar cell to move its voltage working point whereas the resulting current is measured. The design of the simulator shown in fig.6.1 and the global setup is designed to fit the Standard Test Condicions (STC).
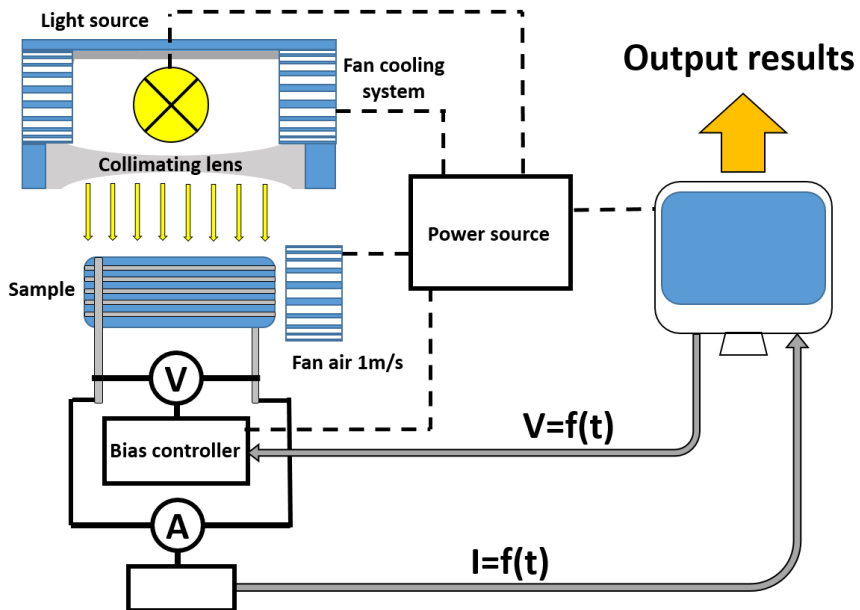
Figure 6.1: Current-Voltage measuring system setup diagram.

From this measurements, different significant values can be obtained:

- The short circuit current $I_{sc}[mA]$ of the sample. This value corresponds to the un-biased current (at $V = 0[mV]$). Therefore, it is the maximum possible current value that can be achieved in the solar cell. At this point, however, the solar cell has no power output as the current would correspond to a zero bias V. Notice that the short-circuit current is an extensive value that depends on the surface. Thus, it is very common to normalise it with the illuminated area in order to obtain the active area short circuit current density $J_{sc}[mA/cm^2]$.

- The open circuit voltage $V_{oc}[mV]$. This working point corresponds to a zero short circuit current density J_{sc}. Therefore, the output power in this case is again zero. Its interest is that this point corresponds to the maximum voltage that can be found between the two sides of the depletion region in fig.2.12.

- An estimation of the shunt resistance. In section 2.5 the different currents involving a solar cell from the P-N junction approach were shown. But this approach was ideal as in the real world a part of the current does not go through the depletion region but using alternative paths, such as surface paths. This power losses can be modelled by using a shunt resistance parallel to the diode model also shown in section 2.5. The shunt resistance should be as big as possible in order to avoid secondary currents. This new electric model is shown in fig.6.2a. An experimental estimation of this shunt resistance correspond to the inverse of the slope $A/V = 1/R$ of the $I - V$ curve at the J_{sc} point (that is, at zero bias).

- An estimation of the series resistance. Again, the equivalent diode model for the electric behaviour of a solar cell shown in section 2.5 neglected other effects in the real world. In this case, the intrinsic electric resistivity of the materials can reduce the output power of the solar cell. In order to model this, an equivalent series resistance can be included, as shown in fig.6.2b. In this case, an experimental aproach corresponds to the inverse of the slope $A/V = 1/R$ of the $I - V$ curve at the V_{oc} (that is, near the zero current point).

The characterisation of the $I - V$ current, therefore, is an interesting (and quick) way of comparing different solar cells from the final output power. It allows to include in the modelling new parameters not previously considered in the diode approximation (eq.2.7), leading to a complete structure as shown in fig.6.2c, or to the intrinsic expression shown in eq.6.1. In this equation, as in

(a) Including a shunt resistance R_{shunt} (b) Including a serie resistance R_{serie} (c) Including both a serie and a shunt resistances
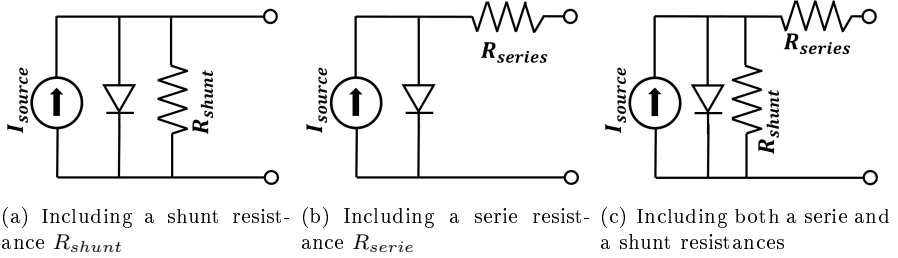
Figure 6.2: Corrected diode model for a solar cell.

section 2.5, the photocurrent sign convention will be changed in order to make it positive as is usual in photovolaics convention.

$$I(V) = I_L - I_0 \left[e^{\frac{q(V+IR_s)}{k_B T}} - 1 \right] - q\frac{V+IR_s}{R_{shunt}} \tag{6.1}$$

Eq.6.1, as an implicit equation, it is difficult to solve, but it is a good model for homojunction solar cells such those relevant to this study. This makes the $I - V$ curve a powerful method. However, in the study of a solar cell, the $I - V$ characterisation does not shed any light on the wavelength dependency of the output power in the solar cell. In order to do this, as has already been introduced in section 2.7, spectral response measurements have to be done. The setup to do this characterisation is shown in fig.6.3.

This is a slightly more complex system: First, from a Xenon lamp white light a single wavelength is chosen with a monochromator. The in-practice monochromatic light is then modulated using a chopper[1]. Then, a beam splitter 50-50 is used in order to separate the exciting signal in two.

The first modulated monochromated light incide on a reference photodiode whose spectral response EQE^{ref} is well known. This allows us to transform the current response in the photodiode directly in electrons (and therefore in incoming photons n_ph) by using the relation shown in eq.6.2

$$\frac{n_{ph}(\lambda)}{s} = \frac{I_{ref}(\lambda)/q}{EQE^{ref}(\lambda)} \tag{6.2}$$

where I^{ref} is the current collected in the reference photodiode and q is the electron charge. The advantage of using the splitting system, is that it leads to a quantitative characterisation of the exciting ligth, with an easy correction for any fluctuation on the overall exciting source radiated power.

---

[1]The light modulation is extremely important not only because it allows to increase the signal-to-noise ratio, but because it will allow to use a bias light during the measurements. This bias light will correct the low shunt resistance issues that lead to uncorrect measurements

UNIVERSITAT
POLITÈCNICA
DE VALÈNCIA

Valencia Nanophotonics Technology Center

ESCUELA TÉCNICA
SUPERIOR INGENIEROS
INDUSTRIALES VALENCIA
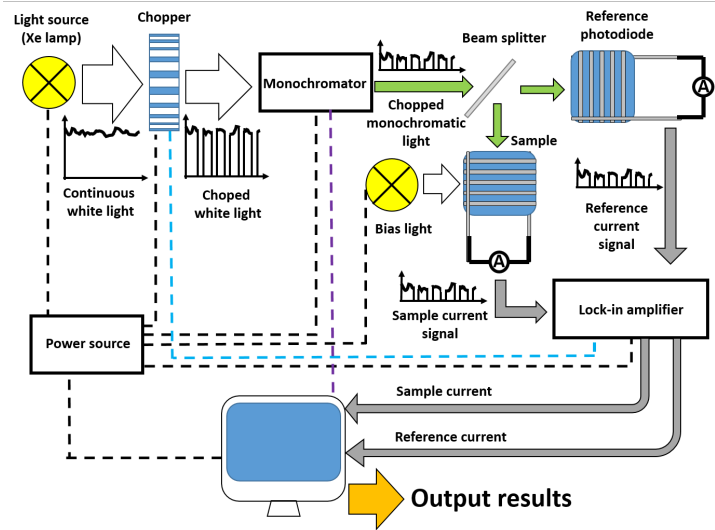
Figure 6.3: External Quantum Efficiency measuring system setup diagram.

The second modulated monochromated light incides on the sample to characterise. Analogously, a current $I(\lambda)$ is measured and related with the incoming photons $n_{ph}(\lambda)$. This ratio between the incoming photons of a certain wavelength and the output current is the spectral response of the solar cell (eq.6.3). When measuring the spectral response at different wavelengths, a characteristical curve is obtained and usually it is called the External Quantum Efficiency (EQE).

$$EQE(\lambda) = \frac{n_{e^-}(\lambda)/s}{n_{ph}(\lambda)/s} = \frac{I(\lambda)/q}{n_{ph}(\lambda)} = \frac{I(\lambda)}{I^{ref}\lambda}EQE^{ref}(\lambda) \qquad (6.3)$$

From the EQE it is possible to estimate the overall short circuit current too. In order to do that, an weighted sum is done for each wavelength using as weigthing factors the standard solar spectrum $AM_{G1.5}$ in $Wm^{-2}s^{-1}$, as shown in eq.6.4

$$J_{sc}^{EQE} = q \int_{\lambda_1}^{\lambda_2} \frac{\lambda}{hc}EQE(\lambda)AM_{G1.5}(\lambda)d\lambda \qquad (6.4)$$

Notice that the EQE sheds light on the current obtained from an incident source of light. This already is a good reference to compare between solar cells. However, sometimes the EQE measurement is normalised using reflectivity measurements, as shown in eq.6.5. This would lead to a comparison between samples attending to the current obtained not for each incoming photon, but

for each non-reflected photon. For $180\mu m$ thick solar cells, from wavelengths between 300-1100nm this is almost equivalent to say for each absorbed photon[2]. Therefore, the IQE and the spectral response are a good experimental estimation of the collection probability of the absorbed photons, as introduced in section 2.7.

$$IQE = \frac{EQE}{1-R} \qquad (6.5)$$

The use of spectral response measurements (EQE and IQE) are powerful tools for this thesis because, when compared, they shed light on the effect of different front surface treatments on the same solar cell.

A final remark should be done related to the bias light that illuminates the sample. Even if it is not necessary in most cases, in some others it allows to reduce the shunt effect of a solar cell when it is important enough to lead to fake results. In fact, when the solar cell has poor shunt resistances, a very small variation in the bias can lead to important differences in the J_{sc}. To understand this, it is useful to think on the approximation of the shunt resistance as the slope near the J_{sc} point and to look to fig.6.4
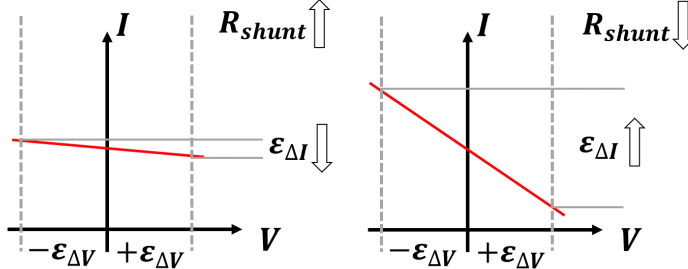
Figure 6.4: Schematic of how short circuit current measuring error is increased at low shunt resistance.

When the shunt resistance is too low, the slope of the I-V curve near zero bias is big. This makes that a small error in the zero-bias position $\pm\epsilon_{\Delta V}$ leads to big differences $\pm\epsilon_{\Delta I}$ in the current estimation. From the electronic and hardware point of view, the bias light allows to control easier the zero bias point it produces a background signal that enhances the noise-signal ratio.

---

[2]This is less exact for 950-1100nm as the absorption probability is reduced and the non-reflected photons can be transmitted, but it is a good strategy

UNIVERSITAT
POLITÈCNICA
DE VALÈNCIA

Valencia Nanophotonics Technology Center

ESCUELA TÉCNICA
SUPERIOR INGENIEROS
INDUSTRIALES VALENCIA

6.2 First approaches

Before the preliminary solar cells were available to use as substrate, a first approach has been done in order to estimate experimentally the behaviour of Ag nanoparticles on a solar cell. In order to do that, the nanoparticles were self-aggregated on glass. and two approaches are used:

- Measuring the Ag NPs directly on glass. This allows to measure not only the reflectivity but also the transmission values. As the glass has low absorption, also the parasitic losses on the NPs can be estimated. However, the refractive index of the surrounding media will not be the same as in the final device, and this results should be, at least, shifted, as shown in fig.4.20.

- Comparing, through indirect measurements, the effect of Ag NPs on the light absorption at the bulk of silicon substrates. Just to estimate or compare different samples on Silicon not only from the reflectivity point of view but also with an absorption trend. In order to do this, minority carrier lifetime measurements can be done as described in [1]. In brief, using a high lifetime c-Si substrate and comparing the two limit photoexcitation regimes it is possible to define an optical factor that is proportional to the amount of light that has been absorbed into the substrate.

6.2.1 Optical measurements on glass

The first fabricated samples are intented to show the scattering properties of an array of nanoparticles. Two samples made from 15nm and 25nm of Ag precursor layer are annealed 1h at 300C. The resulting samples are studied using a spectrophotomer and an integrating sphere and the total reflection, the total transmission and the direct transmission are measured. From those, the diffuse transmission is obtained as the difference between the total and the direct transmission. The absorption is calculated as the complementary of total reflection and total transmission up to 100%.

As the reference for reflection and transmission has been defined using a bare glass substrate, the measured values do not need further corrections to take into account the glass interference in the absorption, reflection or transmission. Therefore, the results shown in fig.6.5 correspond to the nanoparticle array effect.

In fig.6.5 different thicknesses of Ag precursor layer are studied using two processing temperatures. At 180C the self-aggregation will not be produced properly, at least at thicker precursor layers. At 300C, the self aggregation should be produded in all studied thicknesses. From here is concluded that the absorption within the nanoparticles is much increased when the nanoparticles

(a) 6nm Ag precursor 1h at 300C

(b) 6nm Ag precursor 2h at 180C

(c) 3nm Ag precursor 1h at 300C

(d) 10nm Ag precursor 2h at 180C

(e) 25nm Ag precursor 1h at 300C

(f) 15nm Ag precursor 2h at 180C
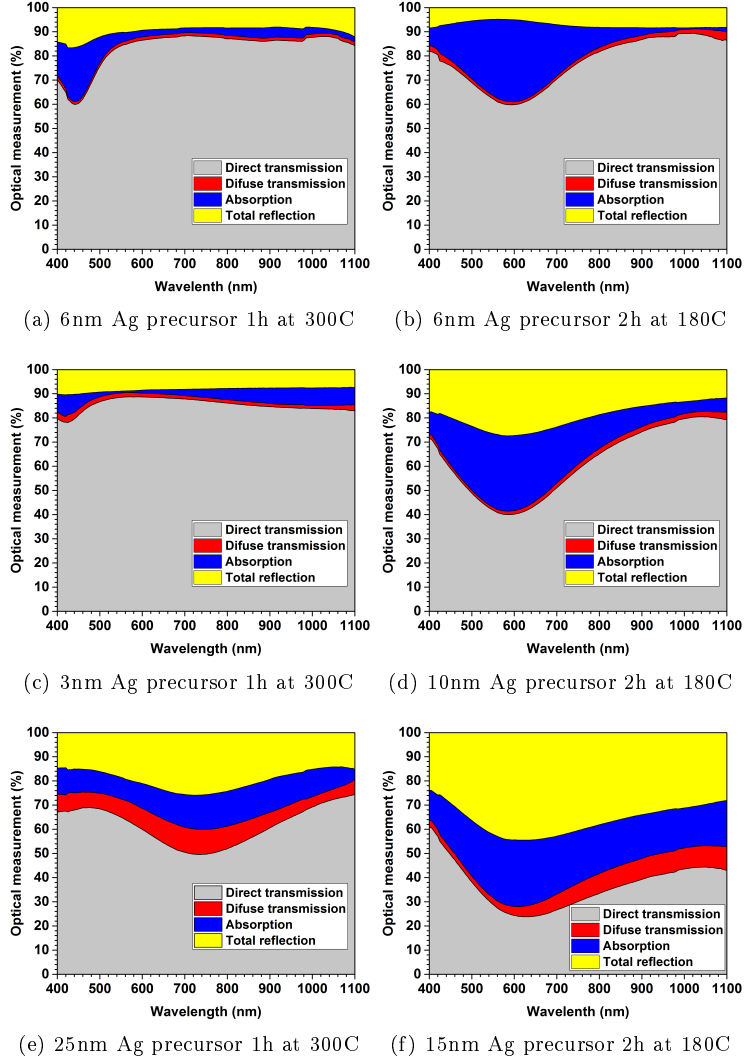
Figure 6.5: Optical behaviour of different Ag nanoparticle arrays on glass.

have not been defined and a quasi-continuous island-type dewetted structure is obtained. The absorption losses are also narrower, more intense and blue-shifted when particles are properly defined and smaller (as shown in section 4.4).This is consistent with the conclusions shown in [2] a similar approach has been done on glass and the resonant wavelength is tuned using the shape of the

particle and the dielectric constant of the embedding medium. In fact, related to the latter, the real effect of the nanoparticle arrays when placed directly on a SiN layer is expected to be shifted due to the higher effective refractive index of the medium.

The smaller structures lead to a higher absorption and a lower scattering, as predicted by Mie. This implies that the diffuse transmission and the reflectivity will be smaller. However, bigger particles lead to more remarkable diffuse transmissions and reflectivity increases.

There is a clear trend looking at fig.6.5: Reflectivity is largely increased when the arrays of nanoparticles are included. At the one hand, this increase in reflectivity will reduce the efficiency of a photovoltaic device as it reduces the amount of light that reaches the photoactive region. At the other hand, even if the diffuse transmission is not maximised, smaller particles seems a more reasonable choice for applying on solar cells.

6.2.2 Optical measurements on silicon

When measuring the minority carrier lifetime of a wafer using contactless photoconductance technigues[1], two limit illumination regimes are available:

- The Photoconductance Decay Method (PC). In this approach, a very short illumination pulse is done, so the all photogenerated carriers $N_{\Delta ph}$ are found at the beginning and therefore most of the data are measured under a purely transient mode while the recombination is produced, so the evolution is defined by:

$$\frac{dN_{ph}}{dt} = -\frac{N_{ph}}{\tau_{eff}}$$ (6.6)

- The Quasi-Static Photoconductance Decay (QSPCD). In this case, the decay of the illuminating source is much slower than the recombination ratio of the photogenerated carriers N_{ph}. This means that the photogeneration $N_{\Delta ph}$ can be considered constant during the recombination and therefore the evolution is expressed as:

$$\frac{dN_{ph}}{dt} = N_{\Delta ph} - \frac{N_{ph}}{\tau_{eff}}$$ (6.7)

where the photogenerated carrier ratio $N_{\Delta ph}$ is defined in eq.6.8 from the wafer thickness W, the electron charge q, the reference cell's short circuit

current density J_{sc}^{ref} at 1 sun ($1000W/m^2$), the light intensity evolution $L_I(t)$ and a factor f_{opt}.

$$N_{\Delta ph} = L_I(t) f_{opt} \frac{J_{sc}^{ref}}{qW} \qquad (6.8)$$

In traditional measurements, f_{opt} values are tabulated depending on the antireflection coating materials of the waver passivation. However, the optical factor value is defined experimentally as the ratio of the photocurrent that could be obtained in the ideal case where all the photogenerated carriers are collected and contribute to the photocurrent, over the photocurrent that is obtained in the reference diode. Thus, the optical factor is directly related with the amount of light that is absorbed in the measured Si substrate and is a meaningful parameter to study the effect of the scattering on the absorption on silicon.

The optical factor f_{opt} can easily be obtained by comparing the measurements under the PCD regime (where the measurement is independent on the initial generation) with the QSSPCD regime (where the optical factor will change the fitting). As both measurements are done on the same wafer, both measurements have to coincide. And the optical factor can be modified in each measurement until this happens.

From this point of view, as the reference Si wafer is always the same, there is a proof of consistency of the measurements: The minority carrier lifetime of the reference wafer must be the same regardless of the glass sample (with or without nanoparticles) placed on the top.

In order to make a general study of the optical factor that includes the dependecy of the wavelength, some dichroic filters are used during measurements. Its optical transmission properties are summarised in fig.6.6.

The schematic of the measured structure is shown in fig.6.7. In brief, the glass suporting the array of nanoparticles is placed on the reference Si wafer. A glycerol layer (with $n = 1.5$) is used as an index-matching layer: It removes the air (n=1) between the glass(n=1.5) and the Si (n=3.4) and prevents from the refractive index mismatch that increases the reflectivity

Notice that even if the nanoparticles are supported on a glass substrate and not directly placed on the silicon wafer (or solar cell), in this thesis no benefits from the near field consequences point of view would be expected, as the final device has 180 μm. However, the scattering is measurable at long distances and therefore the glass substrate would be a valid approximation (even more by using an index matching liquid layer) to estimate the effect when those arrays are placed on solar cells.

The optical factors resulting from these measurements are shown in table 6.1:
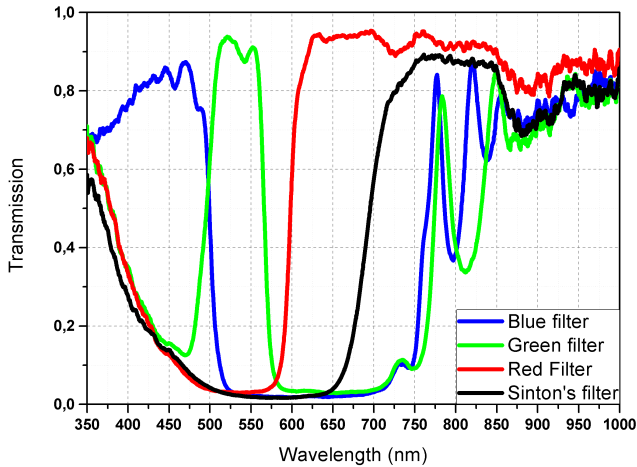
Figure 6.6: Optical transmission of the dichroic filters used for studying the wavelength dependency on the optical factor determination.
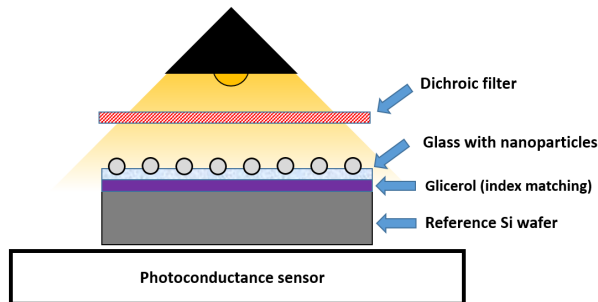
Figure 6.7: Structure used for estimating the relative scattering effect on the light trapping in a solar cell using a reference Si wafer instead of a finished solar cell.

Where the consistency proof of the measurements is shown as the independency of the lifetime measurement in fig.6.8.

The main conclusion is that the nanoparticles do not enhance optically the absorption of light within the underneath silicon wafer. Moreover, as expected, the effect depends on the applied chromatic filter as the extinction properties of the nanoparticles is wavelength dependent. In order to better understand these results, the same strategy has also been done using a traditional solar cell instead of a silicon wafer. However, in this case the reference system includes

Ag precursor (nm)	f_{opt}	f_{opt}	f_{opt}	f_{opt}
Ag precursor (nm)	No filter	Blue Filter	Green filter	Red filter
0	1.2	0.9	0.95	0. 90
20	0.9	0.75	0.75	0.82
25	0.8	0.65	0.65	0.6

Table 6.1: Results for the f_{opt} fitting.
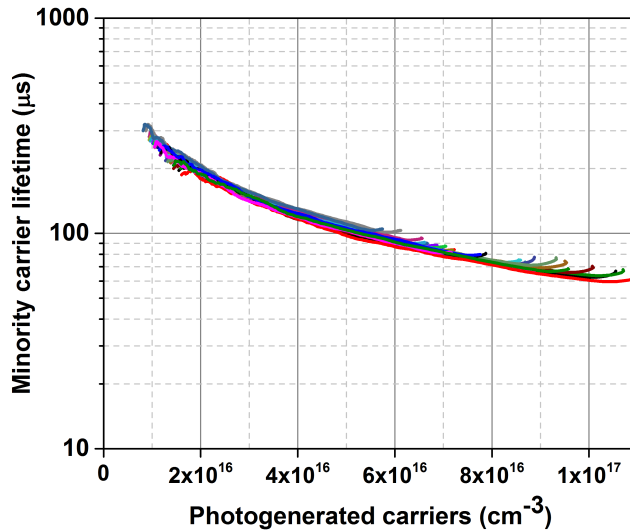
Figure 6.8: Minority carrier lifetime results and consistency proof: The measurement is the same regardless on the nanoparticle array and on the chromatic filter used. Samples made on bare glass from 20 and 25nm of precursor Ag layer annealed 1h at 300C using different dichroic filters.

electric contacts and this allows more accurate electrooptical measurements such as the spectral response. In fig.6.9 the results are shown for the same nanoparticle configuration that were used on a Si wafer. In fig.6.9, the P20 and P25 legends mean a 20nm and a 25nm precursor layer, respectively.

The conclusion is that the glass reduces the absorption within the solar cell (or the silicon wafer). As the glass is considered almost non absorbing, this is mostly related for a higher reflectivity when the glass is included over the solar cell. Moreover, the same behaviour for the chromatic filters shown in fig.6.6 is clearly seen in fig.6.9a. For the rest of subfigures in fig.6.9, the trend is clear:

(a) Effect of the substrate glass and chromatic filters on EQE measurements

(b) Measurements using blue filter and different Ag NPs distributions

(c) Measurements using green filter and different Ag NPs distributions

(d) Measurements using red filter and different Ag NPs distributions
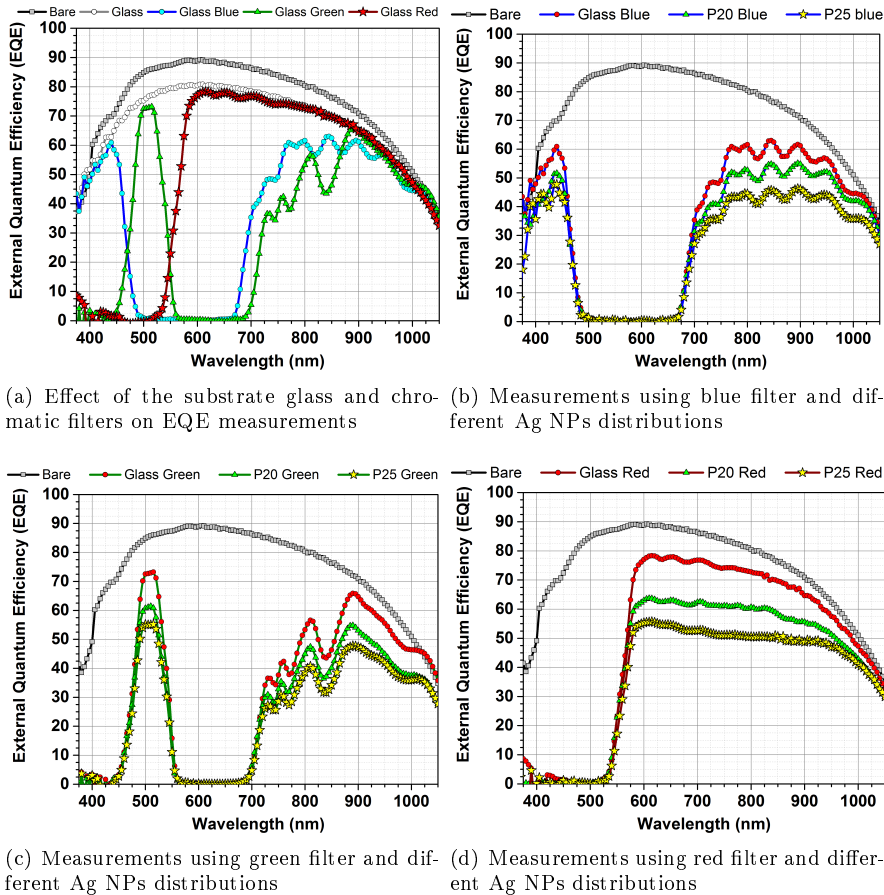
Figure 6.9: EQE measurements using different chromatic filters and different plasmonic distributions on glass.

The thicker the precursor layer used to prepare the nanoparticles is, the less performant is the resulting structure.

Because of the fact that the glass substrate used here does not include any ITO or transparent conductive layer on the top, the SEM analysis was unsuccesful. However, from section 5.2, the 20nm Ag precursor layer at 300C was has already been done and with the differences that the substrate may induce, there is a reference of the resulting size. Moreover, in the same section has been concluded that the average size increases with the precursor layer thickness and that the circularity is reduced at higher thicknesses for the same

temperature. This means that the 25nm Ag precursor layer sample is expected to have bigger particles and less circular.

Bigger particles are expected to have a higher scattering and lower intrinsic absorption losses. This implies that the absorption within the nanoparticles should be reduced and that there can be an increase in diffuse transmission, diffuse reflectivity or both of them due to the scattering.

An interesting result is presented in fig.6.10, where the trends obtained for the relative current variation using the photoconductance approach in minority carrier lifetime measurements are quite similar to the trends obtained using real electrooptic measurements on a solar cell.
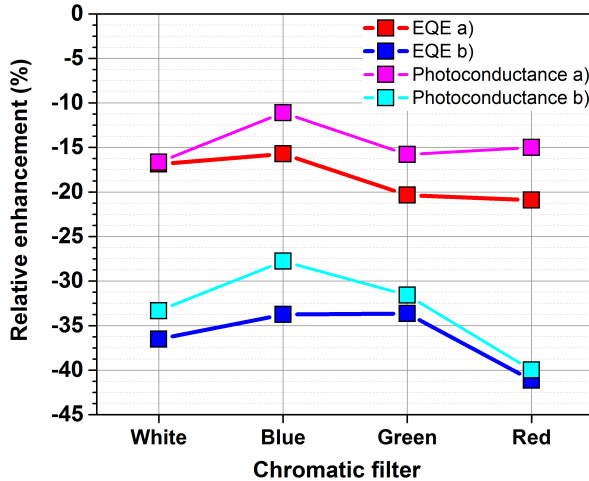
Figure 6.10: Relative short circuit current enhancement due to different Ag NP scatterers on a solar cell, estimated with an EQE measurement and with a photoconductance method. The scatterer a is obtained from 20nm of Ag precursor thickness and scatterer b from 25nm.

These results imply that the approach of fitting the optical factor f_{opt}, as a strategy for estimating the absorption changes due to the presence of nanoparticles is not meaningless. The main advantage for this is that no solar cell was needed for that.

However, these measurements ared not pretended for finding accurate results, because this approach has some limitations. First of all, the accuracy of the absorption results is limited as they are not obtained in a direct way. Moreover, there are some error sources that should not be forgotten:

- There is always a human error as the fitting of the optical factor value depends mostly on a human desicion. Thus, the accuracy of the results

is limited as the values may change slightly depending on that human factor.

- The model that lead to the minority carrier lifetime measurement assumes that the photogenerate carriers are distributed uniformely in the bulk silicon. This is never fully accomplished as different wavelengths have different absorption coefficients (see section 2.6), but it can be accepted for not too energetic photons. Thus, the results using the blue dichroic filter will be less accurate than the others.

- The photoconductivity measurements that are used to determine the lifetime of the substrate are based on the eddy currents that occur within the substrate when this is illuminated. Thus, the presence of a metallic particles, even if nanoparticles, may distort the measurements as its conductivity is much higher than the substrate itself.

Thus, the results can only be taken as indicative. Anyway, as the overall consequence seems to be a lower absorption in the solar cell, the trend is clear and fits well with the rest of measurements and characterisation that will be shown in this thesis.

6.3 Integration on solar cells

6.3.1 LIMA solar cell structure

One of the aims during the the european project LIMA was to develop an IBC solar cell[3]. Therefore, different structures were fabricated in order to find an optimal distribution. The whole details of the P-N junction pitches and many other details this will not be discussed in this thesis as they are out of its scope, but can be found elsewhere[3]. However, the details of the front side[4] are important to understand the properties of the nanoparticles. Fig.6.11 summarised those layouts.

As shown in fig.6.11, different front side structures are studied by the combination of different layers:

- A passivating layer. In order to minimise surface recombination, a passivating layer is mandatory. Two possibilities are found:

    - An antireflection coating made of SiN deposited by Plasma Enchanced Chemical Vapour Deposition (PECVD). This corresponds to the traditional commercial antireflection coating and is the basic reference for the project.

---

[3]www.limaproject.eu
[4]The *front side* will be the side exposed to the incoming light.

(a) Standard IBC solar cell

(b) Standard IBC solar cell with NPs

(c) Quantum dots passivated solar cell

(d) Lima solar cell with Quantum Dots and NPs
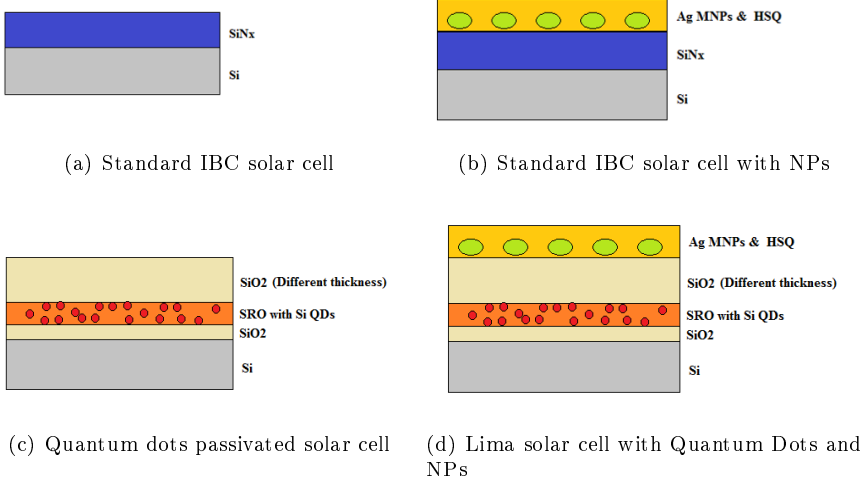
Figure 6.11: Different layouts for the front face of the LIMA solar cells, with reference structures.

- – A SiO_x layer. Usually, PECVD SiO_x layers are not the best passivating choice. Thermal oxide is a better choice in this case, but it needs a high temperature process.

- A Silicon Rich Oxide (SRO) layer[4]. This layer acts as an alternative passivation for the SiN, because the high temperature process needed to create the quantum dots improves the passivation properties of the PECVD deposited interface and makes it closer to the thermal oxide.

- An additional SiO_x layer. This is an optional layer and will only be used in some cases (second LIMA run of solar cells, as shown in section 6.3.3).

- A layer made of Ag NPs. The complete LIMA structure includes an additional layer with an array of metal nanoparticles. The aim is to find the conditions that lead to an improvement in the light trapping at the solar cell. In some cases, this array is going to be capped by an HSQ layer.

6.3.2 First results and measurements

The first results (fig.6.12) show that a local decrease in reflectivity for long visible wavelengths can be obtained when an array of NPs is placed in the front face of the solar cell. This contrasts with another local increase in reflectivity at shorter wavelengths. Therefore, from the optical point of view, no clear conclusion can be drawn.
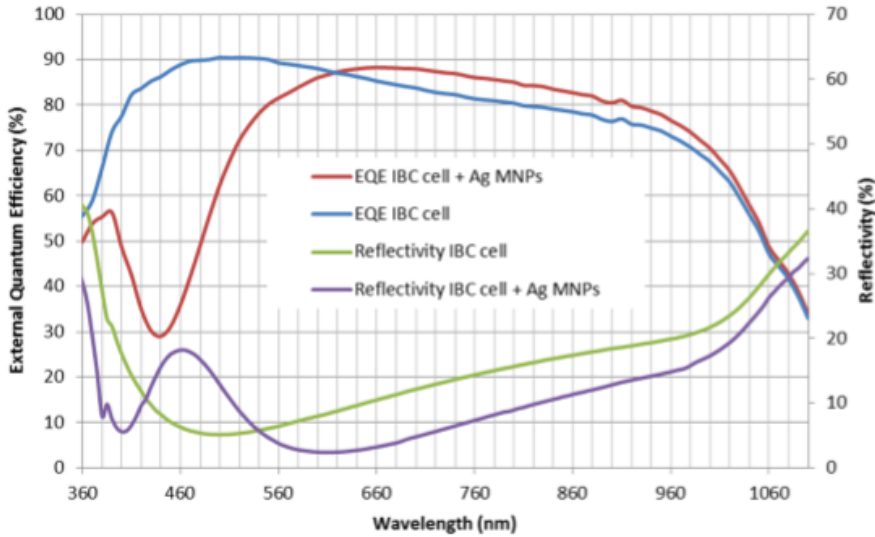
Figure 6.12: First LIMA integrated device measurements, showing optical (Reflectivity) and electrooptical (EQE) values.

The wavelength dependency on the reflectivity change can be understood from Mie theory. In fact, at short visible wavelengths individual resonances (at least for the dipole mode) are expected. As explained in section 3.1, the main difference between the Localised Surface Plasmons (LSP) and the Surface Plasmon Polaritons (SPP) is that the LSP scatter light independently on the exciting visible frequency. Therefore, even if the resonance condition is not fullfiled, the scattering effect of the nanoparticles is present.

Moreover, the wavelength dependency on the scattering properties is not only related with the intensity of the scattering (that is, to the proximity to a resonance) as the trend changes from an increase to a decrease in reflectivity. This can be explained mainly by several facts:

- As shown in section 4.1, the relative phase shift between the incident and the scattered light is wavelength dependent. Therefore, in a complex

layered system, even if it is not easy to predict the final effect, it is perfectly reasonable to expect different responses at different excitation wavelengths.

- As explained in sections 3.3.3 and 3.3.4, from the theoretical point of view, the Mie solution assumes that many independent solutions contribute the overall scattering solution. Each one corresponds to a different current distribution (see fig.3.7) and each one has a different spatial distribution of the scattered power.

- The main issue is that the power distribution in a complex system is usually obtained by using numerical methods and most of the available commercial software uses a far field approximation for this purpose. This works fine for homogeneous media, but not for multilayered substrates.

- As remarked several times in this thesis, the presence of a substrate makes the system anisotropic. Therefore, different responses can be found in different directions.

In short, the different phase shift and the spatial distribution of the scattered power and the multiple reflections that are expected in a multilayered system lead to different effects on the reflection of the original reflectivity of the solar cell, even going from an increase to a decrease in it.

In any case the final effect on the solar cell will not only be defined by the reflectivity. That is why electrooptical characterisation has to be done. It is by including these results that a different landscape is found.

The EQE results in fig.6.12are somehow in agreement with what has already been published by Yang [5]. Yang found the same optical behaviour in reflectivity but he only reports an efficiency increase in terms of current. No spectral response is, however, included in his publication. As shown in this thesis, the spectral response is of great interest to fully understand the system.

In fact, the EQE it is seen that even if there is an enhancement in the spectral response for long visible wavelengths, there is a very significative reduction in the efficiency at shorter wavelengths. When correcting the reflectivity (eq.6.5)it is clearly seen that the enhancement is mainly due to the antireflection properties on the front surface due to the presence of the Ag NPs. However, the loss at shorter wavelengths is not only related with an increase in reflectivity, but mainly to a huge intrinsic loss in the nanoparticles. This loss is found, at first sight, where the plasmonic resonance is expected to be.

The main conclusions at this point are summarised:

- The overall effect of the presence of the array of Ag NPs is a decrease in the solar cell efficiency that is mainly related with a short circuit current density (J_{sc}) loss.
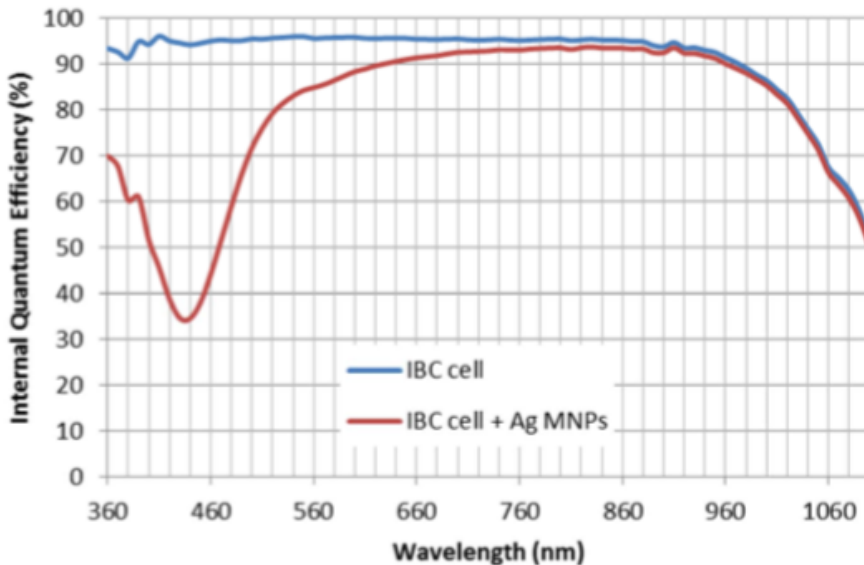
Figure 6.13: First LIMA integrated device measurements, showing the Internal Quantum Efficiency (IQE) with and without nanoparticles.

- The scattering properties of the nanoparticles enhance the light trapping by reducing the reflectivity while increasing the transmission within the solar cell for long visible wavelengths. This is prooved by comparing EQE and IQE measurements.

- The scattering due to the nanoparticles do not affect to the way the light is effectively absorbed. As the solar cell is the same before and after the integration of the NPs, its geometry remains constant and therefore the absorption probability too (see section 2.6). This implies that, the IQE will only be changed if the generation profile change (see section 2.7). In fact, this would be the best strategy to improve the cell and to reduce its thickness, but no evidence of this is found.

In order to improve these results, as the main limitation are the intrinsic losses, different strategies are planned:

- Shifting the resonance towards higher energies (blue or Ultra Violet UV). As the spectral response has to be weighted by the solar spectrum, the intrinsic loss effect will be reduced by just shifting the resonance towards a frequency where there is few incoming power from the sun. This will

also shift the scattering resonance but, as seen in Fig.6.12, the main enhancement in reflectivity is not seen near that resonance.

- Reducing the effect of the loss peak. Even if the intrinsic losses are unavoidable as are directly related with the surface currents that lead to the scattering itself, there is a possibility that should be studied. In fact, as shown in section 3.4.4, the Fano resonance is a likely-to occur. In [6] an analogous approach has been done for regular arrays of nanoparticles with a spacer layer. The results shown there also point towards a coupling effect dealing with Fano resonances.

  However, from the optical point of view, the absorption enhancement shown in [6] does not distinguish between the desired absorption in Silicon and the parasitic absorption in the nanoparticles. This is a limiting feature that has to be verified somehow. In this thesis, however, Quantum Efficiency measurements are done to verify how much of the reduction in reflectivity is effectively transmitted towards the Si substrate. In addition, this thesis deals with random distributions and this is an improvement from [6] (even if a numerical simulation is therefore not feasible).

In order to shift the plasmonic resonance two possibilities are available, taking Mie results in section 4.4 as a reference: Changing the particle size and/or changing the surrounding media. The size is easy to change by reducing the evaporated Ag precursor layer. Related with the surrounding media, it is more difficult to change because of the fact that the nanoparticles have to be integrated in a solar cell structure whose parameters are defined by the LIMA research group.

Figure 6.14 summarises the main pros and cons of changing the nanoparticle average size

In fact, by reducing the size of the nanoparticles the dipole will be the only excited mode and its resonance will be shifted towards higher energies (smaller wavelengths). However, the overall intrinsic losses should be reduced in higher particles, as the scattering efficiency (section 4.4.2) increases with size. There are two opposite trends.

6.3.3 Integration within a Plasmonic Anti Reflection Coating (PARC)

In order to study the effect of the local environment as well as the effect of substrate reflections on possible Fano interferences the spacing between the Nanoparticles and the Silicon is modified by using different SiO_x ARC thicknesses. Moreover, the NPs are going to be embedded within an additional amount of SiO_x. For this purpose, the HSQ approach developped in section 5.4 is followed, as well as the results from fig.5.16
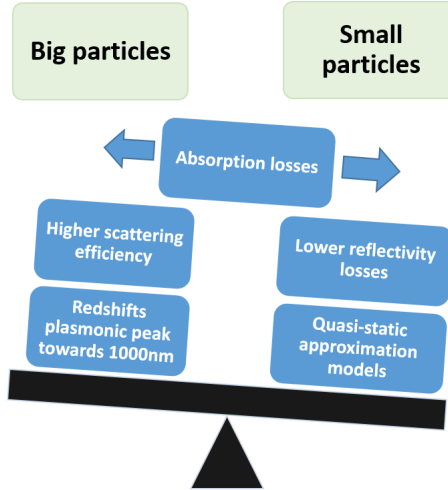
Figure 6.14: Nanoparticle size effect on a IBC solar cell when placed on the front side.

As a design condition, the well-known optimal 100nm of SiO_x ARC will be kept constant. This means that the sum of the spacing between the silicon substrate and the nanoparticles together with the thickness of the capping layer will be kept constant to 100nm. Table 6.2 summarises the different configurations studied, as well as fig.6.15

SiO_x thickness (nm)	HSQ thickness (nm)
10	90
35	65
70	30
100	0

Table 6.2: Different SiO_x and HSQ studied thicknesses for embedded nanoparticles over a Si substrate

In order to study not only the effect of the relative position of the nanoparticles, but also the effect of the size, two quite different arrays of nanoparticles are studied, from two different precursor layers of 3nm and 10nm. In both cases, a thermal self-aggregation is obtained at 300C during 1h.
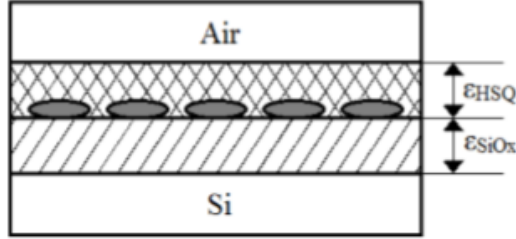
Figure 6.15: Embedding Nanoparticles strategy to modify the relative position between the nanoparticles and the substrate while keeping a global 100nm ARC.

From the image analysis, the equivalent diameter for the arrays obtained under those fabrication conditions and assuming a normal distribution is of $D_{eq}^{3nm} = 14nm$ and $D_{eq}^{10nm} = 55nm$.

The use of HSQ was presented in section 5.4 as a way to prevent the NPs degradation due to exposure to atmosphere. However, in this case there is another motivation for including a capping layer: As shown in fig.6.12, there is an optical loss related with the local increase in reflectivity. The use of a capping layer will help to a better light trapping because of the refractive index mismatch that produces a second interface of decreasing index. Therefore, the backscattered light will be reduced in global terms. At the same time, as any antireflection coating (ARC), the transmission of light through the silicon substrate is enhanced with a smoother refractive index evolution.

In fig.6.16 some interesting facts should be remarked. From the optical point of view, the reflectivity does change very significantly when the nanoparticles are on the substrate, and again once the HSQ covering layer is applied. In order to better compare the evolution, in fig.6.16 and 6.17 the reflectivity for the optimum 100nm SiO_x ARC is included, as well as the intermediate thicknesses shown in table 6.2.

As expected, as the SiO_x thickness of the inicial ARC (under the NPs) increases, the reflectivity is reduced and the minimum is redshifted. This is consistent too with the results that would be obtained with the Fresnel coefficients both in shape and in value. Therefore, the measurements seem to be consistent. Even if the oven step has still not been applied to the evaporated Ag layer, there is an experimental evidence of a resonant-like behaviour similar to what would be obtained expected after the self-aggregation process. This confirms that the self-aggregation is produced before than expected. The main two explanations for this will be:

(a) 0nm SiO_x, 100nm HSQ

(b) 10nm SiO_x, 90nm HSQ

(c) 30nm SiO_x, 70nm HSQ

(d) 50nm SiO_x, 50nm HSQ

(e) 70nm SiO_x, 30nm HSQ

(f) 100nm SiO_x, 0nm HSQ
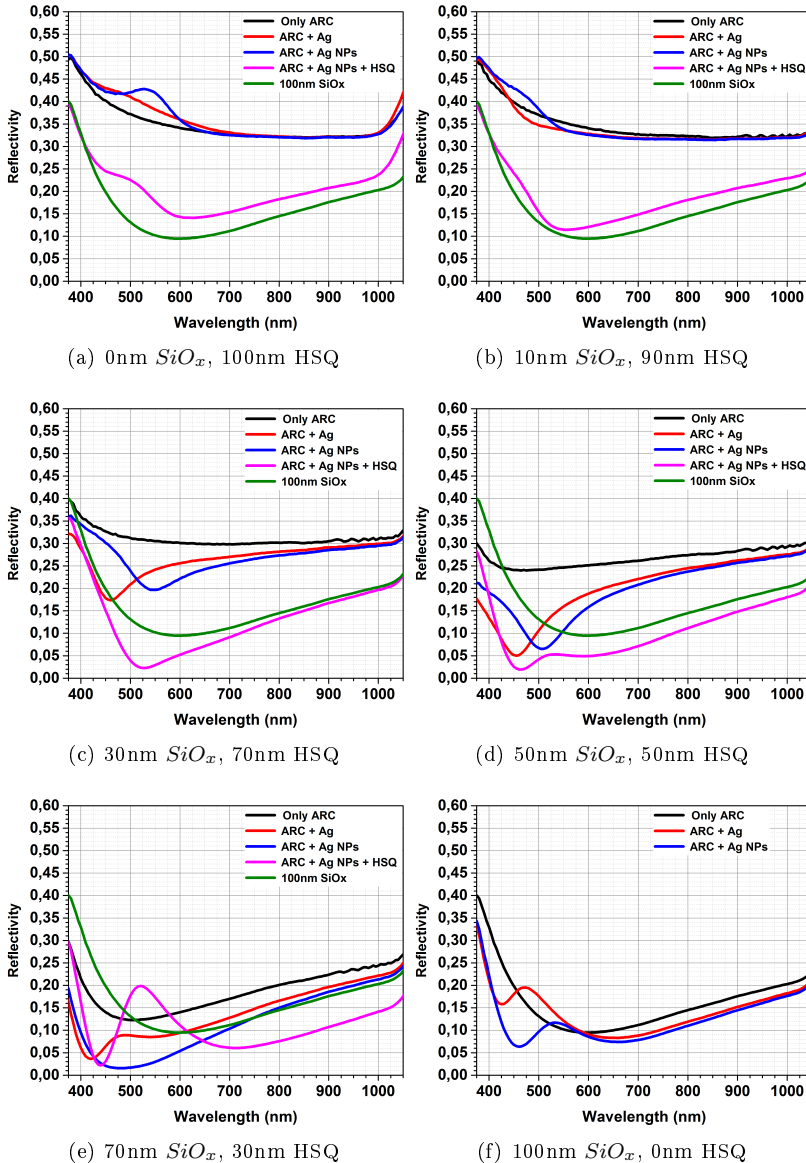
Figure 6.16: Specular reflectivity at normal incidence for different plasmonic antireflection coatings made from 3nm Ag annealed 1h at 200C (+1h 200C for HSQ).

- That there is a critical thickness (eq.5.9) for that structure that has been reached, leading to a natural self-aggregation. This would be typical on real epitaxial growth between two different crystal lattices, whereas the PECVD deposited SiO_x is rather amorphous. Nevertheless, there is always a crystallinity degree that should be studied in future works to check this hypothesis.

- That the substrate temperature is increased during the evaporation process. In fact, as explained in section 5.3, there is not a real control on the substrate temperature and it is likely that the evaporated material, once condensed on the substrate, releases its energy leading to an increase of temperature. This would have the same effect that the latter annealing depending on the reached temperatures.

Even if the optical measurements point towards a self-aggregation during evaporation, the latter thermal process modifies the resulting array of nanoparticles. In fact, the resonance peak is redshifted just like if the resulting nanoparticles become bigger. Moreover, the peak is better defined in most cases and this is consistent with the fact that higher temperatures lead to more circular, bigger and independent particles, as shown in section 5.2.

From the SiO_x thickness effect point of view, there is a very interesting experimental result: When the nanoparticles are placed directly on Si, the resonance peak corresponds to an increase in reflectivity. However, when the nanoparticles become more distant to the Silicon the resonance is presented as a valley in reflectivity. Moreover, this trend is even more pronounced as the distance between the nanoparticles and the Silicon is increased. As the nanoparticles have the same size and are obtained under the same conditions, the resulting distribution will be analogous. Therefore, this effect has to be related with optical interferences.

In [7] a study is done to relate different resulting electromagnetic field profiles at different relative positions from the substrate and how the presence of nodes and antinodes can change the intensity of the extinction of light within the nanoparticle. The studied case deals with a back reflector for a thin film solar cell. However, this conclusions can be extrapolated to the case of a nanoparticle embedded within an Anti Reflection Coating.

Moreover, in [7] only the profile corresponding to the resulting reflections of an incident plane wave on the solar cell, whereas the radiated field by the nanoparticle is not included. Therefore, the experimental comparison with the simulations is not trivial even if the position of the nodes and anti-nodes fits quite well.

In this thesis, the Green Function approach takes into account the reflected field by the different layers in the substrate structure (see fig.4.4), as well as the radiated field by surrounding particles.

In all cases, as expected, the addition of an HSQ capping layer reduces the reflectivity. The reasons, as has already been explained, are related with the matching between refractive indexes and to the reduction of the backscattered light.

When studying fig.6.17 (bigger particles) some of the same trends that for fig.6.16 are found, such as those related with the initial self-aggregation after the evaporator. In this case, however, the differences between before and after the oven step are more remarkable. This is related with the fact that thicker Ag precursor layers are poorly self-aggregated at low temperatures, as shown in section 5.2, and then the uncontrolled substrate temperature is not so critical.

Also, the changes in reflectivity at increasing distance to the Silicon are still found. In this case the trend is not to clear bechause the reflectivity maxima changes its intensity, but there is the same trend for the minimum reflectivity as for the smaller nanoparticles.

However, in this case, the HSQ does not always enhance the reflectivity. In fact, in this case the nanoparticles are big enough so that they are not completely embedded in the ARC matrix when the SiO_x thickness underneath is beyond 50nm.

All these are the general trends found experimentally that point towards a position dependent optical behaviour of the nanoparticles and to the experimental proove that the interferences with the substrate is the main factor that define that trend. However, this qualitive experiment will need further understanding for a quantitative conclusion. This will be done in section 6.4, when comparing the semianalytical modelling with experimental results.

For now, the main interest is to define which are the best configuration as ARC. Nevertheless, in fig.6.16 and 6.17 there are many curves and it is difficult to compare which would be the best configuration from an ARC point of view. In order to do that, and thinking on the final solar cell application, an effective average reflectivity R^{av} can be defined for any wavelength range in the same way that the EQE can estimate the J_{sc}: Weighting each wavelength with the solar spectrum $AM_{G1.5}$. This approach leads to the definition shown in eq.6.9

$$R^{av} = \frac{\int_{\lambda_0}^{\lambda_N} R(\lambda)\lambda AM_{G1.5}(\lambda)d\lambda}{\int_{\lambda_0}^{\lambda_N} \lambda AM_{G1.5}(\lambda)d\lambda} \tag{6.9}$$

Notice that with this definition of R^{av}, an easier comparison for the different configurations of the ARC is possible. In fact, assuming an ideal solar cell with a perfect spectral response ($IQE(\lambda) = 1$ for any λ), eq.6.10 is fulfilled:

$$J_{sc} = J_{sc}^{max}(1 - R^{av}) \tag{6.10}$$

(a) 0nm SiO_x, 100nm HSQ

(b) 10nm SiO_x, 90nm HSQ

(c) 30nm SiO_x, 70nm HSQ

(d) 50nm SiO_x, 50nm HSQ

(e) 70nm SiO_x, 30nm HSQ

(f) 100nm SiO_x, 0nm HSQ
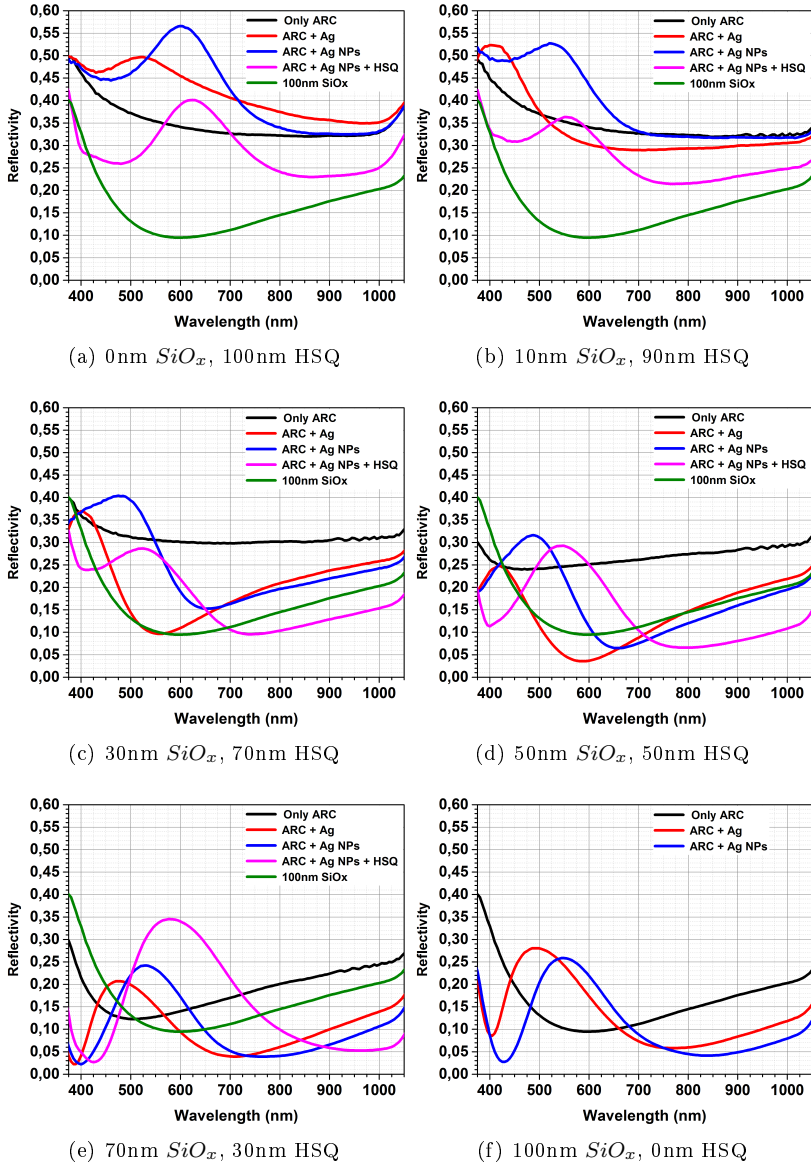
Figure 6.17: Specular reflectivity at normal incidence for different plasmonic antireflection coatings made from 10nm Ag annealed 1h at 300C (+1h 300C for HSQ).

with:

$$J_{sc}^{max} = \frac{q}{hc} \int_{\lambda_0}^{\lambda_N} \lambda AM_{G1.5}(\lambda) d\lambda \qquad (6.11)$$

This approach defines a simple optical parameter that allows to compare easily different ARC in terms of potential short circuit current densities J_{sc} (just like what has been done in section 6.2.2 with the optical factor f_{opt}). From this point of view, the influence of the relative position of the Ag NPs related to the Si substrate is found to be of particular interest, as shown in fig.6.18.

Fig.6.18 shows how it is possible to reduce the reflectivity not only by changing the nanoparticle array but also by changing the substrate structure. For better comparison, the bare Si averaged reflectivity as well as the optimal 100nm SiO_x reflectivity are found. Some of the configurations lead to better antireflection properties than the reference.

Results shown in fig.6.18 agree with S.Pillai et al[8], where an improvement is found when the nanoparticles are not placed direclty on the top of the silicon substrate, but with a small spacer. The main difference between [8] and this results is that fig.6.18 does not take into account any electric aspect and that the loss mechanisms found in section 6.3.2 cannot be seen with optical measurements with an absorbing substrate as Silicon. Therefore, the antireflection properties may be related with higher absorptions, just like was found in section 6.3.2.

The second run of LIMA solar cells has been prepared so that different configurations for the front face are available, as explained in section 6.3.1. Thus, different thicknesses of the SiO_x layer on the top of the SRO layer (see fig.6.11c) have been designed in order to have different relative positions between the nanoparticles and the silicon substrate. Those configurations are summarised in table 6.3.

SiO_x thickness (nm)	HSQ thickness (nm)
0	30
10	30
20	30
55	30

Table 6.3: Different SiO_x and HSQ studied thicknesses for embedded nanoparticles in an integrated LIMA solar cell.

Again, the I-V measurements have shown that there is a reduction in short circuit current density J_{sc}. To have an overall characterisation, spectral response measurements are done, as shown in fig.6.19
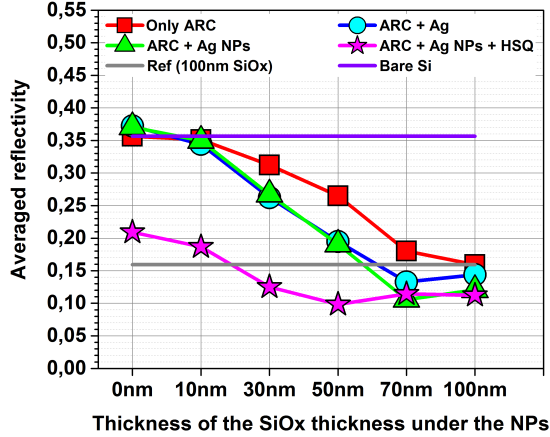
(a) NPs from 3nm Ag 1h 300C
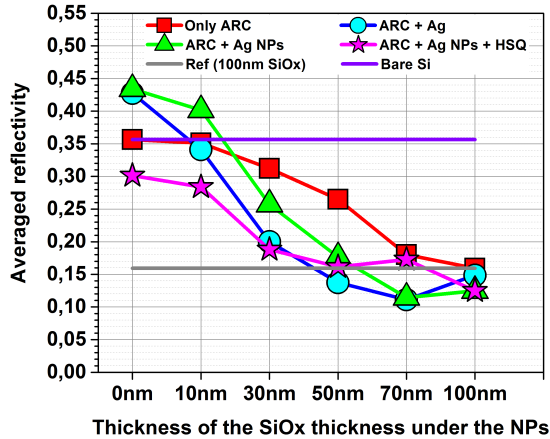
(b) NPs from 10nm Ag 1h 300C

Figure 6.18: Evolution of the averaged reflectivity R^{av} for different configurations of the Plasmonic ARC and the comparison with the bare Si and the tradicional 100nm SiO_x ARC.

There is a possibility that should be verified: Are the differences shown in fig.6.19 related only with a different electric field intensity at that point? In other words, as there is an ARC, multiple reflections lead to a electric field profile in depth for different wavelengths with constructive and destructive interferences. For that reason, the differences between relative positions may be related not to a Fano interference itself, but to a different intensity on the

175

(a) Internal Quantum Efficiency measurement

(b) Reflectivity measurement
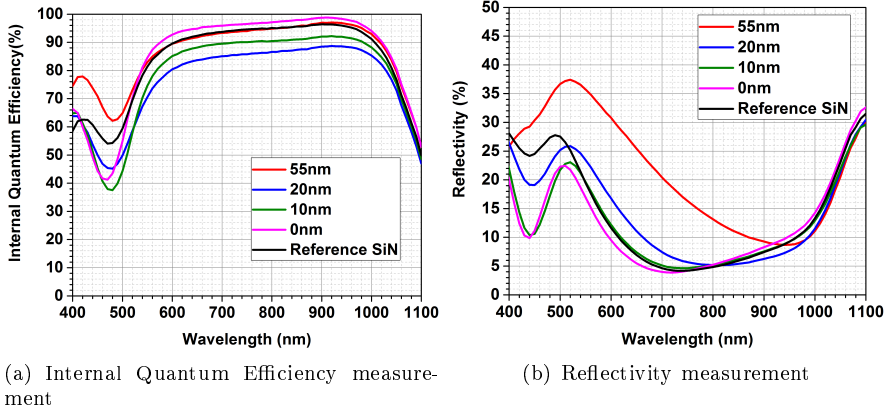
Figure 6.19: Differences in intrinsic losses at different relative position nanoparticle - Si substrate.

excitation. From this point of view, the phase difference in a few nanometers will not be relevant enough to justify such changes in fig.6.19

Even with the reduction of the loss peak, the overall efficiency is still reduced. The main reason for that is that the lower loss peak configuration corresponds to the worst antireflection coating.

6.3.4 Integration at the back

Once the limitations on the front face of the solar cell have been verified, an alternative is considered: Trying the nanoparticles on the back side of the solar cell.

In this case, most of the wavelengths will be absorbed in the silicon substrate before reaching the back side and only the longer wavelengths will interact with the nanoparticles and scattered. This way, the absorption losses found at shorter wavelengths would be avoided and only the photons that do not interact with the solar cell will be backscattered and absorbed. Therefore, from the theoretical point of view the parasitic losses do not affect the efficiency of the cell and only the scattering should be present.

In order to assure a good scattering efficiency, and now that the reflectivity of the nanoparticles has to be maximised, bigger sizes seem to be the most suitable. However, as they have to be integrated in IBC solar cells, there is a limit in practice: The particles must not shunt the contacts and therefore the initial continuous Ag layer has to be properly self-aggregated during the thermal annealing.

Fig.6.20 summarises the pros and cons of choosing big and small particles to be integrated on the back side of the solar cells. In brief, smaller particles are less likely to produce a shunting in the solar cell and allow the use of the dipole approximation for the Green function. However, bigger particles the scattering is bigger than the absorption and the absorption losses at short wavelengths are avoided in Si substrates. A current increase has been estimated using the
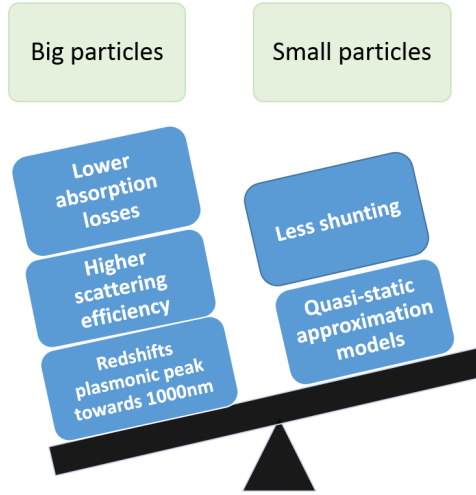
Figure 6.20: Nanoparticle size effect on a IBC solar cell when placed on the back side.

quantum efficiency of the cell and optical measurements of reflectivity and transmission, as shown in eq.6.12

$$\Delta J_{sc} = \frac{q}{hc} \int_{300}^{1100} IQE(\lambda) \Delta A(\lambda) \lambda AM_{G1.5}(\lambda) d\lambda \qquad (6.12)$$

Where, as usual, q is the electron charge, h is the Planck constant, c is the light speed, $IQE(\lambda)$ is the internal quantum efficiency of the reference solar cell, $AM_{G1.5}(\lambda)$ is the standar solar irradiance spectrum and $\Delta A(\lambda)$ is the increase in the global percentage of absorbed photons due to the addition of

the silver nanoparticles. The latter can be estimated using reflectivity (R) and transmission (T) measurements from the integrated cell and the reference cell:

$$
\begin{aligned}
\Delta A(\lambda) = A_{NPs}(\lambda) - A_{ref}(\lambda) = \\
= [100 - R_{NPs}(\lambda) - T_{NPs}(\lambda)] - [100 - R_{Ref}(\lambda) - T_{Ref}(\lambda)] = \quad (6.13) \\
= R_{Ref}(\lambda) - R_{NPs}(\lambda) + [T_{Ref}(\lambda) - T_{NPs}(\lambda)]
\end{aligned}
$$

Using eq.6.12 it is possible to estimate the improvement limit due to a back reflector. To do that, different continuous Ag layers are evaporated on the back side of solar cells and optical measurements are done.
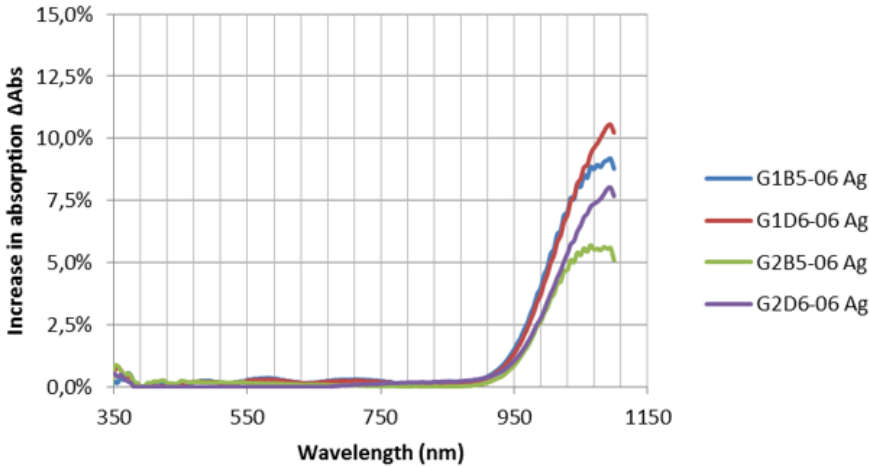
Figure 6.21: Absorption increase estimation on a solar cell due to the increase of the internal reflectivity related with a continuous Ag layer acting as back reflector.

The results in fig.6.21 only proove conceptually that there is a possible enhancement in non fully integrated LIMA solar cells that can be obtained by increasing the short circuit current by improving the light trapping of the visible long wavelengths from the back side of a solar cell. In fact, using eq.6.13 the the specular back reflector can produce a $\Delta J_{sc} = 0.44 mA/cm^2$. This value has to be understood as a optical limit, as no electric considerations are taken into account. Moreover, a plasmonic back reflector is different from a continous back reflector, so the final enhancement will be different.

In any case, this preliminary results are quite encouraging to deposit the nanoparticles on the back. This has been done with the third run of solar cells from LIMA project.

All the EQE measurements that have been done show that the lossy peak from previous trials at the front (fig.6.12) has been avoided, as expected, because those wavelengths are completely absorbed before reaching the nanoparticles. However, the overall efficiency has been reduced much more than before.

When measuring the I-V curves, a huge shunting effect is found. This shunting is in most cases even too important so that the bias light during the EQE measurements can correct it.

The first thought is to relate this shunting with the metallic layer that shunts the interdigitated contacts in the IBC structure. However, there are several reasons to think that this may not be the main reason:

- During the optimization process itself of the strating solar cell, in order to increase the shunt resistance in the IBC structure, the interdigitated contacts are fabricated at two different levels. Therefore, it is even more complicated to have a shunting path between contacts.

- It has been verified by SEM images that the self-aggregation is produced correctly, that is, that Ag seems to have dewetted everywhere on the surface, even in the transition walls between P and N contacts.
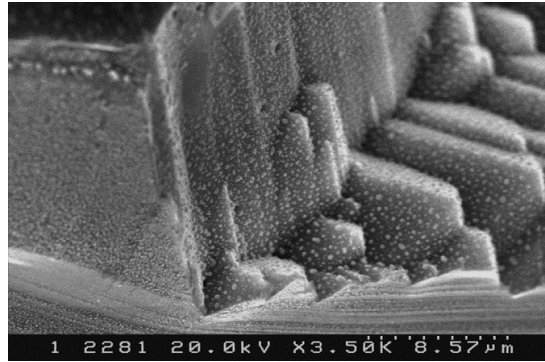
Figure 6.22: SEM image of a P-N junction in the back side of the IBC solar cell, showing the two level structure that avoids shunting issues as well as independent self-aggregated nanoparticles that difficult any shunting metal path from a continous precursor layer.

Moreover, whereas the shunting effect does not follow a clear trend for increasing deposited thickness. In fact, up to 45 nm have been used as precursor layer before complete shunting of the solar cell[5] and the shunting has been

---

[5]For a given temperature and a given anneling time there is a maximum Ag precursor thickness that can be self-aggregated correctly.

better avoided on some samples with thicker precursor layers that for lower ones. In every case, the annealing has been done for 1h at 300C.

To split the optical effect from the electronic effect, new optical measurements are done with nanoparticles on silicon and on glass. In this case, not only a self-aggregated back reflector is used (instead of the continuous layer in fig.6.21). Another difference is that an angular dependency of the scattered light is measured. In order to do this, the setup shown in fig.6.23 is used. Briefly, a goniometer changes the angle of the measured scattered light while a constant incident laser beam at normal incidence reaches the surface. At 90deg, no signal should be measured but the angular resolution makes some signal to be integrated during the measurement.
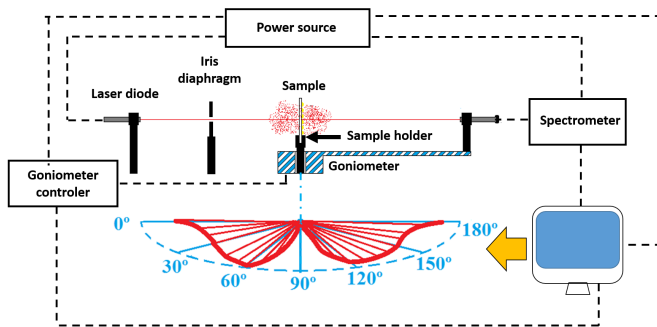
Figure 6.23: Diffuse reflection and transmission measuring system setup diagram.

From results shown in fig.6.24 it can be seen the different effect of an array of NPs on the front and on the back side. The array has been done using 25nm of Ag precursor layer that has been heated up 1h at 300C.

When using a glass substrate with negligeable absorption, the reflection and transmission curves are mainly symmetric for any wavelength and regardless of the relative positon of the nanoparticles (front or back side). The small differences in the absolute values are due to the different reflectivities at different wavelengths.

When a silicon substrate is used, at visible wavelengths there is an significant difference between the front side configuration and the back side: When placed at the back, the reflectivity is the same than for the reference bare silicon substrate as most of photons are absorbed before reaching the nanoparticles. It is remarcable that the laser is powerful enough to that a small part of the photons are transmitted at direct transmission. When placed at the front, however, the big particles arising from such a thick precursor layer lead to an important light backscattering.

At near infrared wavelengths, the silicon substrate is almost transparent as in the case of the glass substrate. However, the difference between the front side and the back side configuration is interesting: At the front side, the reflectivity is increased, as in the case of visible wavelength. There is a symmetric behaviour for the transmission for all the non-absorbed photons. When the back side configuration is used, the transmission is mainly the same but the symmetric behaviour for the reflection leads to smaller values. This points towards an increase in the absorption within the Si substrate, as an absoption loss would be also seen by comparing with the front side configuration. Again, Pillai et al [8] show that the nanoparticle behaviour of nanoparticles is optimised when placed at the back side directly on the silicon surface.

Valencia Nanophotonics Technology Center

ESCUELA TÉCNICA
SUPERIOR INGENIEROS
INDUSTRIALES VALENCIA

UNIVERSITAT
POLITÈCNICA
DE VALÈNCIA

(a) Glass at 532nm

(b) Silicon at 532nm

(c) Glass at 1065nm

(d) Silicon at 1065nm
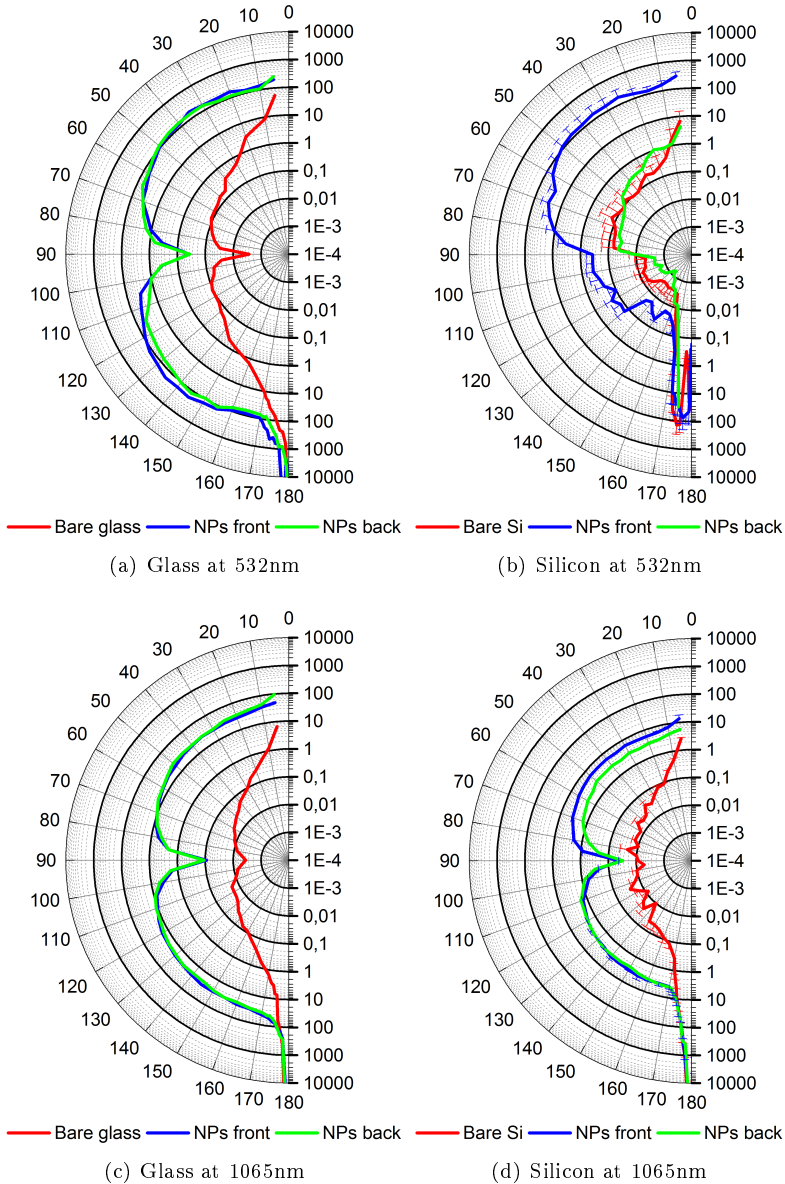
Figure 6.24: Angular power distribution for absorbing and non absorbing substrates with nanoparticles, at different wavelengths. *Front* means that the scatterer is between the exciting source and the substrate, whereas *back* means that the substrate is in between.

6.4 Simulation results and analysis of Green Function approach

To study the accuracy of the Green function based model, a random nanoparticle distribution is simulated on a 180μm c-Si substrate with a 100nm SiO_2 ARC. Two different cases are simulated: A first one assuming that the nanoparticles are sphericals and a second one assuming that the nanoparticles are truncated spheres whose truncation angle lays randomly between 30 and 90 degrees. The results are shown in fig.6.25

A first sight on fig. 6.25 shows a good agreement with the experimental results found for the spectral response measurements (EQE) on solar cells as there is an important loss peak an shorter wavelengths where the resonant behaviour of the extinction is expected from Mie and that leads to a reduction in the amount of light transmitted towards the silicon.

By comparing the truncated sphere simulation with the sphere simulation, there are different conclusions: Looking at the transmission peak, the truncated sphere simulation seems closer to the experimental values because the transmission loss is not as intense as the simulated results for spherical particles. However, looking at the reflexion maxima in the same frequency range, it is the spherical particles that lead to a more accurate result.

As explained in section 4.2.2, the best way of having a realistic array of nanoparticles is by taking SEM images from real self-aggregated samples. Therefore, the results shown in fig.6.25 are done using a real sample whose reflectivity has been measured. This allows us not only to compare a general trend but also specific measurements, as shown in fig. 6.26

When comparing the measured and the simulated reflectivities, the accuracy of the model seems poor: Even if there is a good agreement in the general trend the calculated values are not accurate. This means that one of the assumptions that have been done in the model is not realistic and that some more studies should be done for a better understanding of the differences between simulated and measured data.

In Fig.6.27 it is possible to see that even if the particles are not perfectly spherical from above, this approach seems reasonable. Indeed, making statistics from different SEM images with a total of 1964 analysed NPs, it is found that the average circularity (Fig.6.27c) is of 0.906 ± 0.001. Moreover, the average size of the nanoparticles (Fig.6.27d) is of $R = 9.8 \pm 0.1$nm, small enough to be able to be considered as a dipole using Mie solution (see section 4.4.1) and even under the quasi-static approximation (QSA). Notice that even from the refractive index point of view in that section it has also been shown that when using a SiO_x antireflection coating the dipole should be the predominating excited mode in the nanoparticle.
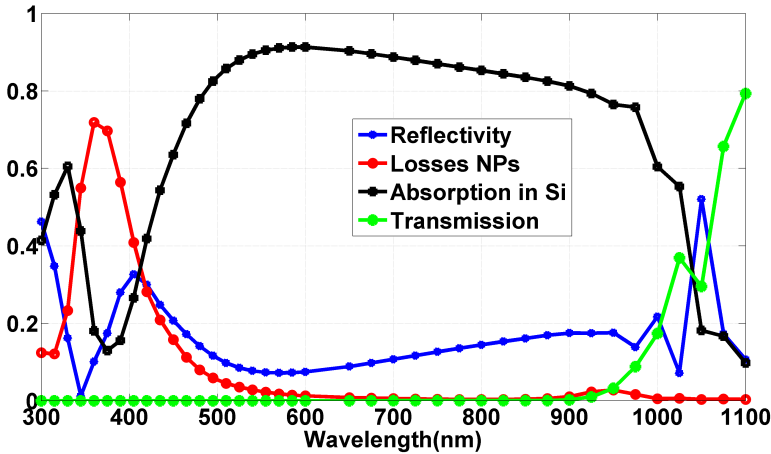
(a) Sphere array of $R_{av} = 10nm$
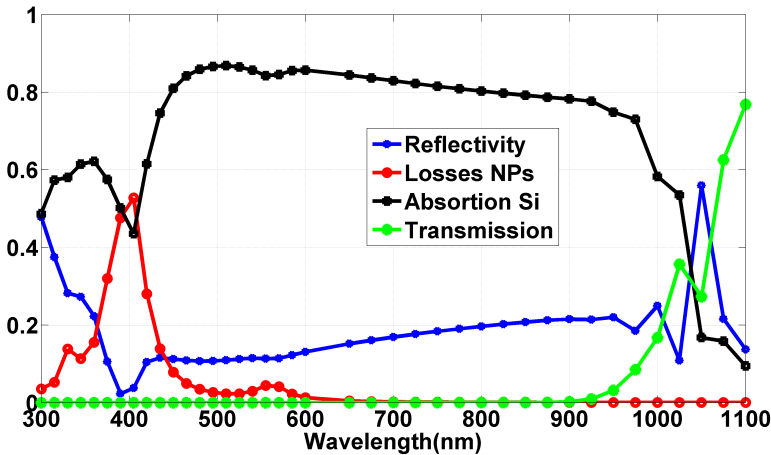
(b) Truncated sphere array of $R_{av} = 10nm$

Figure 6.25: Optical values for Ag arrays of NPs calculated using Green functions assuming that each nanoparticles behave like dipole. The substrate is a 180μm c-Si covered by 100nm of SiO_2. (a) Corresponds to a spherical particle polarisability and (b) corresponds to a truncated sphere polarisability calculated assuming a randomly distributed truncation angle between 30 and 90 degrees.
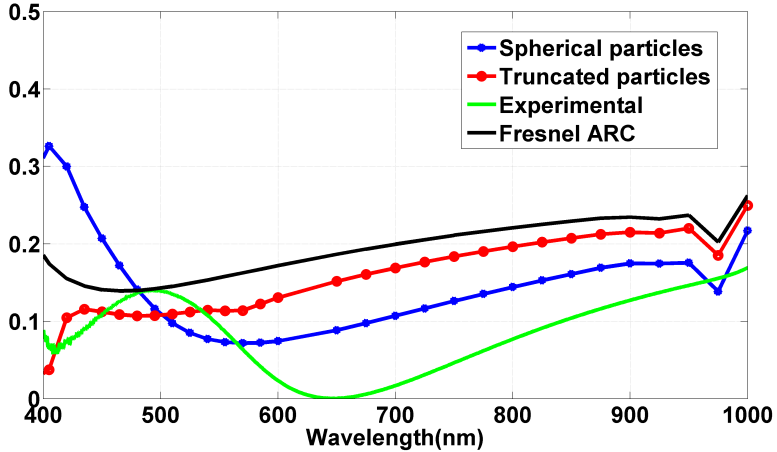
Figure 6.26: Reflectivity comparison for Ag arrays of NPs at different cases:
calculated assuming spherical particles, calculated assuming truncated spheres,
calculated using the Fresnell coefficients assuming no nanoparticles, and exper-
imental measurement with real nanoparticles. The substrate is a 180μm c-Si
covered by 100nm of SiO_2.

The Green Functions used for this simulations have already been tested
in and verified in [9]. Thus, there are different possible reasons for the dis-
crepancies between experimental and modelled results. Further experimental
validation and studies for the Green model is not easy as transmission meas-
urements are not feasible on a 180μm c-Si substrate in the visible range and
only reflection measurements can be done.

A simple way of having more information from the samples is to make
reflectivity measurements at different angles. Polarised light will be used for
those measurements. This will shed some more light on the optical behaviour
of the nanoparticles that can be useful to better define the assumptions for a
more accurate analytical model.

Several arrays of nanoparticles are prepared of different sizes and differ-
ent ARC thicknesses are used to study the effect of the distance between the
nanoparticles and the high index c-Si. The setup that has been used for the
measurements[6] is schematised in fig.6.28

The measurement is done using a FTIR as the main signal treatment equip-
ment and a Si diode (able to measure from 400 to 1000 nm) is used as sensor.
An additional Xe-lamp has been included in order to have a higher power at

---

[6]The author thanks Dr.Stéphane Collin and the Laboratoire of Photonique et Nanostruc-
ture (CNRS-LPN) for allowing to use their setup.
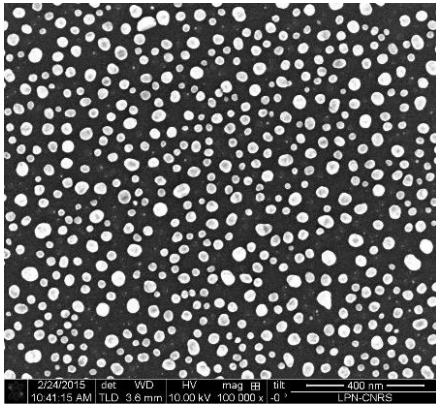
(a) SEM image for simulated array
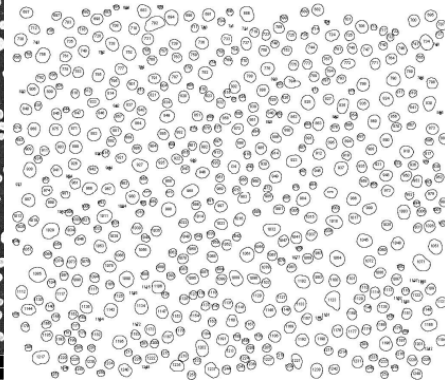
(b) Treated SEM image for NP recognition
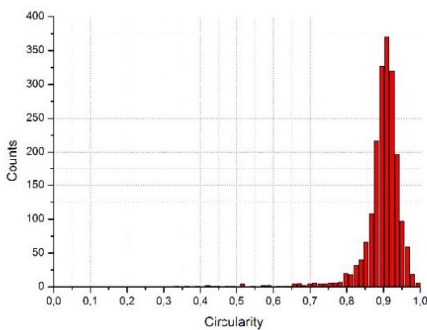
(c) Circularity of the NPs
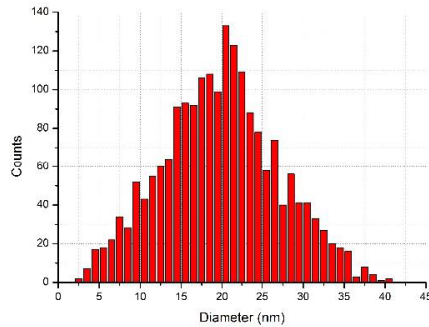
(d) Diameter distribution

Figure 6.27: Characterisation of the real array of nanoparticles whose data have been used as input data in the Green function model simulation.

visible wavelengths, increasing the input power and reducing the noise-to-signal ratio.

A complex mirror system defines the path followed by the light to reach the sample. The alignment of the setup is done periodically using a HeNe laser source. A diaphragm and a polariser are also included. The sample is placed in a holder conected to three michrometers and two goniometers. With all those the sample is correctly placed in the rotation axis so that the direct transmission and the specular reflections are correctly aligned with the incoming light beam too. At normal incidence, the light spot has 1.7mm.

During the measurements, a motion driver moves one of the goniometers in order to change the sample orientation. This makes the beam's angle of
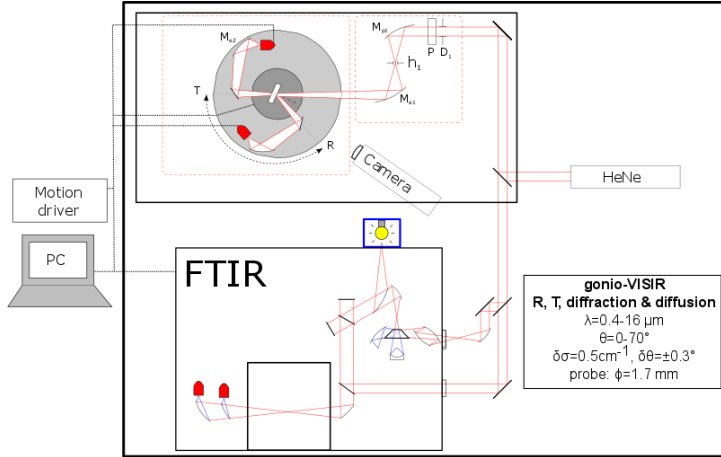
Figure 6.28: Angular dependent optical testing bench setup diagram.

incidence to change in $\Delta\theta$. At the same time, another mirror setup moves accordingly $2\Delta\theta$ to send the reflected light towards the Si diode sensor. All the process is controlled with ad-hoc software.

Some remarks have to be done on the results obtained with this setup.

- The measurements have been done from 3.5 to 65 degrees each 1.5degree and using a wavelength resolution better than 1nm. They have already been normalised so that they can be considered not only as qualitative but also quantitative results. Notice too that at $5deg$, close to the normal incidence where there is no difference between TE and TM polarisation, the measurements lead to the same values. This is a consistency proof for the measurements.

- The results have been substracted from the reflectivity of the original antireflection coating without any nanoparticle array on them. This is the same strategy that is used in numerical calculations in order to quantify the scattering of a nanostructure when a substrate is present[7]. This implies that the following contourplots show the scattering properties of the nanoparticle arrays.

- This strategy leads to both positive and negative values: The positive mean an increase in the scattering and the negative ones mean a decrease in the scattering. Because of the fact that the measurements corres-pond to specular reflectivity, negative values can be related with higher

---

[7]Some comments have been done on the difficulty of making a direct calculations of the Radar Cross Section (RCS) when there is a substrate in section 4.3.2.

transmissions or with higher absorptions within the nanoparticles. In principle, as shown in section 6.3, at long visible wavelengths the optical properties of the nanoparticles lead to an increase in the transmission towards the silicon. That has been verified experimentally in fig.6.12. Thus, there are some evidences for assuming higher transmission values, even if additional studies would be necessary to confirm this.

- When using a TE polarisation, as explained in section 3.5, the electric field is kept constant at any angle of incident as it is always paralel to the substrate whereas the magnetic field is angle dependent. The opposite is found when using a TM polarisation.

In fig.6.29, fig.6.29 and fig.6.30 some interesting facts can be verified. First of all, that the electric modes must be the main contributions to the scattering: Looking at fig.3.15, when using a TE polarised the scattering properties of the nanoparticle arrays are mainly the same, so almost no influence of the magnetic field is present. This has been verified (case a) in the graphs) at different sizes (whose size distribution is shown in fig.6.32).

A different behaviour is found when TM polarisation is used (case b)) as there is a clear trend in the reflectivity change, where the reached minima value is increased and blueshifted. This is consistent with the trends obtained for truncated spheres in section 4.3.2. Again, the angle dependente behaviour is the same for all studied sizes: At increasing incident angles, the vertical polarisability becomes more important in relative terms than the horizontal polarisability. Moreover, the polarisability values are in general smaller for the vertical component. Thus, the bigger the incident angle is, the lower the extinction effect of the nanoparticle will be. Moreover, the vertical polarisability remains almost constant with truncation angles whereas the second one is considerably redshifted with increasing truncation angles. Therefore, for any fixed truncation angle, increasing incident angles will produce a blueshift as the relative contribution of the vertical component will increase.

The main differences between the different sizes of the nanoparticles can be summarised in two conclusions:

- First, as expected from Mie, there is a redshift of the resonances at increasing sizes. Thus, the minima are redshifted from around 580nm for the smaller sizes in fig.6.32, to 700nm for the bigger ones. The effect of different truncation angles can also contribute to this redshift.

- The blueshift at increasing angles is also increased at bigger particles. Again, this can be due to different truncation angles in the sample but in any case the effect of the vertical component in bigger particles will be more important as its absolute polarisabiliy value will be always bigger than for smaller sizes.

When the ARC coating thickness is increased, a different optical behaviour is found for the particles. The arrays of nanoparticles are mainly the same that shown in fig.6.32 as they have been obtained in the same conditions. Therefore, the difference must be related with the substrate reflection effect.

The Green function model has been used to estimate the same results than fig.6.29 and fig.6.33. With the choice of the smaller particles, the dipole approach will be more realistic. The results are shown in fig.6.36

The simulation results do not fit the experimental results at all. But still they are interesting: For 30nm of ARC, the TE polarisation is almost angle independent, as it has been experimentally found. When the thickness of the ARC increase, there appear an angle dependency. Moreover, even if the maxima and the minima that are found in fig.6.29 and fig.6.33 are not clearly seen, the relative shift in intensity of the values follow the same trend.

This suggests that the difference between the simulated results and the experimental ones is not related with incorrect assumptions, but indeed because there are some effects that are not included. In particular, the Fano resonances has already been reported to appear in plasmonic systems and that both surrounding particles[10, 11] or the substrate itself[12, 13] can induce those kind of interference. The most representative of this phenomena, as explained in section 3.4.4 is an analytical asymmetric correcting lineshape (eq.3.4.4) that typically includes an asymmetric maxima and minima (fig.3.12).

Recent analytical studies dealing with spherical small particles have suggested the existence of a different Fano resonance: *an asymmetric lineshape for the intensity of light with a given polarization scattered along a given direction* that has been named *directional Fano resonance*[14]. In this thesis no directional considerations have been included from the analytical point of view, but this would be a very interesting continuation and development in a future work.

Therefore, the Fano resonance as the main difference between the simulated and the measured results is a reasonable hypothesis that should be verified y future studies. However, there are other facts and alternatives that should be studied:

- As explained in section 3.4.4, the b parameter in eq.3.71 can modify the intensity of the Fano resonance. That parameter increases with the intrinsic ohmic losses and thus for small (and lossy) particles the Fano inteference can be almost negligible.

- It has been reported that when metal (Ag) nanoparticles are placed near high index subrates such as Si the resonances are splitted in two types: *At short wavelengths, the resonances localised at the top of the particle, while at longer wavelengths they are localised at the Ag/substrate interface*[15]. This would fit with the experimental behaviour shown in fig.6.12 and should be studied carefully. In fact, using a SiO_2 (dielectric) spacer,

the authors attribute the unexpected resonances to Surface Plasmon Polaritons (SPP) and to geometrical resonances. This would imply that the considerations showed in section 3.4.2 are valid and that SPP can be considered in some cases within nanoparticles.
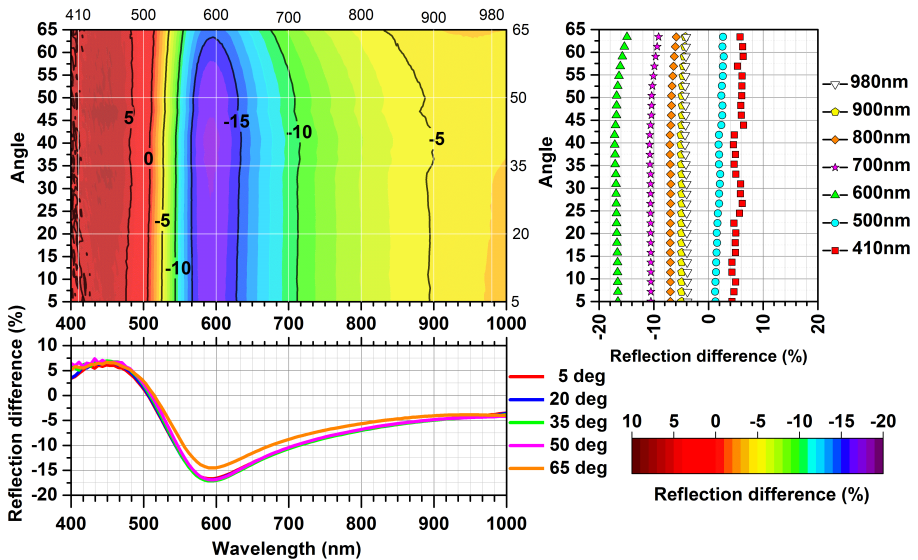
(a) TE ligth polarisation
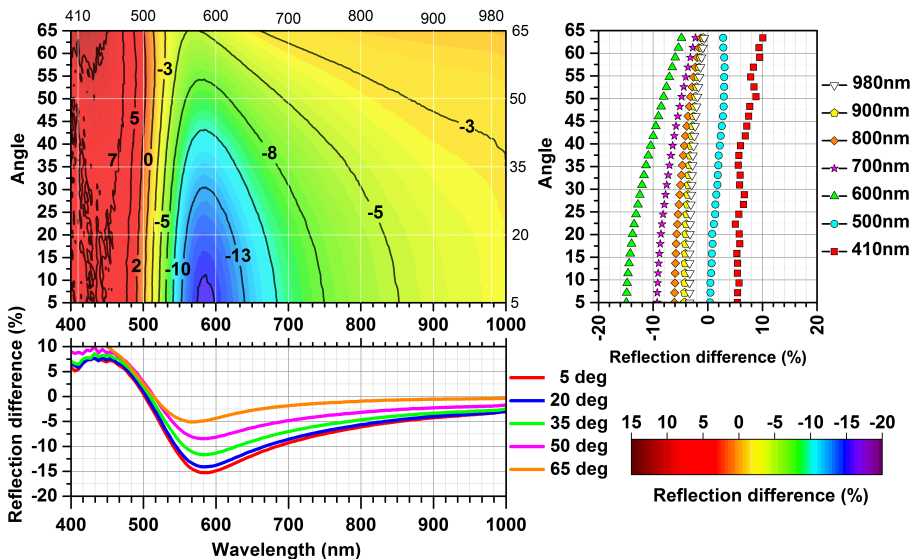
(b) TM ligth polarisation

Figure 6.29: Contour map for the angular dependency on the specular reflectivity for an array of Ag nanoparticles from 3nm of precursor layer on a 30nm SiO_x ARC and Silicon. The measurement is done using TE (a) and TM (b) polarisation. Different slices are done at constant angles and at different constant wavelengths. The angular resolution of the contour is of 1.5 degrees x 1 nm

(a) TE ligth polarisation

(b) TM ligth polarisation

Figure 6.30: Contour map for the angular dependency on the specular reflectivity for an array of Ag nanoparticles from 5nm of precursor layer on a 30nm SiO_x ARC and Silicon. The measurement is done using TE (a) and TM (b) polarisation. Different slices are done at constant angles and at different constant wavelengths. The angular resolution of the contour is of 1.5 degrees x 1 nm

(a) TE ligth polarisation

(b) TM ligth polarisation

Figure 6.31: Contour map for the angular dependency on the specular reflectivity for an array of Ag nanoparticles from 7nm of precursor layer on a 30nm SiO_x ARC and Silicon. The measurement is done using TE (a) and TM (b) polarisation. Different slices are done at constant angles and at different constant wavelengths. The angular resolution of the contour is of 1.5 degrees x 1 nm

Figure 6.32: Size distribution of the resulting array of NPs from different Ag precursor thicknesses on a 65nm SiO_x ARC on Si. The distributions are in arbitrary units, so only the shape and not the absolute values can be compared.
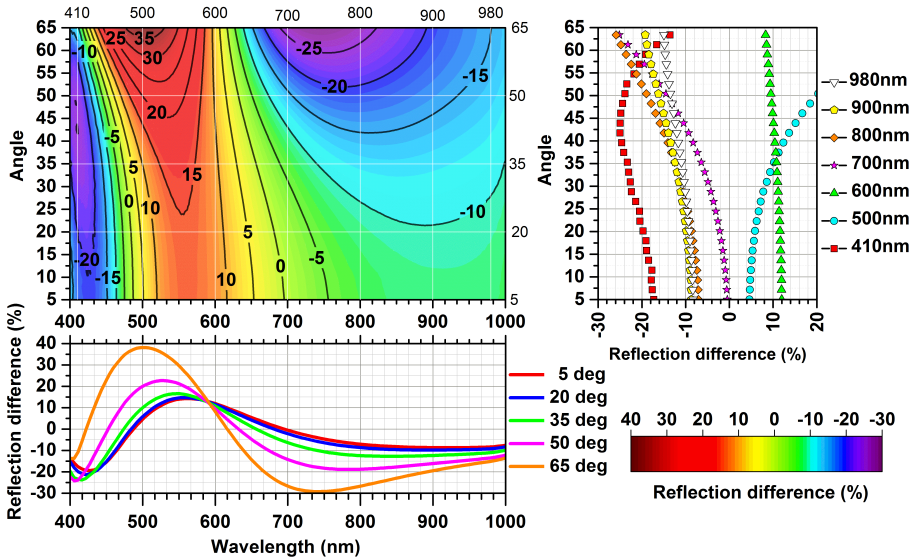
(a) TE ligth polarisation
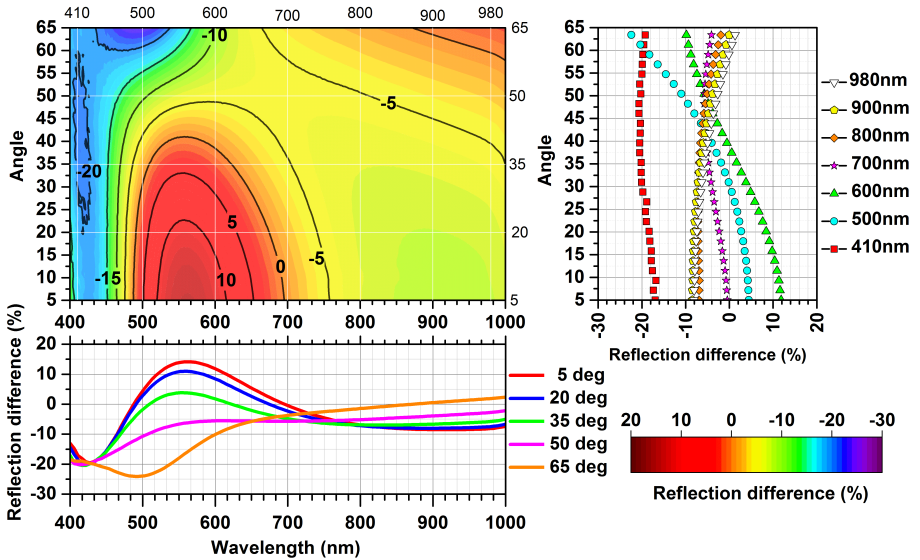
(b) TM ligth polarisation

Figure 6.33: Contour map for the angular dependency on the specular reflectivity for an array of Ag nanoparticles from 3nm of precursor layer on a 100nm SiO_x ARC and Silicon. The measurement is done using TE (a) and TM (b) polarisation. Different slices are done at constant angles and at different constant wavelengths. The angular resolution of the contour is of 1.5 degrees x 1 nm

(a) TE ligth polarisation

(b) TM ligth polarisation

Figure 6.34: Contour map for the angular dependency on the specular reflectivity for an array of Ag nanoparticles from 5nm of precursor layer on a 100nm SiO_x ARC and Silicon. The measurement is done using TE (a) and TM (b) polarisation. Different slices are done at constant angles and at different constant wavelengths. The angular resolution of the contour is of 1.5 degrees x 1 nm

(a) TE ligth polarisation

(b) TM ligth polarisation

Figure 6.35: Contour map for the angular dependency on the specular reflectivity for an array of Ag nanoparticles from 7nm of precursor layer on a 100nm SiO_x ARC and Silicon. The measurement is done using TE (a) and TM (b) polarisation. Different slices are done at constant angles and at different constant wavelengths. The angular resolution of the contour is of 1.5 degrees x 1 nm

(a) TE polarisation at 30nm ARC

(b) TM polarisation at 30nm ARC
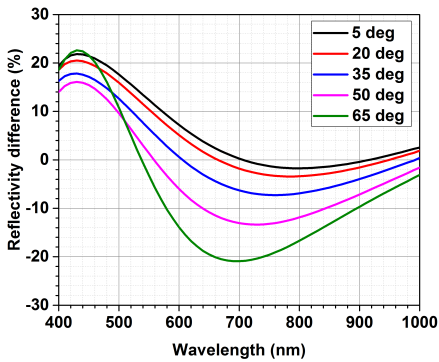
(c) TE polarisation at 100nm ARC
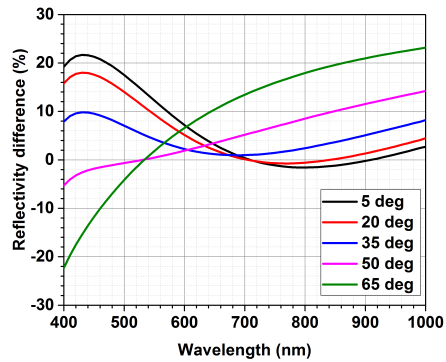
(d) TM polarisation at 100nm ARC

Figure 6.36: Simulated difference on specular reflectivity at different incident angles with the reference substrate with ARC.

Bibliography

[1] Mark J. Kerr, Andres Cuevas, and Ronald A. Sinton. Generalized analysis of quasi-steady-state and transient decay open circuit voltage measurements. *Journal of Applied Physics*, 91(1):399–404, 2002. doi: http://dx.doi.org/10.1063/1.1416134. URL http://scitation.aip.org/content/aip/journal/jap/91/1/10.1063/1.1416134.

[2] R Santbergen, T L Temple, R Liang, A H M Smets, R A C M M van Swaaij, and M Zeman. Application of plasmonic silver island films in thin-film silicon solar cells. *Journal of Optics*, 14(2):024010, 2012. URL http://stacks.iop.org/2040-8986/14/i=2/a=024010.

[3] G Galbiati, VD Mihailetchi, A Halm, R Roescu, and R Kopecek. Results on n-type ibc solar cells using industrial optimized techniques in the fabrication processing. *Energy Procedia*, 8:421–426, 2011.

[4] Zhizhong Yuan, Georg Pucker, Alessandro Marconi, Fabrizio Sgrignuoli, Aleksei Anopchenko, Yoann Jestin, Lorenza Ferrario, Pierluigi Bellutti, and Lorenzo Pavesi. Silicon nanocrystals as a photoluminescence down shifter for solar cells. *Solar Energy Materials and solar cells*, 95(4):1224–1227, 2011.

[5] Cheng Yang, Gang Zhang, Hua Min Li, Won Jong Yoo, Young Jun Park, and Jong Min Kim. Localized surface plasmon resonances caused by ag nanoparticles on sin for solar cell applications. *Journal of the Korean Physical Society*, 56(5):1488–1491, 2010.

[6] P. Spinelli, M. Hebbink, R. de Waele, L. Black, F. Lenzmann, and A. Polman. Optical impedance matching using coupled plasmonic nanoparticle arrays. *Nano Letters*, 11(4):1760–1765, 2011. doi: 10.1021/nl200321u. URL http://dx.doi.org/10.1021/nl200321u. PMID: 21410242.

[7] Rudi Santbergen, Hairen Tan, Miro Zeman, and Arno H. M. Smets. Enhancing the driving field for plasmonic nanoparticles in thin-film solar cells. *Opt. Express*, 22(S4):A1023–A1028, Jun 2014. doi: 10.1364/OE.22.0A1023. URL http://www.opticsexpress.org/abstract.cfm?URI=oe-22-104-A1023.

[8] S Pillai, FJ Beck, KR Catchpole, Z Ouyang, and MA Green. The effect of dielectric spacer thickness on surface plasmon enhanced solar cells for front and rear side depositions. *Journal of Applied Physics*, 109(7):073105, 2011.

[9] Mathieu Langlais, Jean-Paul Hugonin, Mondher Besbes, and Philippe Ben-Abdallah. Cooperative electromagnetic interactions between nanoparticles for solar energy harvesting. *Optics express*, 22(103):A577–A588, 2014.

[10] Boris Luk'yanchuk, Nikolay I Zheludev, Stefan A Maier, Naomi J Halas, Peter Nordlander, Harald Giessen, and Chong Tow Chong. The fano resonance in plasmonic nanostructures and metamaterials. *Nature materials*, 9(9):707–715, 2010.

[11] Nikolay A. Mirin, Kui Bao, and Peter Nordlander. Fano resonances in plasmonic nanoparticle aggregatesâĂ. *The Journal of Physical Chemistry A*, 113(16):4028–4034, 2009. doi: 10.1021/jp810411q. URL http://dx.doi.org/10.1021/jp810411q. PMID: 19371111.

[12] Shunping Zhang, Kui Bao, Naomi J.Halas, Hongxing Xu, and Peter Nordlander. Substrate-induced fano resonances of a plasmonic nanocube: A route to increased-sensitivity localized surface plasmon resonance sensors revealed. *Nano Letters*, 11(4):1657–1663, 2011. doi: 10.1021/nl200135r.

[13] Mikael Svedendahl and Mikael Käll. Fano interference between localized plasmons and interface reflections. *Acs Nano*, 6(8):7533–7539, 2012.

[14] Michael I. Tribelsky. Phenomenological approach to light scattering by small particles and directional fano's resonances. *EPL (Europhysics Letters)*, 104(3):34002, 2013. URL http://stacks.iop.org/0295-5075/104/i=3/a=34002.

[15] FJ Beck, E Verhagen, S Mokkapati, A Polman, and KR Catchpole. Resonant spp modes supported by discrete metal nanoparticles on high-index substrates. *Optics express*, 19(102):A146–A156, 2011.

Chapter 7

General conclusions and future work

From theory and fundamentals in chapters 2 and 3

A short review has been done to understand the behaviour of a homojunction solar cell, as well as the different currents involved and how the absorption properties and the colection probability in a c-Si solar cell are wavelength dependent. This means that the enhancement due to the presence of nanoparticles has to be tuned accordingly with the solar cell behaviour.

From the study of the dispersion diagram in a LSP, it has been shown how a nanoparticle will interact with light at any visible wavelength and incident angle. From that interaction, different simultaneous excitation orders are expected from Mie. Usually there is a predominating excitation order that will be defined at each wavelenght, size, material and surrounding media.

The Mie approach is a very useful and well-known strategy to solve the scattering and extincion of single spherical nanoparticles in homogeneous media. However, the validity of this solution is limited because none of the initial assumptions is fulfilled in the scope of this thesis: Non-spherical particles in arrays on a multilayered substrate. Nevertheless, the general trends are still valid.

One of the deviations from Mie is the excitation with sources different from a plane wave, such as those induced by surrounding nanoparticles. From there, the Fano interferences are expected to appear, as well as from the substrate effect. This phenomena, when applied to a non-conservative system such as a scattering nanoparticle, has to be corrected from the generic form with a parameter taking into account the radiative and intrinsic ohmic losses. The intensity of the inteference can then be reduced. Several Fano-like results have been found during this thesis and some references have been found in the literature that support this idea. Further studies should be done in order to verify whether they are Fano interferences as well as to fit the model parameters for a quantitative study.

From chapter 4 dealing with simulating properties

An analytical approach has been done from the susceptibility definition of a nanoparticle that sheds light on the frequency dependent extinction properties of a nanoparticle from a dipole-like approach. The module and the phase shift trends for the scattered field are shown.

It has also been explained how the substrate can easily be taken into account using Green Functions. For a 3D Helmoltz equation (wave equation), the Sommerfeld identity is a good strategy to include the multiple reflexion and transmissions at interferences. However, there are two main difficulties related with this approach:

- The oscillatory behaviour of the integrands make the resolution quite slow. In order to avoid this, a complex integration path should be used. Different approaches can be found here depending on whether the integration path encloses poles.

- The number of poles becomes unfeasable when a thick silicon substrate (beyond 5μm) is considered. Depending on the wavelength this can be solved by assuming a semiinfinite substrate when the absorption is high and the internal reflection of that finite substrate is negligible.

A Matlab code has been developed following Novotny's results for a 3 layered system simulating a solar cell structure. However, for the final simulations a similar code developed by Dr. Jean-Paul Hugonin[1] from the Insitute d'Optique CNRS-Université de Paris Sud has finally been modified. This code overcomes most of coding an programming issues.

In section 4.3 the model proposed for Jesper Jung for truncated nanoparticles over a substrate has been analysed, showing several numerical issues to take into account. The final results obtained for silver truncated nanoparticles have a good agreement with what is expected analytically for the frequency dependent scattering properties of a metal (section 4.1). When comparing with numerical simulations, some limitations are found related with the intrinsic assumption that is done for this model: The Quasi-Static Approximation (QSA) that neglects retardation effects and therefore the redshift related with increasing sizes.

The truncated sphere approach is taken because the real shape of the fabricated nanoparticles is closer and better results are expected from there. Moreover, it is possible to define a tensor polarisability that is perfectly compatible with the use of the Green functions used for simulations.

---

[1]jean-paul.hugonin@u-psud.fr

From chapter 5 on fabrication of nanoparticles

This chapter includes the experimental details of the nanoparticles fabricated. It is mainly focused on the self-aggregation method because it simplifies the fabrication process as it integrates the nanoparticles on the solar cell at the same time that they are produced. A short review of the thermodynamical details that lead to the self aggregation has been presented to shed light on the main parameters that modify the resulting array of nanoparticles: On the one hand, there is a thermodynamical driving force that modifies the system geometry to reduce the stress and the surface energy in the system. On the other hand, there is a kinetic driving force mainly related with the diffusion of matter. The analytical expressions are complicated and need of several materials properties not easy to obtain experimentally. However, this study has defined which parameters can modify the resulting array and from there some experimentals have been carried out.

From the fabrication point of view, the self-aggregation technique can be controlled to obtain either bigger and separate particles from thick precursor layers (15nm or more) or smaller and closer particles from thin precursor layers (around 3nm). The circularity usually increases with temperatures and time whereas the self-aggregation is not produced properly at very low temperatures, leading to unstable and irregular shapes. In any case, statistical normality tests show that, in most cases, the resulting array of nanoparticles cannot be summarised accurately as a gaussian distribution with an average size, even if in the literature average values are found.

The presence of collapsed and isolated particles are the main reason for that. In fact, more exhaustive image analysis prooves that the distributions that does not fit well with a single gaussian can in most cases be fitted properly with up to three gaussians: One corresponding for very small particles (the isolated ones), another of intermediate size that usually includes most of the data and another whose average size is around twice the average size distribution (pointing towards colapsed particles). This general trend it is not always accomplished as in some cases there are two real size distributions of circular and independent particles.

The main conclusion from here, it that it is not possible to give an accurate and general trend for the resulting array of nanoparticles and thus the simulations should be done using real data from the image analyisis from SEM measurements.

Another experimental issue that has been presented in chapter Chapter 5 is related with the fact that the nanoparticles are spoiled when kept in air and a protective capping layer has been developped to minimise this effect. The particularity of this system is that a flowable oxide resist is used instead of a PECVD process: This keeps the original array distribution almost invariant and avoids the risk of metal contamination of the PECVD reactor chamber. This

strategy has also been used to change the relative position of the nanoparticles within the Si substrate.

Finally, several proposals for improving the fabrication process are included for future works, mainly related with increasing the vaccum during the evaporation.

From chapter 6 for experimental and simulated results on integrated solar cells

Prior to integration on solar cells, optical measurements have been done using glass substrates, showing that there is a relevant scattering effect due to the presence of nanoparticles. This is a good starting point that suggests a possible enhancement in a solar cell. There is also an absorption loss that has to be taken into account.

Apart from purely optical measurements, some efforts have been done to estimate the electrooptical effect on a solar cell. In order to do that, two approaches have been used:

- Using a c-Si wafer and a photoconductance based minority carrier lifetime measurement system. By using two measurements regimes it is possible to fit experimentally an optical factor f_{opt} that is proportional to the amount of light that has been absorbed within the wafer and should be increased for better antireflection properties. The wavelength dependency has been included using dichroic filters.

- Using spectral response measurements (EQE) on a commercial solar cell. This has the advantage that the electrooptic response is directly measured instead of estimated by indirect measurements.

These approaches are interesting even if the studied geometry does not correspond to the finally integrated device: The near-field effects are not expected to be the most relevant in thick (around 180μm) solar cells whereas the scattering properties are still well estimated by using some glycerol that acts as an index matching layer.

A first conclusion from this preliminary study is that the trends obtained by both methods are quite similar and proves the validity of the first approach based on the photoconductance. A second conclusion shows that the effect of the nanoparticles when placed on a solar cell can lead to a decrease of the efficiency rather than to an increase. This decrease is mainly due to the intrinsic losses near an extinction resonance and is similar to the optical measurements shown in section 6.2.1.

The first integrated samples have prooved that there is an enhancement in reflectivity for a wide range of wavelengths. This enhancement seems to be related to the nanoparticle array which scatters preferentially towards the

silicon substrate. This reduction in reflectivity is translated to the electro-optical response (EQE), proving that the reduction in reflectivity is not only related with an increase in absorption but to a better light transmission to the Si substrate. No differences in the absorption profile are found in the IQE. Despite this enhancement, there is another undesirable effect found at shorter wavelengths where an extinction resonance is expected from the Mie calculations: An absorption loss that reduces drastically the spectral response and reduces the overall efficiency. This absorption loss was already seen on the glass samples shown in fig.6.5.

As the addition of the NP is interesting at long wavelengths, three strategies have been followed to reduce the undesirable effects at shorter wavelengths:

The first strategy is reducing the loss peak intensity. The intrinsic losses are difficult to avoid and the main option would be to use another metal (such as Al, which has recently been reported [141] as a better choice than Ag). This would be very interesting for a future study. The second strategy is shifting the resonance towards the UV. For this, the Mie approach points towards smaller particles but this is not feasible as the scattering cross section will be reduced excessively. Another possibility is to reduce the refractive index of the surrounding media. For this, different relative positions between the nanoparticles and the silicon substrate (with high refractive index) are studied. Nanoparticles have also been embedded within a 100nm SiO_x ARC at different positions. This has been done to minimise the back-scattered field that increases the reflectivity as well as to change the relative position of the nanoparticle and the high index Si substrate. From this second strategy, it has been verified that there is a real dependence of the optical properties of nanoparticles on their position relative to the high index substrate. Of special interest is the change in the trend that is found from the reflectivity point of view when the nanoparticles are separated from the substrate: When they are close to the c-Si substrate and before using a capping layer, they are mainly reflective, but as they are separated from the c-Si with a layer of $SiOx$ the reflectivity peak becomes a valley. This is related again with the substrate effect and the light reflected from it that leads to new excitation modes or with constructive/destructive interferences.

When the second strategy is applied to the LIMA samples, the position dependent effect on the intrinsic losses is also seen in the IQE measurements. However, no enhancement is produced because the lower absorption losses correspond to the worst reflectivity values of the Antireflection Coating (ARC). This points towards a reduction of the losses related with a reduction of the electric field exciting the nanoparticle which however implies decreased light scattering light scattering.

Finally, the third strategy is used for integrating the nanoparticles within the IBC solar cells consisting in putting them at the back side. Some optical

measurements have been performed and the maximum current enhancement that was obtained with this strategy is established as $\Delta J_{sc} = 0.44 mA/cm^2$. The losses at shorter wavelengths observed when the nanoparticles are at the front side are now avoided and the back scattering properties of the nanoparticles is the main phenomena. Diffuse reflectivity measurements were carried out to test the suitability of the third strategy. There is evidence for the absorption increase in thick silicon substrates ($> 150\mu$m): When nanoparticles are placed on the front, the increase in reflectivity reduces the overall efficiency. But when placed on the back, the internal reflectivity is increased leading to better light trapping. The main advantage of the nanoparticles when compared with a mirror is that the measurements show the angular power distribution is much more homogeneous due to the scattering effect. However, due to the IBC structure of the reference solar cell and despite efforts to avoid leakage phenomena, the presence of NPs on the back side of the solar cell shunts the solar cell.

To sum up the main conclusions related with the integration of nanoparticles on solar cells, the following ideas are pointed out:

- When big nanoparticles (radius> 100nm) are placed at the front side, the reflectivity is much increased, leading to a lower absorption. When smaller particles are used (radius$< 50nm$) the absorption dominates over the scattering but still some scattering is measured. There is experimental proof showing better antireflection properties in a solar cell for a broad range of visible frequencies. This optical enhancement produces an increase in the spectral response (thus, to a real absorption enhancement). However, that enhancement is eclipsed by the losses around the extinction resonance.

- When the relative positon of the nanoparticles within an antireflection coating is controlled, interesting behaviour is found from the optical point of view, confirming the influence of the substrate and the surrounding media beyond a simple refractive index correction in Mie approach. This strategy also avoids degradation and reduces the increase of reflectivity due to the nanoparticles (back-scattering).

- When the nanoparticles are placed on the back, big nanoparticles are preferred because the front side reflectivity is not limiting anymore and a high internal reflectivity is intended. Special attention must be paid to the integration in IBC solar cells in order to avoid shunting issues.

The overall consequence is that Ag nanoparticles have not lead to any real enhancement: Even if the optical properties of the nanoparticles lead to improved scattering and light interaction within the solar cell, they are not suitable for improving the solar cell efficiency until an appropriate configuration of material and structure is found that reduces the intrinsic losses.

This reduction cannot be enhanced only by changing the relative position of the nanoparticles within the cell because, even if very different behaviours have been obtained, none of them has led to a global increase in current or efficiency. The only realistic alternative was to place them at the back and from the optical measurements an increase of 0.44mA/cm2 would be possible. Unfortunately, the shunting issues related with the presence of metallic nanoparticles have made any electrooptical characterisation unfeasible.

The influence and importance of the quality of the resulting array of nanoparticles in reducing losses and in controlling the resonance position is well known: Irregular shapes, coalesced nanoparticles and strong particle to particle interactions should be avoided for better transmission results. Therefore, alternative approaches to particle fabrication rather than self-aggregation should be used in future studies, such as chemical synthesis. In addition, bigger particles lead to an interesting increase of the diffused transmission, but also to an increase in the backscattered light and reflectivity losses.

The modelling approach followed in this thesis leads to good general trends (fig.6.25 show the same absorption losses than the ones shown in fig.6.12). However, a closer comparison has demonstrated that the agreement is not so good (fig.6.26). Differences between simulated and experimental results may put on doubt the suitability of the analytical model. An experimental study of the model is difficult because of the fact that transmissions measurements are not available in the visible range using silicon substrates. For this reason, angular measurements with polarised light have been carried out. Different nanoparticle sizes and SiO_x spacer thicknesses are studied.

The results show that when the nanoparticles are close to the silicon substrate (separated by only 30nm of SiO_x), the main contribution on the scattered fields is due to the electric component. This has been found for the different studied arrays, whose average radii lay between 10 to 60nm. In this case, the Mie approach predicts that behaviour and the size range points towards an electric dipole scattering mode.

When the same arrays are placed further from the silicon substrate, the behaviour completely changes: There is an angular dependence on both the electric and the magnetic field and this is not expected from the electric dipole approach. The differences are related with multiple reflections in the multilayered substrate as the nanoparticle arrays are equivalent to those for the thinner spacer.

Even if the simulated results do not always fit properly with the experimental ones, the deviation trend is the same for all samples. This suggests that the model assumptions are not wrong but incomplete and some other phenomena should be included in future studies. In particular, a Fano-like resonance can explain the observed deviation and this is something not taken into account in the model and that is proposed for future studies.

Valencia Nanophotonics Technology Center

ESCUELA TÉCNICA
SUPERIOR INGENIEROS
INDUSTRIALES VALENCIA

UNIVERSITAT
POLITÈCNICA
DE VALÈNCIA

In order to shed some light on the suitability of the model, it is useful to compare it with other analytical models for simulating nanoparticles on a substrate. One of the better-known is shown in Johansson [142] . In there, the same Green Function for an homogenous space is used (the one for the Helmoltz equation). However, their corrected expressions are far more complex than the ones that have been used here: They use a multipole expansion for the equivalent radiating sources. This multipole expansion implicitly takes into account the nanoparticle interaction and the substrate effect (similarly to what happens with the image dipole approximation approach cited in point 3.4.3). This will probably lead to more exact solutions because it makes less assumptions. However, the cost of this increase accuracy is a high complexity that makes the physical understanding of the phenomena involved much more difficult. One of the main advantages of this thesis is that, even if the accuracy of the results is not as good as a purely numerical simulation, the chosen analytical expressions have been analysed to obtain a better understanding of the phenomena. The key point for the analytical simplification is related with the dipole assumption done in eq.4.44 and that has allowed us to split the effect of the directional polarisability from the effect of the substrate influence from the radiating source of light. This would not have been feasible with the expressions included in Johansson [142]. The cost of the dipole simplification is, therefore, directly related with the number of higher excitation modes (quadrupoles, etc.) that are not taken into account. In order to minimise this and to give validity to this hypothesis, the Mie approach has been followed in section 4.4 to have a reference, even if not exact, of which are the conditions to be able to assume a dipole-like behaviour. Another limitation during this thesis are the numerical issues that have been found in Jesper Jung approach for calculating the directional polarisability and that may lead to inaccurate results. A different approach would be the one proposed by Mertz[143]. This latter is only valid for non-absorbing surrounding media but for the solar cell application this can be valid as usually SiO_2 and SiN have a very low absorbance in the visible range. This is proposed for future studies. To conclude with, the modelling approach followed in this thesis has his advantages but does not include in its formulation all the phenomena that can be involved. Higher order excitation modes should be included as the electric dipole seems not to be enough. Moreover, more accurate values for the anisotropic polarisability should be obtained. Finally, the experimental results point towards the importance of including Fano resonances of the nanoparticles among themselves or with the substrate.

Bibliography

[1] Key world energy statistics 2014. Free Download, 2014. URL http://www.iea.org/publications/freepublications/publication/keyworld2014.pdf.

[2] Gru Brundtland, Mansour Khalid, Susanna Agnelli, Sali Al-Athel, Bernard Chidzero, Lamina Fadika, Volker Hauff, Istvan Lang, Ma Shijun, Margarita Morino de Botero, et al. Our common future ('the brundtland report'). 1987.

[3] United Nations. Rio declaration on environment and development, June 1992. URL http://www.un-documents.net/rio-dec.htm.

[4] United Nations. Johannesburg declaration on sustainable development, September 2002. URL http://www.un-documents.net/jburgdec.htm.

[5] Horizon 2020. work programme 10: Secure, clean and efficient energy (revised). Technical report, European Commission, April 2015.

[6] International technology roadmap for photovoltaic (itrpv.net) results 2014. Technical report Rev.1., ITRPV, July 2015.

[7] Dennis M Callahan, Jeremy N Munday, and Harry A Atwater. Solar cell light trapping beyond the ray optic limit. *Nano letters*, 12(1):214–218, 2012.

[8] Zhizhong Yuan, Georg Pucker, Alessandro Marconi, Fabrizio Sgrignuoli, Aleksei Anopchenko, Yoann Jestin, Lorenza Ferrario, Pierluigi Bellutti, and Lorenzo Pavesi. Silicon nanocrystals as a photoluminescence down shifter for solar cells. *Solar Energy Materials and solar cells*, 95(4):1224–1227, 2011.

[9] Ira N. Levine. *Química cuántica*. Number ISBN:84-205-3096-4. Prentice Hall, 5th edition, 2001.

[10] Ralph H. Petrucci, William S. Harwood, and Herring F. Geoffrey. *Química General*. Prentice Hall, 2003.

[11] Martin S. Silberberg. *Principles of General Chemistry*. Mc Graw Hill, 2007.

[12] Jenny Nelson. *The physics of solar cells*. Number ISBN-13-978-1-86094-340-9. Imperial College Press, 2009.

[13] S. Salivahanan and Kumar N. Suresh. *Electronic Devices and Circuits*. Mc Graw Hill Education, 2011.

[14] Martin A. Green. Intrinsic concentration, effective densities of states, and effective mass in silicon. *Journal of Applied Physics*, 67(6):2944–2954, 1990. doi: http://dx.doi.org/10.1063/1.345414. URL `http://scitation.aip.org/content/aip/journal/jap/67/6/10.1063/1.345414`.

[15] Alan H. Marshak and Karel M. van Vliet. On the separation of quasi-fermi levels and the boundary conditions for junction devices. *Solid-State Electronics*, 23(12):1223 – 1228, 1980. ISSN 0038-1101. doi: http://dx.doi.org/10.1016/0038-1101(80)90116-1.

[16] Otwin Breitenstein, Jan Bauer, Karsten Bothe, Wolfram Kwapil, Dominik Lausch, Uwe Rau, Jan Schmidt, Matthias Schneemann, Martin C. Schubert, Jan-Martin Wagner, and Wilhelm Warta. Understanding junction breakdown in multicrystalline solar cells. *Journal of Applied Physics*, 109(7):071101, 2011. doi: http://dx.doi.org/10.1063/1.3562200.

[17] F.A. Lindholm, J.G. Fossum, and E.L. Burgess. Application of the superposition principle to solar-cell analysis. *IEEE Transactions on Electron Devices*, 26(3):165–171, 1979. ISSN 0018-9383.

[18] Robert F Pierret et al. *Semiconductor device fundamentals*. Addison-Wesley Reading, MA, 1996.

[19] Neil W. Ashcroft and David N. Mermin. *Solid State Physics*. Thomson Learning, 1976. ISBN 0030839939. URL `http://www.amazon.com/exec/obidos/redirect?tag=citeulike07-20&path=ASIN/0030839939`.

[20] Charles Kittel. *Introduction to Solid State Physics*. John Wiley & Sons, Inc., New York, 6th edition, 1986.

[21] Christiana Honsberg and Stuart Bowden. Pvcdrom, July 2015. URL `www.pveducation.org`.

[22] VL Bonch-Bruevich and EG Landsberg. Recombination mechanisms. *physica status solidi (b)*, 29(1):9–43, 1968. doi: 10.1002/pssb.19680290102.

[23] K Schick, E Daub, S Finkbeiner, and P Würfel. Verification of a generalized planck law for luminescence radiation from silicon solar cells. *Applied Physics A*, 54(2):109–114, 1992.

[24] W Michaelis and MH Pilkuhn. Radiative recombination in silicon p-n junctions. *physica status solidi (b)*, 36(1):311–319, 1969.

[25] T Trupke, Mr A Green, P Würfel, PP Altermatt, A Wang, J Zhao, and R Corkish. Temperature dependence of the radiative recombination coefficient of intrinsic crystalline silicon. *Journal of Applied Physics*, 94 (8):4930–4937, 2003.

[26] S Michael, AD Bates, and MS Green. Silvaco atlas as a solar cell modeling tool. In *Photovoltaic Specialists Conference, 2005. Conference Record of the Thirty-first IEEE*, pages 719–721. IEEE, 2005.

[27] Halvard Haug, Achim Kimmerle, Johannes Greulich, Andreas Wolf, and Erik Stensrud Marstein. Implementation of fermi–dirac statistics and advanced models in pc1d for precise simulations of silicon solar cells. *Solar Energy Materials and Solar Cells*, 131:30–36, 2014.

[28] Chetan S. Solanki, Brij M. Arora, Juzer Vasi, and Mahesh B. Patil. Solar cell simulation using pc1d simulator. In *Solar Photovoltaics*, pages 130–146. Foundation Books, 2012. ISBN 9789382993254. URL `http://dx.doi.org/10.1017/9789382993254.017`. University Publishing Online.

[29] Mark J. Kerr, Andres Cuevas, and Ronald A. Sinton. Generalized analysis of quasi-steady-state and transient decay open circuit voltage measurements. *Journal of Applied Physics*, 91(1):399–404, 2002. doi: http://dx.doi.org/10.1063/1.1416134. URL `http://scitation.aip.org/content/aip/journal/jap/91/1/10.1063/1.1416134`.

[30] U.S.A. National Nanotechnology Initiative. Nanotechnology definition. url: www.nano.gov/nanotech-101/what/definition, May 2014.

[31] SA Maier. *Plasmonics: Fundamentals and Applications*. Springer, 2007. URL `http://www.springer.com/west/home/librarians/springer+news?SGWID=4-40157-22-173660338-0`.

[32] Joseph Larmor. A dynamical theory of the electric and luminiferous medium. *Proceedings of the Royal Society of London*, 54(326-330):438–461, 1893.

[33] Mathieu L Juan, Maurizio Righini, and Romain Quidant. Plasmon nano-optical tweezers. *Nature Photonics*, 5(6):349–356, 2011.

[34] Gustav Mie. Beiträge zur optik trüber medien, speziell kolloidaler metallösungen. *Annalen der Physik*, 330(3):377Ű445, 1908.

[35] John Strutt. On the transmission of light through an atmosphere containing small particles in suspension, and on the origin of the blue of the sky. *Philosophical Magazine, series 5*, 47:375–394, 1899.

[36] Alexandra Boltasseva and Harry A. Atwater. Low-loss plasmonic metamaterials. *Science*, 331(6015):290–291, 2011. doi: 10.1126/science. 1198258.

[37] Fritz Rohrlich. Dynamics of a charged particle. *Phys. Rev. E*, 77:046609, Apr 2008. doi: 10.1103/PhysRevE.77.046609. URL http://link.aps. org/doi/10.1103/PhysRevE.77.046609.

[38] Philip Pearle. Classical electron models. In *Electromagnetism*, pages 211–295. Springer, 1982.

[39] H. A. Haus. On the radiation from point charges. *American Journal of Physics*, 54(12):1126–1129, 1986. doi: http://dx.doi.org/10.1119/ 1.14729. URL http://scitation.aip.org/content/aapt/journal/ ajp/54/12/10.1119/1.14729.

[40] Craig F. Bohren and Donald R. Huffman. *Absorption and Scattering of Light by Small Particles*, chapter Absorption and Scattering by a Sphere, pages 82–129. Wiley Interscience, 2007.

[41] DF Swinehart. The beer-lambert law. *Journal of chemical education*, 39 (7):333, 1962.

[42] S Sivasubramanian, A Widom, and YN Srivastava. The clausius–mossotti phase transition in polar liquids. *Physica A: Statistical Mechanics and its Applications*, 345(3):356–366, 2005.

[43] F. W. J. Olver, D. W. Lozier, R. F. Boisvert, and C. W. Clark, editors. *NIST Handbook of Mathematical Functions*. Cambridge University Press, New York, NY, 2010. National Institute of Standards and Technology.

[44] Timothy J. Davis, Kristy C. Vernon, and Daniel E. Gómez. Effect of retardation on localized surface plasmon resonances in a metallic nanorod. *Opt. Express*, 17(26):23655–23663, Dec 2009. doi: 10.1364/ OE.17.023655. URL http://www.opticsexpress.org/abstract.cfm? URI=oe-17-26-23655.

[45] Jerome Nappa, Isabelle Russier-Antoine, Emmanuel Benichou, Christian Jonin, and Pierre-François Brevet. Wavelength dependence of the retardation effects in silver nanoparticles followed by polarization resolved hyper rayleigh scattering. *Chemical Physics Letters*, 415(4âĂŞ6):246 – 250, 2005. ISSN 0009-2614. doi: http://dx.doi.org/10.1016/j.cplett.2005. 08.143. URL http://www.sciencedirect.com/science/article/pii/ S0009261405012480.

[46] Viktor Myroshnychenko, Jessica Rodríguez-Fernández, Isabel Pastoriza-Santos, Alison M Funston, Carolina Novo, Paul Mulvaney, Luis M Liz-Marzán, and F Javier García de Abajo. Modelling the optical response of gold nanoparticles. *Chemical Society Reviews*, 37(9):1792–1805, 2008.

[47] Shoji Asano and Giichi Yamamoto. Light scattering by a spheroidal particle. *Appl. Opt.*, 14(1):29–49, Jan 1975. doi: 10.1364/AO.14.000029. URL http://ao.osa.org/abstract.cfm?URI=ao-14-1-29.

[48] I. Gurwich, N. Shiloah, and M. Kleiman. The recursive algorithm for electromagnetic scattering by tilted infinite circular multilayered cylinder. *Journal of Quantitative Spectroscopy and Radiative Transfer*, 63 (2-6):217–229, 1999. doi: 10.1016/S0022-4073(99)00017-5. URL http://www.scopus.com/inward/record.url?eid=2-s2.0-0032694504&partnerID=40&md5=1e8f94f04debeb9331b025a6451cb9d1. cited By 16.

[49] I. Gurvich, N. Shiloah, and M. Kleiman. Calculations of the mie scattering coefficients for multilayered particles with large size parameters. *Journal of Quantitative Spectroscopy and Radiative Transfer*, 70 (4âĂŞ6):433 − 440, 2001. ISSN 0022-4073. doi: http://dx.doi.org/10.1016/S0022-4073(01)00021-8. URL http://www.sciencedirect.com/science/article/pii/S0022407301000218. Light Scattering by Non-Spherical Particles.

[50] Yuriy A Akimov and Wee Shing Koh. Design of plasmonic nanoparticles for efficient subwavelength light trapping in thin-film solar cells. *Plasmonics*, 6(1):155–161, 2011.

[51] Kim Un-Chol and Jiang Xiao-Qing. Numerical analysis of efficiency enhancement in plasmonic thin-film solar cells by using the silvaco tcad simulator. *Chinese Physics Letters*, 29(6):067301, 2012.

[52] Luigi La Spada, Renato Iovine, and Lucio Vegni. Nanoparticle electromagnetic properties for sensing applications. *Advances in Nanoparticles*, 1(2):9–14, August 2012. doi: 10.4236/anp.2012.12002.

[53] Piotr J. Flatau. Improvements in the discrete-dipole approximation method of computing scattering and absorption. *Opt. Lett.*, 22(16):1205–1207, Aug 1997. doi: 10.1364/OL.22.001205. URL http://ol.osa.org/abstract.cfm?URI=ol-22-16-1205.

[54] Bruce T Draine and Piotr J Flatau. User guide for the discrete dipole approximation code ddscat 7.3. *arXiv preprint arXiv:1305.6497*, 2013.

[55] DW Mackowski and MI Mishchenko. A multiple sphere t-matrix fortran code for use on parallel computer clusters. *Journal of Quantitative Spectroscopy and Radiative Transfer*, 112(13):2182–2192, 2011.

[56] E. Prodan, C. Radloff, N. J. Halas, and P. Nordlander. A hybridization model for the plasmon response of complex nanostructures. *Science*, 302 (5644):419–422, 2003. doi: 10.1126/science.1089171. URL http://www.sciencemag.org/content/302/5644/419.abstract.

[57] Shu-Chun Yang, Hiromu Kobori, Chieh-Lun He, Meng-Hsien Lin, Hung-Ying Chen, Cuncheng Li, Masayuki Kanehara, Toshiharu Teranishi, and Shangjr Gwo. Plasmon hybridization in individual gold nanocrystal dimers: Direct observation of bright and dark modes. *Nano Letters*, 10(2): 632–637, 2010. doi: 10.1021/nl903693v. URL http://dx.doi.org/10.1021/nl903693v. PMID: 20058898.

[58] Prashant K. Jain and Mostafa A. El-Sayed. Plasmonic coupling in noble metal nanostructures. *Chemical Physics Letters*, 487(4âĂŞ6):153 – 164, 2010. ISSN 0009-2614. doi: http://dx.doi.org/10.1016/j.cplett.2010.01.062. URL http://www.sciencedirect.com/science/article/pii/S0009261410001193.

[59] Fuyi Chen, Negash Alemu, and Roy L. Johnston. Collective plasmon modes in a compositionally asymmetric nanoparticle dimer. *AIP Advances*, 1(3):032134, 2011. doi: http://dx.doi.org/10.1063/1.3628346. URL http://scitation.aip.org/content/aip/journal/adva/1/3/10.1063/1.3628346.

[60] P. Nordlander, C. Oubre, E. Prodan, K. Li, and M. I. Stockman. Plasmon hybridization in nanoparticle dimers. *Nano Letters*, 4(5):899–903, 2004. doi: 10.1021/nl049681c. URL http://dx.doi.org/10.1021/nl049681c.

[61] Y. Ekinci, A. Christ, M. Agio, O. J. F. Martin, H. H. Solak, and J. F. Löffler. Electric and magnetic resonances in arrays of coupled gold nanoparticle in-tandem pairs. *Opt. Express*, 16(17):13287–13295, Aug 2008. doi: 10.1364/OE.16.013287. URL http://www.opticsexpress.org/abstract.cfm?URI=oe-16-17-13287.

[62] Giuseppe Parisi, Pierfrancesco Zilio, and Filippo Romanato. Complex bloch-modes calculation of plasmonic crystal slabs by means of finite elements method. *Opt. Express*, 20(15):16690–16703, Jul 2012. doi: 10.1364/OE.20.016690. URL http://www.opticsexpress.org/abstract.cfm?URI=oe-20-15-16690.

[63] DS Kim, SC Hohng, V Malyarchuk, YC Yoon, YH Ahn, KJ Yee, JW Park, J Kim, QH Park, and Ch Lienau. Microscopic origin of surface-plasmon radiation in plasmonic band-gap nanostructures. *Physical review letters*, 91(14):143901–143901, 2003.

[64] HL Offerhaus, B van den Bergen, M Escalante, FB Segerink, JP Korterik, and NF van Hulst. Creating focused plasmons by noncollinear phasematching on functional gratings. *Nano letters*, 5(11):2144–2148, 2005.

[65] H. Ditlbacher, J. R. Krenn, G. Schider, A. Leitner, and F. R. Aussenegg. Two-dimensional optics with surface plasmon polaritons. *Applied Physics Letters*, 81(10):1762–1764, 2002. doi: http://dx.doi.org/10.1063/1.1506018. URL http://scitation.aip.org/content/aip/journal/apl/81/10/10.1063/1.1506018.

[66] Grzegorz Grzela, Djamila Hourlier, and Jaime Gómez Rivas. Polarization-dependent light extinction in ensembles of polydisperse vertical semiconductor nanowires: A mie scattering effective medium. *Physical Review B*, 86(4):045305, 2012.

[67] Marc A. Taubenblatt and Tuyen K. Tran. Calculation of light scattering from particles and structures on a surface by the coupled-dipole method. *J. Opt. Soc. Am. A*, 10(5):912–919, May 1993. doi: 10.1364/JOSAA.10.000912. URL http://josaa.osa.org/abstract.cfm?URI=josaa-10-5-912.

[68] Kristy C Vernon, Alison M Funston, Carolina Novo, Daniel E Gómez, Paul Mulvaney, and Timothy J Davis. Influence of particle- substrate interaction on localized plasmon resonances. *Nano letters*, 10(6):2080–2086, 2010.

[69] Shunping Zhang, Kui Bao, Naomi J.Halas, Hongxing Xu, and Peter Nordlander. Substrate-induced fano resonances of a plasmonic nanocube: A route to increased-sensitivity localized surface plasmon resonance sensors revealed. *Nano Letters*, 11(4):1657–1663, 2011. doi: 10.1021/nl200135r.

[70] Gallinet Benjamin and Olivier J.F.Martin. Influence of electromagnetic interactions on the line shape of plasmonic fano resonances. *ACS Nano*, 5(11):8999–9008, 2011. doi: 10.1021/nn203173r.

[71] Joe S. Yong, Satanin Arkady M., and Kim Chang Sub. Classical analogy of fano resonances. *Physica S*, 74:259–266, 2006. doi: 10.1088/0031-8949/74/2/020.

[72] Benjamin Gallinet, A. Lovera, T. Siegfried, H. Sigg, and O.J.F.Martin. Fano resonant plasmonic systems: Functioning principles and applications. volume 18, 2012. doi: http://dx.doi.org/10.1063/1.4750081.

[73] Mikael Svedendahl and Mikael Käll. Fano interference between localized plasmons and interface reflections. *Acs Nano*, 6(8):7533–7539, 2012.

[74] D.S. JONES. {CHAPTER} 1 - {THE} {REPRESENTATION} {OF} {THE} {ELECTROMAGNETIC} {FIELD}. In D.S. JONES, editor, *The Theory of Electromagnetism*, pages 1 – 99. Pergamon, 1964. ISBN 978-0-08-013686-8. doi: http://dx.doi.org/10.1016/B978-0-08-013686-8.50006-X. URL `http://www.sciencedirect.com/science/article/pii/B978008013686850006X`.

[75] I.V. Lindell. Time-domain te/tm decomposition of electromagnetic sources. *Antennas and Propagation, IEEE Transactions on*, 38(3):353–358, Mar 1990. ISSN 0018-926X. doi: 10.1109/8.52242.

[76] SergeyN. Savenkov. Jones and mueller matrices: structure, symmetry relations and information content. In AlexanderA. Kokhanovsky, editor, *Light Scattering Reviews 4*, Springer Praxis Books, pages 71–119. Springer Berlin Heidelberg, 2009. ISBN 978-3-540-74275-3. doi: 10.1007/978-3-540-74276-0_3. URL `http://dx.doi.org/10.1007/978-3-540-74276-0_3`.

[77] D.J. Griffiths. *Introduction To Electrodynamics 3Rd Ed.* Prentice-Hall Of India Pvt. Limited, 2007. ISBN 9788120316010. URL `https://books.google.es/books?id=3LbMygAACAAJ`.

[78] P. Boulanger and M.A. Hayes. *Bivectors and Waves in Mechanics and Optics*. Applied Mathematics. Taylor & Francis, 1993. ISBN 9780412464607. URL `https://books.google.es/books?id=QNOKs3fTPpAC`.

[79] MA Dupertuis, B Acklin, and M Proctor. Generalization of complex snell–descartes and fresnel laws. *JOSA A*, 11(3):1159–1166, 1994.

[80] MA Dupertuis, B Acklin, and M Proctor. Generalized energy balance and reciprocity relations for thin-film optics. *JOSA A*, 11(3):1167–1174, 1994.

[81] Malvin Carl Teich Bahaa E.A. Saleh. *Fundamentals of Photonics*. Wiley-Interscience, 2nd edition edition, 2007. ISBN: 978-0-471-35832-9.

[82] Paul Drude. Zur elektronentheorie der metalle. *Annalen der Physik*, 306: 566, 1900. doi: DOI:10.1002/andp.19003060312.

[83] H.A. Lorentz. The motion of electricity in metals. In *Collected Papers*, pages 307–332. Springer Netherlands, 1935. ISBN 978-94-015-2216-8. doi: 10.1007/978-94-015-3449-9_13.

[84] K.H. Lee, I. Ahmed, R.S.M. Goh, E.H. Khoo, E.P. Li, and T.G.G Hung. Implementation of the fdtd method based on lorentz-drude dispersive

model on gpu for pplasmonic applications. *Progress in Electromagnetics Research*, 116:pp. 441–456, 2011.

[85] A. Sommerfeld and H. Bethe. Elektronentheorie der metalle. In *Aufbau Der ZusammenhÃdngenden Materie*, volume 24/2 of *Handbuch der Physik*, pages 333–622. Springer Berlin Heidelberg, 1933. ISBN 978-3-642-89260-8. doi: 10.1007/978-3-642-91116-3_3.

[86] M. Quinten. *Optical Properties of Nanoparticle Systems: Mie and Beyond*. Wiley, 2010. ISBN 9783527633159. URL https://books.google.es/books?id=X9hDAfDAP-kC.

[87] J. V. Ortiz. Quasiparticle approximations and electron propagator theory. *International Journal of Quantum Chemistry*, 95(4-5):593–599, 2003. ISSN 1097-461X. doi: 10.1002/qua.10632.

[88] P.B. Johnson and R.W. Christy. Optical constants of the noble metals. *Physical Review B*, 6:4370–4379, 1972. doi: 10.1103/PhysRevB.6.4370.

[89] E.J. Borowski and J.M. Borwein. *Collins Dictionary of Mathematics*. Collins Dictionary of Series. HarperCollins, 2002. ISBN 9780007102952. URL https://books.google.es/books?id=XyA6AQAAIAAJ.

[90] E.T. Whittaker. *The Calculus of Observations - A Treatise on Numerical Mathematics*. Read Books, 2012. ISBN 9781447457657. URL https://books.google.es/books?id=Htk3MAEACAAJ.

[91] Ivar Stakgold and Michael J Holst. *Green's functions and boundary value problems*, volume 99. John Wiley & Sons, 2011.

[92] Dean G. Duffy. *GreenŠs Functions with Applications*, volume 99. John Wiley & Sons, second edition edition, 2015.

[93] Kin Hung Fung and C. T. Chan. Analytical study of the plasmonic modes of a metal nanoparticle circular array. *Phys. Rev. B*, 77:205423, May 2008. doi: 10.1103/PhysRevB.77.205423. URL http://link.aps.org/doi/10.1103/PhysRevB.77.205423.

[94] C.A. Balanis. *Antenna Theory: Analysis and Design*. Number v. 1 in Antenna Theory: Analysis and Design. John Wiley & Sons, 2005. ISBN 9780471667827. URL https://books.google.es/books?id=jwjeAwAAQBAJ.

[95] JP Connolly, C David, P Rodriguez, A Griol, P Welti, L Belliéres, J Ayucar, J Hurtado, R Lopez, G Sanchez, et al. Analysis of plasmonic nanoparticle fabrication techniques for efficient integration in photovoltaic

devices. In *Proceedings of the 25th European Photovoltaic Solar Energy Conference and Exhibition/5th World Conference on Photovoltaic Energy Conversion, Valencia, Spain*, pages 6–10, 2010.

[96] Lukas Novotny. Allowed and forbidden light in near-field optics. i. a single dipolar light source. *JOSA A*, 14(1):91–104, 1997.

[97] Lukas Novotny. Allowed and forbidden light in near-field optics. ii. interacting dipolar particles. *JOSA A*, 14(1):105–113, 1997.

[98] S.R.J. Brueck. Radiation from a dipole embedded in a dielectric slab. *Selected Topics in Quantum Electronics, IEEE Journal of*, 6(6):899–910, Nov 2000. ISSN 1077-260X. doi: 10.1109/2944.902140.

[99] Jesper Jung, Thomas Søndergaard, Thomas Garm Pedersen, Kjeld Pedersen, Arne Nylandsted Larsen, and Brian Bech Nielsen. Dyadic greenŠs functions of thin films: Applications within plasmonic solar cells. *Physical Review B*, 83(8):085419, 2011.

[100] John M. Howie. *Complex Analysis*. Number ISBN:978-1-4471-0027-0. Springer, 1st edition, 2003.

[101] Gregory J Gbur. *Mathematical Methods for Optical Physics and Engineering*. Cambridge University Press, 2011.

[102] Didier Felbacq. Finding resonance poles by means of cauchy integrals. In *2011 13TH INTERNATIONAL CONFERENCE ON TRANSPARENT OPTICAL NETWORKS (ICTON)*, pages 1–4, 2011.

[103] Didier Felbacq. Numerical computation of resonance poles in scattering theory. *Phys. Rev. E*, 64:047702, Sep 2001. doi: 10.1103/PhysRevE. 64.047702. URL http://link.aps.org/doi/10.1103/PhysRevE.64. 047702.

[104] Lukas Novotny and Bert Hecht. *Principles of nano-optics*. Cambridge university press, 2012.

[105] Walter Gautschi. Gauss-kronrod quadratureŮa survey. *Numerical methods and approximation theory III*, 3:39–66, 1988.

[106] Ruzica Golubovic, Athanasios G Polimeridis, and Juan R Mosig. Efficient algorithms for computing sommerfeld integral tails. *Antennas and Propagation, IEEE Transactions on*, 60(5):2409–2417, 2012.

[107] Mathieu Langlais, Jean-Paul Hugonin, Mondher Besbes, and Philippe Ben-Abdallah. Cooperative electromagnetic interactions between nanoparticles for solar energy harvesting. *Optics express*, 22(103):A577–A588, 2014.

[108] Jesper Jung and Thomas G Pedersen. Polarizability of supported metal nanoparticles: Mehler-fock approach. *Journal of Applied Physics*, 112(6): 064312, 2012.

[109] E. Stefan Kooij, Waqqar Ahmed, Harold J. W. Zandvliet, and Bene Poelsema. Localized plasmons in noble metal nanospheroids. *The Journal of Physical Chemistry C*, 115(21):10321–10332, 2011. doi: 10.1021/jp112085s. URL http://dx.doi.org/10.1021/jp112085s.

[110] H.G. Merkus. *Particle Size Measurements: Fundamentals, Practice, Quality*. Particle Technology Series. Springer Netherlands, 2009. ISBN 9781402090165. URL https://books.google.es/books?id=lLx4GzA-7AUC.

[111] S V Fomichev and D F Zaretsky. Vlasov theory of mie resonance broadening in metal clusters. *Journal of Physics B: Atomic, Molecular and Optical Physics*, 32(21):5083, 1999. URL http://stacks.iop.org/0953-4075/32/i=21/a=303.

[112] J Sancho-Parramon. Surface plasmon resonance broadening of metallic particles in the quasi-static approximation: a numerical study of size confinement and interparticle interaction effects. *Nanotechnology*, 20(23): 235706, 2009. URL http://stacks.iop.org/0957-4484/20/i=23/a=235706.

[113] Howard R. Stuart and Dennis G. Hall. Absorption enhancement in silicon on insulator waveguides using metal island films. *Applied Physics Letters*, 69(16):2327–2329, 1996. doi: http://dx.doi.org/10.1063/1.117513. URL http://scitation.aip.org/content/aip/journal/apl/69/16/10.1063/1.117513.

[114] Tristan L. Temple and Darren M. Bagnall. Broadband scattering of the solar spectrum by spherical metal nanoparticles. *Progress in Photovoltaics: Research and Applications*, 21(4):600–611, 2013. ISSN 1099-159X. doi: 10.1002/pip.1237. URL http://dx.doi.org/10.1002/pip.1237.

[115] C.J. Davisson. The diffraction of electrons by a crystal of nickel. *Bell System Technical Journal, The*, 7(1):90–105, Jan 1928. ISSN 0005-8580. doi: 10.1002/j.1538-7305.1928.tb00342.x.

[116] B. J. Spencer, S. H. Davis, and P. W. Voorhees. Morphological instability in epitaxially strained dislocation-free solid films: Nonlinear evolution. *Phys. Rev. B*, 47:9760–9777, Apr 1993. doi: 10.1103/PhysRevB.47.9760.

[117] A. A. Golovin, S. H. Davis, and P. W. Voorhees. Self-organization of quantum dots in epitaxially strained solid films. *Phys. Rev. E*, 68:056203, Nov 2003. doi: 10.1103/PhysRevE.68.056203.

[118] W. T. Tekalign and B. J. Spencer. Evolution equation for a thin epitaxial film on a deformable substrate. *Journal of Applied Physics*, 96(10):5505–5512, 2004. doi: http://dx.doi.org/10.1063/1.1766084.

[119] Y. W. Zhang. Surface stability and evolution of biaxially strained epitaxial thin films. *Applied Physics Letters*, 87(12):121916, 2005. doi: http://dx.doi.org/10.1063/1.2053367.

[120] Yaoyu Pang and Rui Huang. Nonlinear effects of stress and wetting on surface evolution of epitaxial thin films. *Physical Review B*, 74:075413–1, 075413–11, 2006. doi: 10.1103/PhysRevB.74.075413.

[121] B. J. Spencer. Asymptotic derivation of the glued-wetting-layer model and contact-angle condition for stranski-krastanow islands. *Phys. Rev. B*, 59:2011–2017, Jan 1999. doi: 10.1103/PhysRevB.59.2011.

[122] Jan H. van der Merwe. Misfit dislocation generation in epitaxial layers. *Critical Reviews in Solid State and Materials Sciences*, 17(3):187–209, 1991. doi: 10.1080/10408439108243751.

[123] D. J. Eaglesham and M. Cerullo. Dislocation-free stranski-krastanow growth of ge on si(100). *Phys. Rev. Lett.*, 64:1943–1946, Apr 1990. doi: 10.1103/PhysRevLett.64.1943.

[124] J. A. Floro, S. J. Hearne, J. A. Hunter, P. Kotula, E. Chason, S. C. Seel, and C. V. Thompson. The dynamic competition between stress generation and relaxation mechanisms during coalescence of volmer-weber thin films. *Journal of Applied Physics*, 89(9):4886–4897, 2001. doi: http://dx.doi.org/10.1063/1.1352563.

[125] Seweryn Morawiec, Manuel J Mendes, Salvatore Mirabella, Francesca Simone, Francesco Priolo, and Isodiana Crupi. Self-assembled silver nanoparticles for plasmon-enhanced solar cell back reflectors: correlation between structural and optical properties. *Nanotechnology*, 24(26): 265601, 2013. URL `http://stacks.iop.org/0957-4484/24/i=26/a=265601`.

[126] Hairen Tan, Rudi Santbergen, Arno H. M. Smets, and Miro Zeman. Plasmonic light trapping in thin-film silicon solar cells with improved self-assembled silver nanoparticles. *Nano Letters*, 12(8):4070–4076, 2012. doi: 10.1021/nl301521z. URL `http://dx.doi.org/10.1021/nl301521z`. PMID: 22738234.

[127] Kevin M. McPeak, Sriharsha V. Jayanti, Stephan J. P. Kress, Stefan Meyer, Stelio Iotti, Aurelio Rossinelli, and David J. Norris. Plasmonic

films can easily be better: Rules and recipes. *ACS Photonics*, 2(3):326–333, 2015. doi: 10.1021/ph5004237. URL http://dx.doi.org/10.1021/ph5004237. PMID: 25950012.

[128] T W H Oates, M Losurdo, S Noda, and K Hinrichs. The effect of atmospheric tarnishing on the optical and structural properties of silver nanoparticles. *Journal of Physics D: Applied Physics*, 46(14):145308, 2013. URL http://stacks.iop.org/0022-3727/46/i=14/a=145308.

[129] Wei Cao and Hani E. Elsayed-Ali. Stability of ag nanoparticles fabricated by electron beam lithography. *Materials Letters*, 63(26):2263 − 2266, 2009. ISSN 0167-577X. doi: http://dx.doi.org/10.1016/j.matlet.2009.07.052. URL http://www.sciencedirect.com/science/article/pii/S0167577X09005692.

[130] G. Baraldi, M. Carrada, J. Toudert, F. J. Ferrer, A. Arbouet, V. Paillard, and J. Gonzalo. Preventing the degradation of ag nanoparticles using an ultrathin a-al2o3 layer as protective barrier. *The Journal of Physical Chemistry C*, 117(18):9431–9439, 2013. doi: 10.1021/jp401421m. URL http://dx.doi.org/10.1021/jp401421m.

[131] R Santbergen, T L Temple, R Liang, A H M Smets, R A C M M van Swaaij, and M Zeman. Application of plasmonic silver island films in thin-film silicon solar cells. *Journal of Optics*, 14(2):024010, 2012. URL http://stacks.iop.org/2040-8986/14/i=2/a=024010.

[132] G Galbiati, VD Mihailetchi, A Halm, R Roescu, and R Kopecek. Results on n-type ibc solar cells using industrial optimized techniques in the fabrication processing. *Energy Procedia*, 8:421–426, 2011.

[133] Cheng Yang, Gang Zhang, Hua Min Li, Won Jong Yoo, Young Jun Park, and Jong Min Kim. Localized surface plasmon resonances caused by ag nanoparticles on sin for solar cell applications. *Journal of the Korean Physical Society*, 56(5):1488–1491, 2010.

[134] P. Spinelli, M. Hebbink, R. de Waele, L. Black, F. Lenzmann, and A. Polman. Optical impedance matching using coupled plasmonic nanoparticle arrays. *Nano Letters*, 11(4):1760–1765, 2011. doi: 10.1021/nl200321u. URL http://dx.doi.org/10.1021/nl200321u. PMID: 21410242.

[135] Rudi Santbergen, Hairen Tan, Miro Zeman, and Arno H. M. Smets. Enhancing the driving field for plasmonic nanoparticles in thin-film solar cells. *Opt. Express*, 22(S4):A1023–A1028, Jun 2014. doi: 10.1364/OE.22.0A1023. URL http://www.opticsexpress.org/abstract.cfm?URI=oe-22-104-A1023.

[136] S Pillai, FJ Beck, KR Catchpole, Z Ouyang, and MA Green. The effect of dielectric spacer thickness on surface plasmon enhanced solar cells for front and rear side depositions. *Journal of Applied Physics*, 109(7): 073105, 2011.

[137] Boris Luk'yanchuk, Nikolay I Zheludev, Stefan A Maier, Naomi J Halas, Peter Nordlander, Harald Giessen, and Chong Tow Chong. The fano resonance in plasmonic nanostructures and metamaterials. *Nature materials*, 9(9):707–715, 2010.

[138] Nikolay A. Mirin, Kui Bao, and Peter Nordlander. Fano resonances in plasmonic nanoparticle aggregatesâĂ. *The Journal of Physical Chemistry A*, 113(16):4028–4034, 2009. doi: 10.1021/jp810411q. URL http://dx.doi.org/10.1021/jp810411q. PMID: 19371111.

[139] Michael I. Tribelsky. Phenomenological approach to light scattering by small particles and directional fano's resonances. *EPL (Europhysics Letters)*, 104(3):34002, 2013. URL http://stacks.iop.org/0295-5075/104/i=3/a=34002.

[140] FJ Beck, E Verhagen, S Mokkapati, A Polman, and KR Catchpole. Resonant spp modes supported by discrete metal nanoparticles on high-index substrates. *Optics express*, 19(102):A146–A156, 2011.

[141] Yu A Akimov and WS Koh. Resonant and nonresonant plasmonic nanoparticle enhancement for thin-film silicon solar cells. *Nanotechnology*, 21 (23):235201, 2010.

[142] Peter Johansson. Light scattering from disordered overlayers of metallic nanoparticles. *Phys. Rev. B*, 64:165405, Oct 2001. doi: 10.1103/PhysRevB.64.165405. URL http://link.aps.org/doi/10.1103/PhysRevB.64.165405.

[143] Jerome Mertz. Radiative absorption, fluorescence, and scattering of a classical dipole near a lossless interface: a unified description. *J. Opt. Soc. Am. B*, 17(11):1906–1913, Nov 2000. doi: 10.1364/JOSAB.17.001906. URL http://josab.osa.org/abstract.cfm?URI=josab-17-11-1906.

List of Figures

List of Tables